Massachusetts Institute of Technology
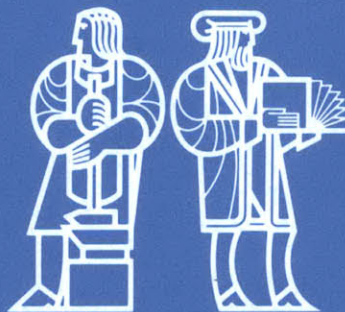
Department of Nuclear Engineering

MODELING OF CORIUM/CONCRETE INTERACTION

by

M. Lee and M.S. Kazimi

MITNE - 267

Department of Nuclear Engineering

Massachusetts Institute of Technoloogy

June 1985

MODELING OF CORIUM/CONCRETE INTERACTION

by

M. Lee and M.S. Kazimi

MODELING OF CORIUM/CONCRETE INTERACTION

ABSTRACT

In the highly unlikely event of a loss of cooling accident in a LWR followed by failure of certain engineered safety features of the reactor system, the core may eventually melt due to the generation of decay heat. If the safety features of the reactor system fail to arrest the accident within the vessel, the molten core debris (corium) will fall into the reactor cavity and attack the concrete walls and floor.

The heat transferred from the core melt to concrete can lead to concrete decomposition accompanied by gas generation, which along with direct heating of the atmosphere will lead to a pressure rise in the containment. The cooling rate of the core melt and the amount of gas generated by concrete decomposition will also affect the degree to which fission products may be released from the melt.

In this work some of the uncertainties in estimating the heat transfer resistances surrounding the melt and the freezing phenomena involved in the pool are investigated. A semiempirical correlation for calculating the downward heat transfer coefficient is derived based on periodic contact between the liquid pool and the underlying solid in simulant experiments of water or benzene on dry ice. The correlation predicts that the downward heat transfer coefficient across the corium/concrete interface increases with superficial gas velocity. The experimental data on interfacial heat transfer between bubble agitated immiscible layers are reviewed and a new model based on the surface renewal concept is proposed. The hydrodynamic instability of a liquid jet is used to determine the onset of bubble induced entrainment at low gas velocity. It is concluded that the bubble induced liquid entrainment will not occur in the Corium/Concrete Interaction at low gas velocity, unlike the observed behavior in oil/water simulant experiments.

The proposed downward and interfacial heat transfer models have been incorporated into an integral analysis code, CORCON Mod1, developed by Sandia laboratories. The proposed models are qualified by comparison to the results of the German BETA experiments of several hundred kg steel melt internally heated by induction.

Based on these comparisons, the following approach is proposed to calculate the downward heat transfer coefficient of a corium pool. If the temperature of the melt is initially very high, the heat flux will be high enough to stabilize a gas film, and the interaction can be modeled with the CORCON gas film model until the gas velocity decreases below a minimum stable gas film limit. After the film collapses, the heat transfer can be described by the periodic contact model. If the initial temperature is not high enough to generate a film the heat transfer will be via periodic contact

throughout the time until freezing takes place. CORCON/Mod1 has been modified accordingly. and the results of BETA high melt temperature tests can be reproduced. However. the calculated results are sensitive to the assumed minimum gas velocity limit for a stable gas film.

A simplified containment model based on thermal equilibrium among all materials within the containment is developed, and is integrated with the modified CORCON/Mod1. The combined model. called CORCELL. is used to study the impact of Corium/Concrete Interaction on containment pressurization. It is found that the downward heat transfer model is very important in determining the concrete erosion rate. For the cases studied, the containment pressurization rate is less sensitive to the amount of gas generated. Should combustion of H_2 and CO occur, the containment pressure would be larger for higher downward heat transfer. For containment pressurization, the interfacial and upward convective heat transfer coefficients are relatively unimportant. However, the temperature profile of the corium pool will be affected by these parameters. It is also found that by considering the heat conducted into the containment concrete wall, the containment pressure can be significantly reduced.

The stability of a horizontal crust layer under the impact of gas injection is studied by a simulant experiment. A test apparatus is built with heat removal via Freon-12 cooling of a porous plate at the bottom. Water freezing with air injection is observed in the experiments. For the cases studied. a stable solidified layer is formed across the bubble agitated horizontal liquid/solid interface. Hence. such a layer should be considered in the integral analysis codes of reactor accident.

ACKNOWLEDGEMENTS

TABLE OF CONTENTS

Chapter 1 INTRODUCTION AND BACKGROUND

Chapter 2 IMPACT OF CORIUM HEAT TRANSFER TO CONCRETE ON CONTAINMENT PRESSURE

Chapter 6   INTEGRAL ANALYSIS OF MELT/CONCRETE INTERACTION

Chapter 7   LWR CONTAINMENT PRESSURE RESPONSE: THE CORCELL MODEL

Chapter 8 SUMMARY AND CONCLUSION

LIST OF TABLES

LIST OF FIGURES

NOMENCLTURE

A	$(\sigma/g(\rho_p - \rho_{ms}))^{0.5}$, Laplace constant (m)
A	total cross section of interface (m^2) (Chapter 4)
A	heat transfer area of containment inner wall (m^2) (Chapter 7)
A_b	surface area swept by one bubble (m^2)
A_{jet}	surface area of liquid jet (m^2)
C_g	initial gas weight fraction of concrete
C_p	specific heat (J/kg)
f	bubble generation frequency $(1/sec)$
h	heat transfer coefficient $(W/m^{2\,c}K)$
h_{decom}	decomposition enthalpy of concrete (J/kg)
h_j	specific enthalpy of material $'j'$ (J/kg)
h_{sf}	fusion heat of substrate (J/kg)
H'	height of gravitation center of jet (m)
H_{max}	maximum length of liquid jet (m)
$I(t)$	impulse (N) (Chapter 4)
J_f	superficial velocity of rising fluid (m/sec)
J_g	superficial gas velocity (m/sec)
K	thermal conductivity $(W/m\ sec)$
L	thickness of containment concrete wall (m) (Chapter 7)
M	molecular weight (Chapter 6)
M_i	mass of material $'i'$ in the containment (kg)
$\dot{M}_j$	mass flow rate of material $'j$ out of the containemnt (kg/sec)

$\dot{N}_i$	number of bubbles produced per unit time
Nu	Nusselt number
n/A	bubble population density $(1/m^2)$
P	system pressure (N/m^2)
P_o	initial power of reactor (MW) (Chapter 2)
Pr	Prandtl number
$\dot{Q}_k$	rate of heat addition by process $'k'$ (J/sec)
Ra	Rayleigh number
Re	Reynold number
r_b	equivalent bubble radius (m)
R_d	bubble departure radius (m)
r_{jet}	radius of liquid jet (m)
S	slip ratio of gas and slag
T_D	decomposition temperature of solid $(^\circ K)$
T_p	pool bulk temperature $(^\circ K)$
T_I	interface temperature $(^\circ K)$
T_o	initial temperature of containment concrete wall $(^\circ K)$
T_∞	containment atmosphere temperature $(^\circ K)$
t_d	bubble departure period (sec)
u_i	specific internal energy of material $'i'$ (J/kg)
U	total internal energy of containment atmosphere (J)
U_o	velocity of liquid jet (m/sec)
V_b	volume of bubbles (m^3)
V_{jet}	volume of liquid jet (m^3)

V_{ter}	terminal velocity of bubble (m/sec)
x	initial gas weight fraction of concrete
x	mole fraction (Chapter 6)
ρ	density (kg/m^3)
ν	kinematic viscosity (m^2/sec)
μ	viscosity $(kg/m\ sec)$
σ	surface tension (N/m)
α	thermal diffusivity (m^2/sec)
α	void fraction (Eq. 3.33)
θ_d	bubble departure angle
β	volumetric thermal expansion coefficient $(1/^\circ K)$ (Eq. 4.2)
τ	time constant of impulse (sec)

Subscripts

a	air $(N_2 + O_2)$
combustion	chemical energy from the gas combustion
decay	decay heat
g	gases generated from the decomposed concrete (Chapter 2)
g	gas (Chapter 3)
g'	noncondensible gases depleted in combustion and metallic reactions
ℓ	liquid
L	lower liquid layer
metallic	chemical energy from metallic reaction
ms	melted solid

NC	natural convection
p	pool
$removed$	heat transferred out of the containment via the fan coolers
s	structural material in the containment (Chapter 2)
s	solid substrate
SR	surface renewal
U	upper liquid layer
wa	accumulator water
wc	water vapor in the containment atmosphere
wp	spray water
ws	primary water
1	initial state of containment
2	end state of containment

CHAPTER 1

INTRODUCTION AND BACKGROUND

1.1 Motivation for This Work

A potential risk to the public of operating a commerical Light Water Reactor (LWR) is due to an uncontrolled release of a large amount of radioactivity. The only way that a large amount of radioactivity could be released is by melting the fuel in the reactor core. All accidents involving some fuel melting are beyond the design basis and termed "Degraded Core Accidents". In the current design of nuclear power plants, an essentially leaktight containment building is provided to prevent the initial dispersion of the airborn radioactivity into the environment. Although several features are able to ensure the integrity of the containment for some time after a nuclear core meltdown, the containment may ultimately fail causing a release of radioactivity if the engineered features do not function properly.

The failure potential of the containment is accident sequence dependent. The time delay to the release of radioactivity is important in evaluating the consequence of the core meltdown accidents because of the presence of many short half life fission products, and the increase probability for fission products deposition and retention on the available surface.

In the highly unlikely event of a LWR degraded core accident with complete failure of normal and emergency coolant flow, the decay heat would cause fuel rods to heat up to temperatures above the design limit. If the cooling failure presisted for extended time periods, the combination of decay heat and the exothermic zirconium/water reaction would cause melting of the reactor core. This could lead to slumping of the molten core material (corium) down into the vessel lower plenum,

followed by vessel failure and deposition of these materials into the concrete reactor cavity. Corium could then attack the concrete of the cavity floor, releasing gas and vapor (CO_2 and H_2O) and ablating the solid concrete, a phenomenon known as Molten Core/Concrete Interaction (MCCI).

The potential hazard of a MCCI is the threat to the integrity of the containment building due to any of the following:

1. The possibility of a basemat meltthrough.
2. Containment over-pressurization due to the generation of noncondensible gases.
3. Oxidation of combustible gases generated from the chemical reactions between water vapor, carbon dioxide and the metallic elements in the corium pool.
4. Meltthrough of the containment steel liner and subsequent loss of containment leak-tightness.

Another important implication for reactor safety assessment is the MCCI effect on releasing fission products from the corium pool; the generation of aerosols which may escape the containment building if leaktightness is lost.

WASH-1400 is the first work which attempted to quantify the physical process involved in MCCI. The calculations in WASH-1400 were approximation given the crude state of knowledge then. Since these early calculations the phenomena of MCCI have been the subject of both experimental and analytical research.

1.2 Scope of This Work

One of the major concerns of modeling the debris pool is the partition of heat from the radioactivity decay and chemical reactions between the containment atmosphere and surrounding concrete. This depends on the heat transfer resistance through each path and also on the freezing phenomena involved in the pool. In this work, the downward heat transfer across the horizontal corium/concrete interface and the interfacial heat transfer between the bubble agitated immiscible liquid lay-

15

ers are investigated. An understanding of the freezing phenomena will be obtained through a simulant experiment.

The proposed models are validated by comparsion to the results of the German BETA experiments of several hundred kg steel melt internally heated by induction. A simplified containment model based on thermal equilibrium among all the materials within the containment is developed and used to study the impact of Corium/Concrete Interaction on containment pressurization.

1.3 BACKGROUND

1.3.1 General

There are three types of concrete: (1) basaltic aggregate, (2) limestone aggregate/common sand and (3) limestone aggregate. The first two of these concrete types are representative of concrete in a large number of LWRs. The major constituent of basaltic aggregate concrete is SiO_2, hence sometimes referred to as siliceous concrete. The major constituent of the other two types concrete is $CaCO_3$. hence sometimes referred to as calcareous concrete. The compositions of these concrete types are summarized in Table 1.1.

In the event of a melt through, the MCCI begins while the temperature of corium lies between 2400 $^\circ K$ and 3100 $^\circ K$ (depending upon its composition). The concrete would heat up and melt. A number of events occur as concrete is heated from room temperature to the melting point [P5]. First. the evaporable water amounting to 2.3 $\sim$ 3 weight percent of concrete is lost over the temperature range of 300 $^\circ K$ to 520 $^\circ K$. Then. chemically constituted water which makes up 1.5 $\sim$ 2.0 weight percent of concrete is lost between 650 $^\circ K$ to 700 $^\circ K$. Both loss of evaporable water and chemically constituted water are the results of decomposing species in the cementituous phase of the concrete. The final decomposition reaction of concrete is decarboxlation of both cementituous species and concrete aggregate. This reaction,

16

Table 1.1

Specifications of Concrete [M3]

Species	Basaltic	Limestone/ Commmon Sand	Limestone
	Weight %	Weight %	Weight %
SiO_2	54.84	35.80	3.60
TiO_2	1.05	0.18	0.12
MnO	0.00	0.03	0.01
MgO	6.16	0.48	5.67
$CaCO_3$	10.32	52.45	81.10
Na_2O	1.80	0.082	0.078
K_2O	5.39	1.22	0.68
Fe_2O_3	6.26	1.44	1.20
Al_2O_3	8.32	3.60	1.60
Cr_2O_3	0.00	0.014	0.004
$(H_2O)_{evap}$	3.86	2.70	3.94
$(H_2O)_{bound}$	2.00	2.00	2.00
Total Gas Content	7.26	25.85	41.64

which becomes significant at temperature as low as 820 $^\circ K$, involves a loss of about 23 ~ 35 weight percent in the case of calcareous concrete but only 1 weight percent in the case of basaltic concrete. Finally the concrete melts in the range 1350 $^\circ K$ to 1875 $^\circ K$.

In WASH-1400 [R1], it was assumed that the mechanism for erosion of concrete by corium was rapid spallation of the first 0.5 m of concrete followed by decomposition and dissolution of the remaining concrete. It was estimated that the corium penetrates the 3 m thick concrete basemat in approximately $18(+10, -5)$ *hours*. The calculations in WASH-1400 were approximations given the crude state of knowledge then. Several experimental observations made after 1974, as described in the following section, provide a better assessment of the MCCI events. These experiments are summarized in Table 1.2.

1.3.2 Melt/Concrete Interaction Experiments

1.3.2.1 Sandia National Laboratory (USA)

A research program to investigate Corium/Concrete Interaction was initiated at Sandia Laboratories in July 1975. Based on the characteristics of the experiments, their experimental works can be divided into the following categories:

(1)Concrete Surface Heating Experiments

The objective of this phase of study was to investigate the response of concrete exposed to a high heat flux on one surface in the absence of chemical interactions with corium. In those experiments, cylindrical test samples ($d = 145.6\ mm$) were exposed either to a 2-Megawatt plasma jet [M2,P5] or to a radiant heat facility[C4,P5]. The surface heat flux varied from 0.3 ~ 3.0 MW/m^2.

Those experiments led to the following conclusions [M1]:

- The dominant erosion mechanism for both calcareous and basaltic concrete

18

Table 1.2

Melt/Concrete Interaction Experiment

Investigater	Experiment	Concrete Type	Melt Material	Initial Temp.($^\circ K$)	Amount of Melt kg	Generated by	Internal Heating	Ref
Sandia	Large Scale	Basaltic/ Steel	Mild	~1970	200	Induction Furnace	no	M1,S1
	Calcareous							
Sandia	Small Scale	Basaltic/	Steel	~3300	12	Thermite	no	M1,P7
	Calcareous					Reaction		
Sandia	Coil 1 &	Basaltic/	Steel	~1970	~200	Induction	Induction	P6
	CC1,CC2	Calcareous				Furnace	Heating	
Sandia	Burn Series	Basaltic/	Corium/	Varied	Varied	Thermite/	Induction	S2,S3
		Calcareous	Steel			Induction	Heating/no	
ANL		Limestone	Steel	Varied	1	Induction heating	Induction Heating	B1
ANL		Limestone	UO_2	~3100	1	Thermite	Resistance Heating	B1
ANL		Limestone	UO_2	~3100	6.5	Thermite	Resistance Heating	F2.S5
KfK		Basaltic/ Calcareous	Corium	Varied	0.1 ~10	Thermite	no	P2
KfK	BETA	Basaltic	Iron,Steel Al_2O_3, SiO_2	2173 ~2473	max. 600	Thermite	Induction Heating	R4.A5

appears to be melting of the cementituous material in the matrix accompanied by dehydration and decomposition of the underlying concrete.

– Erosion is a quiescent process with negligible spallation that becomes a steady processes with an essentially constant erosion rate 30 to 60 *sec* after initiation of heating.

– From the post-test examinations of concrete samples, a dehydration layer was found under the melt front.

– The effect of exposed reinforcing rods on concrete erosion is negligible.

(2)<u>Melt/Concrete Experiments without Internal Heating</u>

In Large Scale [M1,P7] and Small Scale [M1,S1] experiments of Sandia, melt steel was poured on the basaltic or calcareous concrete crucibles. The melt was generated either by thermite reaction or inside an induction furnace. The erosion rate was traced by the response of thermocouples embedded in the concrete crucibles. The conditions of these experiments are summarized in Table 1.2.

From these experiments, the following general conclusions were made:

– Basaltic concrete and calcareous concrete behave in qualitatively similar ways when exposed to high temperature melts.

– Contact between the melt and concrete is marked by the vigorous evolution of gas. This evolution is sufficient to levitate and disrupt the molten pool.

– Evolved gases burn brilliantly in air and are self-limited. Chemical analysis shows the compositions of the gases to be predominantly a mixture of CO, CO_2, H_2, and H_2O. Carbon dioxide and water are from the thermal decomposition of concrete. H_2 and CO are formed as H_2O and CO_2 percolate through, and are chemically reduced by the metallic melt.

– The decomposition products (slag) of concrete are largely immiscible with steel melt. Density driven stratification of the melt into slag and metal phases occures quickly and is not greatly disrupted by the gas evolution process.

– The erosion rates at radial and axial directions are approximately the same and are proportional to the temperature of the melt. The rates in the Large Scale tests were 0.25 ± 0.15 m/hr for both types of concrete. Results of the Small Scale, high temperature tests, indicated penetration rates as high as 1.3 ± 0.50 m/hr.

(3) Melt/Concrete Experiment with Sustained Internal Heating

Several attempts have been made at Sandia Laboratories to provide internal heating within the melt to simulate the decay heat generation of corium. The conditions of these experiments are also summarized in Table 1.2.

In COIL1 [P6], a coaxial induction coil was embedded in the calcareous concrete crucible to maintain sustained heating of steel melt by induction. It was found that the erosion was predominantly downward and radial erosion of the cavity was fairly insignificant. Quantiative results for this test are not available. Tests CC1 and CC2 [S4] are designated for the purpose of code comparison. They had the same set up as that of COIL1 test. The results of those test have not been published.

The series of BURN [P8,S1,S2,S3] experiments at Sandia contain 10 small scale tests. In this series the attack on concrete by hot solidified prototypic core material was studied. In BURN2 [S1], a 5 kg cylindrical steel slug was centered in the cavity of calcareous concrete crucible. Then, the crucible was located in a helical induction coil. The temperature of the steel rose rapidly (0.3 ~ 1.2 $°K/min$) until it reached near 1650 ± 20 $°K$. When the steel reached a temperature of 470 $°K$, steam began to condense about the test apparatus. At a steel temperature of 1170 $°K$, more vigorous gas evolution occured. At 1610 ± 10 $°K$ liquid oxide were spewed out of the crucible through the gaps. The erosion rates were 31.75 mm/hr and 22.10 mm/hr in axial and radial directions respectively.

An $X - Ray$ imaging technique was employed [P8] to directly observe the

melt/concrete interaction in real time in some of the BURN tests. However, the resolution of the $X - Ray$ (~ 30 mm) was too large to tell what was happening at the melt/concrete interface. From the frames of the $X - Ray$, it was seen that the pool level swelling due to the gas flow could be as much as 250% of the gas-free pool depth for a pool with 0.8 kg melt. Again, most results of the BURN tests have not been published.

1.3.2.2 Argonne National Laboratory (USA)

At ANL, the dehydration of concrete was studied by placing the concrete sample on top of an induction heated plate [B1]. A temperature of 1070 $^\circ K$ could be reached at the concrete surface. In another experiment, a disc of stainless steel, ~ 20 mm thick, was placed on top of the concrete and heated rapidly to melting by induction [B1]. In some of the tests, small scale spalling of concrete was observed. In the molten UO_2/concrete experiment of ANL, the UO_2 powder was packed into the concrete cavity and then heated up by a combination of thermite reaction and electric current [B1]. It was found that the molten oxide from the concrete was mutually soluble with UO_2. This solution process could proceed even if the UO_2 was not molten [F2,S5]. In these experiments, a single large cavity was formed within the solidified UO_2/slag mixture configuration. The top surface of the mixture was displaced upward and solidified into a mountain-like protrusion, bearing a vent in its apex [F2].

1.3.2.3 Kernforschungszentrum Karlsruhe (FRG)

A complete summary of the early German experimental work on melt/ concrete interaction was given in Reference [P2]. The results were consistent with those mentioned above.

BETA [A5,R4], a key experimental program of melt/concrete interaction is currently undertaken at KfK. The BETA facility is unique with regard to size and experimental capability. The results of BETA experiments will be used to verify

the existing melt/concrete interaction analysis codes. Maximum amounts of 300 kg metallic and 300 kg oxidic melt can be generated by a thermite reaction and then poured into a concrete crucible. The melt can be heated by induction to maintain the characteristic temperature of a certain test. The maximum heating power that can be generated is 1.7 MW.

The test matrix of BETA experiments is divided into high and low temperature phases. In the high temperature phase, the highest temperature will be above 2270 $°K$ and the lowest about 1770 $°K$ just before solidification. The main objectives are to determine the heat transfer rate from the melt, the penetration velocity of the melt in the axial and radial directions, the released composition of the gaseous products, as well as the aerosol release and the general behavior of all materials. The main interest in the low temperature phase is focused on the behavior of the solidifying melt and the long term behavior of the whole system with respect to heat transfer and the material behavior during the crust formation.

The completed tests at the time of this writing are in the high temperature phase. The main results are [A5]:

- Downward propagation of the melt dominated for all high temperature experiments. This differs from the various transient experiments without sustained heating which gave similar axial and radial erosions. However, this is consistent with the results of COIL1 test of Sandia.
- Entrainment of the metallic phase into the oxidic phase occurs mainly at high temperature levels of the melt and seems to be controlled by the gas release rate.
- Relatively insignficant amount of aerosols were observed.

In all the tests that have been made the concrete crucible were from the basaltic concrete typical for German nuclear power plants. Some tests with calcareous concrete crucible are scheduled to be made in the summer of 1985.

1.3.2.4 Miscellaneous

Due to the extremely high temperature involved in the melt/concrete interaction experiments, the physical details of the interaction process have been difficult to interpret. Some simulant experiments have been performed [A2,F1,P3]. Among those, the one by M. Plys [P3] preserved most of the major phenomena of melt/concrete interaction. In his experiment, the melt pool was simulated with adipic acid, the concrete was simulated with azelcai acid, sodium bicarbonate plus polythylene glycol as binder. On decomposition, gas was generated and the remainder of the melt substrate became miscible with the pool material. The decay heat generation of the corium was simulated with an immersed heater. From the experiment, it was observed that after a few minutes of interaction a crust (solidified pool material) was formed around the entire periphery (except the top) and the gas flow rate decreased and finally ceased after about 5 min. Typical overall erosion distances are $1 \sim 3$ mm downward and $4 \sim 8$ mm sideward. This trend is different from that of BETA high temperature experiments.

1.3.3 Physical Phemonena of Corium/Concrete Interaction

From the phenomena observed in the above experiments, the following physical picture can be developed for Corium/Concrete Interaction.

The MCCI is a long term endothermic erosion of concrete by high temperature corium. The erosion of concrete is a quasi-static process with negligible spallation and accompanied by the generation of large amount of gases.

The experimental evidence shows that the various oxide in the corium are highly miscible, as are the metallic species, but that the two groups are mutually immiscible. Buoyancy forces may be sufficient to separate the molten debris into two layers, even in the presence of vigorous mixing by the decomposition gases. The concrete decomposition gases, initally CO_2 and H_2O, may percolate through the pool unless

they can escape at the pool periphery, e.g. the gases generated from the sideward erosion. The presence of the gases in the pool will elevate the pool surface and increase the layer thickness. therefore changing the geometry of the corium pool. The bubbling of gases through the pool tends to enhance the heat transfer between layers and create mixing within the layer. The heat transfer process between corium and concrete is also complicated by this gas percolation.

The gases which pass through the pool may encounter some metallic elememts, e.g. *Zr, Fe, Ni* etc, and be reduced as the metal is oxidized. These chemical reactions will change the composition of the pool, add energy to the pool and generate flammable gases H2 and CO. The composition of the pool is also changed by the addition of slag to the oxidic phase of corium. The slag will dilute the oxidic layer, decrease its power density and reduce the freezing point.

As time progresses, the pool grows, its surface area increases and decay heating decreases. Therefore, pool temperature and interface heat flux decrease, and the possibility of freezing arises. Because the corium freezing temperature is above the concrete decomposition temperature, the erosion of concrete will proceed. From then on the attack on the concrete shifts from the molten pool to partially solidified debris. It is believed that the attack on concrete by solidified or partially solidified debris will presist for few days.

1.3.4 Analysis of Corium/Concrete Interaction

The analytical studies of MCCI Interaction can be divided into two parts. The modeling of the corium pool and/or partially solidified debris and the modeling of concrete response. The two parts are coupled together by the heat transfer rate between the corium and concrete. Knowing the heat flux, the concrete response model calculates the gas generation and erosion rates which serve as input to the debris behavior model for the determination of the heat transfer rate.

1.3.4.1 Behavior of the Corium Pool

The behavior of the corium pool is governed by a simple energy balance. Decay heat (and some heat from chemical reactions) is generated in the pool and may be lost either through its top surface or to concrete. The partition of energy between concrete and the top surface is determined by the ratio of thermal resistances of the corresponding paths.

Many efforts have been focused on the prediction of these heat transfer coefficients. The heat transfer phenomena invovled are: convective heat transfer within internally heated pool, heat transfer between immiscible liquid layers with gas agitation, erosion of miscible and immiscible substrates, heat transfer at erosion interface with gas injection. M.Plys [P4] presented an excellent review of these effort. Some of those works will also be mentioned in the following Chapters.

Several computer codes have been developed for an integral analysis of Corium/ Concrete Interaction. Those are INTER1 [M4], CORCON [M3,C6], GROWS II [B2], DECOMP [H4], EROS [P4], WECHSL [R2] and KAVERN. The first of such programs, INTER1, was developed by W.B.Murfin at Sandia in 1977. This model was a preliminary one and intended as a qualitative tool for sensitivity analysis. INTER1 has been incorporated into the MARCH [W3] code which is an integral analysis code to calculate the containment response. CORCON, a successor of INTER1, was also developed at Sandia. GROWS II was developed by ANL for the Fast Breeder Reactor safety. DECOMP (a proprietary code) was developed for the IDCOR (Industrial Degraded Core Rulemaking) program integrated analysis package known as MAAP. WECHSL was developed by KfK and KAVERN was developed by KWU of West Germany. General features of these codes are summarized in Table 1.3 and will be discussed here.

Significant efforts were also devoted to the calculations of the thermophysical properties of the corium e.g. thermal conductivity, viscosity, solidus and liquidus

Table 1.3

Features of MCCI Analysis Code

MCCI Model	Developed by	Freezing Model	Downward Heat Transfer Coef.	Interfacial Heat Transfer Coef.	Cavity Shape
INTER	Sandia	No	User	User Specified	Hemispherical Segment Intersected by a Cylinder
CORCON/Mod1	Sandia	No	Film Model [A4,D2]	Konsetov's Bulk Convection[K3]	Two-dimensional Axisymmetric
CORCON/Mod2	Sandia	Yes	Film Model [A4,D2]	Sezekely's Surface Renewal Model Modified by Greene[C6]	Two-dimensional Axisymmetric
WECHSL	KfK	Yes	Film[A4,D2] Discrete Bubble	Werle's Model [W2]	Two-dimensional Axisymmetric
DECOMP	IDCOR Program	Yes	–	–	Cylindrical

27

temperatures etc. These efforts are numerous and do not impact crux of this work, therefore, the details will not be covered here.

(1)CORCON

In CORCON, the molten pool is divided into several layers, the interafce with concrete is divided into several regions and various processes are mechanistically modeled. Figures 1.1 and 1.2 illustrate its fundamental regions.

CORCON assumes immediate separation of the immiscible phases of corium into metallic and oxidic layers, as shown in Fig.1.1 , it allows a three-layer structure for corium pool. Each layer is considered as a control volume for mass and energy balance. However, this configuration. oxide/metal/oxide, does not last long if it occurs at all. The heavy oxide (principally fuel) is diluted by concrete oxide until the mixture is less dense than the metal and the pool 'rolls over' into a configuration with all oxides in a single layer above the metal. CORCON calculations [M3] suggested that the three-layer configuration can not last more than about one hour.

In CORCON, it is assumed that each layer is essentially isothermal due to the agitation of concrete decomposition gases. The temperature drop from the layer bulk to the periphery, across the thermal boundary layer δ_t in Fig.1.2. is characterized by natural convection with thermal and bubble buoyancy terms [B6]. The weighting factors for thermal and bubble buoyancy terms are different for different regions in Fig.1.2. Based on the observations of a water/dry ice experiment [D2], a layer of gas film is assumed to exist at the corium/concrete interface. On a horizontal surface, the gases are allowed to bubble up into the pool. On vertical surfaces the gases are assumed to collect as a flowing boundary layer film. The heat transfer between corium and concrete is controlled by radiative and convective processes across the film. The drift flux model [W1] of two phase flow is employed in CORCON to calculate the void fraction and the swelling level of pool layers.
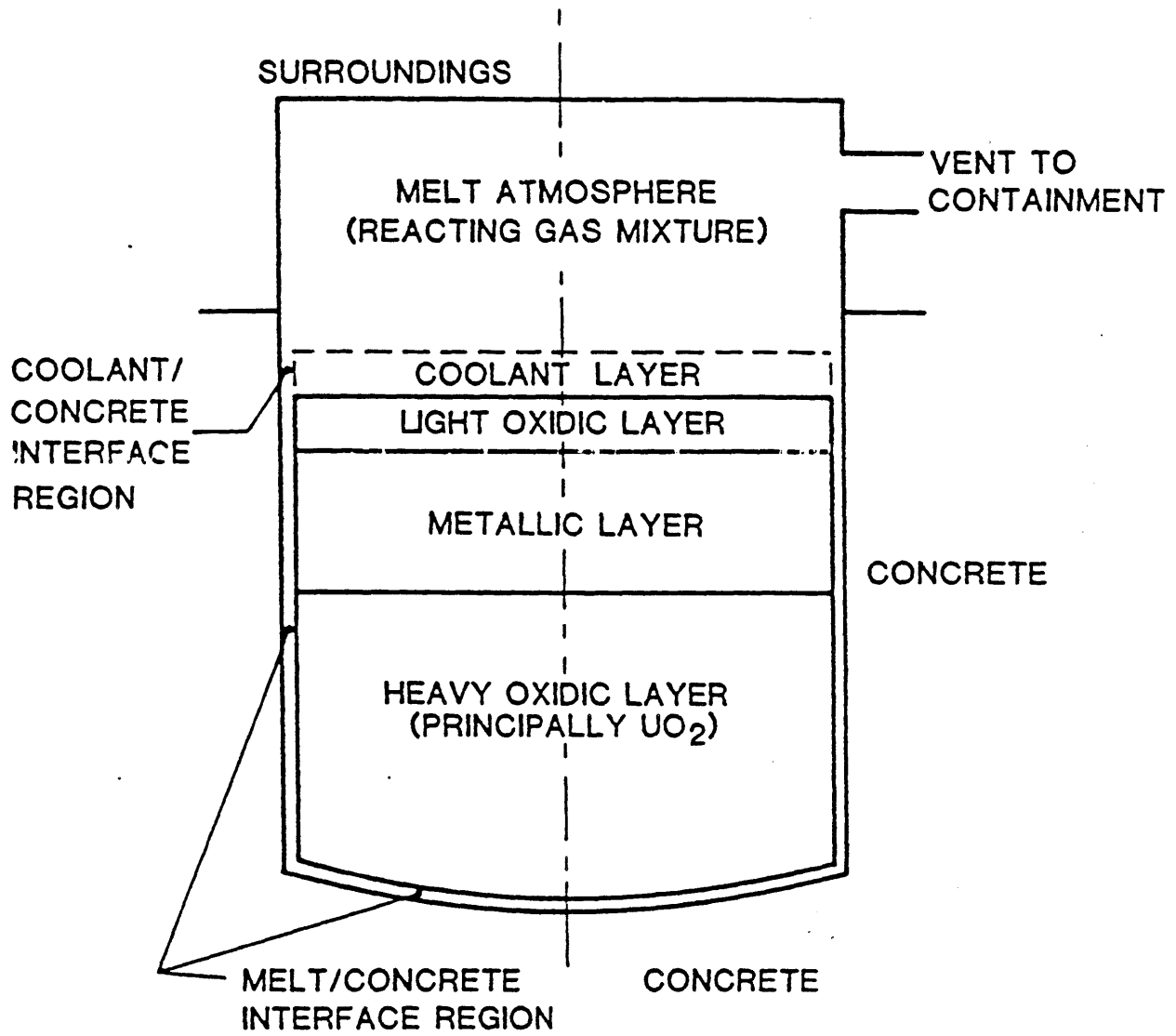
Figure 1.1 Schematic of CORCON System
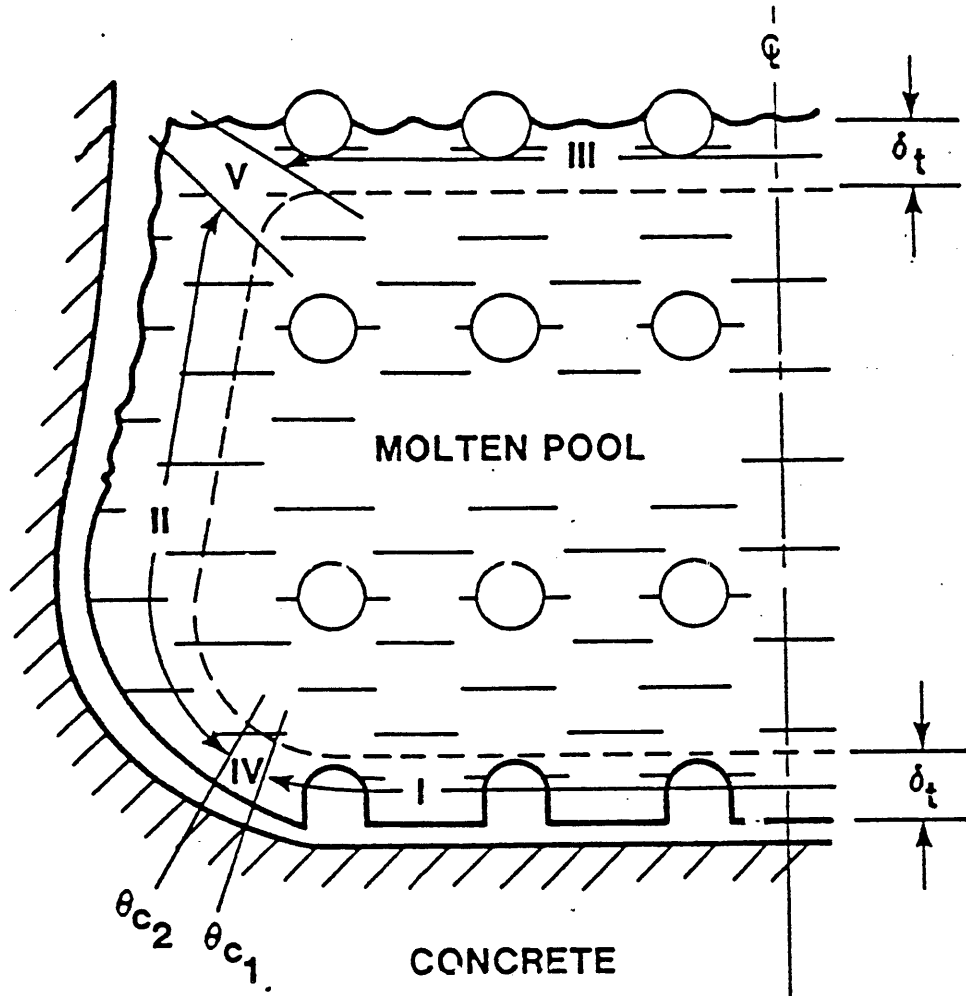
REGION	CONDITION
I, III	SURFACE WITH GAS INJECTION
II	SURFACE WITH BUBBLE AGITATION
IV, V	TRANSITION REGIONS

Figure 1.2 Pool Internal Heat Transfer Regions of CORCON

The first version of CORCON (Mod1) was completed in 1982 and was intended to calculate the initial high temperature molten pool attack on the concrete. The second version (Mod2) was released in 1984 [C6]. The major improvements of Mod2 include: a simple quasi-steady-state crust formation model developed by R.K.Cole [C5] to calculate the long term attack on the concrete of a partially solidified debris pool. A full representation of the boiling curve was also included to model the interaction between the corium pool and the overlying coolant layer. Some modifications of the interfacial heat transfer between layers were also made.

CORCON/Mod1 has been modified by different organizations. At U. of Wisconsin, a simple heat transfer model was included to calculate the heat transfer between the corium and an overlying coolant layer and an aerosol source model was incorporated to account for aerosol production and subsequent transport to containment [V1]. At MIT, a simplified one cell containment pressure model was incorporated to study the impact of different heat transfer correlations on containment pressurization [K1].

(2)WECHSL

The WECHSL code developed by M.Reimann and W.B.Murfin [R2] at KfK uses the same basic structure as that of CORCON. However, it only allows two layers. The metallic layer is always at the bottom. WECHSL employs a completely different model to calculate the pool heat transfer. The ratio of the thickness of the hydrodynamic boundary layers in the gas film and liquid is calculated following a proposal of Lock's [L1]. This is converted into a ratio of thermal boundary-layer thickness using a standard method. For interlayer heat transfer, a natural convection correlation with an extra multiplier to account for the effect of gas agitation is used [W2].

Figure 1.3 shows the possible combinations of heat transfer situations at the corium/concrete interface of WECHSL. Again, a gas film (Fig.1.3a) is assumed at

31
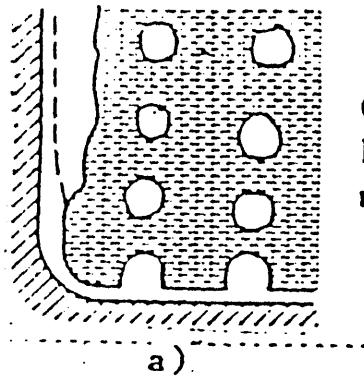
a)   Gas film with adjacent boundary layer in the melt
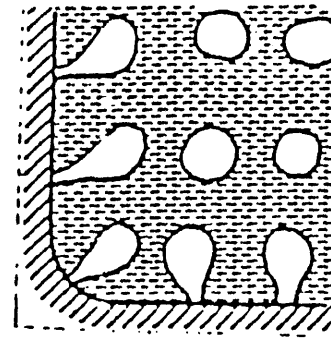
b)   Discrete bubble model
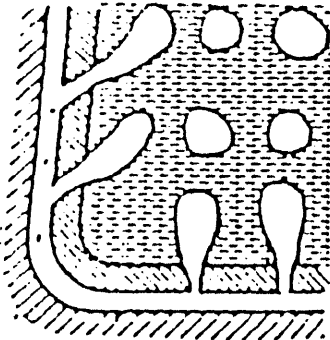
c)   Transient growing gas permeable crust with film (outside) and discrete bubble model (inside)
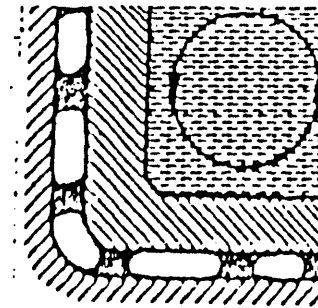
d)   Gas tight crust with two-phase (outside) and natural convection heat transfer (inside)

Figure 1.3   Downward Heat Transfer Models of WECHSL

the concrete surface. However, a discrete bubble model. Fig.1.3b, was also included to calculate the heat transfer rate when a stable gas film can no longer exist. The transition between the film model and the discrete bubble model is based on Beren-son's minimum stable gas film criterion [B5]. Models in Fig.1.3c and 1.3d are for the attack on concrete of partially solidified debris. The transitions between models depend on the thickness of the solidified layer. These criteria are somewhat arbitrary and need further justifications.

(3)DECOMP and EROS

DECOMP attacks the problem from a rather simplified point of view. Detailed modeling of the heat transfer mechanismes involved in the Corium/Concrete Inter-action is not considered. The heat fluxes from the upper surface by radiation and through the corium/concrete interface are assumed large enough to quickly cool the corium pool to its solidus temperature. From then on, the corium pool temperature remains at its solidus point and the concrete attack is a self-limiting process. The amount of heat conducted through the crust to the concrete is equal to the total decay and chemical reactions heat minus the heat radiated from the upper surface. In DECOMP, the thickness of the crust is determined by the conduction limit, i.e. if the crust is too thick to transfer the energy out it becomes thinner and vise versa. The thicknesses of the crust at the bottom and the sides are assumed to be equal.

Based on the same approach as that of DECOMP, M.Plys [P4] developed EROS. The model consists of six coupled, ordinary differential equations, derived from the energy balance equation for four control volumes (pool, downward crust, sideward crust and upward crust) and two interface balance conditions (sideward and down-ward erosion). In EROS, the thickness of the crust at different locations can be varied dynamically. With EROS, Plys was able to predict the results of his own simulant experiment.

1.3.4.2 Modeling of Concrete Response

On the assumption that the concrete erosion is a quasi-static process, the simplest way to calculate the concrete response is to lump all the sensible heat, reactions heat and latent heat into an effective decomposition enthalpy. Then, the concrete ablation rate is determined by the energy balance at the decomposition interface. This is equivalent to assuming that all the decomposition processes i.e., dehydration, decarboxylation etc. occur at the same temperature. This approach neglects the heat conducted into the concrete. The CORCON series and DECOMP use this approach to calculate the concrete response. However, in DECOMP the gas generation rate is calculated by a simple rate equation with a prespecified exponential temperature profile in the solid concrete.

For WECHSL, Alsmeyer and Reimann [A4] formulated the decomposition processes into different layers and heat is absorbed by chemical or physical reactions at the boundaries of the layers. For each layer, separate energy equations are written for the solid and flowing gaseous component. The two equations of each layer were coupled together by the conservation of mass. By assuming that the system coordinate is moving with a constant ablation velocity, a second order spatial differential equation for each layer is obtained. With a prespecified boundary temperature i.e. the transition temperature of certain chemical or physical reaction, the differential equations can be solved. This led to an effective decomposition enthalpy which is different from the one mentioned above. Although this approach considers the decomposition process in depth and removes the assumption that all the decomposition processes occur at the same temperature, it is still a quasi-static one. The heat conducted into the concrete is still not included in the calculation. This transient effect is only important if the debris temperature and therefore the heat flux is low, or the heat flux is strongly time dependent [R2].

Corradini [C8] proposed a simplified one-dimensional transient ablation model. He solved the conduction equation which included the convective term from ablation

integrally with a predetermined quadratic temperature profile. By this way. a thermal penetration depth was defined. Conceptually. one can imagine that there is a thermal front moving ahead of the decomposition front. and the concrete beyond the thermal front is unaltered. The distance between the thermal front and melt front is the thermal penetration depth. The model can predict the erosion history of Sandia Surface Heating Experiment C4 . This approach considered the heat conducted into concrete in an integral way. However. it perserved the assumption that all the decomposition processes occured at the same temperature.

A finite-difference conduction program. USINT B3 . was developed at Sandia for detailed modeling of the temperature profile, dehydration and decomposition phenomena of concrete erosion. It has provided reasonable results for concrete dehydration tests. However, this kind of calculation is both time and storage consuming for a computer. Hence it is difficult to incorporate it into an integral analysis code of MCCI.

To track the shape of the concrete cavity is another important part in modeling the concrete response. In CORCON and WECHSL. a series of 'body points' is defined along the concrete surface (as shown in Fig.1.4) and cavity shape is considered to be axially symmetric. As the ablation proceeds. the 'body points' recede to a new position and define a new concrete surface. The recession rate of each body point depends on the local heat transfer rate. This model has the flexibility of allowing the cavity shape to change freely in a two-dimensional sense. In DECOMP, the cavity is in cylindrical form and the penetration rates in the downward and sideward directions are assumed to be equal. In EROS the cavity is also in cylindrical form. however. the downward and sideward erosions are calculated separately.

1.3.5 Comparsions between the Experiments and Codes Predictions

The predictions of CORCON and WECHSL compare reasonably well with the transient experiments (without sustained heating) of Sandia and KfK. In those
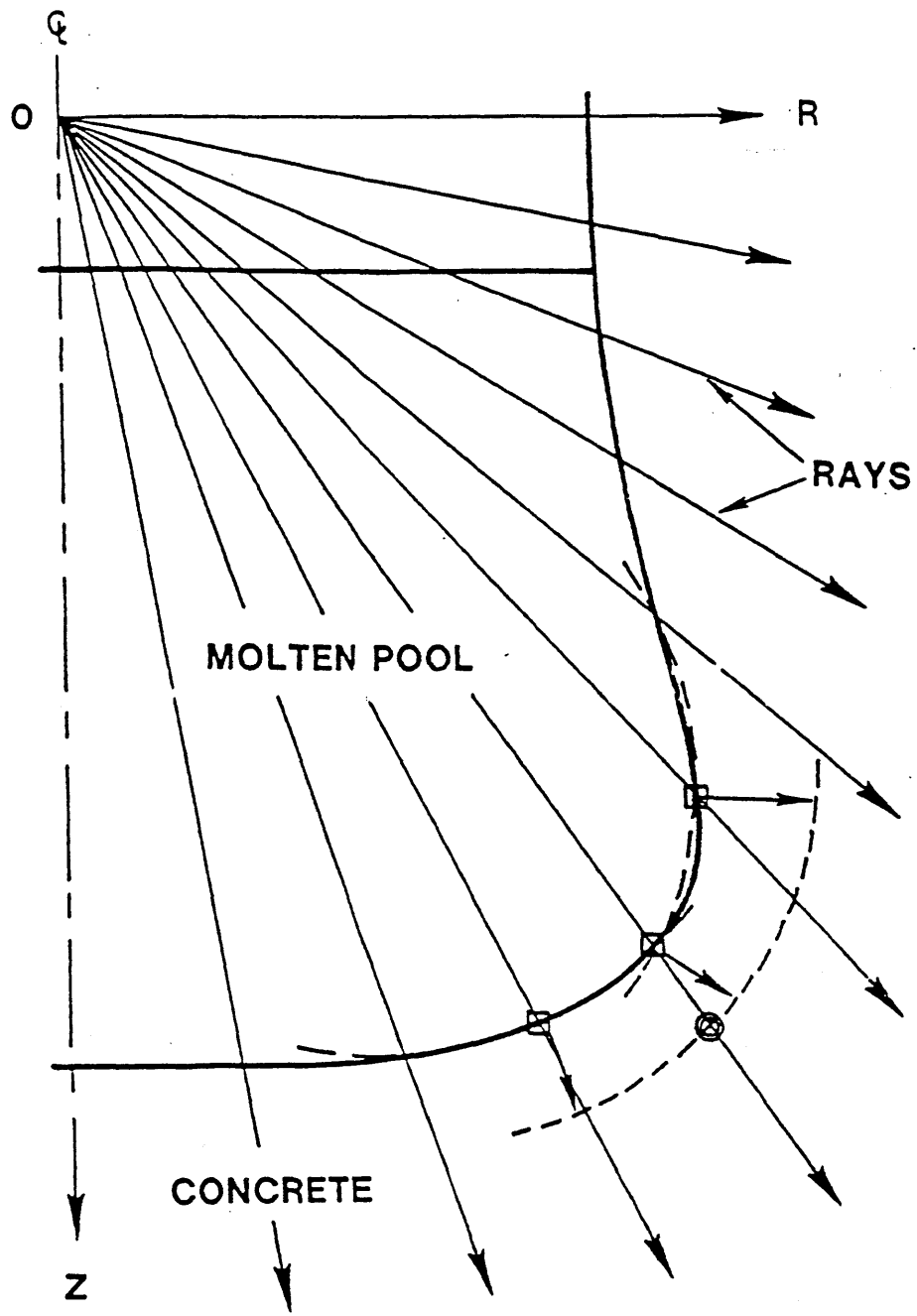
Figure 1.4   Cavity Shape Change Procedure for CORCON and/or WECHSL

experiments. the melt froze within several minutes and the erosion rates in the sideward and downward directions are about equal. In both codes. the gas film is assumed to exist on the side and the bottom of the corium pool. Therefore, it is expected that both codes predict approximately the same amount of axial and radial erosion. However. the agreement between the code predictions and experiments is violated by the recent results of the BETA experiments.

In the BETA experiment. the long term attack on concrete by the high temperature melt is achieved by induction heating in the metallic melt. The results show that the erosion of concrete is dominant in the axial direction. Neither of the codes can reproduce this trend. This means that the gas film model in both codes is not always valid for calculating the downward heat transfer. By changing the transition criterion for the gas flow rate needed to change the gas film model to the discrete bubble model in WECHSL. Reimann R3 can improve the prediction of the results of the BETA experiments. However. the criterion is not unique for every test, it has to be adjusted from test to test in order to fit the experimental results.

The DECOMP code can predict [H2] the experimental results for concrete attack by the solidified melt for one of the Sandia's BURN series test. However. it can not simulate the BETA experiments. It inherently assumes that the downward and sideward erosion are equal. Direct comparsion between the EROS code and real material experiments has not been made. Its application to the Corium/Concrete Interaction reveals that the predicted downward and sideward erosion are about equal.

1.4 Structure of This Work

First. a simplified model is developed in Chapter 2 to quantify the impact of heat transfer from core melt to concrete on the pressure rise in the containment. The primary purpose is to determine the extent to which the partition of heat transfer between the two paths may affect the containment pressure under very severe

conditions. A secondary objective is to identify the sensitivity of the potential for containment overpressure to some areas of uncertainty concerning chemical reactions among the various materials involved.

In Chapters 3 to 5, the heat transfer phenomena involved in the corium pool are studied. This includes a heat transfer model for horizontal corium/concrete interface based on a periodic contact mechanism, an interfacial heat transfer model between bubbles agitated immiscible liquid layers and a simulant experiment to study the stability of a solidified layer across the horizontal bubbles agitated liquid/solid interface.

For real materials, a gas film has not actually been observed, but only inferred from the simulant tests of water or benzene on dry ice. The results of BETA experiment indicate that there is a possibility that the gas film at the horizontal corium/concrete interface is not stable. An alternative view is proposed in Chapter 3 to interpret the water or benzene/dry ice experimental data of Dhir et al.[D2]. A semiempirical heat transfer correlation for calculating the downward heat transfer coefficient is derived. The correlation predicts that the heat transfer coefficient across the corium/concrete interface increases with superficial gas velocity as well as with corium temperature.

In Chapter 4, the experimental data on interfacial heat transfer between bubble agitated immiscible layers are reviewed and a new mechanistic model is proposed. The proposed model is based on Szekely's [S6] surface renewal concepts. A simple model based on the hydrodynamic stability of a liquid jet is proposed to model the bubble induced entrainment. It is concluded that the bubble induced entrainment would not occur in Corium/Concrete Interaction if the concrete erosion rate is low and therefore the superficial gas velocity is low.

The stability of horizontal crust layer under the impact of gas injection is studied by a simulant experiment. A test apparatus was designed, with heat removal from

the cell via pourous plates at the boundaries. Water and air are used in the experiment. The detailed design of apparatus and experimental results will be presented in Chapter 5.

In Chapter 6, the integral effects of the proposed downward and interfacial heat transfer correlations on the analysis of melt/concrete interaction are investigated. The proposed correlations are incorporated into CORCON/Mod1. A comparison of the concrete erosion rate between the code predictions and the results of BETA experiment is made.

The CORCELL code which combines the simplified containment model developed in Chapter 2 with modified CORCON/Mod1 is used in Chapter 7 to study the impact of the Corium/Concrete Interaction on containment pressurization.

Finally, conclusions are drawn in Chapter 8 and recommendations for future work are made.

CHAPTER 2

IMPACT OF CORIUM HEAT TRANSFER TO CONCRETE
ON CONTAINMENT PRESSURE

2.1 Objective

In Corium/Concrete Interaction, the decay heat, the chemical reactions heat generated within the corium pool as well as the sensible heat of the pool would be transferred either directly to containment atmosphere or to the concrete surrounding the pool. The partition of energy between the two paths can not be exactly defined at present, given the limited amount of experimental data and the uncertainties about the effect of gas bubbling on the heat transfer at the corium pool interface. The two heat transfer paths tend to pressurize the containment in different ways. Direct heat transfer to containment will increase the internal energy of the constituents of the containment atmosphere. Heat transferred to concrete will increase the amount of noncondensible gases in the containment.

The primary purpose of this chapter is to determine the extent to which the partition of heat transfer between the two paths may affect the containment pressure under very severe conditions. A secondary objective is to identify the sensitivity of the potential for containment overpressure to some areas of uncertainty concerning chemical reactions between various materials involved.

2.2 Model Formulation

2.2.1 Basic Equations

The approach taken here involves a large degree of simplification by concentrating on the pressure in the containment a few hours following the accidents thus

deleting the sequential natural of the events. By considering the significant energy sources and heat dissipation paths, the pressure of the containment can be determined by the first law of thermodynamics, applied to the containment atmosphere as a control volume (see Fig.2.1). Thus, the first law of thermodynamics may be written as:

$$\frac{d}{dt} \sum_i M_i u_i = - \sum_j \dot{M}_j h_j + \sum_k \dot{Q}_k \qquad (2.1)$$

where

M_i = mass of material 'i' in the containment

$\dot{M}_j$ = mass flow rate of material 'j' out of the containment

u_i = specific internal energy of material 'i'

h_j = specific enthalpy of material 'j'

$\dot{Q}_k$ = rate of heat addition by process 'k'

The containment mass constituents are taken to be: (1) primary water initially in the reactor coolant system, M_{wp}, (2) emergency cooling water from the accumulator, M_{wa}, and the spray system, M_{ws}, (3) metallic structures within the containment e.g. steel liner, RCS pumps, steam generators, pressurizer and refueling machines etc, M_s, (4) containment air, M_a, water vapor, M_{wc}, and the noncondensible gases generated from MCCI , M_g.

The decay heat is assumed to be released to containment via two routes (Fig.2.1):
1. By direct heating of the gaseous atmosphere
2. By transferring to the concrete, which leads to its endothermic decomposition and the release of gases. The gases may in turn react with the metallic elements producing H_2 and CO_2 which can also burn with the oxygen in the containment.

The amount of decay transferred to concrete is taken as a parameter which can be varied as a fraction, f, of decay heat and heat generated in the corium due to the metallic reactions with the decomposition gases.

41
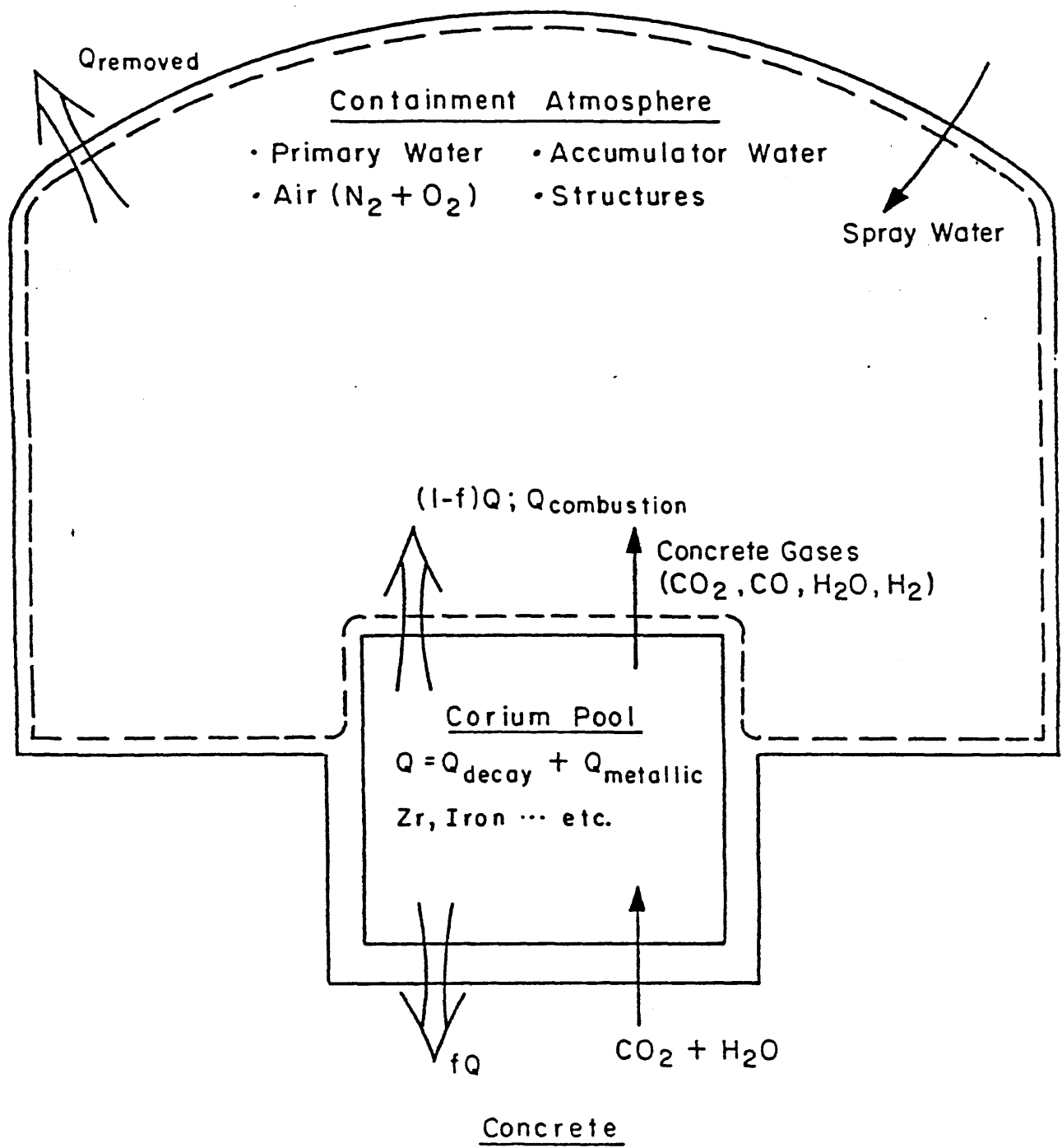
Figure 2.1   Control Volume for Calculation of the Pressure Rise of Containment

42

Integrating Eq.2.1 over time, and assuming that the enthalpies of the influent materials, h_j , are independent of time, which is a reasonable assumption for this case, we get:

$$U_2 - U_1 = M_{ws}h_{ws} + M_{wa}h_{wa} + M_g h_g + Q \qquad (2.2)$$

where

$$
\begin{aligned}
U_2 &= (\sum_i M_i u_i)_2 \\
&= (M_{wp} + M_{wa} + M_{ws} + M_{wc})u_{w2} \\
&\quad + M_a u_{a2} + M_g u_{g2} + M_s u_{s2}
\end{aligned} \qquad (2.3)
$$

$$
\begin{aligned}
U_1 &= (\sum_i M_i u_i)_1 \\
&= M_{wp}u_{wp1} + M_{wc}u_{wc1} + M_a u_{a1} + M_s u_{s1}
\end{aligned} \qquad (2.4)
$$

$$Q = (1 - f)(Q_{decay} + Q_{metallic}) + Q_{combustion} - Q_{removed}$$

$$M_g = f\,\frac{(Q_{decay} + Q_{metallic})C_g}{h_{decom}} - M_{g'}$$

and

$$Q_{decay} = \text{decay heat}$$
$$Q_{metallic} = \text{chemical energy from metallic reactions}$$
$$Q_{combustion} = \text{chemical energy from the gas combustion}$$
$$Q_{removed} = \text{heat transferred out of the containment via the}$$
$$\text{engineered safety features e.g. fan coolers}$$
$$h_{decom} = \text{decomposition enthalpy of concrete}$$
$$C_g = \text{initial gas weight fraction in concrete}$$

the subscripts refer to :

$$wa : \text{accumulator water}$$

43

wc : water vapor in the containment atmosphere

wp : primary water

ws : spray water

a : air $(N_2 + O_2)$

g : gases generated from the decomposed concrete

g' : noncondensible gases depleted in the combustion and metallic reactions.

s : structural material

2 : end state

1 : initial state

For a reactor that has been operating at a constant power P_o (MWt) for a period of one year, the total decay heat generated at t seconds after reactor shutdown can be expressed as [G3]:

$$Q_{decay}(MJ) = \frac{1}{8}\left((t + 10)^{0.8} - 0.87(t + 2.0 \times 10^7)^{0.8} - (t + 3.15 \times 10^7)^{0.8}\right.$$
$$\left. + 0.87(t + 5.15 \times 10^7)^{0.8} + 3.1475 \times 10^5\right) P_o(MW)$$

(2.5)

2.2.2 Model Assumptions

In the real situation, the determination of the amount of the chemical energy is quite complicated. It depends on the kinetics of the chemical reactions. In this simplified calculation, only the chemical reactions listed in Table 2.1 are considered [H3]. It is further assumed that a reaction that has a higher reaction heat will have a higher priority to react. Also it is assumed that the chemical reactions will proceed to completion, i.e. reactions will stop only if one of the reactants is exhausted. With this assumption, the calculated chemical energy is the maximum possible energy that can be extracted from the chemical reactions.

It is also assumed that thermal equilibrium exists among all the constituents in

Table 2.1

Chemical Reactions Considered in This Analysis

	Reactions	Reaction Heat [H3]
Metallic	$Zr + 2H_2O \rightarrow ZrO_2 + 2H_2 \uparrow$	6.53 MJ/kg (Zr)
Reactions	$Zr + 2CO_2 \rightarrow ZrO_2 + 2CO \uparrow$	5.83 MJ/kg (Zr)
	$Fe + 4H_2O \rightarrow Fe_3O_4 + 4H_2 \uparrow$	0.74 MJ/kg (Fe)
	$Fe + 4CO_2 \rightarrow Fe_3O_4 + 4CO \uparrow$	-0.38* MJ/kg (Fe)
Combustion	$2CO + O_2 \rightarrow 2CO_2 \uparrow$	17.68 MJ/kg (O_2)
Reactions	$2H_2 + O_2 \rightarrow 2H_2O \uparrow$	15.10 MJ/kg (O_2)

* endothermic

the containment atmosphere which is an acceptable approximation for the conditions prevailing several hours after the accidents. Then the internal energy in Eq.2.2 are only functions of P_2 and T_2 . Using the steam table and the assumption of ideal gas behavior in the fixed containment volume, Eq.2.2 can be solved iteratively. Therefore, for a known initial state and a given time, t, we can determine the pressure of the containment as a summation of partial pressure of water, air and noncondensible gases.

2.3 Cases Analyzed

Several calculations have been performed for a 2440 MWt PWR with a large dry containment. The initial state is assumed to be that of normal operation of 2000 $psia$ primary water and atmospheric containment pressure. The change in the internal energy of fuel is not considered. All the heat generated is assumed to be ultimately deposited either to containment atmosphere or concrete. The corresponding values of parameters in Eq.2.2 are summarized in Table 2.2. The assumptions for each case analyzed are summarized in Table 2.3.

The accident conditions were varied over a wide range of parameters. The amount of spray water is arbitrarily assumed to be 3 times to that of the primary water. This amount of water is approximately 50% of the usual inventory in the refueling water storage tank.

It is further assumed that the fan coolers are partially available and when available they operate at a reduced efficiency so that the net effective rate of fan cooling is roughly 10% of the rated capacity (~ 7 MW). The amount of structural materials that can act as a passive heat sink is assumed to be equivalent to 1000 $tons$ of steel. The heat conducted into the concrete wall of containment buliding is not considered in the present calculations but will be examined in Chapter 6. The amount of Zr available for metallic reactions is assumed to be equal to that of the fuel cladding (approximately 19 $tons$). The amount of iron in the corium depends on the accident

46

Table 2.2

Parameters Used in the Analysis of the Reference PWR Large Dry Containment

	Mass (kg)	Internal Energy at Initial State kJ/kg
Primary Water	2.34×10^5	1327
Accumulator Water	1.10×10^5	398.1
Water in the Containment Atmosphere	1.05×10^3	2405
Spray Water	7.03×10^5	157.5
Containment Air	6.00×10^4	Ideal Gas
Amount of Zr in the Corium pool	1.91×10^4	

Table 2.3

PWR Cases Analyzed[a]

	Case 1 a|b|c	Case 2 a|b|c	Case 3 a	Case 4 a	Case 5 a	Case 6 a	Case 7 a|b|c	Case 8 a|b|c
Time After Accident (*hrs*)	6	6	6	6	6	6	Varied	Varied
ConcreteType[b]	A|B|C	A|B|C	A	A	A	A	A|B|C	A|B|C
Accumulator Water	Yes	Yes	Yes	Yes	Yes	Yes	Yes	Yes
Spray water	Yes	Yes	Yes	Yes	Yes	No	Yes	Yes
Fan Cooler (% eff.)	10%	10%	10%	–	20%	–	10%	10%
Structure (1000 *tons*)	Yes	Yes	No	Yes	Yes	Yes	Yes	Yes
Chemical Energy	Yes	No	Yes	Yes	Yes	Yes	Yes	No

[a] Large Dry Containment.

[b] A: Limestone/Common Sand, B: Basaltic, C: Limestone.

sequence. In the present calculations. it is assumed that there are equal amounts of Zr and Fe in the corium pool.

Three kinds of concrete were used in the analyses in order to identify the impact of the concrete types on containment pressurization. Those are basaltic concrete, limestone/common sand concrete and limestone concrete. The heat necessary to raise the concrete from room temperature and convert it to melt is estimated by the following equation [P7]:

$$h_{decom} = \int_{T_o}^{T_D} C_p dt + \sum_{i=1}^{3} \phi_i + L \tag{2.6}$$

where

T_o = initial temperature of concrete

T_D = decomposition temperature of concrete

C_p = specific heat capacity of concrete

ϕ_i = heat of decomposition associated with

(1) loss of free water

(2) loss of bound water

(3) decarboxylation of the concrete

L = latent heat of concrete melting

The decomposition enthalpy and the initial concentration of gases of various kinds of concrete are listed in Table 2.4. In those estimations, the heat of decomposition is based on the data in Ref. [P7] and the temperature dependency of heat capacity is obtained from Ref. [S3]. All values and equations used are summarized in Appendix A.

The impact of corium heat transfer on different types of containments are also

49

Table 2.4

Decomposition Enthalpy and Gas
Concentration of Concrete

	Limestone/ Common Sand Concrete	Basaltic Concrete	Limestone Concrete
Free Water (Weight%)	2.7	2.9	2.3
Bound Water (Weight%)	2.0	2.0	1.8
Carbon Dioxide (Weight%)	22.0	1.5	35.7
Fractional Gas Content C_g	0.267	0.064	0.418
Melting Temp. Range ($^\circ C$)	1150~1400	1080~1380	1450~1650
Decomposition Enthalpy MJ/kg	3.58	2.89	4.14

studied. Three types of containment are considered. These are PWR large dry containment, PWR ice condenser containment, BWR supression pool Mark I containment. The important parameters for each type of containment are summarized in Table 2.5 for comparison.

2.4 Results

2.4.1 Impact of Fraction of Heat to Concrete

It is clear from the assumption of limited heat removal away from the containment that the containment pressure will rise above the initial pressure. For a PWR large dry containment, the pressure of the containment generally decreases as the fraction of decay heat, f, transferred to concrete increases above 30% (Fig.2.2). The total pressure is due to three constituents: water steam, air and noncondensible gases. Among those, the water steam makes the major contribution to the total pressure. For the concrete with higher gas content, however, the noncondensible gases can make significant contribution ($\sim$ 30%) to containment pressure if a large fraction of heat is assumed to be transferred to concrete (Fig.2.2).

For basaltic concrete (Fig.2.3) the total pressure is found to decrease as f increases. As the fraction exceeds 60%, the pressure remains below 0.69 MPa (100 psi) all the time. However, this is not true for a concrete that contains greater than 20% by weight of gases. From Fig.2.4, it can be seen that for limestone/common sand concrete the total pressure increase slightly as f is increased from 10 to 30% and then decreases at higher value. This is because, for concrete with a high gas concentration, as f increases the amount of chemical energy increases significantaly. However, the generation of chemical energy will reach a saturation value due to the limited amount of metallic substances (Zr, Fe) and oxygen available in the containment.

2.4.2 Effect of Concrete Types

Figure 2.5 shows a comparison between the pressure responses of containment to

Table 2.5

Containment Characteristics

	PWR Large Dry	PWR Ice Condensor	BWR Mark I
Thermal Power MWt	2440	3250	3293
Operating Pressure of NSSS ($psia$)	2250	2250	1020
Containment Free Volume (m^3)	525000	35000	11700
Ice ($tons$)	—	1000	—
Water in Supression Pool ($tons$)	—	—	3800
Structure Heat Sink Assumed ($tons$ of Steel)	1000	1000	1000
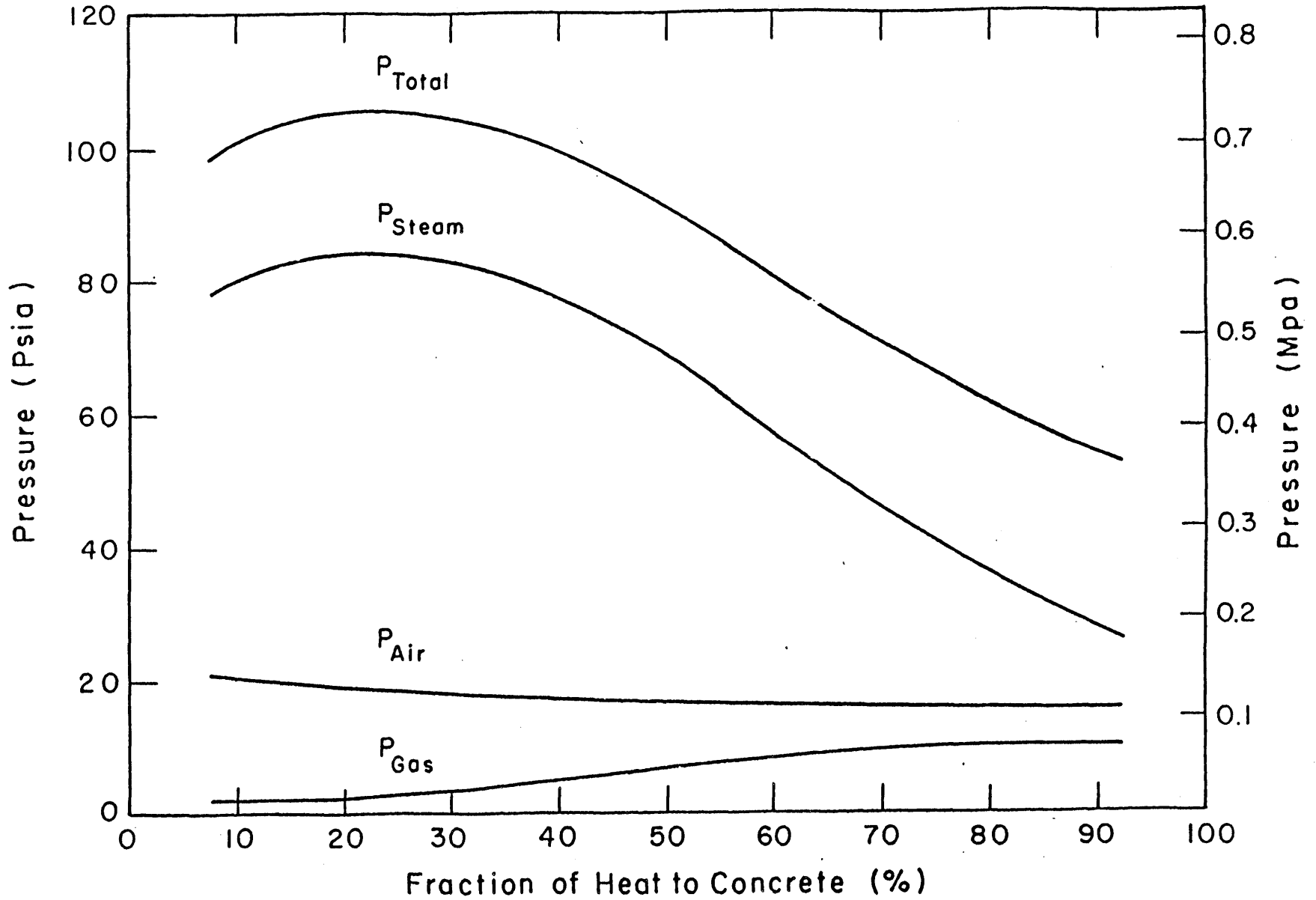
Figure 2.2   Constituents of PWR Large Dry Containment Pressure (Case 1a)
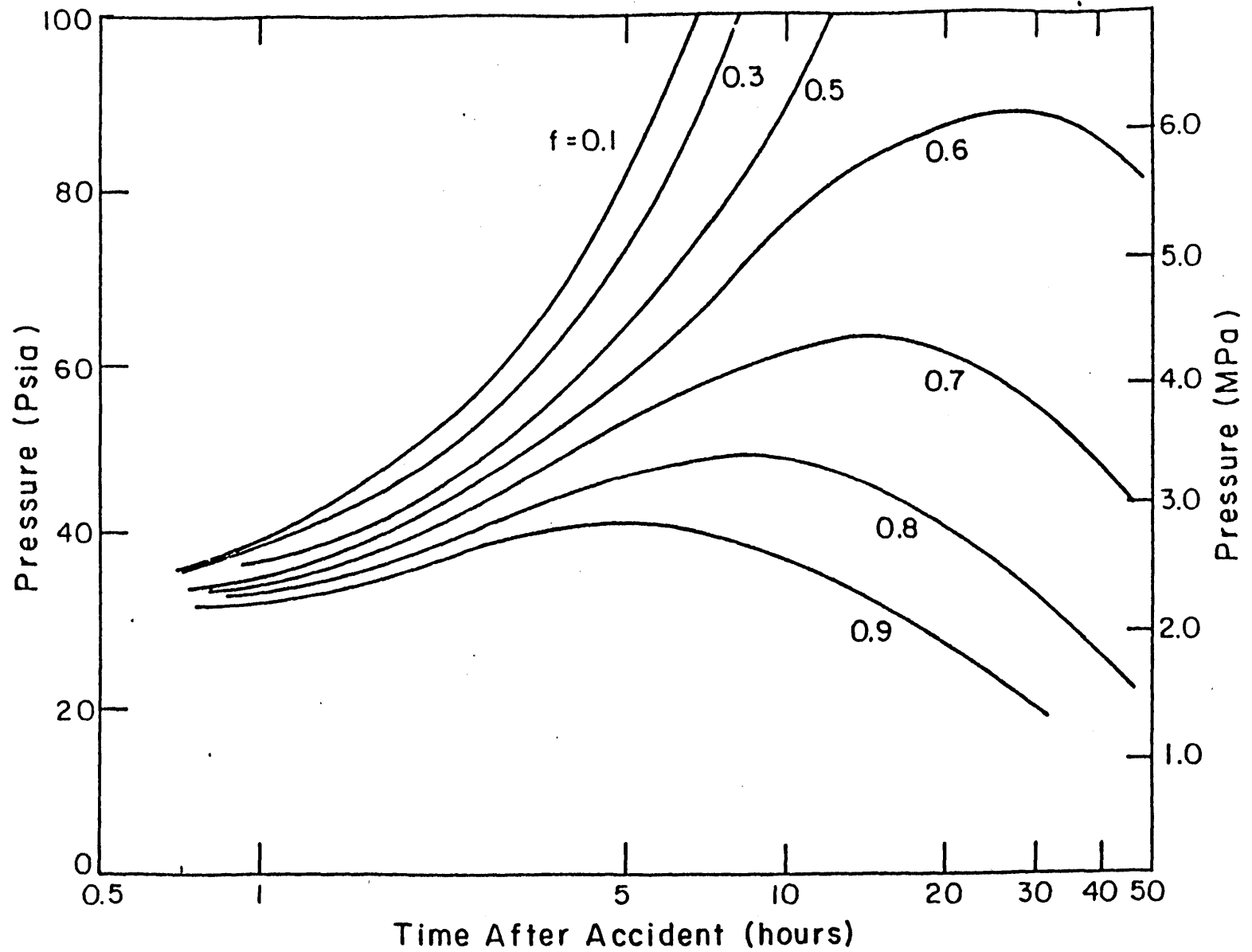
Figure 2.3   Pressurization Rate for Containment with Basaltic Concrete (Case 7b)
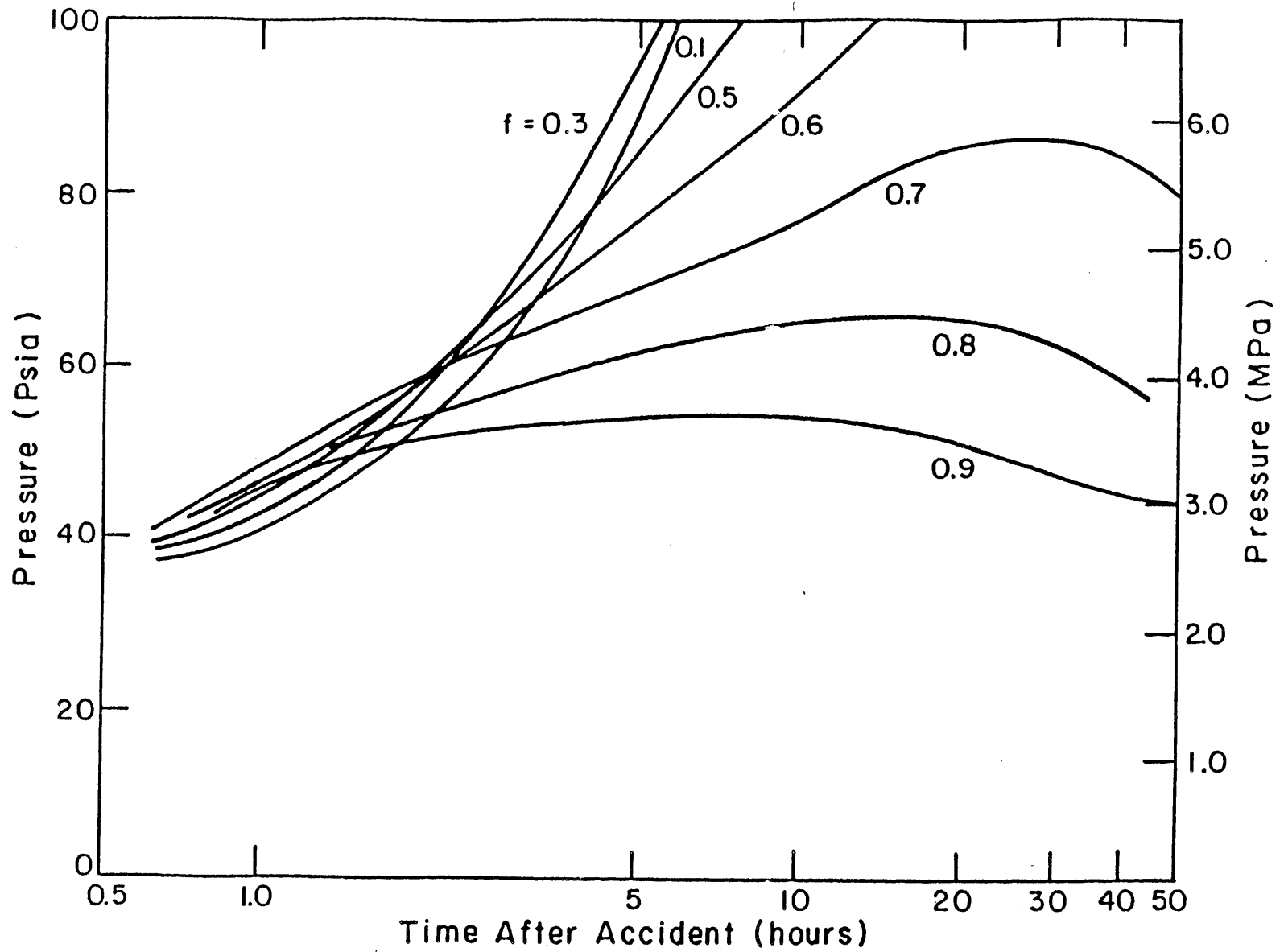
Figure 2.4   Pressurization Rate for Containment with Limestone/Common sand Concrete
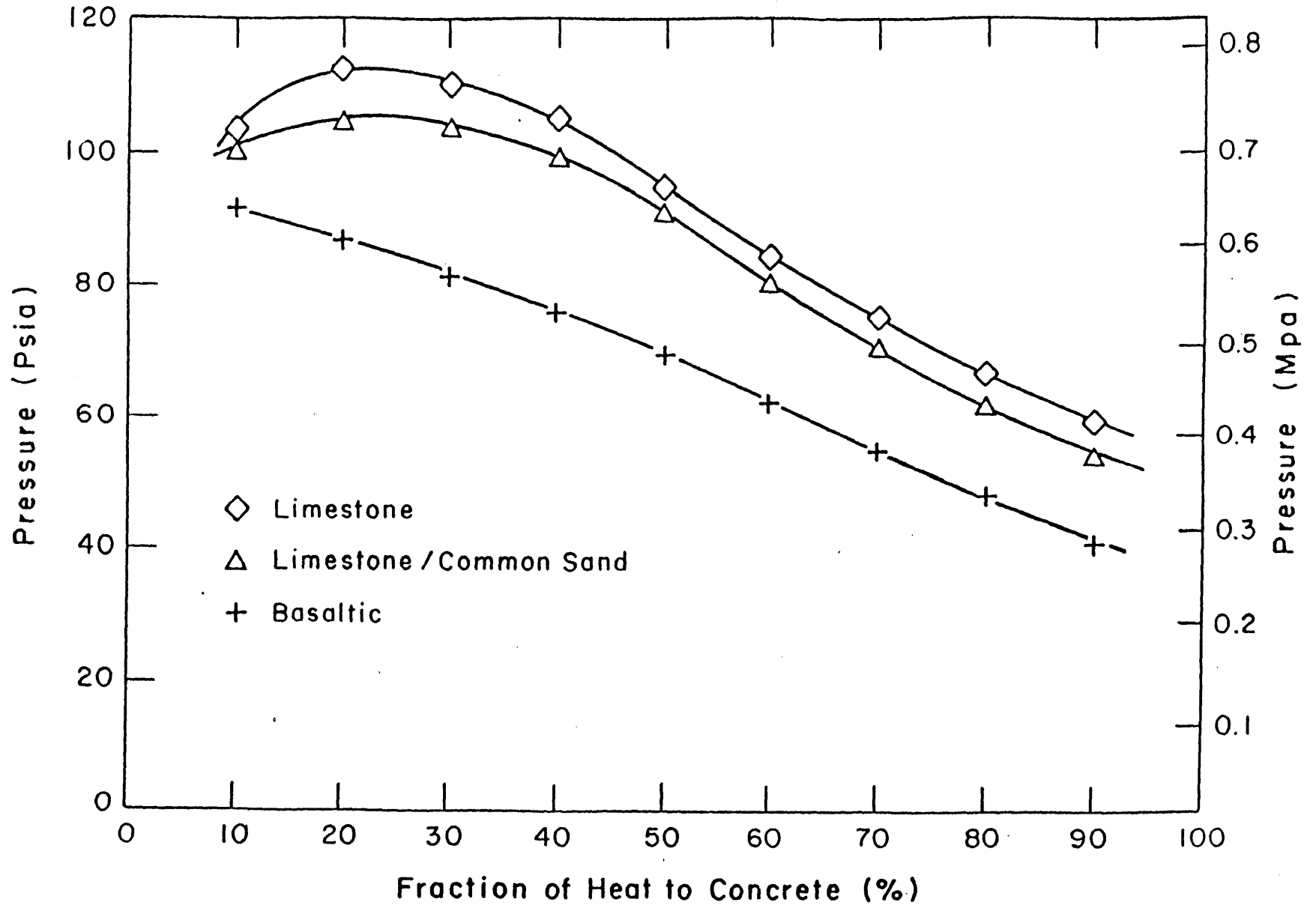
Figure 2.5 Comparison among Different Kinds of Concrete (with chemical energy, Case 1)

different kinds of concrete at $t = 6\ hr$. In general, for low values of f, for the concretes with high gas concentration the pressure will reach a maximum and then decrease as f increases. The results are different, however, if we exclude the chemical energy from the calculations (Fig. 2.6). The maximum difference ($\sim$15 psia) between the pressure responses of the containment with basaltic and limestone/common sand concrete occurs at high value of f due to the large amount of noncondensible gas generation.

2.4.3 Comparisons among Different Types of Containment

The pressure responses of different containment types at 6 hr. after the accidents are shown in Fig.2.7. From Fig.2.7, it can be seen that, for a PWR ice condenser containment the pressure in the containment is relatively insensitive to the fraction of heat transferred to concrete. For a BWR supression pool containment, as the fraction of heat transferred to concrete increases the pressure increases. The primary reason for that is the BWR containment is relatively small, and has a large amount of water to quench the steam. Thus, the pressure of concrete gases becomes the dominant one and this component will increase as the fraction of heat to concrete increases.

2.4.4 Sensitivity Studies

A sensitivity study has been performed for a PWR large dry containment with limestone/common sand concrete. The assumptions for each case are summarized in Table 2.3 and the results are shown in Fig.2.8.

(1) <u>Chemical Energy</u>

By comparing Case 1a and Case 2a in Fig.2.8, it can be seen that the chemical energy liberated from the metallic and combustion reactions can increase containment pressure significantly, especially for low value of f. The amount of chemical energy increases significantly as f increases from 10 to 30% and then begins to level off. In

57
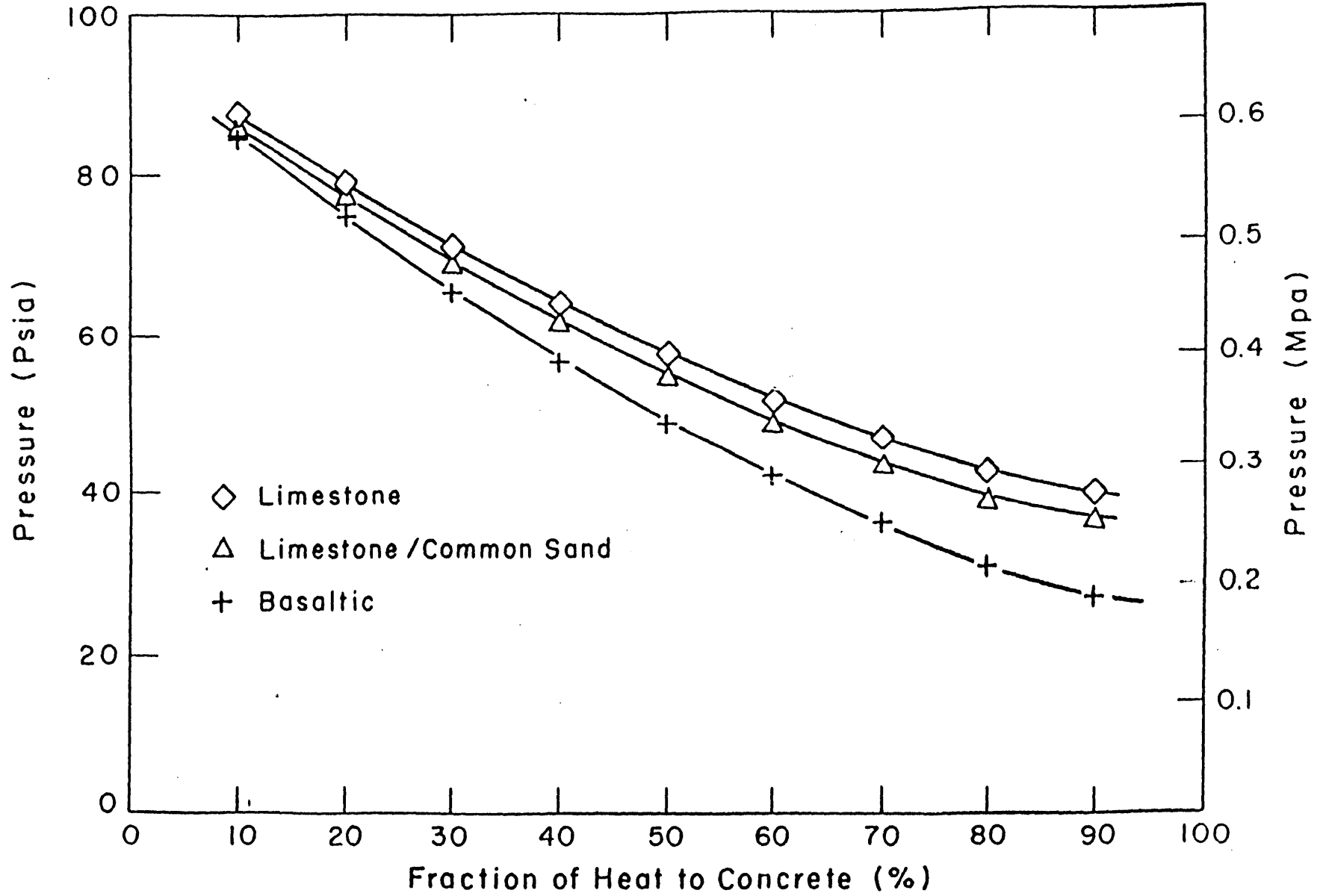
Figure 2.6   Comparison among Different Kinds of Concrete (without chemical energy, Case 2)

58
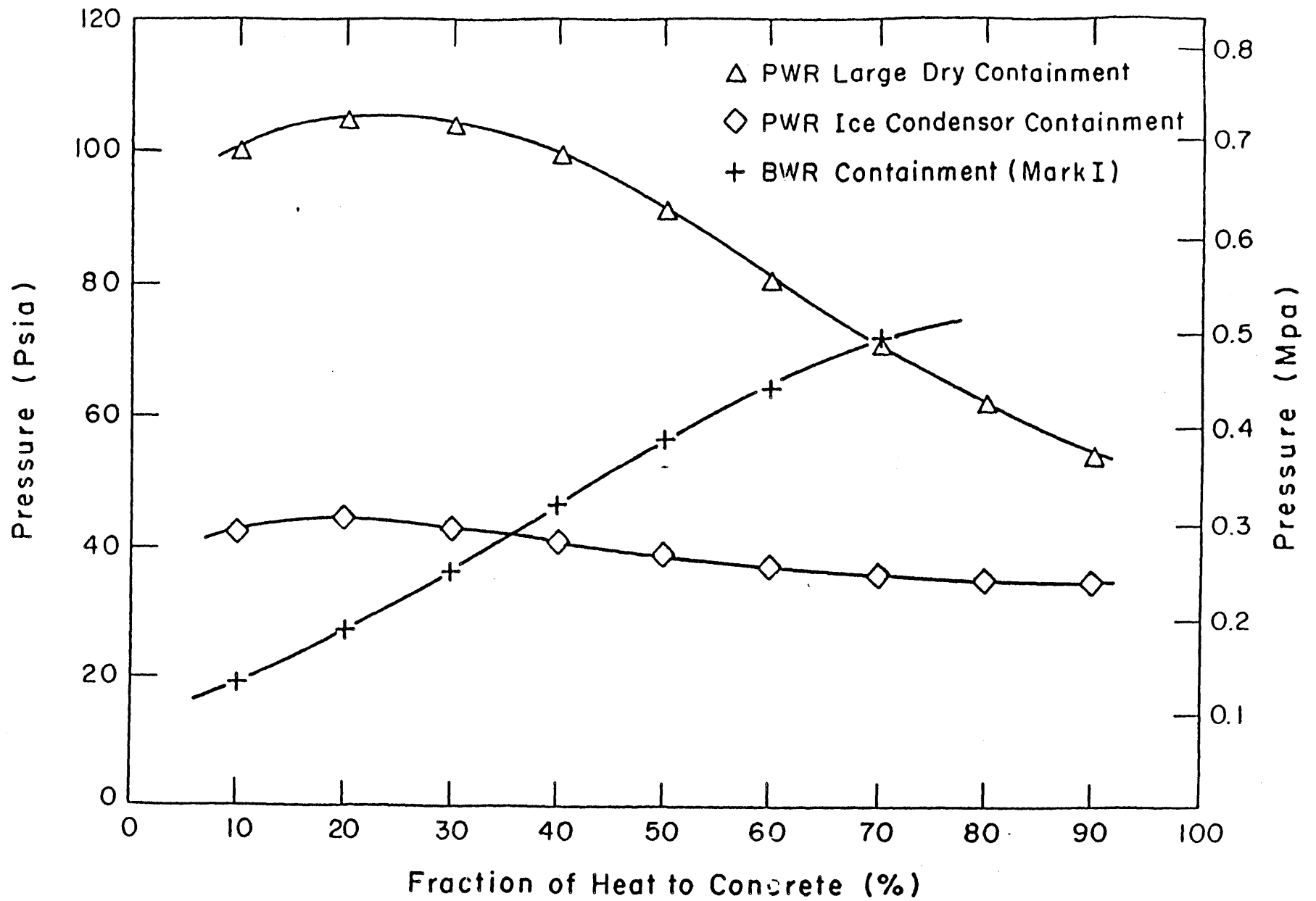
Figure 2.7　Pressure Response of Different Types of Containment
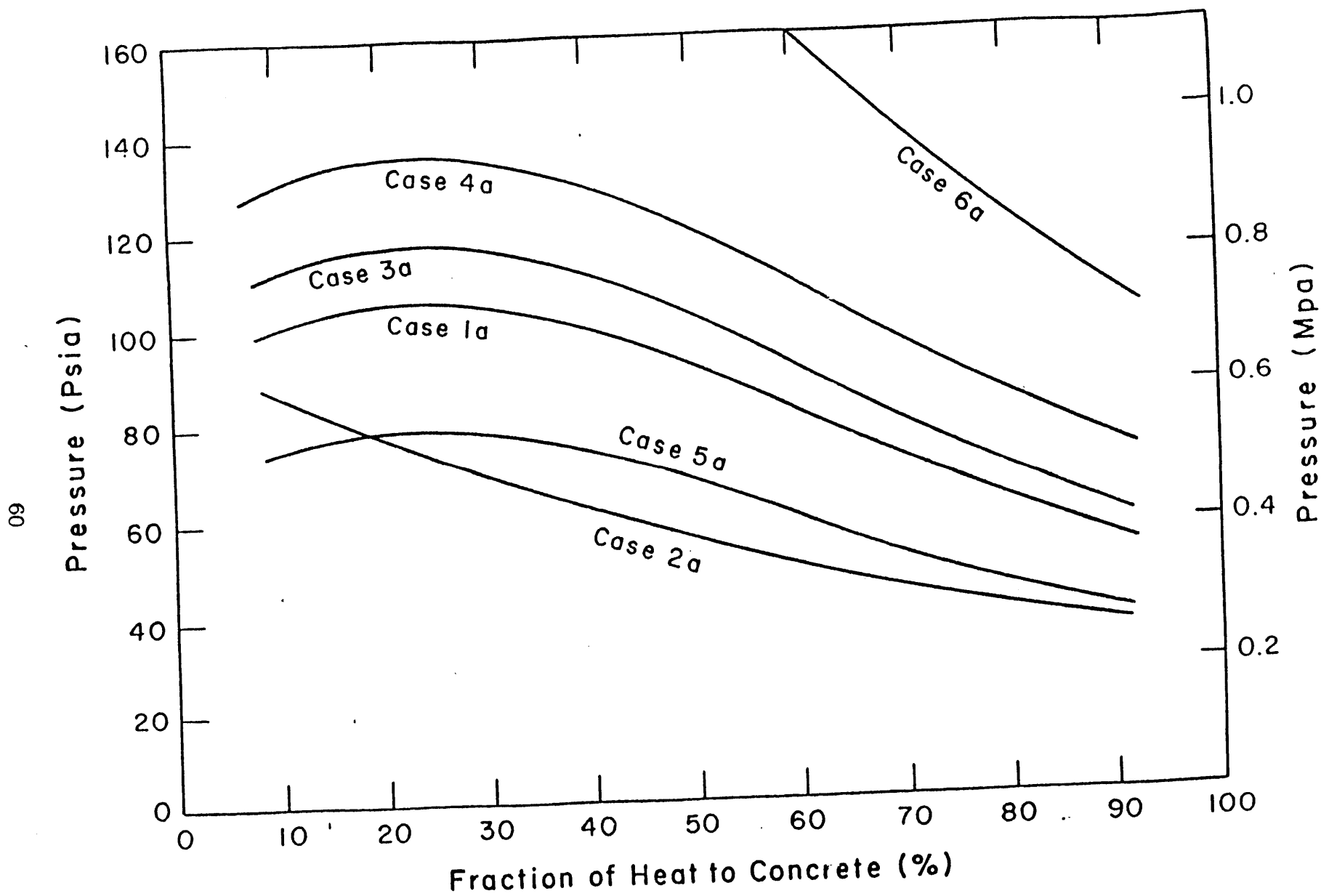
Figure 2.8   Sensitivity of Containment Pressure to Various Assumptions

the calculation of chemical energy. an assumption of the amount of iron in the corium pool is needed. However. the results are indifferent to the assumed amount of iron even this value is changed by six folds, i.e. from 20 to 120 *tons*. This is because the reaction heats between Fe and H_2O, CO_2 are relatively small and $Fe - CO_2$ reaction is endothermic. In this calculation the maximum chemical energy calculated is 40% of the 6 hours decay heat.

(2) Passive Heat Sink

From Fig.2.8 (Case 1a and Case 3a) it can be seen that even if only 1000 tons of structure material are available as passive heat sink, the containment pressure can be reduced by 9 to 10%.

(3) Active Heat Sinks

The availability of a fan cooler or other engineered safety features to remove the heat out of the containment is crucial to the determination of the containment integrity. A partially operable fan cooler (10% or 20%) can reduce the containment pressure by significant amount (Case 1a, 4a, and 5a in Fig.2.8) especially for low value of f. If we assume that there is no spray (Case 6a), the pressure in the containment reaches an unreasonable value when f is small.

It is interesting to point out here, that no matter what assumptions are used in the calculations, the containment pressure always depends on the fraction of heat transferred to concrete. especially for values of f between 40% and 90%.

2.5 Discussion

In the Reactor Safety Study [R1]. in some cases it was assumed that all the heat was transferred into the concrete. However. for PWR large dry containment when the heat removal away from the containment is much less than the design capacity of

61

engineered safety features. more heat transfer to concrete leads to a lower pressure rise. Therefore. based on the consideration of pressurization rate. the assumption in the Reactor Safety Study is not always conservative.

The extent of chemical reactions between the gases generated by concrete decomposition and core melt will be very important in determining the pressurization rate of the containment. In Fig.2.9 the time required to pressurize the PWR large dry containment to 0.69 MPa is shown. In the presence of complete chemical reactions of those gases. the fraction of heat transferred to concrete does not significantly impact the pressurization rate if the value of that fraction is between 10 and 40%. The results of molten steel/concrete experiment [P7] at Sandia showed that the fraction of heat to concrete depends on the rate of gas evolution and range from 20 to 45%. The more recent BETA experiments at KfK showed that this fraction is more than 80%. In the absence of chemical reactions. more heat transfer to concrete leads to a much lower pressurization rate and much longer time to reach 0.69 MPa pressure.

2.6 Conclusion

1. The fraction of heat transferred to concrete is important in determining the pressurization rate of containments. In a PWR large dry containment. for limited chemical reactions and heat removal away from the containment. a higher heat transfer rate to concrete reduces the pressure rise in the containment.

2. The extent of chemical reactions between the concrete gases and core melt will be a major factor in determining the pressurization rate of containment. especially for a concrete type with high gases content.

3. The components and structures within the containment act as a valuable passive heat sink during the accidents. This sink is especially important for a PWR large dry containment.
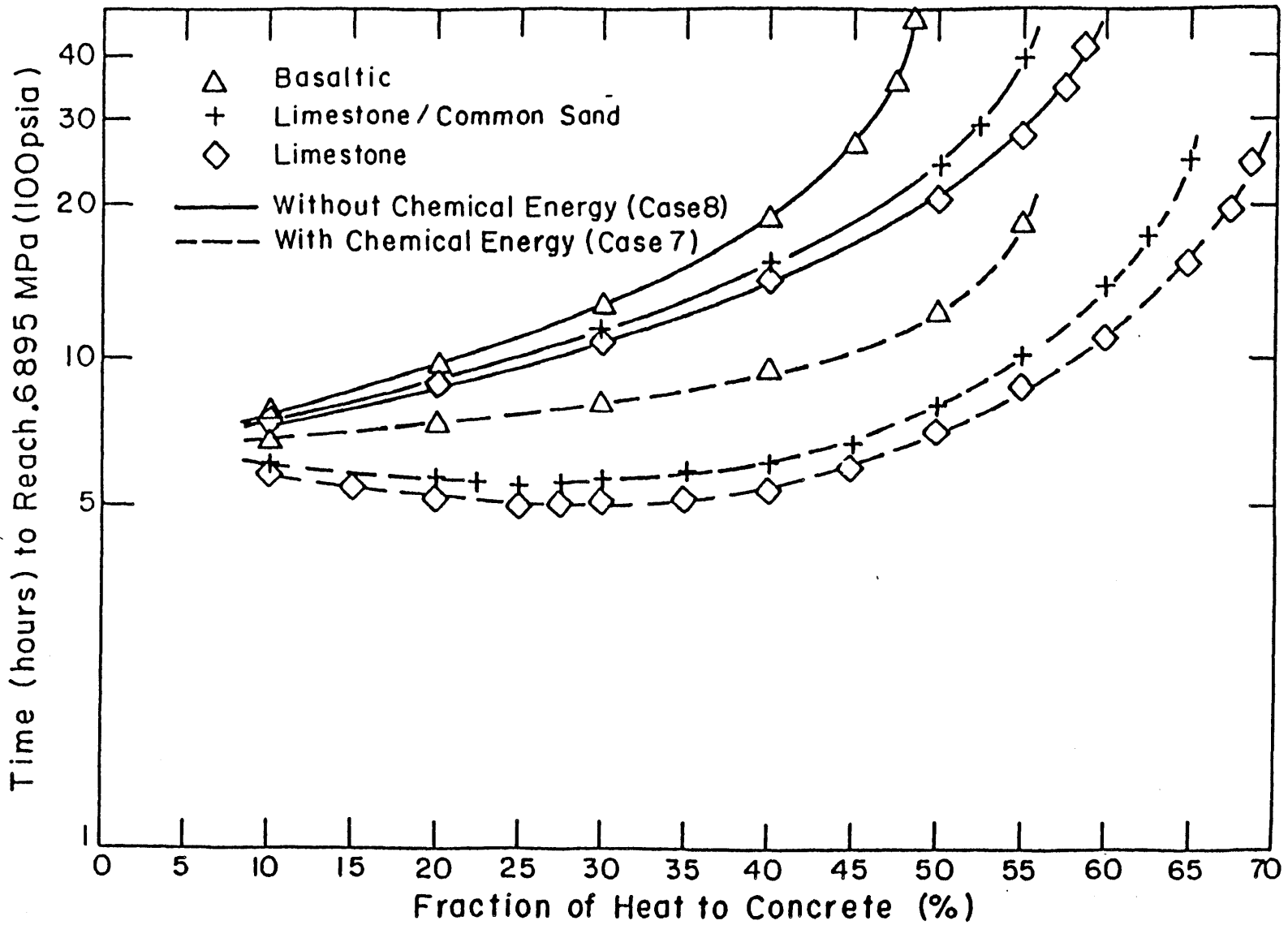
Figure 2.9   Time Required to Pressurize a PWR Large Dry Containment to 0.69 Mpa (100 psia)

4. Based on the thermal equilibrium model used in this approach, it is desirable to have as large an amount of water as possible, to act as a heat sink.

CHAPTER 3

A HEAT TRANSFER MODEL FOR HORIZONTAL
CORIUM/CONCRETE INTERFACE

3.1 Heat Transfer at An Erosion Interface

The problem of melting of a horizontal solid by an overlying hot liquid pool has
been extensively studied by many investigators. Their works can be classified into
the following categories: erosion of a miscible substrate, erosion of an immiscible
substrate and erosion with gas injection.

3.1.1 Erosion of A Miscible Substrate

Farhadieh and Baker [F3] used carbowax 1500 (density is 1150 kg/m^3) as the
solid substrate and aqueous $NaBr$ or KI solution as the liquid pool. The melted solid
and liquid pool are mutually soluble. A plane heater was used as the heat source. The
initial liquid density ranged between 1068 and 1750 kg/m^3, which was obtained by
variation of the solute concentration. It was found that the melting system is highly
sensitive to density differences. As the density ratio, density of pool to that of melted
solid, increases the heat transfer rate to substrates increases. When the density ratio
is less than unity, the system is gravitationally as well as thermally stable. When the
density ratio is greater than unity, the system, although thermally stable, becomes
gravitationally unstable, and convective processes are initiated. If the density ratio
is less than 1.09, the flow regime appears to be laminar and is characterized by
needle-like streams of low density which penetrate the overlying liquid. When the
density ratio is equal to 1.09. there is a sharp transition to a turbulent region and is
characterized by the presence of vortices which results in considerable increase in heat
transfer and melting rates. As the density ratio is greater than 1.25, the turbulence

becomes even more vigorous and the increase of the heat transfer coefficient with the density ratio is faster than before.

Catton. et al. [C9] performed miscible erosion experiments in different ranges of density ratios (1.72 ~ 2.38). They placed frozen benzene underneath the carbon tetrachloride (CCl_4) or diiodomethane (CH_2I_2). It was found that, at high density ratios. the heat flux to an eroded substrate was independent of the temperature difference between the pool and substrate. It only depended on the density difference. This is consistent with their theoretical derivation based on the Rayleigh- Taylor instability theory. Werle and coworkers studied erosion of miscible substrate of frozen polyethylene glycol 1500 (PEG, $\rho = 1100\ kg/m^3$) and $ZnBr_2$, $NaBr$ solutions [E1, F6]. Both plane heating and internal joule heating were used in their experiments. The results of the test with plane heating agreed with those of Farhadieh and Baker qualitively. But in contrast to the tests with plane heating where the melt layer disappeared by a dissolving process, with internal heating it was destroyed by the action of large scale thermal convection in the bulk of the liquid. This was accompanied by a remarkable increase in heat transfer.

3.1.2 Erosion of An Immiscible Substrate

Several investigations have been made of the melting of solid by an overlying hot liquid pool immiscible with the molten phase of the solid. A qualitative experimental studies of the melting of frozen benzene and frozen o-xylen under warm water were made by Alsmeyer and Reimann [A4]. Tafreshi et al. [T1] studied the phenomena by placing frozen olive oil beneath a pool of water. Their careful studies of the structure of the melt film indicated that the melting process is best described as a Taylor instability. The postexperiment examination of the substrate also supports this arguement. A model. based on the Berenson's film boiling theory, was developed which showed that the melting rate or transport of heat across the melt film depends

on the 1/4 power of a modified melt-layer Rayleigh number i.e.:

$$Nu = C\ Ra^{1/4} \qquad (3.1)$$

where C is a constant and Ra, Nu are defined as:

$$Ra = \frac{(h_{sf} + 0.5C_p\Delta T)_{ms}\ g(\rho_p - \rho_{ms})}{(\nu K)_{ms}\Delta T}\left(\frac{\sigma}{g(\rho_p - \rho_{ms})}\right)^{\frac{3}{2}} \qquad (3.1a)$$

$$Nu = hA/K \qquad (3.1b)$$

and

$$A = \left(\sigma/g(\rho_p - \rho_{ms})\right)^{0.5} \qquad \text{(Laplace Constant)} \qquad (3.1c)$$

h = heat transfer coefficient

h_{sf} = fusion heat of substrate

C_p = specific heat

K = thermal conductivity

ρ = density

ν = kinematic viscosity

σ = surface tension

ΔT = temperature difference between pool and substrate melting point

and subscripts are referred to:

ms = melted solid

p = pool

The above conclusions have been checked by Farhadieh and Epstein experimentally [F4]. In their experiments. many pool - solid material pairs were used, covering wide ranges of density differences between the material. melt-layer viscosity and the heat of fusion. Materials selected for the solid phase were pentadecane, p-xylene. paraffin wax. frozen olive oil and polyethylene glycol 6000. The overlying liquids were water. KI and $ZnBr_2$ solutions. With their choice of frozen substrate - liquid pool combinations, melting heat transfer observations with the modified melt-layer Rayleigh numbers ranging from approximately 10^4 to 10^7 were possible. Their results showed that almost all the data lay between two $Nu \sim Ra^{1/4}$ relations with C equaled to 0.20 and 0.43. The former was derived by Tafreshi [T1] and the latter was based on Berenson's film boiling model [B5]. They also pointed out that the experimental data could be better represented by a $Nu \sim Ra^{1/5}$ relation with a proportionality constant equaled to 0.63. This relation was obtained from the problem of laminar film condensation [G6].

3.1.3 Erosion Heat Transfer with Gas Injection

In Corium/Concrete Interaction. the decomposition of concrete is accompanied by large amounts of gas generation. Several simulant experiments have been performed for studying this phenomenon, i.e. the heat transfer at an eroded interface with gas injection. At UCLA and KfK, the phenomenon was studied by placing the dry ice underneath the hot water or benzene. In these experiments. a continuous gas film (CO_2) was observed separating the pool and substrate. At U. of Wisconsin. the same phenomenon was studied by injecting gas through a porous plate into a volumetrically heated pool. In these tests no continuous gas film was observed. These different results lead to different models for calculating the interfacial heat transfer between the pool and melting substrates. The details of those experiments and models will be described in the following subsections

3.1.3.1 Gas Film Model

It has been observed [A5,D2] that after placing a horizontal slab of dry ice beneath a pool of warm water, the solid surface was immediately covered with a gas blanket from which CO_2 bubbles started to leave in a very regular fashion. The interface wavey pattern oscillated initially, but soon the surface becomes uneven and a standing wave pattern is estabilished. During each cycle, the interface was found to grow, collapse and regrow at the same location rather than alternate nodes and antinodes as observed in film boiling on flat plates and cylindrical heaters. Based on this observation, and using the same kind of analysis as that of Berenson's film boiling, Dhir et al.[D2] and Alsmeyer et al.[A5] arrived at the following correlation independently:

$$h = C_o \left(\frac{K_g^3 h_{sf} \rho_g (\rho_p - \rho_g) g}{\mu_g \Delta T \sqrt{\sigma / g (\rho_p - \rho_g)}} \right)^{0.25} \tag{3.2}$$

where the subscripts g and p denote gas and pool respectively and C_o is 0.43 and 0.36 for Alsmeyer and Dhir respectively. This correlation is exactly of the same form as that of Eq.3.1. The proposed correlation can predict part of Dhir's data, as shown in Fig.3.1.

Equation 3.2 can be rearranged into the following form:

$$h = C_c' \frac{K_g}{A} \left(\frac{\sigma}{\mu_g J_g} \right)^{1/3} \tag{3.3}$$

where J_g is the superficial gas velocity, A is Laplace's constant defined by Eq.3.1c and C_c' is 0.326 and 0.256 for Alsmeyer and Dhir respectively. This model is used in the CORCON and WECHSL codes.

It was also found by Dhir [D2] that as the liquid pool temperature is increased beyond a certain limit, the heat transfer coefficient begins to increase with the
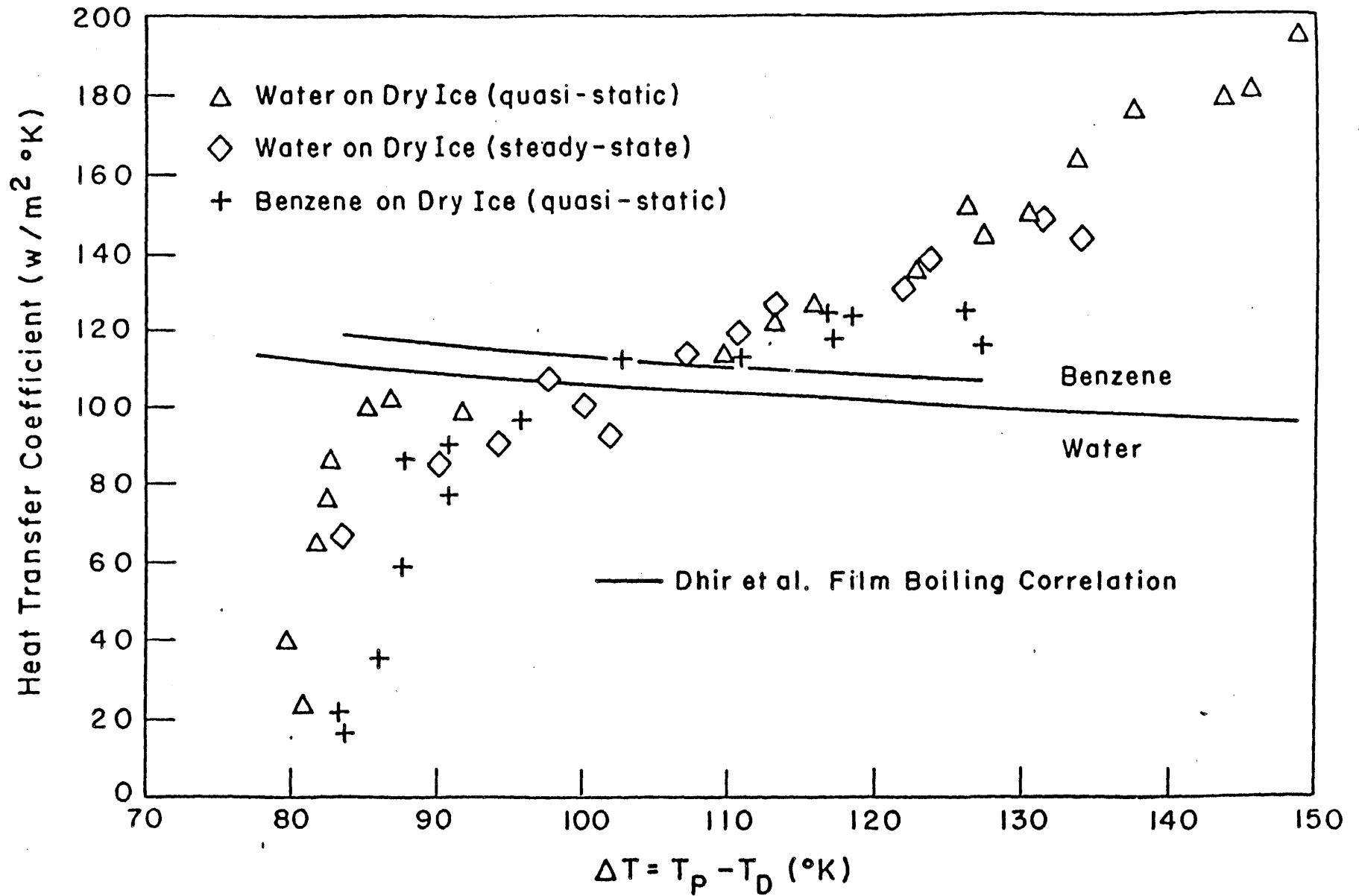
Figure 3.1 Variation of Heat Transfer Coefficients with Temperature Difference between Pool and Dry Ice Sublimation Temperature

temperature difference. This is contrary to the predictions of Eq.3.2. Dhir [D2] argued that the increase of the heat transfer coefficient is due to the ripply or turbulent nature of film. He proposed that in turbulent film regime. for constant Prandtl number of 0.7. the heat transfer coefficients should be correlated with the Reynold numbers i.e.:

$$h = 11.37 \frac{K_g}{A} Re^{0.5} \quad \text{for} \quad Re > 3.68 \tag{3.4}$$

where

$$Re = \frac{\rho_g J_g A}{\mu_g}$$

Again A is the Laplace constant. The corresponding superficial gas velocity of this transition for water/dry ice system is about 7.8 mm/sec, for corium/concrete system is about 380 mm/sec. Equation 3.4 has not been used in any MCCI code.

According to the Kelvin-Helmhotlz [H5] theory, a stable gas film will exist only if the superficial gas velocity exceeds a certain limiting value. The minimum required superficial gas velocity. based on the model proposed by Kutateladze and Malenkov [K5] at 1978. is given as:

$$\left(J_g\right)_{film} = K_s \sqrt{\sigma/\rho_g A} \tag{3.5}$$

where

$$K_s = \begin{cases} 30. \ M^{2/3} & Ar > 10^4 \\ 6.3 \ M^{2/3} Ar^{1/6} & Ar < 10^4 \end{cases}$$

$$M^2 = \rho_g g A / P$$

$$Ar = g A^3 / \nu^2$$

$$A = \left(\sigma/g(\rho_\ell - \rho_g)\right)^{0.5}$$

where P is the system pressure and subscripts ℓ and g refer to liquid and gas respectively.

71

The values of the minimum required supericial gas velocity and the correspond-
ing ablation rate, $\dot{Y}$, for different types of concrete beneath oxidic corium are sum-
marized in Table 3.1. The corresponding values for those thermophysical properties
used in this calculation are summarized in Appendix B. Table 3.1 also shows the
corresponding values for forming a slag layer across the interface if it were governed
by the same mechanism as described above. From Table 3.1, it can be seen that both
a stable gas film and a stable slag layer exist only under considerably high ablation
rates. Up to now, the existence of a gas film across the corium/concrete interface has
not been proven in any real material experiments.

The Kutateladze criterion was also used to analyze the dry ice experiment of Dhir
et al. [D2]. It was found that the superficial gas velocity required ($\sim 800 \; mm/sec$) for
forming a stable gas film is far beyond the data range of the experiments (as shown
in Fig.3.2). Nevertheless, it can be argued that the gas film in the erosion process
of dry ice is controlled by Taylor instability. Therefore, the minimum superficial gas
velocity required to form a stable gas film is determined by Berenson's [B5] minimum
stable film criterion.

$$(J_g)_{min} = 0.09 \left(\frac{g\sigma(\rho_\ell - \rho_g)}{(\rho_\ell + \rho_g)^2} \right)^{0.25} \tag{3.6}$$

where ℓ and g denote liquid pool and gas respectively. A calculation based on the
Eq.3.6 shows that the required superficial gas velocity is $\sim 15 \; mm/sec$. This is within
the data range of the dry ice experiment.

The experimental data of Dhir et al. [D2] were plotted based on the superficial
gas velocity of carbon dioxide and the results are shown in Fig.3.2. The solid lines in
Fig.3.2 correspond to the value predicted by Eq.3.3. From Fig.3.2, it can be seen that
the heat transfer coefficient increases with the superficial gas velocity. This is not
the characteristic of film boiling. For film boiling the heat transfer coefficient should
decrease as the superficial gas velocity increases, as predicted by Eq.3.3, because the

72

Table 3.1

The Minimum Superficial Velocity Required to Form a Film Across the Interface

Concrete	C_g	Gas Film $(J_g)_{film}$ m/sec	$\dot{Y}$ mm/sec	Slag Layer $(J_g)_{film}$ m/sec	$\dot{Y}$ mm/sec	$\delta_{gas}/\delta_{slag}$
Basaltic	0.065	3.442	3.361	0.0309	35.92	0.4903
Limestone/ Common sand	0.267	3.160	1.255	0.0309	45.82	0.7188
Limestone	0.416	3.109	0.862	0.0309	55.79	0.8482
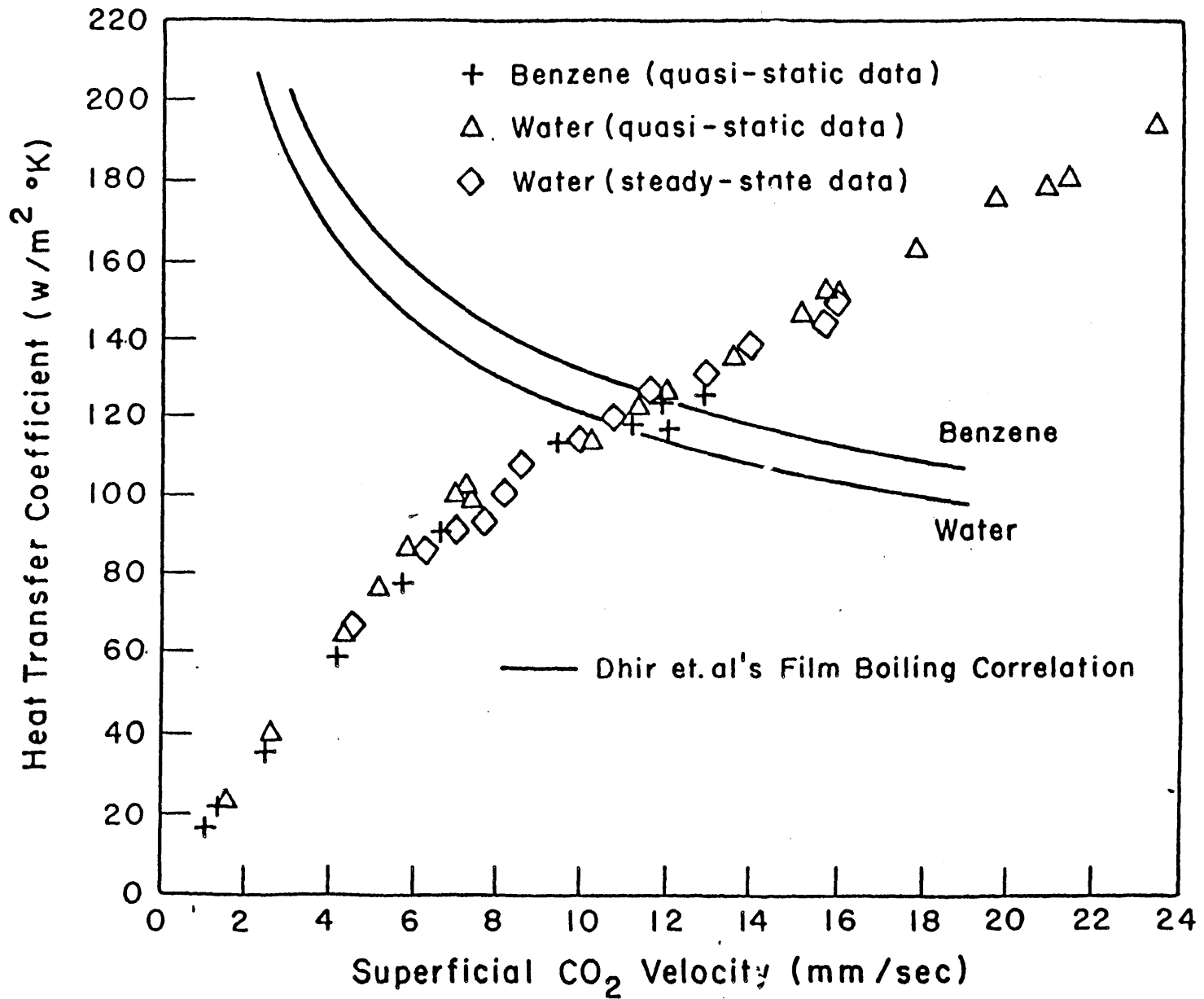
Figure 3.2   Variation of Heat Transfer Coefficients with Superficial Carbon Dioxide Velocity
(Compared with Film Boiling Correlation)

film will then be thicker.

According to the data trend shown in Fig.3.2, the process is more like that of nucleate boiling. A comparison between the experimental results and the values calculated from a nucleate boiling correlation of Kutateladze [K4] is shown in Fig.3.3. The correlation is:

$$h = 0.44 \frac{K_\ell}{A} Pr_\ell^{0.35} Re_g^{0.7} \left(\frac{P \times 10^{-4}}{(\sigma g(\rho_\ell - \rho_g))^{0.5}} \right)^{0.7} \tag{3.7}$$

where P is system pressure. From Fig.3.3, it can be seen that although the trend predicted is correct. The calculated values are an order of magnitude higher than the experimental results. Hence, a typical nucleate boiling correlation can not predict the results of dry ice experiment.

3.1.3.2 Model of U. of Wisconsin

At U. of Wisconsin, a volumetrically-heated pool with gas injection at boundaries was used to simulate the heat transfer process taking place at an eroding surface with gas injection [F5]. In their apparatus, the electrically heat fluid (0.05 molar $CuSO_4$ solution) is bound from the bottom and two sides by water-cooled porous brass plates. Measurements of the upward, downward and sideward heat transfer rate at the pool boundaries were made over wide ranges of power density. superficial gas velocity (between 0.0 ~ 20 mm/sec [A1] which is above the Berenson's stable gas film limit, 14.6 mm/sec) and aspect ratios (ratio of width and depth of the pool). In their tests, the continuous film was not observed. Based on the results of the experiment, purely empirical correlations for the downward and sideward heat transfer were proposed. The one for the downward heat transfer is of the following form [A1]:

$$h = 5.69 \frac{K_\ell}{A} \left(\frac{\rho_\ell J_g^3}{g\mu_\ell} \right)^{0.043} \tag{3.8}$$

Note that the thermal conductivity in the above correlation is that of the liquid
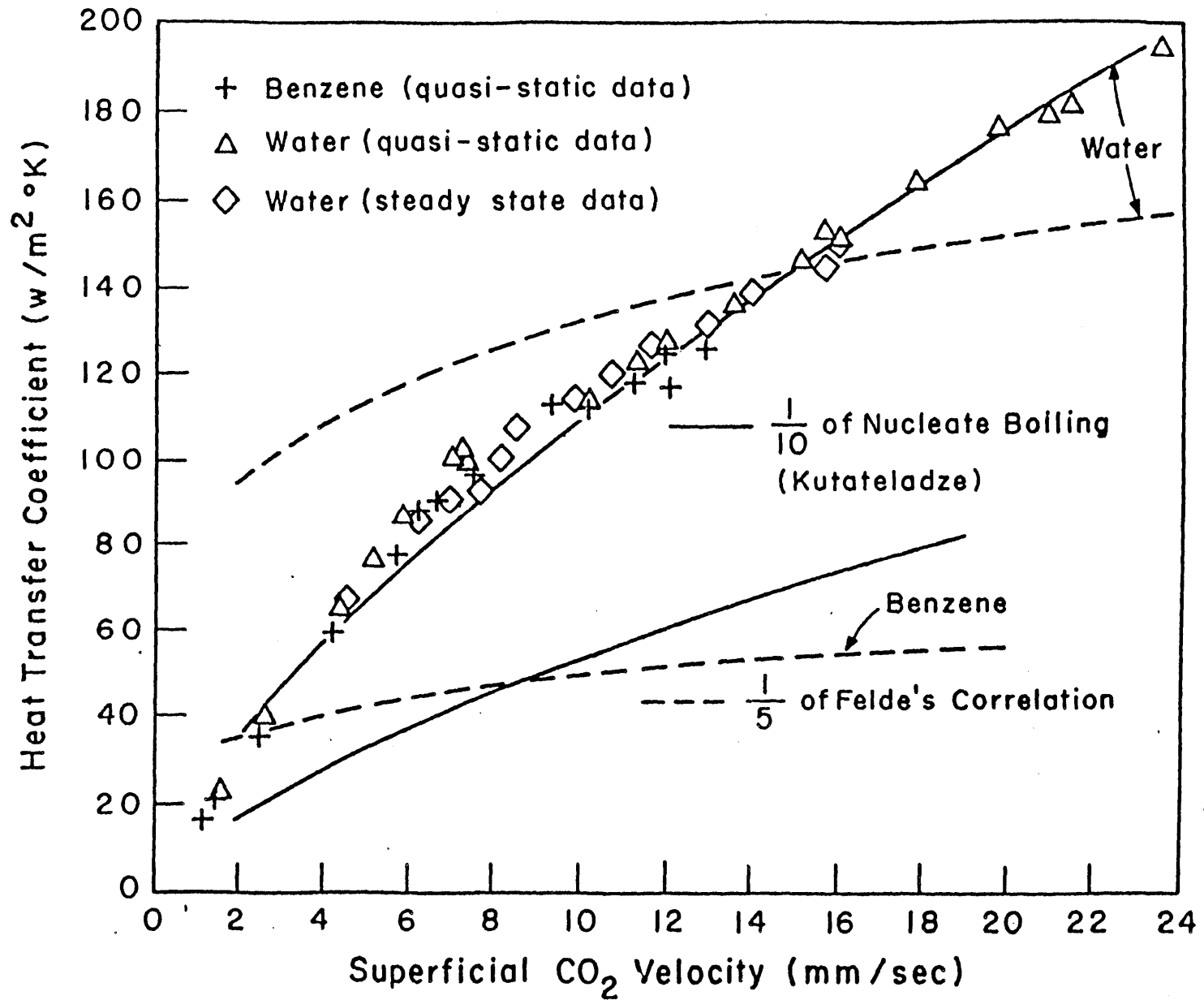
Figure 3.3   Variation of Heat Transfer Coefficients with Superficial Carbon Dioxide Velocity
(Compared with Nucleate Boiling Correlation)

pool. This correlation has been compared with the data of water or benzene/dry ice. The result is shown in Fig.3.3. It can be seen that the correlation predicts that the heat transfer coefficient will increase with the superficial gas velocity. However, the calculated values are approximately five times higher than the experimental results.

The direct application of Eq.3.8 to the analysis of Corium/Concrete Interaction is questionable. The correlation was obtained by empirical curve fitting based on the data of an experiment without involving the melting phenomenon - the major physical process of MCCI. Nevertheless, their experiment suggested that proposed another possible physical picture might occur at the horizontal corium/concrete interface - a process like that of the nucleate boiling.

The heat transfer coefficient in the nucleate boiling regime could be as much as ten to twenty times larger than the film boiling regime. Paik et al. [P1] examined the effect of these heat transfer uncertainties on the behavior of Corium/Concrete Interaction. The CORCON/Mod1 code was modified so that one could selectively alter individual heat transfer coefficient by a constant value. In their studies, the convective heat transfer coefficients at the interface were taken to be an order of magnitude above or below nominal CORCON value. It was found that this causes the gas generated and the concrete eroded to be altered by 20~30% from the base case calculation after about two hours of Corium/Concrete Interaction.

From the above, it is concluded that the pseudo film boiling heat transfer model can only predict a small portion of water or benzene/dry ice experimental results. If the data are analyzed based on the superficial gas velocity, the data trend is more like that of nucleate boiling. A simple calculation based on the flooding limit of Kutateladze's shows that the assumption of a stable film boiling process across the corium/concrete interface might be unrealistic for the potentially realizable ablation rate. The other problem associated with the film assumption in the analysis of MCCI is it neglects the presence of slag.

U. of Wisconsin's experiment pointed out that the heat transfer process across the eroded interface with gas injection might be nucleate boiling. Different assumptions on the flow regimes can result in different predictions on the behavior of MCCI. To account for this, a new model was proposed to interpret the results of water or benzene/dry ice experiments [D2] and a new semiempirical correlation was derived.

3.2 Model Formulation

3.2.1 Physical Picture

If the gas film does not exist, or the gas film is dramatically thinned in each bubbling cycle, the fundamental heat transfer mechanism across the corium/concrete interface can be considered as a transient heat conduction process between the hot pool and the relatively cold concrete surface. As this transient heat conduction proceeds, the decomposition gas bubbles will rise up and away from the surface due to the buoyancy force. The interface will be stirred and some hot liquid will be brought into contact with the cold surface as shown in Fig.3.4a. This phenomenon, similar to nucleate boiling, leads to periodic contact between the hot pool material and the concrete.

In the present model, the interface is divided into a number of square regions and bubbles are assumed to be released from the center of each square region. This is consistent with what has been observed in water/dry ice experiment. The following derivations are focused on this square region, where it is assumed that the mechanism of periodic contact is the dominant mode for heat transfer across the interface.

3.2.2 Transient Heat Conduction

As a hot pool at temperature T_p is brought into contact with a relatively cold solid, at temperature T_s , the temperature at the interface immediately assumes a value T_I . The temperature history of a semi-infinite medium with a step change in surface tempatute from T_p to T_I is [C1]:

78
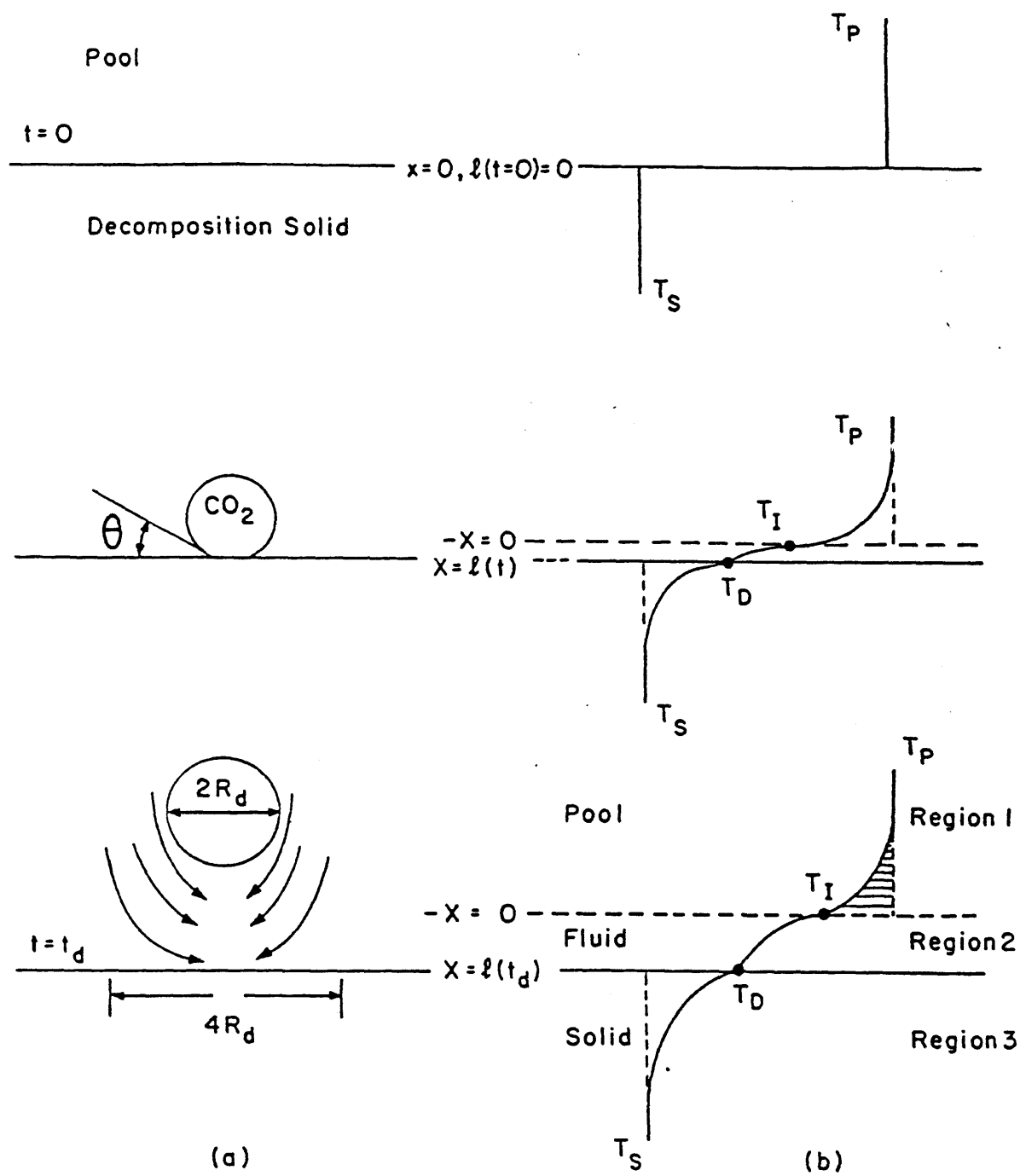
Figure 3.4   Illustration of Periodic Contact Heat Transfer Model

$$T(x,t) = T_p - (T_p - T_I)\, erfc(x/2\sqrt{\alpha_p t}) \tag{3.9}$$

where α_p is the thermal diffusivity of the pool.

The amount of heat transfer out of the pool per unit area within a certain time period t_d can be obtained by the following integration:

$$q = \int_0^\infty \rho_p C_p (T_p - T(x,t_d))\, dx$$

That is:

$$q = \frac{2\rho_p C_p \sqrt{\alpha_p t_d}}{\sqrt{\pi}} (T_p - T_I) \tag{3.10}$$

3.2.3 Bubble Dynamics

Assuming that the bubble growth rate is proportional to the gas (rising fluid) generation rate, J_f, then the rate of bubble growth is given by :

$$S(R)\rho_f \frac{dR}{dt} = L^2 \rho_f J_f \tag{3.11}$$

where S(R) is the surface area of the bubble whose radius is R, and L is the dimension of the square region under consideration. The surface area of the bubble can be approximated by that of a spherical bubble times a correction factor $C_1(\theta)$, where θ is the contact angle between the bubble and the solid surface. Then we have:

$$\int_0^{R_d} 4\pi R^2 C_1(\theta)\, dR = \int_0^{t_d} L^2 J_f\, dt \tag{3.12}$$

where R_d and t_d are the bubble departure radius and bubble contact time respectively. For constant $C_1(\theta)$ and an average J_f, integration of Eq.3.12 results in:

$$t_d = \frac{4}{3} C_1(\theta_d) \frac{R_d^3}{L^2 (J_f)_{ave}} \qquad (3.13)$$

It is further assumed that the bubbles will depart from the solid surface when the surface tension can no longer hold the bubbles on the surface against the buoyancy force. Then at the point of departure:

$$\left(\frac{4}{3}\pi R_d^3\right)g(\rho_p - \rho_f)\phi(\theta_d) = 2\pi R_d\sigma \qquad (3.14)$$

This leads to

$$R_d = \frac{3}{2} \phi(\theta_d)\left(\frac{\sigma}{g(\rho_p - \rho_f)}\right)^{0.5} \qquad (3.15)$$

where θ_d is the departure angle and $\phi(\theta_d)$ is a correction factor to take into account the non-spherical part of the bubbles.

As the bubble moves away from the surface, it will strip some liquid along with it. Assume that the region influenced by the bubble is proportional to the square of the bubble departure radius [H2], the total amount of heat, Q, transferred out of the pool in each square region within the time period t_d is:

$$Q = C_2 q R_d^2 \qquad (3.16)$$

where C_2 is a proportionality constant.

The bubble population density is assumed to be proportional to the inverse of the square of Taylor instability wavelength. Thus, the dimension of the square region, L, is proportional to the Taylor wavelength:

$$L \propto \frac{\sqrt{3}}{2\pi}\left(\frac{\sigma}{(\rho_p - \rho_f)}\right)^{0.5} \qquad (3.17)$$

81

Combining Eqs. (3.10), (3.13), (3.15), (3.16) and (3.17) and defining the heat transfer coefficient, h, as follows:

$$h = \frac{Q}{L^2(T_p - T_D)t_d} \qquad (3.18)$$

we get:

$$h = C_c\sqrt{(\rho KC)_p}\,(J_f)_{ave}^{0.5}\frac{T_p - T_I}{T_p - T_D}\frac{1}{A^{0.5}} \qquad (3.19)$$

where the constant C_c is the combination of several other constants. After some manipulation, Eq.3.19 can be cast into the following form:

$$Nu_f = C_o\frac{\beta_p}{\beta_f}\,(Re_fPr_f)^{0.5}\frac{T_p - T_I}{T_p - T_D} \qquad (3.20)$$

where

$$Nu_f = hA/K_f \qquad (3.21)$$

$$Pr_f = C_f\mu_f/K_f \qquad (3.22)$$

$$Re_f = \rho_f J_f A/\mu_f \qquad (3.23)$$

$$\beta = \sqrt{\rho KC}$$

$$A = \sqrt{\sigma/g(\rho_p - \rho_f)}$$

In these equations ρ, C, K are the density, specific heat and thermal conductivity respectively. The subscripts f and P stand for the rising fluid and pool respectively.

3.2.3 Interface Temperature

The interface temperature T_I, when two materials with different temperature are brought together, depends on the physical process involved at the interface regions [C1].

If there is no phase change, the interface temperature can be calculated by the follwing equation:

$$\frac{T_p - T_I}{T_I - T_s} = \sqrt{\frac{(\rho K C)_s}{(\rho K C)_p}}$$

(3.24)

where subscripts p and s denote the hot and cold materials respectively. However, if one of the materials undergoes phase change, as in the dry ice experiment, the interface temperature can be determined by a three region approach as shown in Fig.3.4b. The interface equation is [C1]:

$$T_I = \frac{T_p K_p \alpha_f^{0.5} + T_D K_f \alpha_p^{0.5}}{K_p \alpha_f^{0.5} erf\lambda + K_f \alpha_p^{0.5}}$$

(3.25)

where T_D is the decomposition temperature of solid and parameter λ is determined by the following equation written based on the energy balance at the melt front.

$$\frac{K_p \alpha_f^{0.5}(T_p - T_D)}{K_p \alpha_f^{0.5} erf\lambda + K_f \alpha_p^{0.5}} e^{-\lambda^2} - \frac{K_s \alpha_f^{0.5}(T_D - T_s)}{K_f \alpha_s^{0.5} erfc(\lambda \frac{\alpha_f^{0.5}}{\alpha_s^{0.5}})} e^{-\lambda^2 \frac{\alpha_f}{\alpha_s}}$$
$$= \frac{h_{fc} \lambda \sqrt{\pi}}{C_f}$$

(3.26)

where f denotes the melt phase of the cold solid. Under the limiting condition of $\lambda = 0$, from Eq.3.25 $T_I = T_D$, and Eq.3.26 reduces to Eq.3.24.

he two region approach, Eq.3.24, will be used in the following derivation. It is also believed that after few bubbling cycles, the temperature at the solid surface will be fixed at its decomposition temperature T_D. Therefore, the T_s in Eq.3.24 will be replaced by T_D.

83

3.3 Periodic Contact Model for Erosion Heat Transfer with Gas Injection

3.3.1 Proposed Correlation

Substituting Eq.3.24 into Eq.3.20 and assuming $T_s = T_D$ we have:

$$Nu_f = C_o \left(\frac{1}{1 + \beta_f / \beta_p} \right) (Re_f Pr_f)^{0.5} \tag{3.27}$$

The average superficial velocity, $(J_f)_{ave}$, in Re_f can be calculated from a simple heat balance:

$$(J_f)_{ave} = \frac{h(T_p - T_D)}{\rho_f h'_{sf}} \tag{3.28}$$

In the above equation an effective heat of fusion, h'_{sf}, is used in order to consider the sensible heat absorbed by the rising fluid and the solid.

$$h'_{sf} = h_{sf} + C_f \frac{(T_I - T_D)}{2} + C_s(T_D - T_s) \tag{3.29}$$

The experimental data of Dhir et al. [D2] were analyzed with the dimensionless group in Eq.3.27. The results are shown in Fig.3.5. Combining Eqs. 3.27 and 3.28 we have:

$$Nu_f = C_o^2 \left(\frac{1}{1 + \beta_f / \beta_p} \right)^2 \left(\frac{C_f(T_p - T_D)}{h'_{sf}} \right) \tag{3.30}$$

The experimental data of Dhir et al. [D2] were analyzed with the dimensionless group in Eq.3.30. The results are shown in Fig.3.6. It can be seen that the experimental data for each fluid fall on a nearly straight line except few data points at low temperature. Those are believed to be induced by the freezing process at the interface which could happen if the pool temperature is low. This phenomenon was not considered in the above derivations. An actual calculation based on Eqs.3.25

84
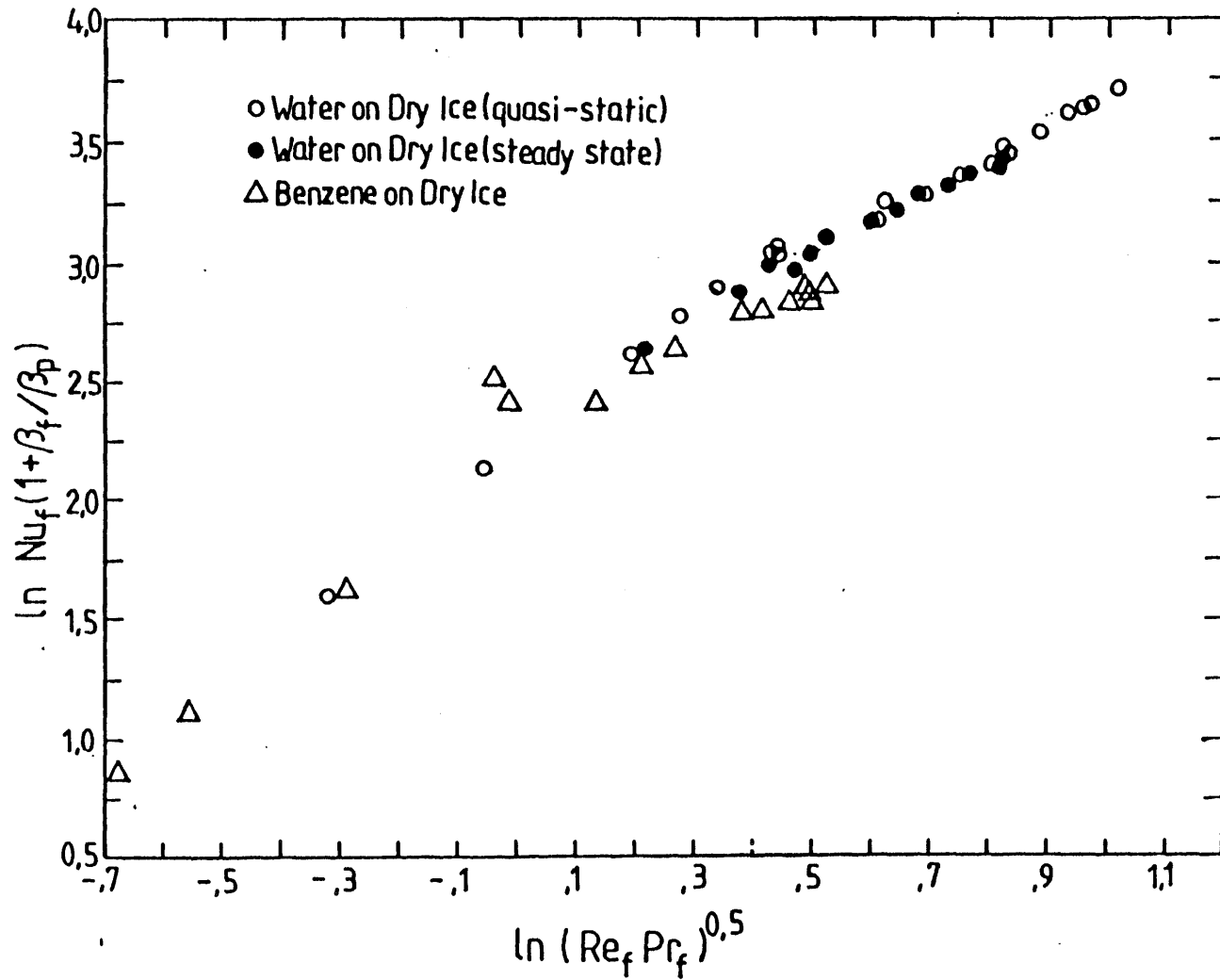
Figure 3.5   Behavior of Correlation Parameters (Eq.3.27)
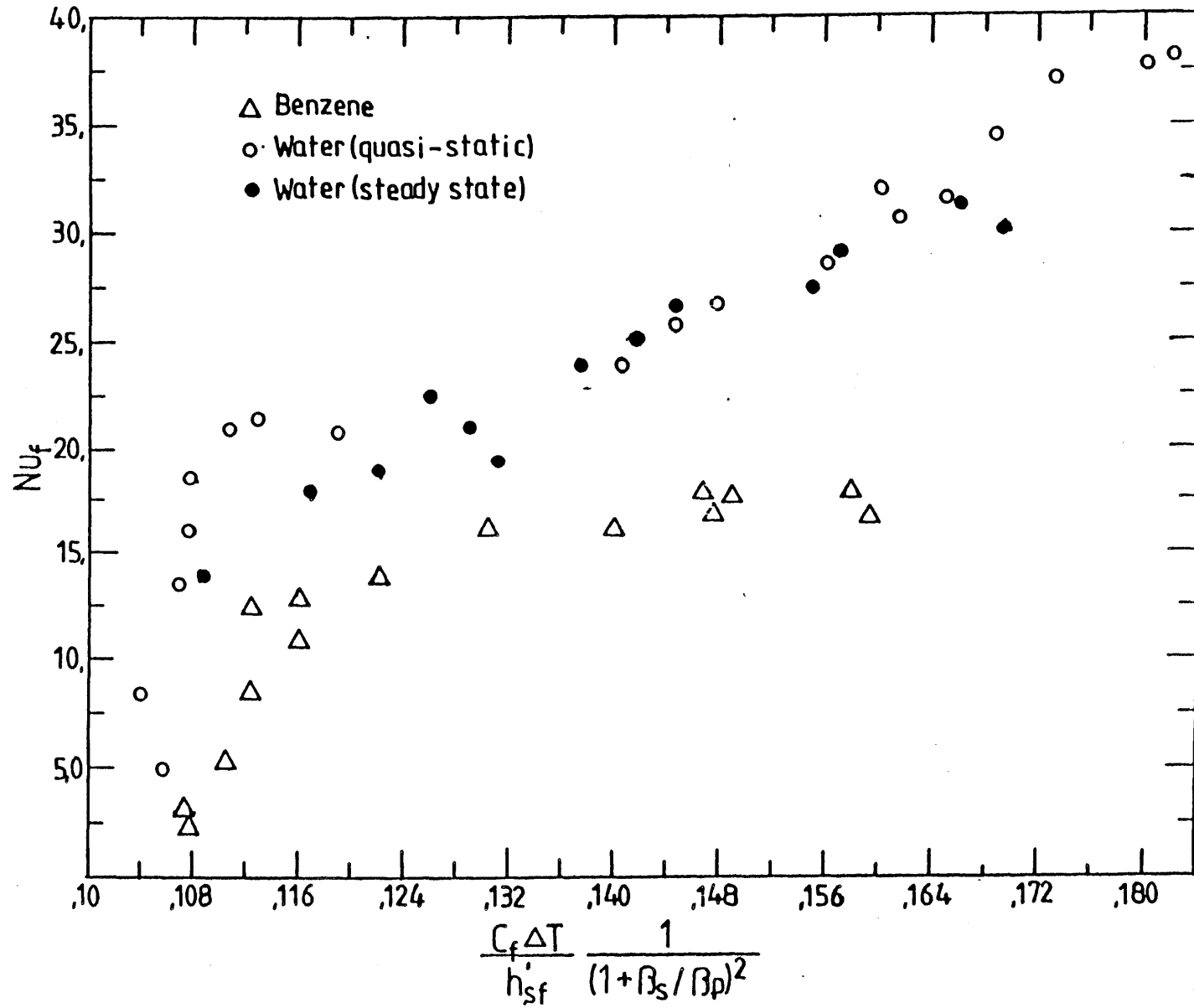
Figure 3.6   Behavior of Correlation Parameters (Eq.3.30)

98

and 3.26 showed that the interface temperature. T_I, for those data points indeed fell below the freezing point of pool material.

Accordingly, a correlation may be based on the following modification to the form of Eq.3.30:

$$Nu_f = C'_o \left(\frac{1}{1 + \beta_f/\beta_p}\right)^2 \left(\frac{C_f(T_p - T_d)}{h'_s f}\right)^n \left(\frac{K_p}{K_s}\right)^m \tag{3.31}$$

In Eq.3.31 a correction factor (K_p/K_s) has been applied in order to bring the experimental data of water and benzene closer. A correction factor of this form is not unreasonable because in the above derivations we neglected any direct contact between the pool and solid (Fig.3.4a), which is unrealistic. The constant C'_o, n and m are to be determined by a least squared curve fitting of the experimental data. By the help of the definition of Re_f and Eq.3.28 , Eq.3.31 can be rearranged into the following form:

$$Nu_f = \left(C'_o \left(\frac{1}{1 + \beta_f/\beta_p}\right)^2 (Re_f Pr_f)^n \left(\frac{K_p}{K_s}\right)^m\right)^{\frac{1}{1+n}} \tag{3.32}$$

The following constants are arrived at by a least square curve fitting of experimental data of Dhir et al., $n = 1.528$, $m = 0.32$, $C'_c = 767.13$. Two data points of water and three data points of benzene were discarded during the curve fitting due to the reason stated above.

The heat transfer coefficients calculated by Eqs.3.31 and 3.32 are compared with experimental data in Fig.3.7 and 3.8 respectively. It can be seen that, except those with small T_p, the proposed correlation, based on either the superficial gas velocity or on the temperature difference, fit the experimental results very well. The discrepancy is believed to be induced by the freezing at the interface, which was not accounted for in the proposed model.

87
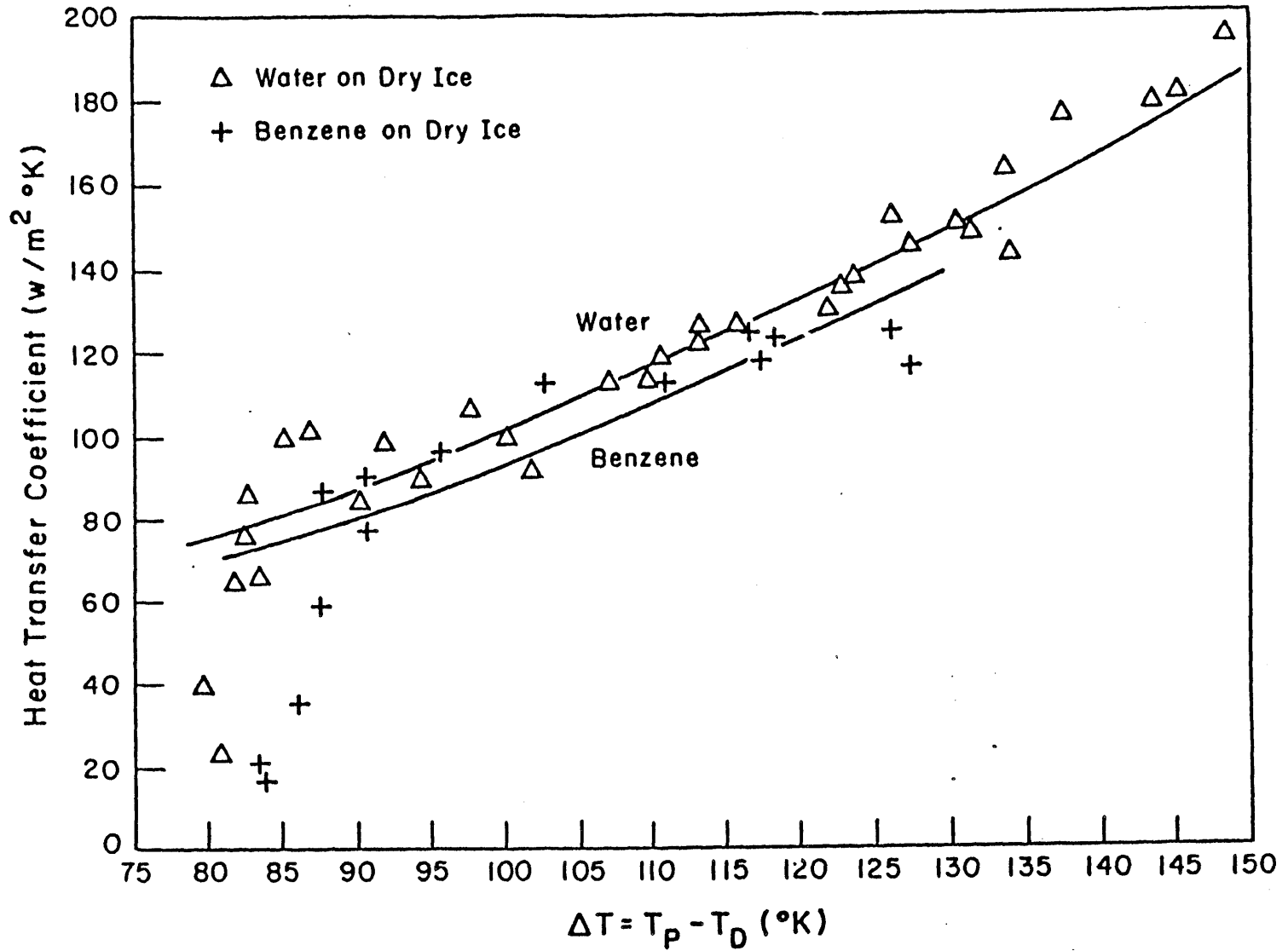
Figure 3.7 Comparison between the Predicted Values andDry Ice Experimental Results (Based on Temperature)
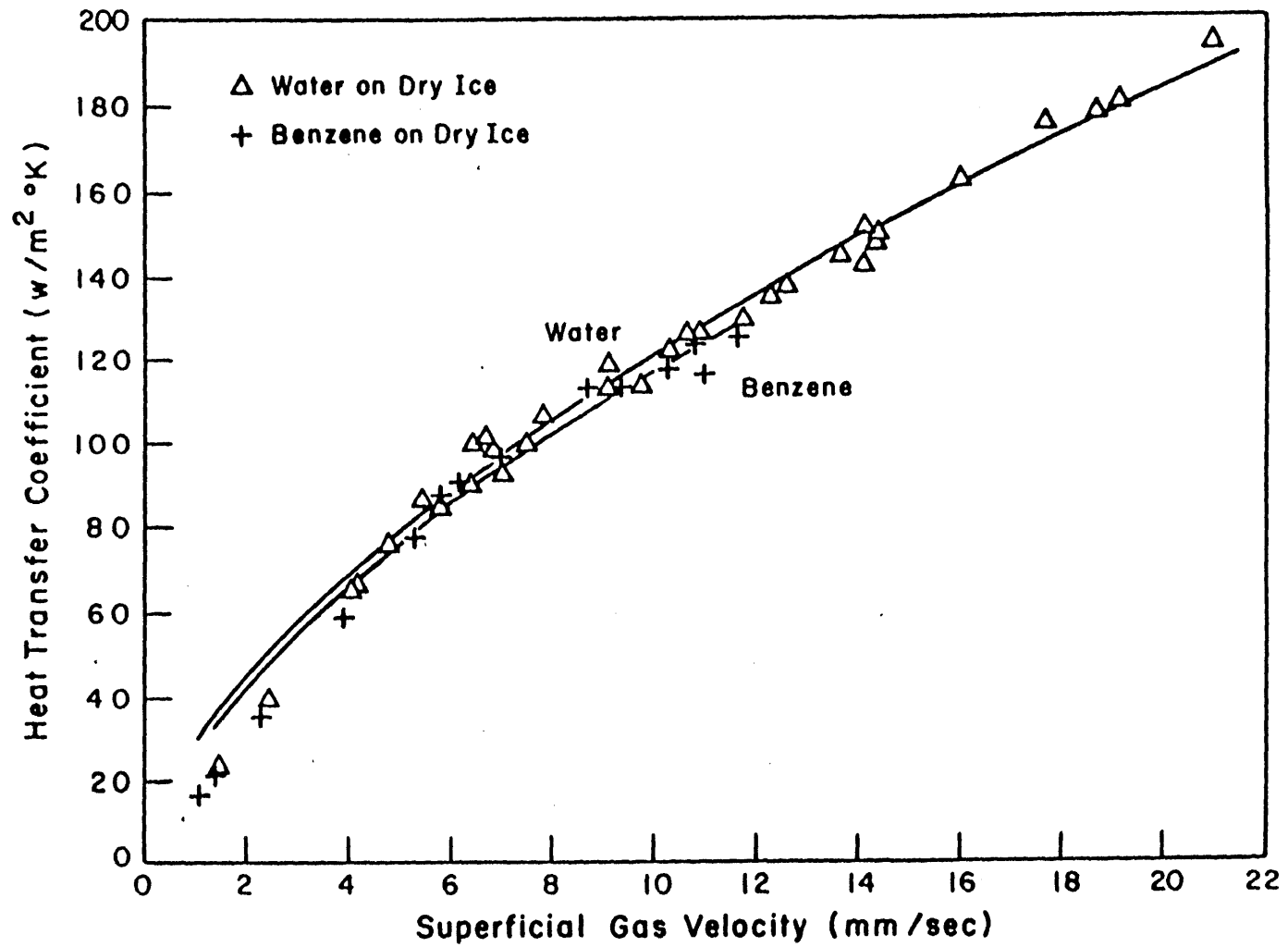
Figure 3.8 Comparison between the Predicted Values and Dry ice Experimental Results (Based on Superficial Gas Velocity)

3.3.2 Application of the Proposed Correlation to MCCI

Based on the observations [P8] of BURN1 test the melt/concrete contact was greatest midway between the localized gas emission site (~70% of the time) and the lowest contact occured at localized generation site (20% to 30% of the time). As assumed in the proposed model, the separation of the bubble sites can be predicted by the Taylor instability model. For the conditions of the BURN1, the calculated bubble separation is 53 mm. The observed separation in the test was 40 ± 7 mm.

In Sandia's Large Scale tests [P7], the concrete crucibles were exposed to steel melt several times. Gas evolution rate in repeat crucibles were markedly less than that observed in tests with virgin concrete. The molten steel pools in the repeat tests apparently cooled more slowly than the pool in tests with virgin material. This is consistent with the trend of the proposed correlation i.e. the heat transfer rate will increase with the gas generation rate.

In the application of the proposed correlation to analysis of MCCI, several problems are encountered due to the fact that the concrete is a heterogenous mixture of several different substances. These problems are:

1. The decomposition temperature is not precisely defined but is known to lie between the solidus and liquidus temperatures. The situation is even more complicated by the fact that concrete loses its gas constituents continuously as temperature increases. Most of the decomposition gases of concrete are formed directly at the corium/concrete interface, and part of the gases will be released through the cracks in the concrete.

2. The decomposition enthalpy of concrete is not also well defined.

3. As concrete decomposes, two 'rising fluids' exist, i.e. gases and slag. This makes the determination of thermophysical properties of effective rising fluid very difficult.

The following approximations were made here:

1. The decomposition temperature T_D is chosen as the average of the solidus and liquidus temperature of concrete.

2. The decomposition enthalpy is calculated by Eq.2.6.

3. It is assumed that the slag and gases will move away from the interface with a slip ratio S. From this slip ratio and the gas weight fraction, x, of the concrete we can determine the void fraction of the rising fluid with the following equation:

$$\alpha = \frac{1}{1 + ((1 - x)/x)(\rho_f/\rho_p)S} \tag{3.33}$$

Then, the density and thermal conductivity of the rising fluid are determined by this void fraction. The specific heat of the rising fluid is, however, determined by weight fraction.

Based on the above approximations, several calculations have been made for the metallic corium attack of basaltic and limestone/common sand concrete. In those calculations the thermophysical properties of metallic corium and slag are taken from Reference B6 and those of gases are from CORCON code (see Appendix B). As shown in Fig.3.9, the predicted heat transfer coefficients are different for different assumption on the calculation method of slip ratio. The slip ratio can be set equal to either the square root or cubic root of the density ratio of slag to gas. The former corresponds to minimizing the two phase specific momentum under critical flow condition and the latter corresponds to minimizing the specific kinetic energy of the two phase mixture [C7]. The first one gives higher slip ratio and lower void fraction and therefore higher thermal conductivity for the rising fluid and results in higher heat transfer coefficient. The calculated heat transfer coefficients differ by 40% for the two cases for metallic corium on top of basaltic concrete. The proposed correlation also gives different heat transfer coefficients for different system pressures (Fig.3.9). As the system pressure increases, the density of the gas increases leading
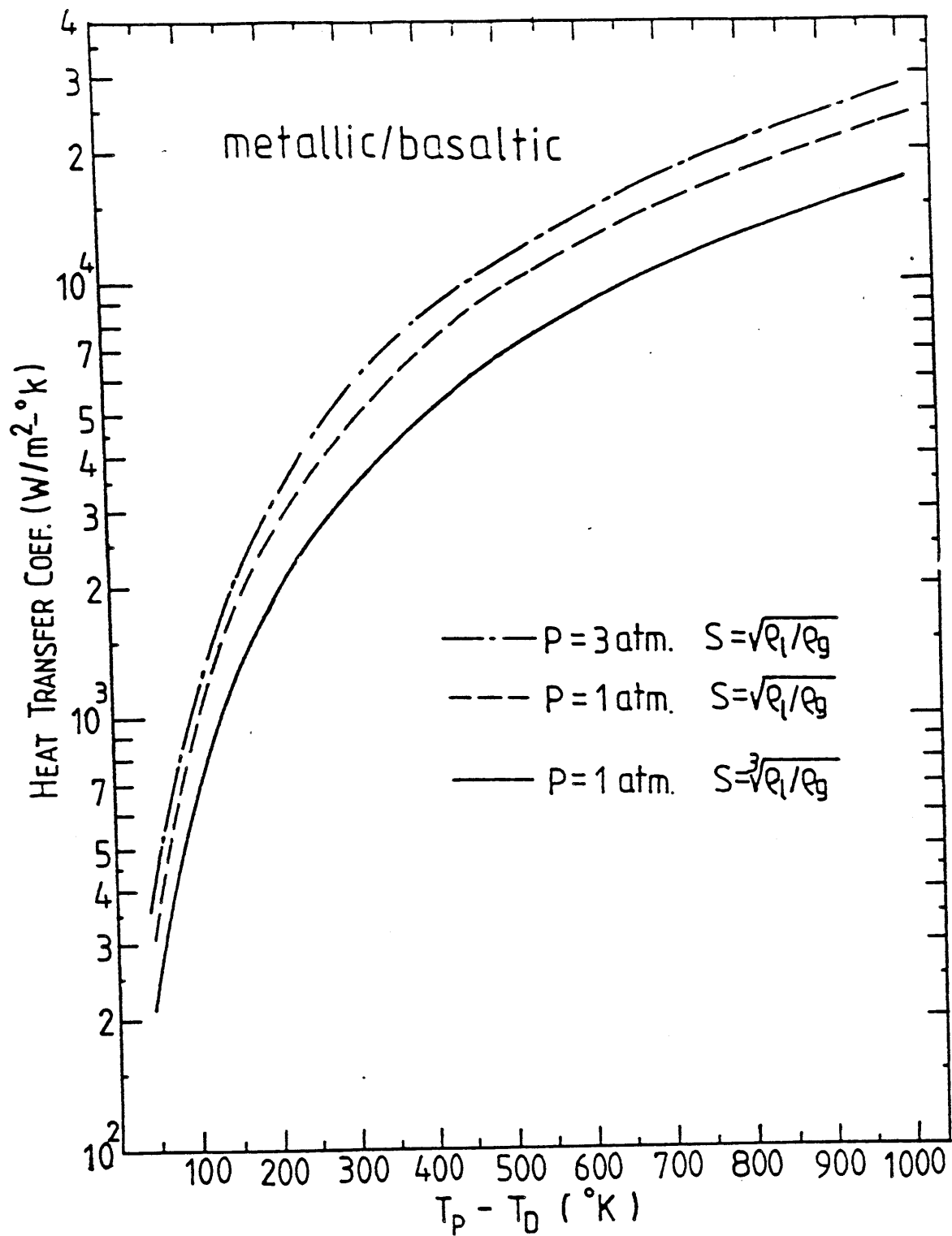
Figure 3.9   Predicted Heat Transfer Coefficients for Corium/ Concrete Interaction
with Proposed Periodic Contact Model

to lower void fraction and therefore higher thermal conductivity of the rising fluid. For metallic corium on top of basaltic concrete with system pressure equal to 3 and 1 atm, the calculated heat transfer coefficients differ by approximately 18%.

A comparison between the predicted heat transfer coefficients for metallic corium on top of basaltic and limestone/common sand concrete is shown in Fig.3.10. For a slip ratio equal to the cubic root of the density ratio of slag to gases, the heat transfer coefficients of limestone/ common sand concrete are higher by approximately 17%. For metallic corium on top of limestone/common sand concrete, different assumptions on the slip ratio can only result in about 7% difference in heat transfer coefficient. This is because the limestone/common sand concrete has higher gas content and the void fraction of its rising fluid is relatively insenitive to the slip ratio.

3.4 Discussion and Conclusions

In CORCON/Mod1, the calculation of downward heat transfer from corium pool to underlying concrete can be divided into three parts. Figure 3.11 shows the equivalent circuit of those heat transfer processes. The corresponding heat transfer correlations used in CORCON/Mod1 are also shown in Fig.3.11. In general, h_{pool} is so large and makes insignificant contribution to the overall heat transfer resistance. Figure 3.12 shows the heat transfer coefficients for metallic corium/concrete system predicted by CORCON model. From Fig.3.12. it can be seen that if the temperature difference is small the heat transfer process is convectively controlled. Therefore the overall heat transfer coefficient decreases with temperature difference. If the temperature difference is large, the heat transfer process is radiatively controlled, the overall heat transfer coefficient increases with temperature difference. Figure 3.12 also shows the heat transfer coefficients calculated with the proposed model. The heat transfer coefficient predicted by the proposed model is 2 to 10 times higher than that of CORCON model in the temperature range of interest.

In Fig.3.13, the proposed model is compared with the discrete bubble model of
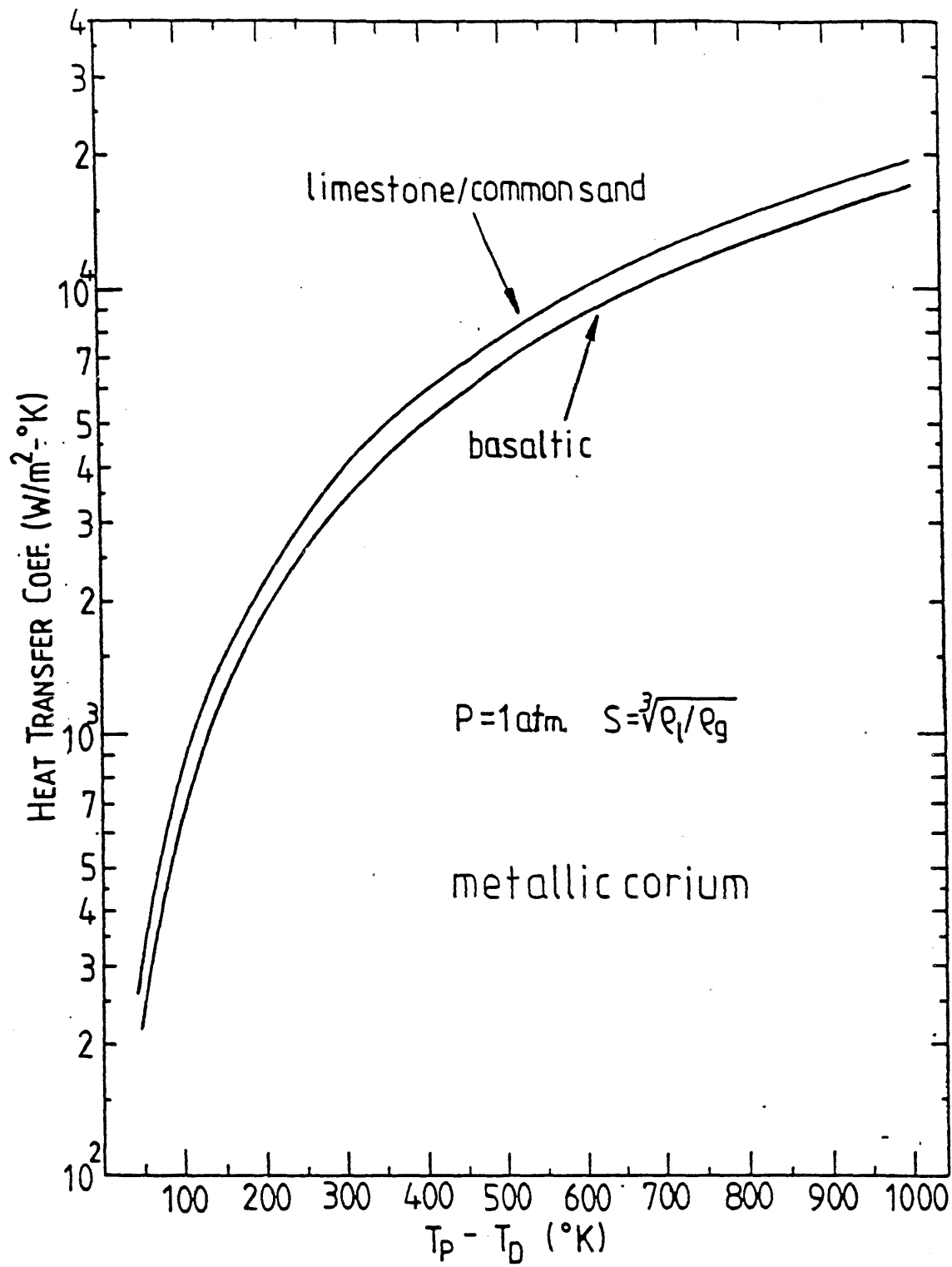
Figure3.10   Predicted Heat Transfer Coefficients for Corium/ Concrete Interaction
with Proposed Periodic Model
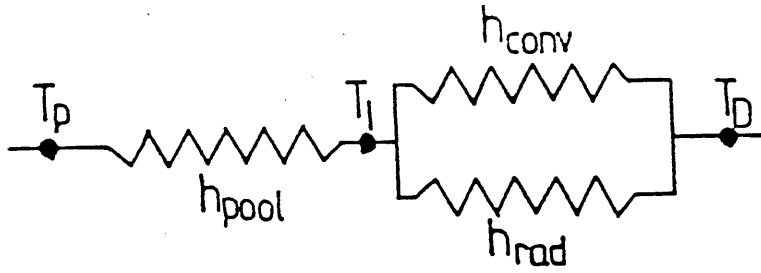
$$h_{pool} = K_p \left(Pr_p \frac{\varrho_p^2 g}{\mu_p^2} \right)^{1/3} (0.0003 \beta \Delta T + 0.4 \alpha^2)^{1/3}$$

$$\alpha = \frac{J_g}{J_g + V_{ter}} \qquad V_{ter} = 1.53 \left(\frac{g \sigma_p}{\varrho_p - \varrho_g} \right)^{1/4}$$

$$h_{conv} = 0.326 \frac{K_g}{A} \left(\frac{\sigma_p}{\mu_g J_g} \right)^{1/3}$$

$$A = \left(\frac{\sigma_p}{g (\varrho_p - \varrho_g)} \right)^{1/2}$$

$$h_{rad} = \sigma F (T_I^4 - T_D^4)$$

$$F = \frac{1}{\frac{1}{E_p} + \frac{1}{E_c} - 1}$$

$$h_{film} = h_{conv} + h_{rad}$$

$$h_{total} = 1 / \left(\frac{1}{h_{pool}} + \frac{1}{h_{film}} \right)$$

Figure 3.11   Downward Heat Transfer Model of CORCON
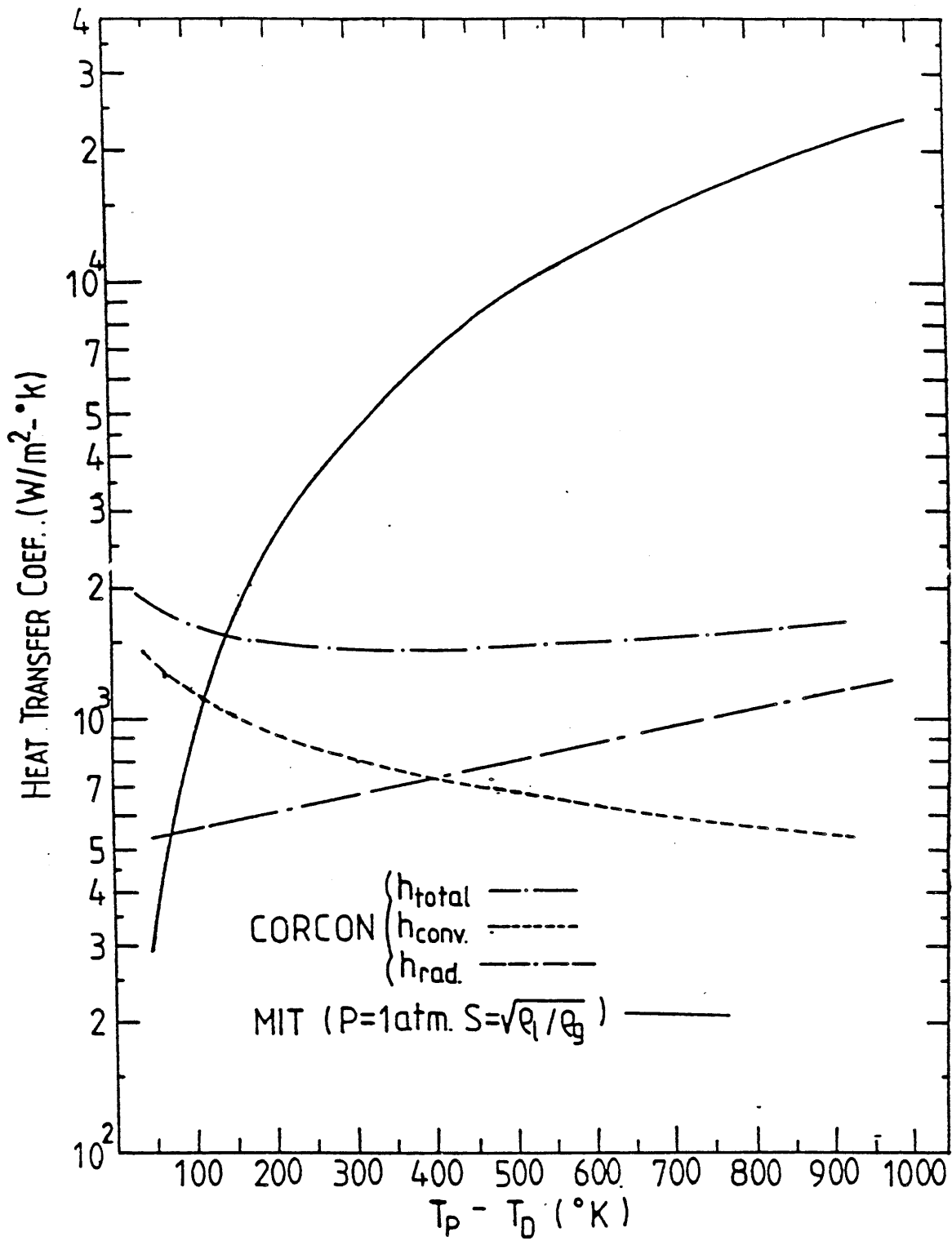
Figure 3.12   Comparison between the Heat Transfer Coefficients Predicted of CORCON/Mod1 and Proposed Model for Metallic melt and Basaltic Concrete
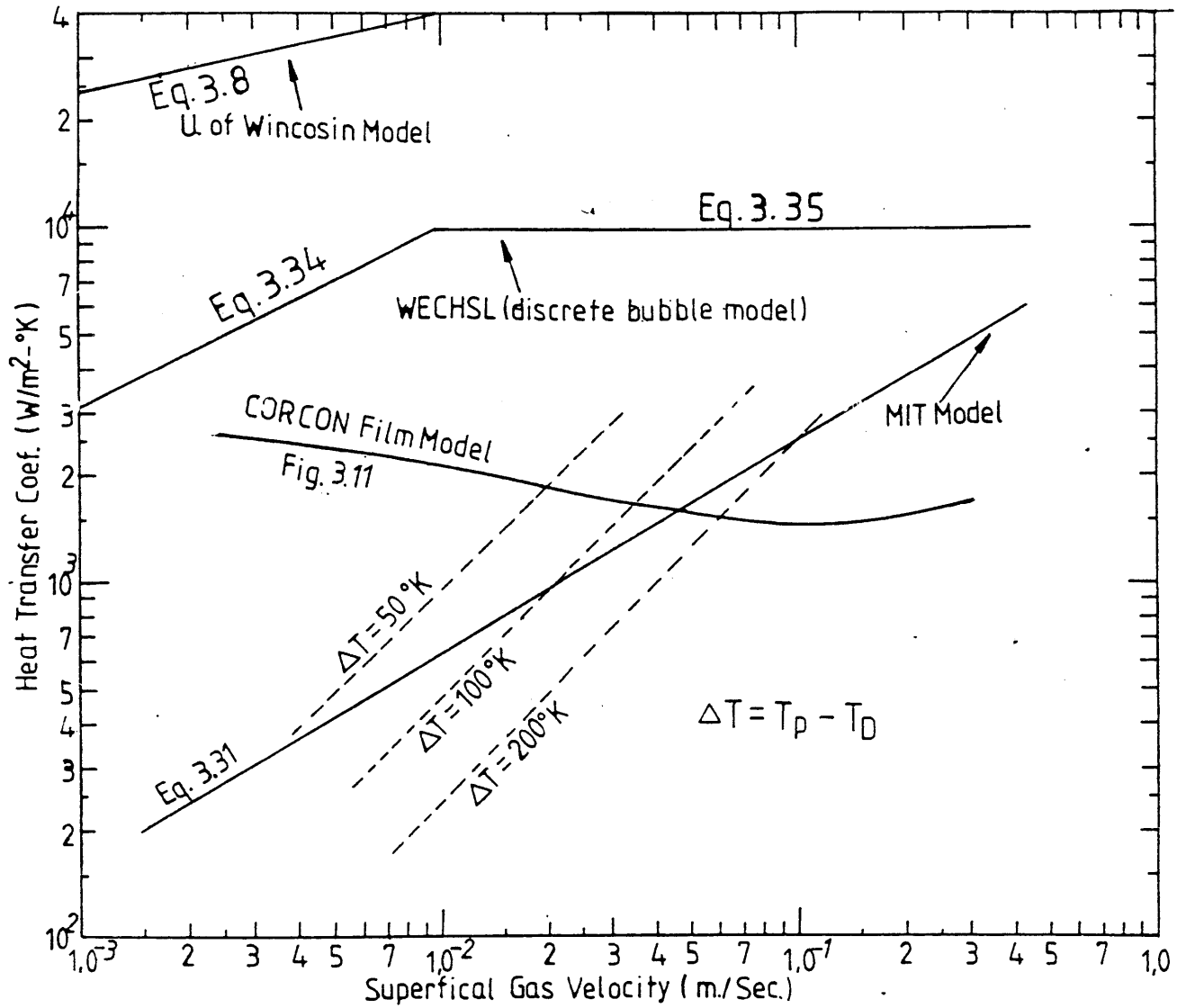
Figure 3.13 Comparsions of the Predictions of the Heat Transfer Coefficients between the Metallic Melt and Basaltic Concrete

WECHSL, model of U. of Wisconsin and CORCON model. The comparison is based on the superficial gas velocity. The discrete bubble model of WECHSL code has the following form [R2]:

$$h = \frac{1.65}{6^{0.25}} \frac{K_p}{A} Re_g^{0.5} Pr_p^{0.5} \left(\frac{\rho_{water}}{\rho_g}\right)^{0.5} \tag{3.34}$$

where

$$Re = (\rho_g J_g A / \mu_p)$$

$$A = (\sigma / g(\rho_p - \rho_g))^{0.5}$$

and ρ_{water} is the density of water. Based on some hydrodynamic considerations, the following limitation is imposed on Eq.3.34 i.e. the calculated heat transfer coefficient can not be higher than the value calculated by the following equation [R6]:

$$h = 3.43 \frac{K_p}{A} Pr_p^{0.38} \tag{3.35}$$

From Fig.3.13, it can be seen that the model of U. of Wisconsin gives a very high heat transfer coefficient. The results of the discrete bubble model, the CORCON model and the proposed MIT model are comparable, the differences are within a factor of 3 over the gas velocity range above 10^{-2} m/sec. Both MIT and CORCON models predicted lower heat transfer coefficient than WECHSL, but with varying trends.

The dotted lines in Fig.3.13 are lines of constant temperature difference $(T_p - T_D)$. The interactions of the dotted lines and solid curves are the operating points of the corresponding model, e.g. for $\Delta T = 200\ ^\circ K$, CORCON model predictes that $h = 1550\ W/m^2\ ^\circ K$ and $J_g = 55\ mm/sec$, MIT model predicts that $h = 2500\ W/m^2\ ^\circ K$ and $J_g = 95\ mm/sec$. From Fig3.13, it can be seen that the predicted values at low superficial gas velocity for certain models are of no physical meaning because the heat transfer coefficient is so high that the temperature difference becomes so small and the pool temperature drops below the freezing point.

98

The intergal effect of proposed model on the analysis of Corium/Concrete Interaction and the containment pressurization rate will be described in Chapter 5 and Chapter 6 respectively.

CHAPTER 4

INTERFACIAL HEAT TRANSFER BETWEEN BUBBLE AGITATED IMMISCIBLE LIQUID LAYERS

4.1 Introduction and Literature Review

4.1.1 Introduction

In MCCI, the immiscible metallic and oxidic phases will be separated into two layers due to the large density difference, provided that the intermixing due to gas agitation is limited. The interfacial heat tranefer between these immiscible layers is important in characterizing MCCI process. As the inter-layer heat transfer rate increases, the heat transferred downward into the concrete from the initially heavy oxidic layer is reduced and the upward heat flux into the overlaying metallic layer is increased. The situation might be reversed as the oxidic phase is diluted by the decomposed concrete and becomes less dense than the metallic phase. As shown in Chapter 2, how the decay heat and stored heat of corium are distributed between the concrete basemat and atmosphere of containment is important in determination of the containment pressurization rate.

The heat redistribution also affects the generation rate of noncondensible concrete gases. One of the important implications of gas generation rate is its effect on aerosol generation which is directly related to the source term analysis of the accidents. It has been suggested that increasing the magnitude of the interfacial heat transfer by factors of 10 and 100 in CORCON model reduces the gas generation rate by factors from 2 to 5 [G2].

In this Chapter the information about heat transfer between bubble agitated liquid layers will be examined and modified so as to select the correlation that should

be applied to analyze the MCCI conditions.

4.1.2 Literature Review

The interfacial heat transfer between the immiscible layers is complicated by the agitation of gas flow. Several correlations have been proposed to characterize this complicated heat transfer phenomena.

Konsetov [K3] considered that the bubble agitated system has the same flow configuration as that of the natural convection. Based on the similarity to natural convection, with the characteristic parameters evaluated for a bubbling liquid layer, he proposed a correlation in terms of the void fraction of the liquid layer. The void fraction can be expressed as a function of the superficial gas velocity. By Konsetov's correlation the heat transfer coefficient will be zero when the superficial gas velocity is zero. This is unrealistic for two liquid layers with different temperatures. Therefore, Blottner [B6] suggested that the interfacial heat transfer coefficient would be better calculated by a combination of Konsetov's correlation with a natural convection correlation. In the correlation proposed by Blottner, the constants in Konsetov's correlation were modified in order to fit limited experimental data. However, when this correlation was used to predict the oil/water experimental data of KfK [W2] considerable discrepancy resulted. The correlation underpredicted the experimental data. This correlation is used in CORCON/Mod1.

Grief [G4] developed a correlation similar in form to that of Konsetov's except for the dependency on void fraction. His correlation also underpredicted the experimental data of KfK [W2,F6].

Werle [W2] proposed that the heat transfer between two horizontal liquids with gas injection can be modeled as a natural convection process with an extra multiplier to account for the effect of gas agitation. Based on the results of oil/water and oil/wood's metal experiments [W2] Werle correlated the multiplier as a function of

superficial gas velocity and density difference between liquids. In his correlation, the natural convection correlation proposed by Haberstroh and Reinders [H1] was used. The proposed model can well predict the experimental results of oil/wood's metal system. But it underpredicts the data of oil/water system. This model is used in WECHSL.

Based on the assumption of transient heat conduction between the arrival of successive bubbles, Szekely [S6] derived an overall heat transfer coefficient for bubble stirred interface of two immiscible liquids. His correlation was later modified by Blottner [B6] to a more general form. These models will be described in following section.

Greene [G5] classified the interfacial heat transfer into two categories: those with entrainment and those without entrainment. A typical fluid pair for the latter is oil/wood's metal [W2] and that of the former is oil/water [G5,W2]. The interfacial heat transfer coefficients for these with entrainment are approximately an order of magnitude higher despite the fact that the thermal conductivity of wood's metal is higher than that of oil. From Fig.4.1 it can be seen that without entrainment the surface renewal model of Szekely [S6] modified by Blottner [B6] represents a lower bound on both the water/mercury and oil/wood's metal data. For those with entrainment, Greene [G5] suggested that an extra term should be added to the surface renewal model to account for the contribution of liquid entrainment. He proposed a purely empirical formula for this extra term, in which the heat transfer coefficient from entrainment is proportional to the product of density, specific heat of the bottom liquid and the superficial gas velocity. He also found that with the proportionality constant between 0.3 and 1.0 all the data points can be enclosed. Since the density ratio of metallic and heavy oxidic layers (around 0.86) is similar to that of oil/water (around 0.9) system, Greene [G6] suggested that the bubble induced entrainment should be taken into consideration in modeling the Corium/Concrete Interaction.

It can be concluded that, when a temperature difference exists between two im-
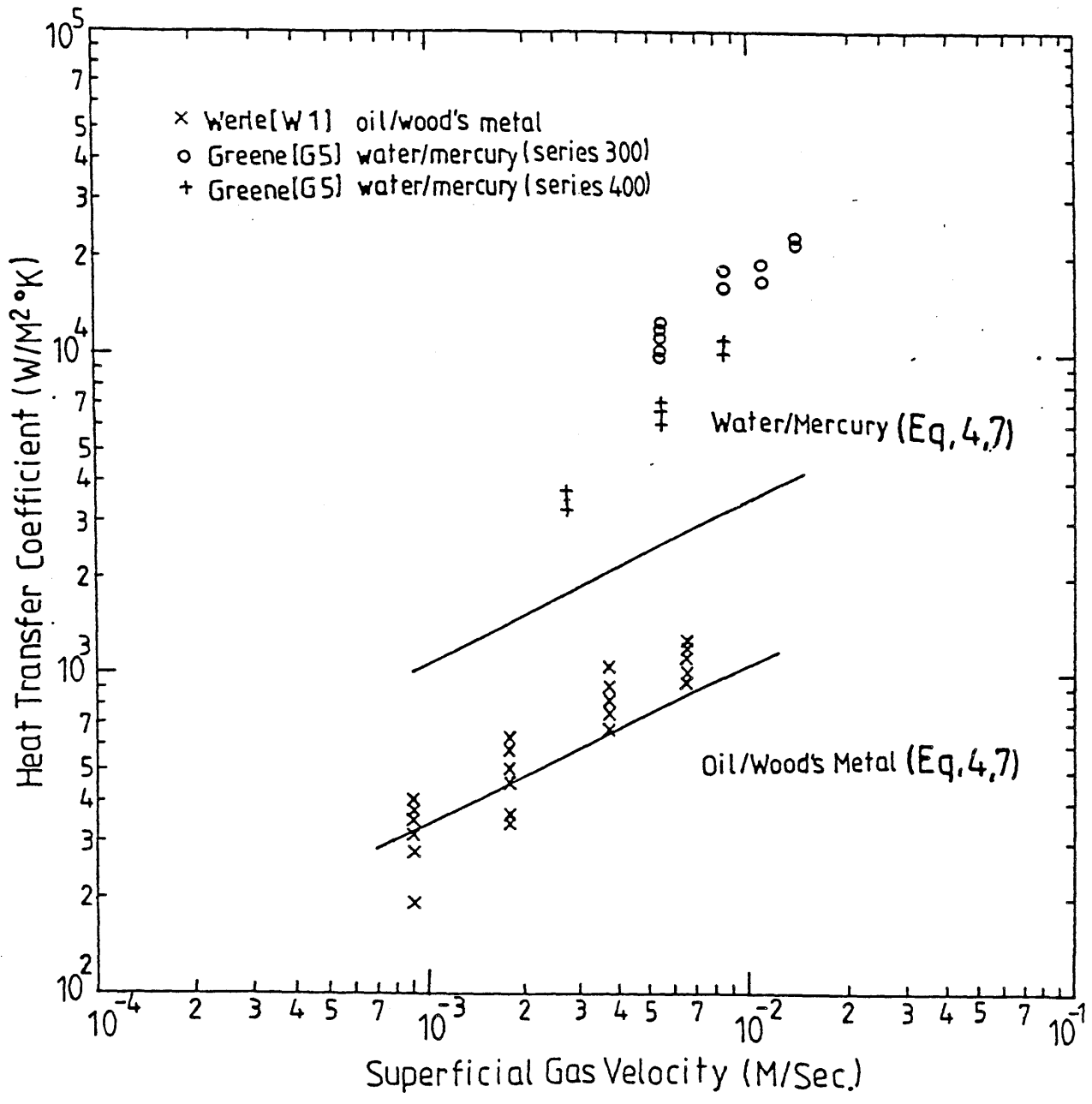
Figure 4.1   Heat Transfer Coefficient at Water/Mercury and
Oil/Wood's Metal Interface with Bubble Agitation

miscible liquid layers, the heat transfer coefficient between these layers should be characterized by natural convection. As bubble agitation is imposed on the layers by a transverse gas flow, a second mechanism - surface renewal - should be included. For certain liquid pairs, the consideration of third mechanism - entrainment - is necessary. The following section summarizes the studies performed on each mechanism. However, it should be pointed out that all the experiments mentioned above were conducted with a relatively low superficial gas velocity. The following relation has been proposed by Kataoka and Ishii [K2] to characterize the transition between the ideal bubbly flow and the churn-turbulent flow:

$$J_g = 0.325 \left(\frac{\sigma g (\rho_\ell - \rho_g)}{\rho_\ell^2} \right)^{0.25} \tag{4.1}$$

where

J_g = superficial gas velocity

ρ = density

σ = surface tension

and subscripts refer to:

ℓ = liquid

g = gas

Accordingly, only the regime of ideal bubbly flow has been studied to date by all the aforementioned studies.

4.2 Fundamental Mechanisms

4.2.1 Natural Convection

For a horizontal heated plate facing upward, the Nusselt number was found to be proportional to the cubic root of the Rayleigh number. Coefficients were variously given between 0.13 and 0.31. More recent work, since the mid-1970's, has focused upon the internally heated pool. Blottner summarized these works in Reference [B6].

Haberstroh and Reinders [H1] examined the heat transfer between two fluid layers with fixed bottom and top temperatures. The heat transferred through each liquid layer is modeled as turbulent convection between parallel flat plates with heating from below. The total heat transfer coefficient is then considered as two thermal conductances in series. Greene [G5] found that, in the limit of zero gas flow rate, his data converged asymptotically to a lower limit calculated by the conducting sheet model of Haberstroh and Reinders. The correlation is:

$$h_{NC} = 0.0535 \frac{(R_U R_L)^{1/3} |T_U - T_L|^{1/3}}{(R_U^{0.25} + R_L^{0.25})^{4/3}} \tag{4.2}$$

where the Rayleigh number is given by:

$$R = K^3 \frac{g\beta}{\nu^2} Pr^{1.252}$$

and

K = thermal conductivity

β = volumetric thermal expansion coefficient

ν = kinematic viscosity

Pr = Prandtl number

and U and L refer to upper and lower liquid respectively. After substituting for the thermal-physical properties into Eq.4.2, the heat transfer coefficient is equal to a constant times the cubic root of the temperature difference, i.e.:

$$h_{NC} = const \ |T_U - T_L|^{1/3} \tag{4.3}$$

The constants for different liquid pairs are summarized in Table 4.1. The physical properties of liquids are based on the values listed in References [B6] and [W2].

Comparing the values of h_{NC} with the experimental results in Fig.4.1, it can

105

Table 4.1

Contribution of Natural Convection

Liquid Pairs	Constant in Eq.(4.3)
Oil/water	16.25
Oil/Wood's Metal	25.36
Water/Mercury	63.08
Metallic/oxidic	142.68

be found that h_{NC} is very small, sometimes even within the uncertainty of the experimental data. Therefore, in the following analysis the contribution of natural convection will be neglected.

4.2.2 Surface Renewal

As the bubble moves across the liquid/liquid interface, it disrupts the temperature gradients at the interface. Transient conduction acts to renew the gradients until the arrival of the subsequent bubble. This phenomenon is referred to as surface renewal.

A heat transfer correlation based on this transient heat conduction mechanism was developed by Szekely [S6]. It has the following form:

$$h_{SR} = \frac{2}{\sqrt{\pi}} \frac{K_U \alpha_U^{-1/2} K_L \alpha_L^{-1/2}}{K_U \alpha_U^{-1/2} + K_L \alpha_L^{-1/2}} \frac{1}{\sqrt{t_e}} \tag{4.4}$$

where α is the thermal diffusivity and t_e is the time interval between the arrival of consecutive bubbles. Szekely suggested that t_e can be calculated as :

$$t_e = \frac{A}{A_b N_o} \tag{4.5}$$

where

A = total cross section of interface

A_b = surface area swept by one bubble

N_o = number of bubbles produced per unit time

This equation was later modified by Blottner (B6) as:

$$t_e = \frac{A V_b}{A_b N_o V_b} = \frac{V_b}{A_b J_g} = 0.445 \frac{r_b}{J_g} \tag{4.6}$$

107

where V_b is the volume of the bubbles and r_b is the equivalent bubble radius. Combining Eq.4.4 and Eq.4.6 together, we get:

$$h_{SR} = 1.69 \frac{K_U \alpha_U^{-1/2} K_L \alpha_L^{-1/2}}{K_U \alpha_U^{-1/2} + K_L \alpha_L^{-1/2}} \frac{J_g^{0.5}}{r_b^{0.5}} \tag{4.7}$$

A comparsion of this correlation with the experimental data is shown in Fig.4.1. It can be seen that the correlation predicts part of the oil/wood's metal data but underpredicts the water/mercury data. From Fig.4.1 it can also be seen that the dependency of heat transfer coefficient on the superficial gas velocity is incorrect, it is underpredicted.

In the above derivation, it is assumed that the time interval between the arrival of consecutive bubbles is inversely proportional to the square root of the superficial gas velocity, J_g. However, this is not necessarily true. If the pool is in an ideal bubbly flow regime, the time interval should be approximately equal to the inverse of the bubble generation frequency, f. Another factor to be considered is that as the bubble moves up in the liquid pool some liquid will be carried along with it. When the bubble reaches the interface, the carried liquid also reaches the interface and thus contributes to the heat transfer process. If the bubble is spherical with diameter D_b, then this influential area will be πD_b^2 [R5]. Assuming n/A is the bubble population density we have:

$$h_{SR} = \frac{2}{\sqrt{\pi}} \frac{K_U \alpha_U^{-1/2} K_L \alpha_L^{-1/2}}{K_U \alpha_U^{-1/2} + K_L \alpha_L^{-1/2}} \sqrt{f} \frac{n}{A} \pi D_b^2 \tag{4.8}$$

This equation can be rearranged as:

$$h_{SR} = \frac{12}{\sqrt{\pi}} \frac{K_U \alpha_U^{-1/2} K_L \alpha_L^{-1/2}}{K_U \alpha_U^{-1/2} + K_L \alpha_L^{-1/2}} J_g \frac{1}{\sqrt{D_b}\sqrt{D_b f}} \tag{4.9}$$

For this hydrodynamically controlled bubble growth process, $D_b f$ in the above equation can be correlated as [I1,Z1]:

108

$$D_b f = 1.18 \left(\frac{\sigma g(\rho_\ell - \rho_g)}{\rho_\ell^2} \right)^{0.25}$$ (4.10)

where ℓ and g refer to liquid and gas respectively.

A assumption about the bubble diameter is still necessary. Fortunately, the bubble diameter in various liquid pools of interest are all of the same order of magnitude. For $D_b = 2$ mm, it is found that a factor of two is needed in the new correlation in order to fit both the water/mercury and oil/wood's metal data (Fig.4.2). Therefore the following equation, with $D_b = 2$ mm, is suggested as the heat transfer coefficient from the surface renewal mechanism.

$$h_{SR} = 12.5 \frac{K_U \alpha_U^{-1/2} K_L \alpha_L^{-1/2}}{K_U \alpha_U^{-1/2} + K_L \alpha_L^{-1/2}} \left(\frac{g(\rho_L - \rho_g)\sigma_L}{\rho_L^2} \right)^{-0.125} \frac{J_g}{D_b^{0.5}}$$ (4.11)

The empirical factor of two is not surprising. The bubbles will not be spherical in the liquid pool; and are more likely to be spheroidal or bell shaped with the longer axis parallel to the interface [Z1]. This means the influential area will be larger than πD_b^2.

From Fig.4.2 it can be seen that the newly proposed model tends to overpredict the dependency of heat transfer coefficient on the superficial gas velocity. Based on the experimental results, the correct power should lie between 0.5 (Eq.4.7) and 1.0 (Eq.4.11). This power can be determined by empirical curve fitting. However, because of the limited amount of experimental data, it may not be productive to improve the fit anymore.

A comparsion between the predictions of this correlation and the oil/water experiment is shown in Fig.4.3. It can be seen that the oil/wood's metal data is well predicted but the data of oil/water tests are not predicted by the correlation. The discrepancy is due to the presence of bubble induced entrainment. As mentioned above, the correlation can only be applied in the ideal bubbly flow regime.
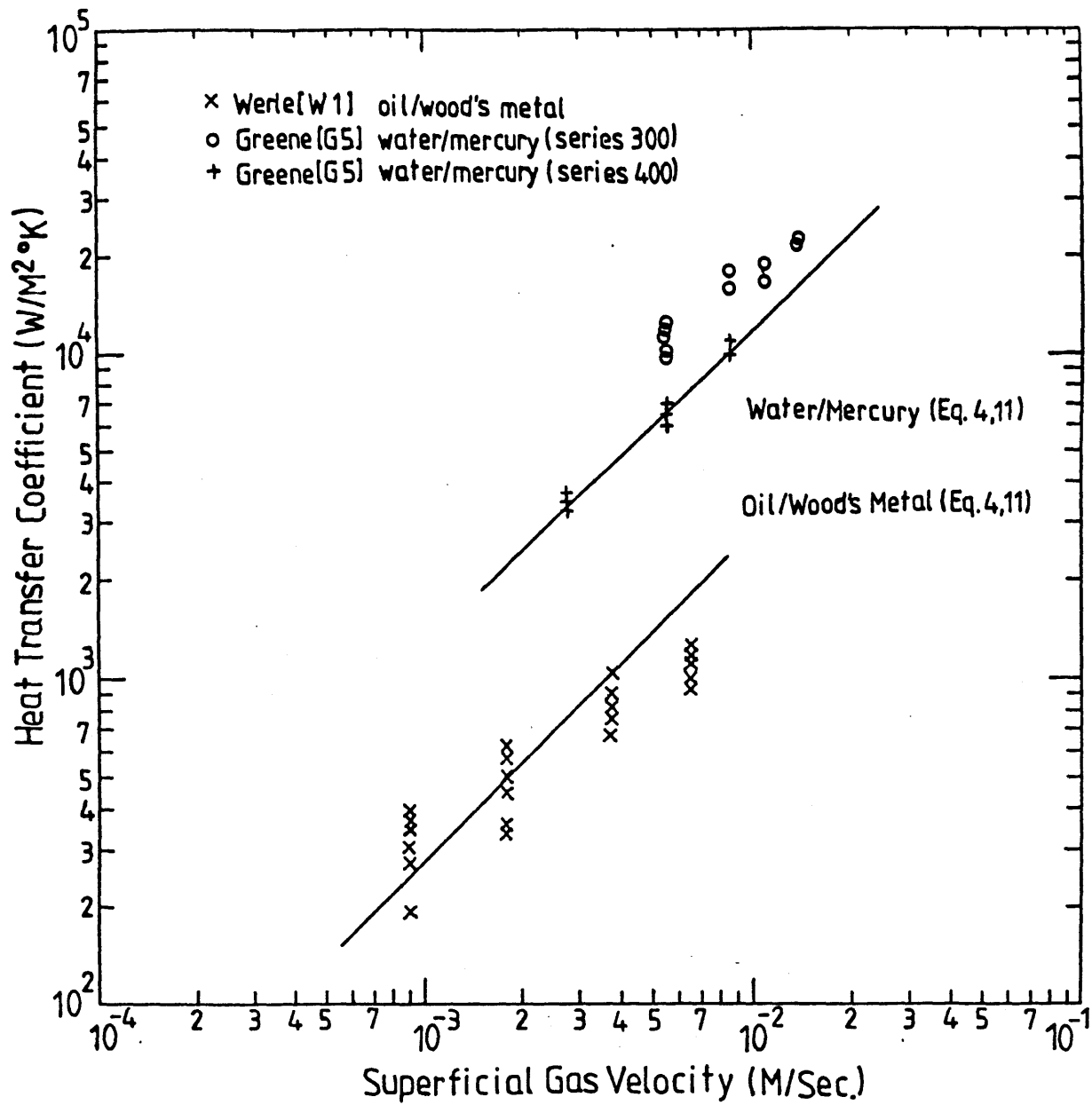
Figure 4.2   Comparsion of Experimental Data with Surface Renewal Model
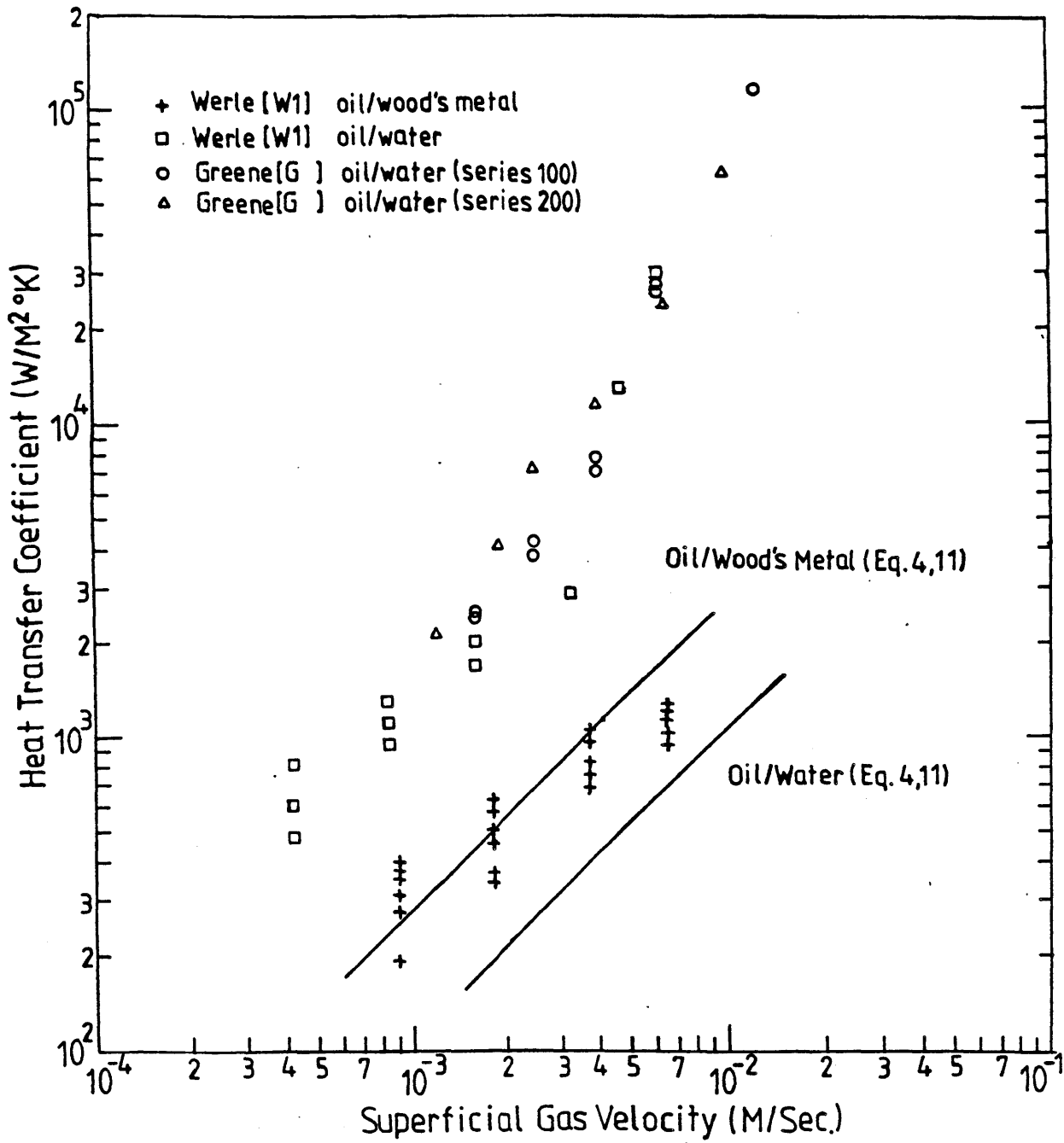
Figure 4.3 Comparsions of Experimental Data with Surface Renewal Model

In the churn-turbulent flow regime, the agglomeration becomes significant and the flow pattern becomes agitated and unsteady. Probably the interface between the two immiscible liquid layers is no longer well defined.

4.2.3 Bubble Induced Entrainment

Liquid entrainment can be cauased by two mechanisms [G1]: splashing and bursting of bubbles at the interface. Splashing occurs in any system containing both liquid and gas where there are localized areas of high velocity. A typical example of splashing is the entrainment of liquid in the annular flow regime of two phase flow. A simple calculation based on the criterion for the onset of entrainment in annular flow [C7] shows that the required superficial gas velocity is orders of magnitude higher than the ranges of the above experiments. Therefore, the entrainment observed in oil/water experiment is not caused by splashing.

The physical phenomena involved in bubble bursting at the interface are shown in Fig.4.4 [N1]. In an ideal bubbly flow regime, as the bubble reaches the surface of the liquid it usually rebounds back and forth with decreasing amplitude until it comes to rest with its upper part projecting above the surface in the form of a hemispherical dome (Fig.4.4b). Liquid drains from the dome until the upper part is so weakened that the internal pressure causes the formation of a secondary cap (Fig.4.4c). This cap subsequently disintegrates, giving rise to droplets of few microns in diameter (Fig.4.4d). After the bubble disintegrates, a well defined crater is left behind at the interface (Fig.4.4e). As the liquid fills in, the momentum of the inflowing liquid produces a jet which rises at high velocity (Fig.4.4f, 4.4g). Under certain circumstances, the liquid jet will break up due to capillary instability [C2] and create some liquid droplets with diameters on the order of hundreds of microns (Fig.4.4h). It is those droplets which contribute to entrainment. The lifetime of the bubble at the interface is of the order of ten milliseconds, the actual bubble burst will last a few microseconds, while events subsequent to the burst extend over a few milliseconds [N1]. The same phenomena were observed in the oil/water experiment at BNL [G6].
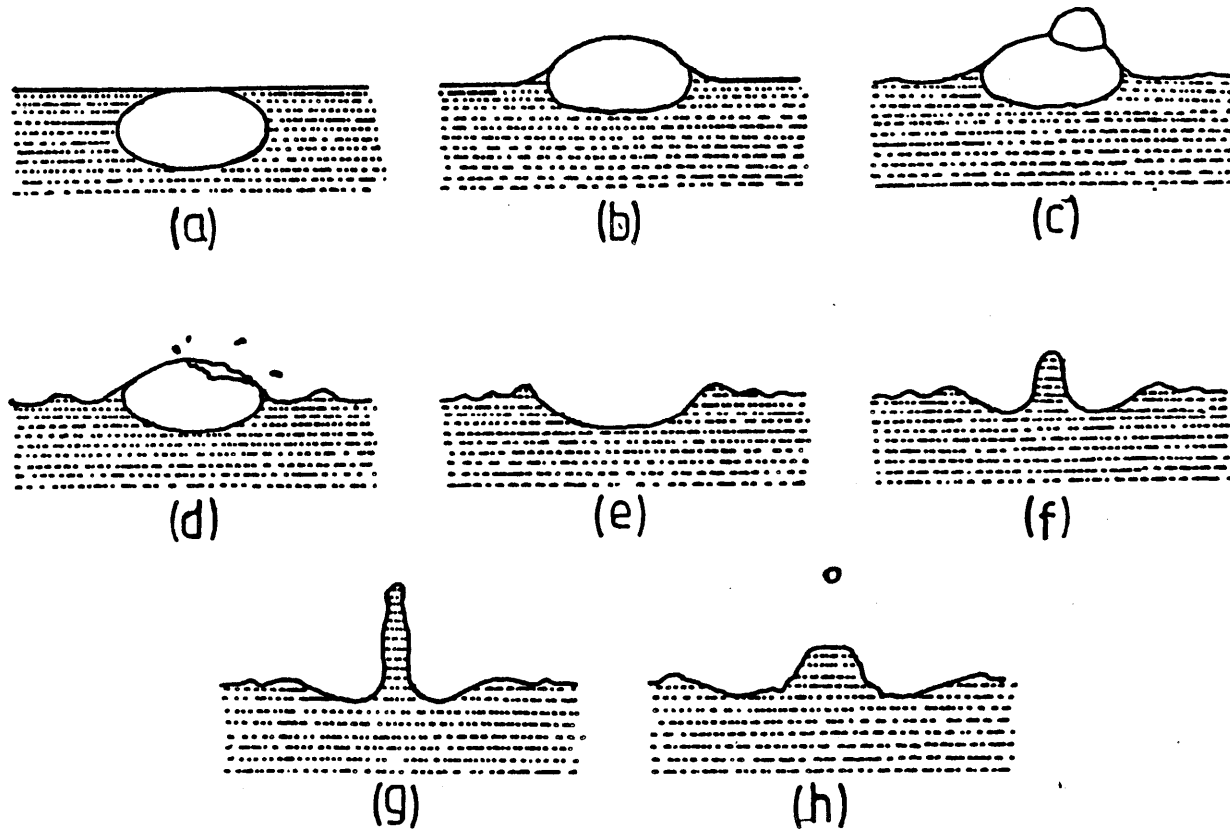
Figure 4.4   Mechanism of the Burst of a Bubble at the Surface of Liquid

As mentioned above, a hydrodynamic instability mechanism - capillary instability - is responsible for the disintegration process. The stability criterion of the capillary instability is that the liquid will break into droplets if the length of the jet is larger than the circumference of the jet [C2]. For certain liquids, the jets generated by bubble bursting will not be long enough to disintegrate and cause entrainment. Therefore, we can use the ratio of jet length to circumference as a criterion to determine the onset of this entrainment mechanism.

As the bubble bursts through the interface, a surface of circular section is eliminated and its associated surface energy is released. At the instant of bursting, the bubble gas escapes, leaving a partial vacuum behind [N1], which provides an impulse force thus setting the liquid in motion. The associated kinetic energy together with the released surface energy is used to raise the liquid jet and create the new surface of the jet (see Fig.4.5). Hence, the following energy balance equation can be written:

$$\pi r_b^2 \sigma + \frac{2}{3}\pi r_b^3 (\frac{1}{2}U_\circ^2) = \frac{2}{3}\pi r_b^3 \rho_\ell H' + A_{jet}\sigma \qquad (4.12)$$

where

$$r_b = \text{radius of the bubble}$$

$$H' = \text{height of gravitation center of jet}$$

$$A_{jet} = \text{surface area of jet}$$

In the above equation it has been assumed that the amount of liquid set in motion is equal to that of a hemisphere with the radius of the gas bubble and the same amount of liquid is used to form the liquid jet. From a momentum balance, the velocity of the liquid jet can be expressed as:

$$U_\circ = \frac{\int_0^\infty I(t)dt}{\frac{2}{3}\pi r_b^3 \rho_\ell} \qquad (4.13)$$

where $I(t)$ is the impulse. It can be related to the absolute pressure, $P_\circ$, by (N1):

114
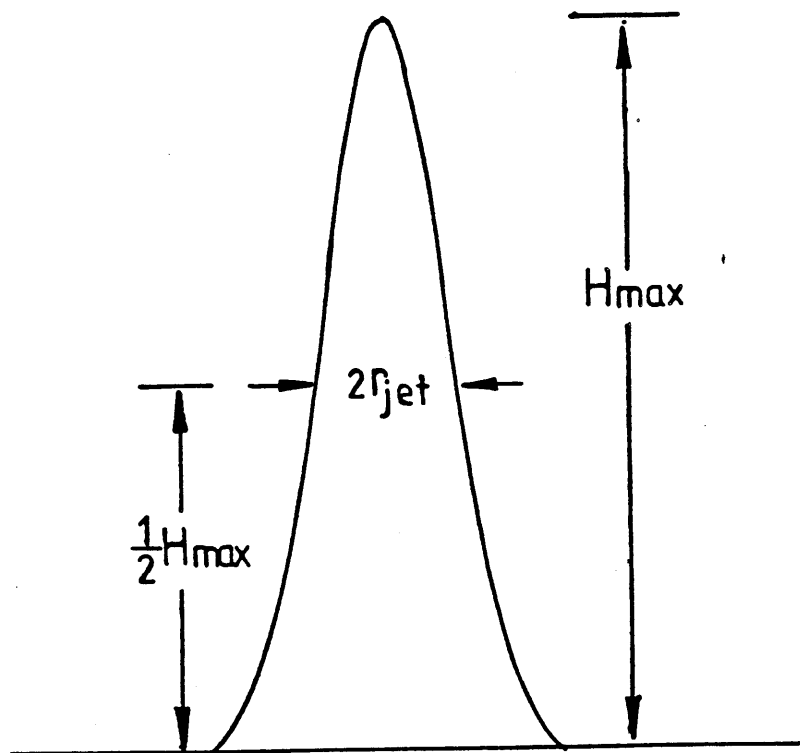
Figure 4.5　Liquid Jet

$$I(t) = \pi r_b^2 \left(P_0 + \frac{2\sigma}{r_b} \right) e^{-t/\tau} \tag{4.14}$$

In Eq.4.14, it has been assumed that the major portion of the impulse comes from the atmospheric pressure. Although it is unclear whether there is an instantaneous partial vacuum immediately after the bubble breaks. This arguement has been strongly supported by some evidence from entrainment experiments with water [A3,N1]. Here it is also assumed that the impulse force decays exponentially with time. According to Davies [D1], for air flow through water at low pressures the bursting process is completed within 30 μs. Therefore, it is reasonable to assume that the time constant, τ, is about 6 μs.

It is further assumed that the liquid jet can be represented by a Gaussian curve, as shown in Fig.4.5.

$$H(r) = H_{max} e^{-0.693 r^2 / r_{jet}^2} \tag{4.15}$$

By performing some integrations, the volume, the surface area and the gravitation center of the jet can be expressed as:

$$V_{jet} = \frac{\pi}{0.693} H_{max} r_{jet}^2 \tag{4.15}$$

$$A_{jet} = \frac{\pi \sqrt{\pi}}{\sqrt{0.693}} H_{max} r_{jet} \tag{4.17}$$

$$H' = H_{max}/4 \tag{4.18}$$

The jet radius can be related to the bubble radius, r_b, in the following way:

$$r_{jet} = \left(\frac{2}{3} \frac{0.693}{H_{max}} r_b^3 \right)^{0.5} \tag{4.19}$$

116

Combining all the above equations, a second order equation in terms of $\sqrt{H_{max}}$ is arrived at. For a specified bubble radius, H_{max}, can be found. and by Eq.4.19, r_{jet} can be found. Then whether the liquid jet is stable or not can be found by the ratio of H_{max} and $2\ \pi r_{jet}$. If the ratio is greater than unity the jet is unstable. Several liquids have been analyzed by this method, the results are shown in Fig.4.6.

From Fig.4.6, it can be seen that for all liquids the instability increases as the bubble diameter decreases. This is consistent with the experimental results of Newitt et al. [N1]. They measured the size and the number of droplets by bubbling air through a pool of water with different bubble diameters. They found that the number of droplets formed increases as the bubble diameter decreases. They also found that the diameter of droplets becomes larger as the bubble diameter increases. This is also consistent with the prediction i.e. the jet becomes thicker and r_{jet} increses as the bubble diameter increases. According to the prediction of this simple model, for water, as the bubble diameter is larger than 5 mm the jet can no longer generate droplets. This had been verified by Garner et al. [G1] experimentally. The analysis also indicates that for gas bubbling through mercury the jet will be stable so that there is no droplet formation and hence no entrainment.

In the above analysis, the effects of the upper liquid layer were not considered. However, according to the observation of Greene [G6], the liquid jet rises in the wake of the bubble. Therefore, there is little contact bteween the upper layer and the jet before the jet breaks. It is believed that the effects of the upper liquid layer are only of secondary importance.

Figure 4.6 also shows that the jets from metallic and oxidic corium are stable even when the bubble diameter is as small as 1 mm. In Corium/Concrete Interaction, the bubble diameter will definitely be greater than this value [B6]. One of the very important implication of this analysis is that in Corium/Concrete Interaction we need not consider the liquid entrainment due to bubble burst in calculating the upward or interfacial heat transfer.
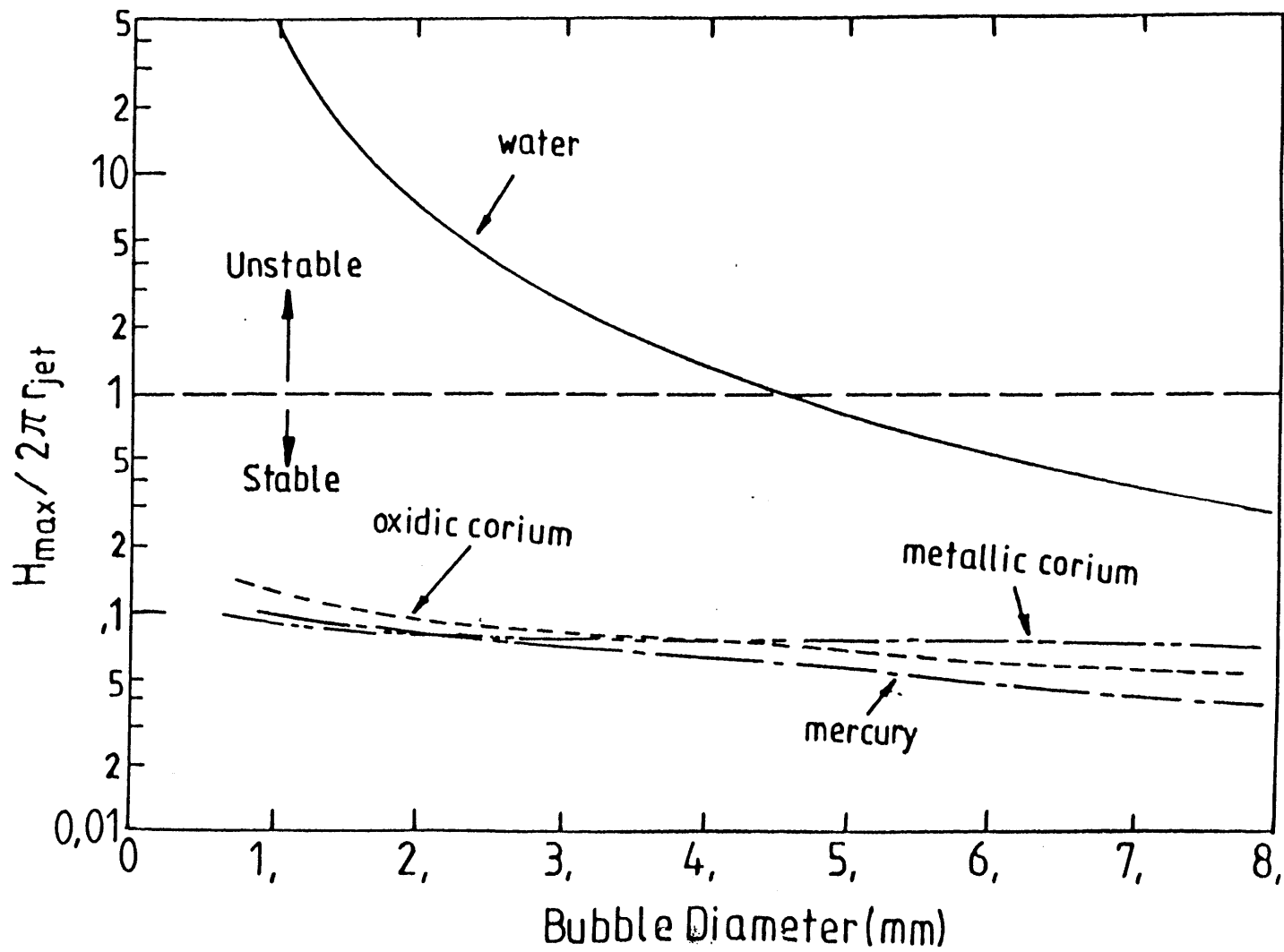
Figure 4.6   The Stability of the Liquid Jet

The above analysis only yields a method to determine whether this entrainment mechanism should be considered in calculation of the interfacial heat transfer coefficient of certain liquid pairs. The entrainment process is too complicated to treat analytically, and more experiments are needed to build up the empirical evidence to quantify the entrainment.

In recent high power tests of BETA experiment of KfK considerable amount of iron was entrained into the upper Al_2O_3 layer. In one particular run, the ablation rate of concrete was ~ 0.20 mm/sec. The corresponding superficial gas velocity is ~ 0.25 m/sec, therefore the flow regime was either churn-turbulent or patch flow. In those flow regimes the entrainment mechanism is changed from bubble bursting to momentum exchange [K2]. Also under such high superficial gas velocity both layers are highly agitated, there is a possibility that a mixing layer is formed between the two liquid layers.

In the low power test of BETA experiments which has lower concrete ablation rate, the entrainment was not observed. This is consistent with the above analytical model.

4.3 Conclusions

In ideal bubbly flow there are three mechanismes responsible for the interfacial heat transfer between the bubble agitated immiscible layers. Those are: natural convection, surface renewal and bubble induced entrainment. A new method is proposed to modify the surface renewal model proposed by Szekely. The new correlation compares favorably with the results of water/mercury and oil/wood's metal experiments.

A simple analytical medel was developed to decide whether the bubble will induce entrainment. The model explains the observed difference between the oil/water and oil/wood's metal pairs. From this analytical model, it is concluded that the bubble induced liquid entrainment resulted from bubble bursting will not occur in Corium/Concrete Interaction at low velocity of the penetrating gases.

The newly modified Szekely's correlation is suggested to calculate the interfacial

119

heat transfer coefficient. A comparsion of this correlation with others is shown in Fig.4.7.

The impact of the proposed correlation on integral analysis of Corium/Concrete Interaction and the containment pressurization rate will be described in Chapter 5 and Chapter 6 respectively.
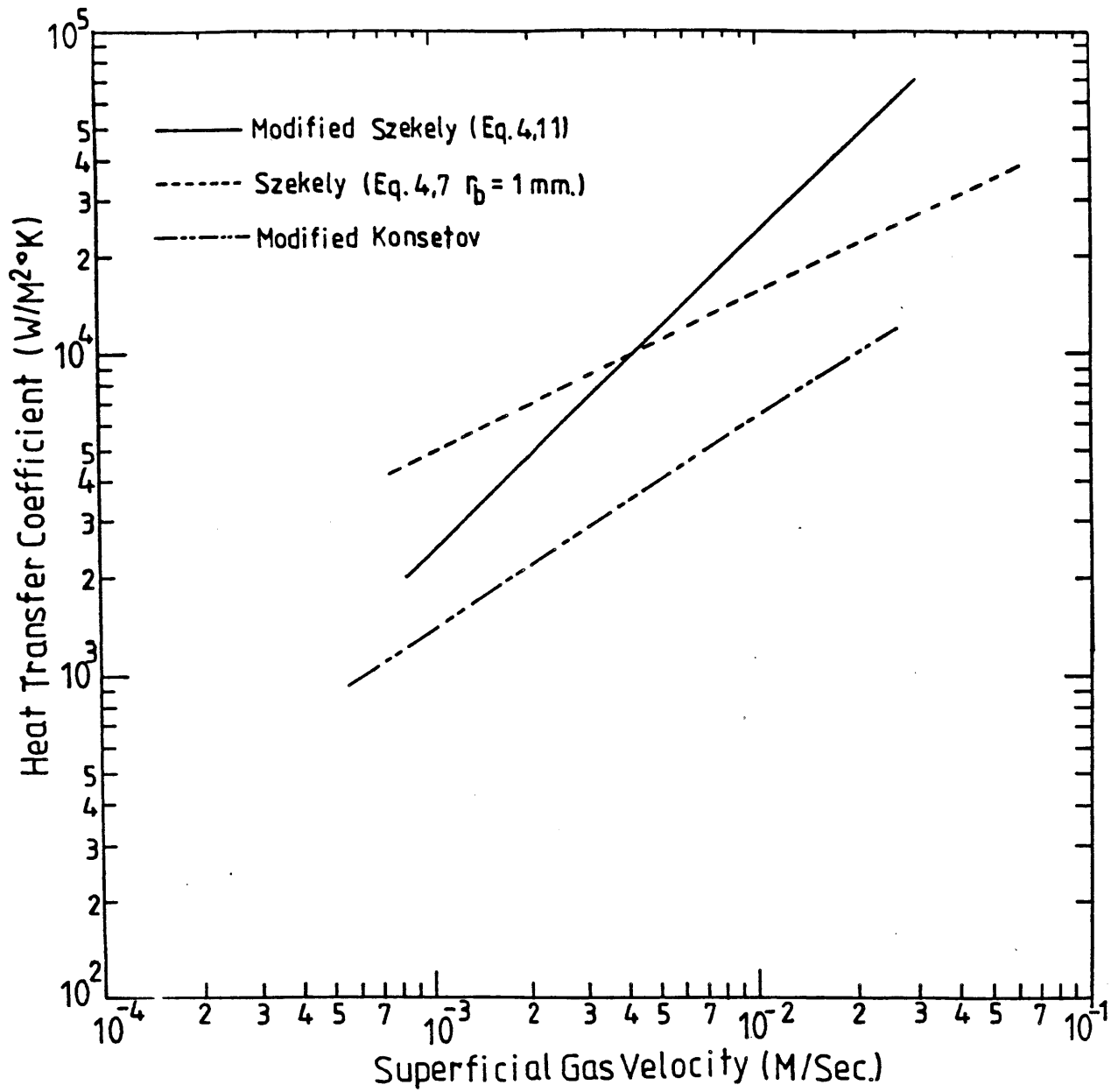
Figure 4.7 Heat Transfer Coefficient at Metallic/Oxidic Corium Interface

CHAPTER 5

CRUST STABILITY EXPERIMENTS

5.1 Introduction

After some period of Corium/Concrete Interaction. the temperature of the corium will fall below the liquidus temperature and solidification will begin. There are two possible situations for melt freezing: (1) solid and liquid corium will mix together and form a slurry pool. (2) solid will exist as a crust layer on the periphery of the pool.

The freezing characteristics of a debris pool are important in determining the heat transfer rate between the corium pool and concrete. If a slurry pool forms, the heat transfer between the corium pool and concrete will be convectivelly controlled. If the solid exists as a crust layer. for a given liquid temperature. it will limit convective heat transfer because the boundary temperature of the liquid can not fall below the solidification temperature. In addition. the crust provides an additional thermal resistance between the interior of the pool and its boundary. Therefore. for the situation with a solid crust layer, the heat transfer rate between the corium pool and the concrete is conductivelly controlled which is ordinarily far less effective than a convectivelly controlled process.

In Chapter 3. the periodic contact model was proposed to calculate the downward heat transfer coefficient. The analyses in Chapters 5 and 6 showed that the downward heat transfer rate is always governed by the periodic contact model when corium starts to freeze. If a crust layer is formed upon freezing. the solidified layer across the corium/concrete interface will impede the contact between the corium and the concrete. This will limit the applicability of the proposed model. In order to know

the applicable temperature ranges of the proposed model, it is important to know the freezing characteristics of the corium pool.

Another very important implication of crust formation is its effects on the aerosol generation. If a stable crust is formed around the periphery of the pool the amount of concrete decomposed gas passing through the pool could be significantly reduced. This reduces the potential of generating volatile and nonvolatile aerosols.

5.2 Literature Review

The decomposition of concrete is accompanied by generation of concrete gas. As the gas attempts to move through the debris pool, it will tend to break up the crust formed around the periphery of a molten region. Bascially, the motion of a frozen crust between two different fluids under the buoyancy induced excitation is similar to that at the plane interface between two fluids. An approach similar to that of Taylor instability has been proposed by Epstein [E2] to study the problem. With the formulation of a classical Taylor instability theory, by adding an extra term to account for the elastic forces within the crust, Epstein could estimate the time constant, τ, for the crust breakup which depends on the crust thickness and the depth of the lower fluid layer. The crust growth time, τ_f, is obtained independently from heat conduction and is set equal to τ to obtain both the frozen crust thickness at the onset of instability and the breakup criterion.

Several simulant experiments were performed by Epstein [E2] to validate his analytical approach. In these experiments, a relatively hot, heavy liquid was suddenly poured over a column of lighter cold material (liquid or solid). The lower liquid was placed in a glass test vessel (diameters varied from 30 to 300 mm). If the lower material is in solid form, the liquid was frozen in place at the bottom of the vessel. The material pairs used in the experiments were $Freon - 122A/H_2O$, $lead/gallium$, $H_2O/Liquid\ C_8H_{18}$, and $H_2O/solid\ C_8H_{18}$. The density ratios of these material pairs ranged between 1.95 and 1.43. The results of these simulant experiments showed

that the stability of a crust between two liquid layers could be predicted by Epstein's model. However, for the cases of crusts under a molten pool but over a melting substrate, Epstein's analysis failed to reproduce the experimental results.

Epstein's analysis predicted that the crusts in a $H_2O/solid$ C_8H_{18} system would be unstable if the diameter of the glass test vessel was greater than 160 mm. In the simulant experiments of $H_2O/solid$ C_8H_{18} within a 300 mm diameter glass test vessel, a stable crust was observed.

In Epstein's derivations, the depth of the lower fluid layer was considered as a constant which is not the case when the lower fluid layer is generated by melting a solid substrate. In the Corium/Concrete Interaction simulant experiments of M.Plys [P4], it was observed that after some period of interaction, few minutes, the height of the pool collapsed and the gas flow rate decreased and finally ceased after about five minutes. Plys explained this transition as resulting from crust formation around the periphery of the molten pool.

In the current modeling of Corium/Concrete Interaction, all the integral analysis codes reviewed in Chapter 1 assume that the solidified portion of corium will precipitate out and form a crust layer on the periphery of the corium pool. Due to the limitations of the experimental techniques the crust layer has never been actually observed in any integral real material or simulant experiments. Therefore, the following experiment was designed to study the freezing characteristics at the bottom of a bubble agitated liquid pool.

5.3 Experimental Apparatus

5.3.1 General Features

The design of the experimental apparatus is determined by two fundamental modeling requirements, namely, gas evolution at the pool boundary, the capability of cooling the pool material below its freezing point. Simulation of gas evolution from

the pool boundary is accomplished by forcing a noncondensible gas (air) through porous plates which are used to construct the walls of the test cell. The cooling capability of the test cell is provided by a $Freon - 12$ refrigeration cycle.

In the design of the experimental apparatus, both sideward and downward injections were made possible. This allows the experimental apparatus to be used to investigate the crust stability at horizontal and vertical interfaces. In the present stage of experiments, only the stability of the crust on a horizontal interface will be studied.

The other principal feature of Corium/Concrete Interaction, the volumetric heat generation within the corium pool, will not be simulated in this experiment. According-ing to the calculations of CORCON/Mod1 in Chapter 7, by the time the corium starts to freeze, metallic corium would have settled on the bottom. Since the metal-lic phase does not contain a lot of fission products, the internal heat generation will be of low magnitude.

5.3.2 Apparatus

A schematic diagram of the experimental apparatus is shown in Fig.5.1. It con-tains three major parts, a test cell, a cooling unit to remove heat from the test cell and an air supply unit to simulate the gas evolution.

5.3.2.1 Cooling Unit

A schematic diagram of the cooling unit is shown in Fig.5.1. The major part of the cooling unit is a Tecumseh AH7514AC condensing unit. The maximum capacity is 16800 BTU/hr (4.92 kW). The cooling unit contains three independent cooling loops and can be controlled by refrigeration shut off valves. A back pressure regulator is installed between the suction and discharge lines of freon compressor to control the operating pressure and temperature of the condensing unit.
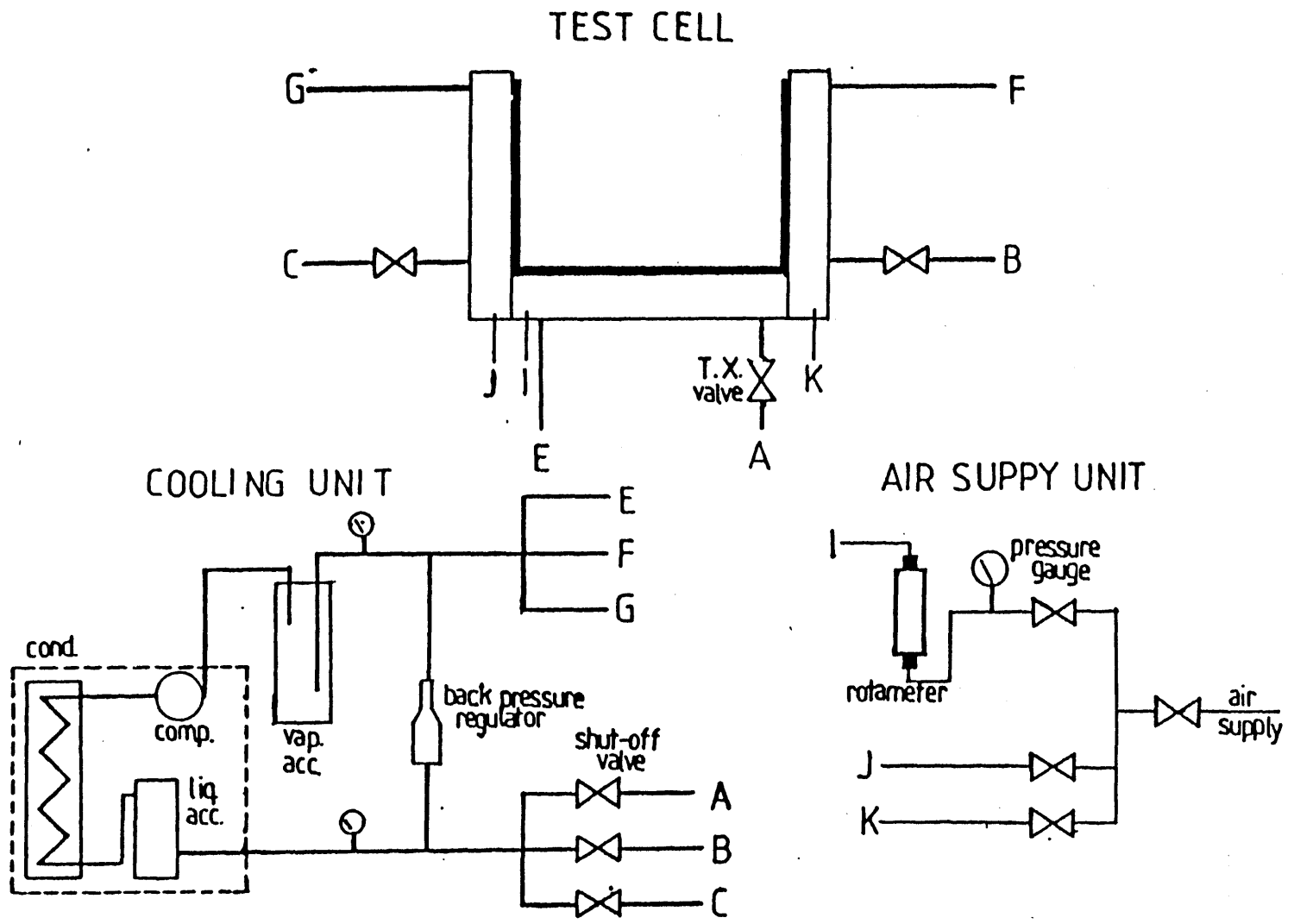
Figure 5.1 Schematic Diagram of Experimental Appartaus

5.3.2.2 Air Supply Unit

The air supply unit is connected to the air compressor of the laboratory building. The volumetric gas flow rate is measured by a Fisher & Porter 10A3557 series (tube size 12.7 mm) rotameter. The maximum gas flow rate of the rotameter is 6.43 *standard cubic feet per min* (3.03 × 10^{-3} m^3/sec). A pressure gauge is installed at the upstream of rotameter to measure the system pressure.

5.3.2.3 Test Cell

The dimensions of the test cell used in this investigation are shown in Fig.5.2. The pool is bounded from the bottom and two sides by freon cooled bronze porous plates mounted on 12.7 mm thick stainless steel structure. Air can be injected into the pool through these three porous plates simultaneously or independently. The front and back walls of the test cell are made of 6.35 mm thick transparent plexiglass plates from which the behavior of the pool can be observed.

A detailed diagram of the porous bronze cooling assembly is shown in Fig.5.3. A 9.525 mm diameter copper cooling coil is soldered to a copper cooling plate to serve as the flow channel of refrigerant - freon 12. Figure 5.4 shows the flow direction of freon 12. The double spiral pattern of the flow channel results in nearly uniform cooling of the porous plate. On the other side of the copper cooling plate (as shown in Fig.5.5), 11 × 11 holes, 3.175 mm in depth, are drilled to serve as holders of the cooling fins. The diameters of these holes are slightly less than these of the cooling fins (9.525 mm). The cooling fins are squeezed into the fin holders. Then, the entire copper cooling plate with cooling fins in place is mounted on the structure ring, which is a part of the main structure of the test cell, and then tightened to the porous plate with screws and bolts. After assembly, these cooling fins are directly in contact with the porous plate to enhance the heat transfer between the porous and copper cooling plates. During the experiment, the temperature distribution of the cooling fins at some specific locations (as shown in Fig.5.5) are measured with

POROUS
PLATE

244.5 mm

244.5 mm

304.8 mm

225.4 m.m

339.7 mm
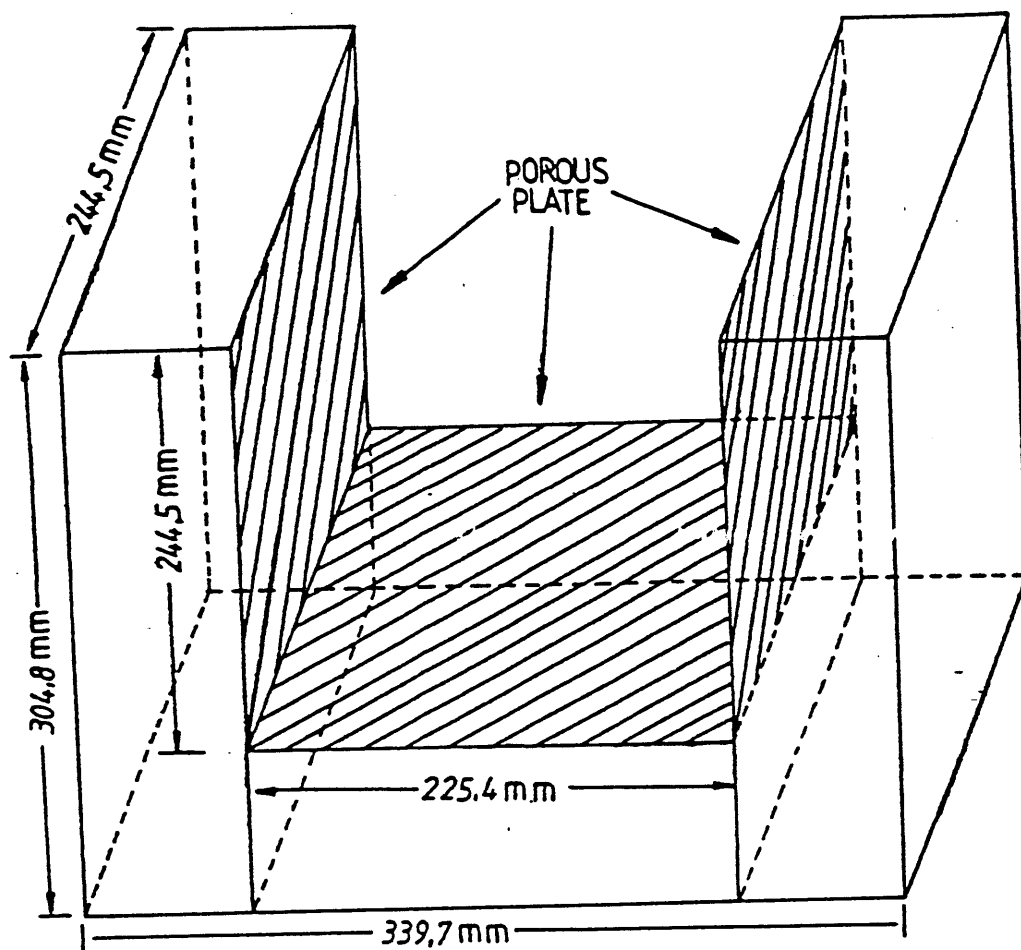
Test Cell

Figure 5.2   Test Cell
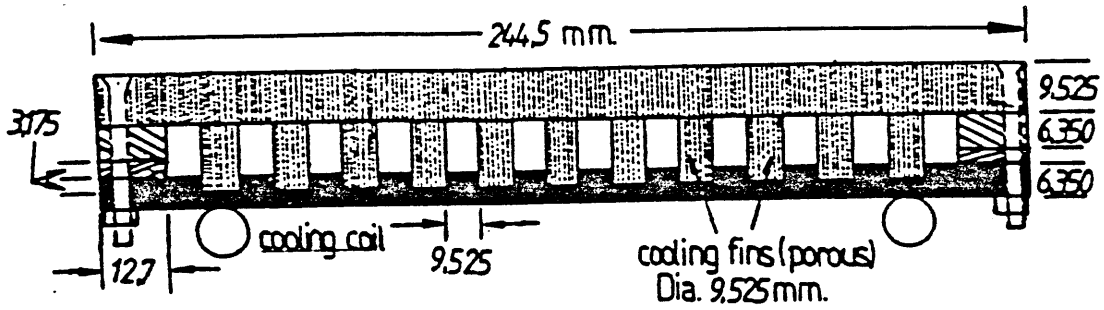
Figure 5.3   Diagram of Cooling Assembly
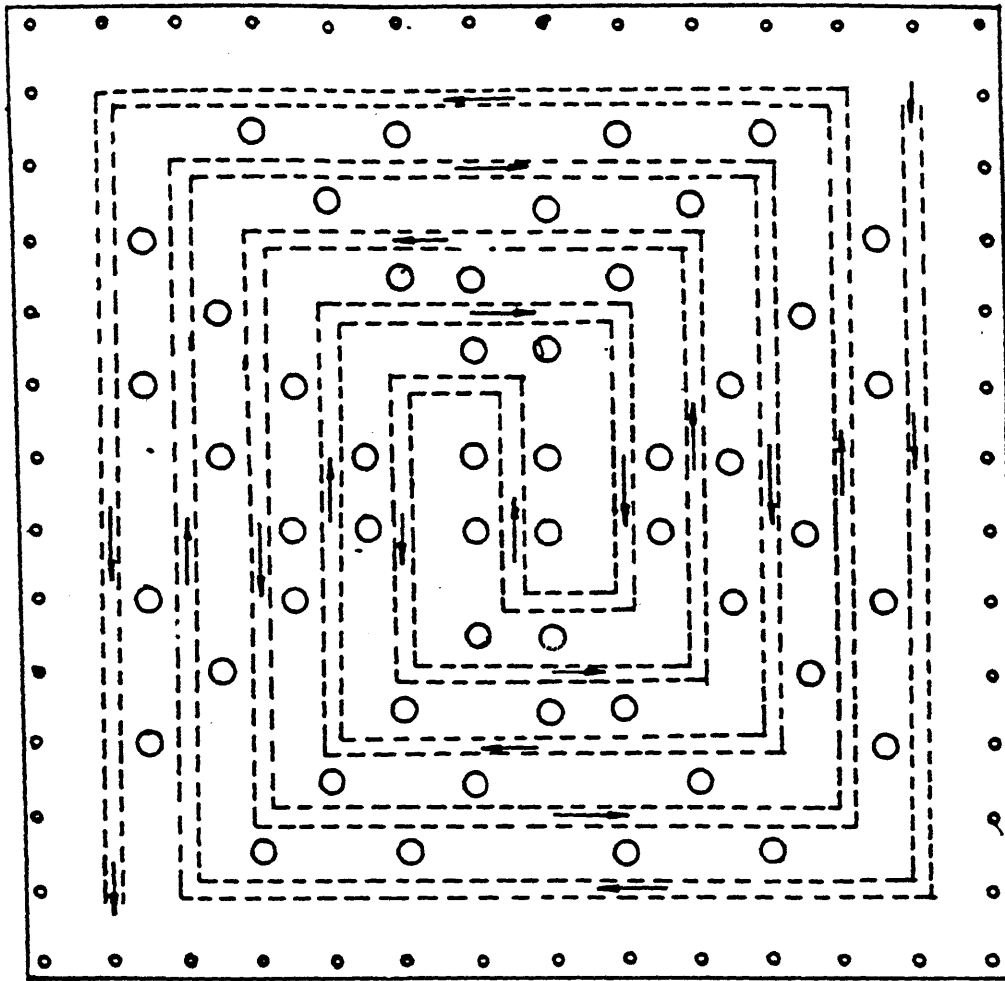
=== copper tube (dia: 6,350 mm.)

O   holes for gas flow (dia: 6,350 mm.)

COOLING PLATE (bottom view)

Figure 5.4   Copper Cooling Plate (Bottom View)
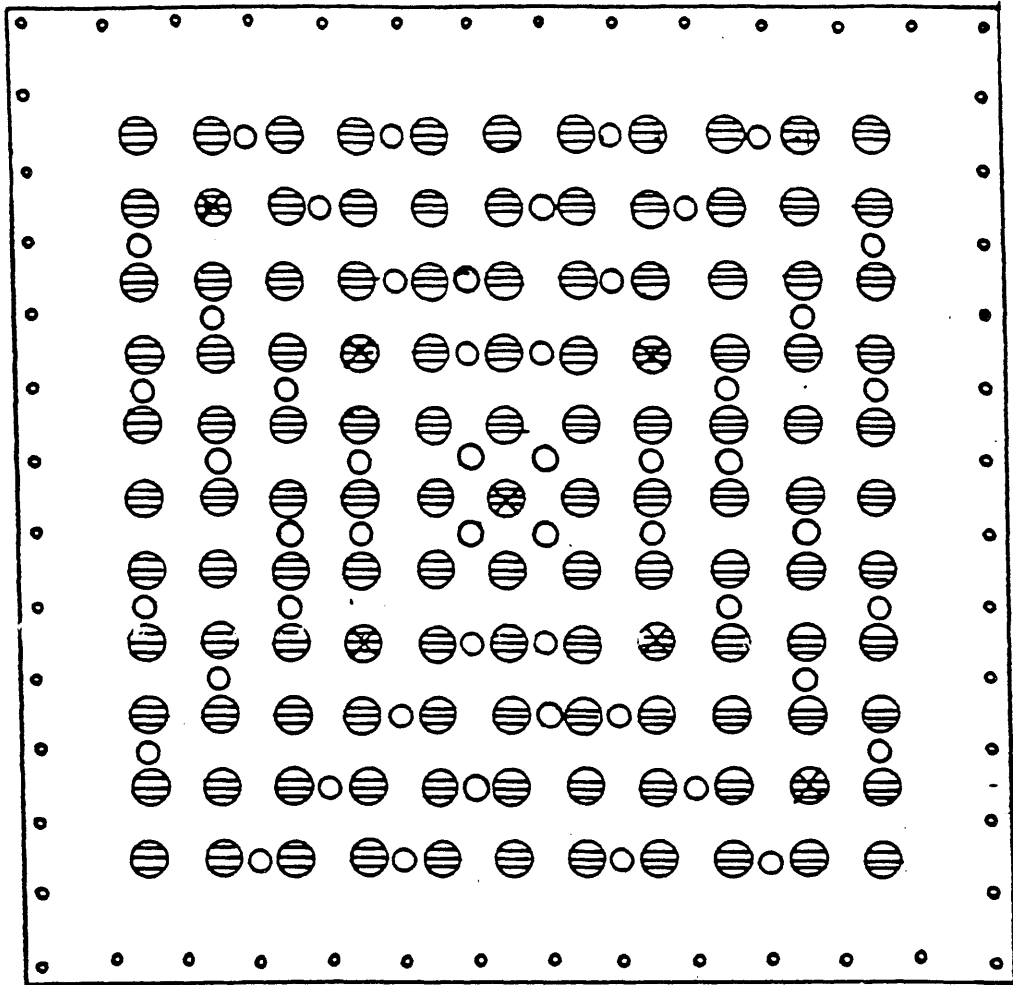
⊜ cooling-fin holders (depth: 3,175 mm.)

⊛ fin with thermocouples

○ holes for gas flow (dia.:6,350mm.)

COOLING PLATE (top view)

Figure 5.5   Copper Cooling Plate (Top View)

embedded type E thermocouple wires. Totally. the temperature distributions of 7 cooling fins are measured. These fins are uniformly distributed over the porous plate. The locations of thermocouples within the cooling fins are shown in Fig.5.6.

The copper cooling plate also contains 52 holes. 6.35 mm in diameter, to allow the injected gas to move into the open space between the porous and copper cooling plates. These holes can also serve as the penetrations of thermocouple wires used in measuring the temperature distributions of cooling fins.

The porous plates are made of sintered bronze (89.5 ~ 90.5% *copper* and 10.5 ~ 9.5% *tin*). The maximum pore size is around 5 μm and the porosity is about 40%. The size of the porous plate is 244.5 × 244.5 × 9.525 mm. This is the maximum size that can be made by the manufacturer. This limits the size of the test cell.

5.3.2.4 Characteristics of Downward Heat Flux

In the design of the experiment. the heat is removed from the pool by evaporating freon 12 in the cooling coil. The two phase nature of the cooling system prohibits a direct measurement of the heat removal rate.

The downward heat flux will be inferred from the measured temperature distribution of the cooling fins. The HEATING3 [T2] computer code was used to analyze the three dimensional heat conduction problem of the cooling fin. HEATING3 is a three dimensional finite difference heat conduction code. With specified boundary conditions. the code can calculate the temperature distribution within a three dimensional body. In the present calculation, the porous plate was divided into 121 regions. each region has an attached cooling fin. The dimensions and boundary conditions used in this analysis are shown in Fig.5.6.

In Fig.5.6, Boundary A corresponds to the part of the cooling fin that is embedded in the copper cooling plate. Constant temperature was assumed for this boundary. Boundary B corresponds to the parts of the cooling fin and the porous
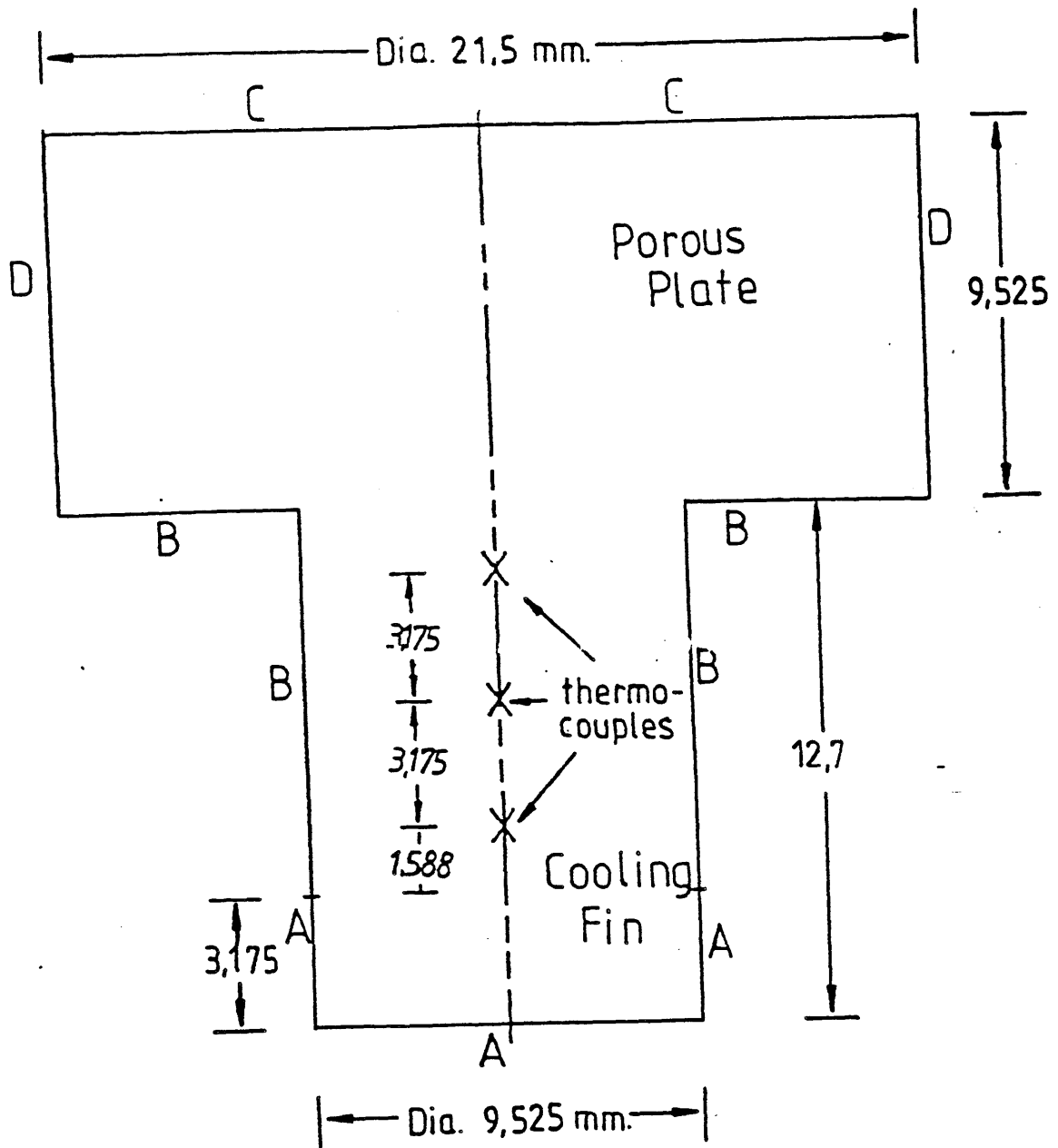
Boundary Types

A: Constant Temperature
B: Insulated
C: Constant Heat Transfer Coef.
D: Symmetric

Figure 5.6   Geometry of Cooling Fin

plate that are in contact with air. and were assumed to be insulated. Boundary C is the upper surface of the porous plate which is directly in contact with the pool. A constant heat transfer coefficient was specified for this boundary. Boundary D are the interfaces with other regions. In this calculation. the heat transfers into the porous plate through Boundary C and then transfers out of cooling fin through Boundary A. The calculations of HEATING3 provided the temperature distributions along the Boundary C and within the cooling fin. Based on the calculated temperature distribution along the Boundary C, the rate of heat transferred into the porous plate can be determined. Dividing this rate by the cross section of the cooling fin we obtained q''_{2D}. Based on the temperature distribution within the cooling fin. another heat flux, q''_{1D} can be obtained by applying the one dimensioal heat conduction equation i.e.

$$q''_{1D} = K_{porous} \frac{\triangle T}{\triangle x} \tag{5.1}$$

where K_{porous} is the thermal conductivity of the porous plate and $\triangle T$ is the temperature drop with respect to $\triangle x$. The calculated values of q''_{1D}/q''_{2D} along the cooling fin are shown in Fig.5.7. The horizontal axis is the length fraction of the cooling fin from the top of the fin, the end that in contact with the porous plate. The curve shown in Fig.5.7 is used as a calibration curve in analyzing the experimental data.

During the experiments. the temperature distribution along the centerline of the cooling fin is measured. Based on the measured $\triangle T$, the q''_{1D} can be determined by Eq.5.1. By applying the correction factor shown in Fig.5.7, q''_{2D}. the actual heat flux within the cooling fin can be obtained. From q''_{2D}. the downward heat flux from the pool can be obtained.

In making the above HEATING3 calculation. the numerical values of the boundary conditions shown in Fig.5.6 have to be specified. These values are not available before the experiments. A sensitivity study was performed on these uncertainties. The heat transfer coefficient at boundary C. the temperature of boundary A and

134
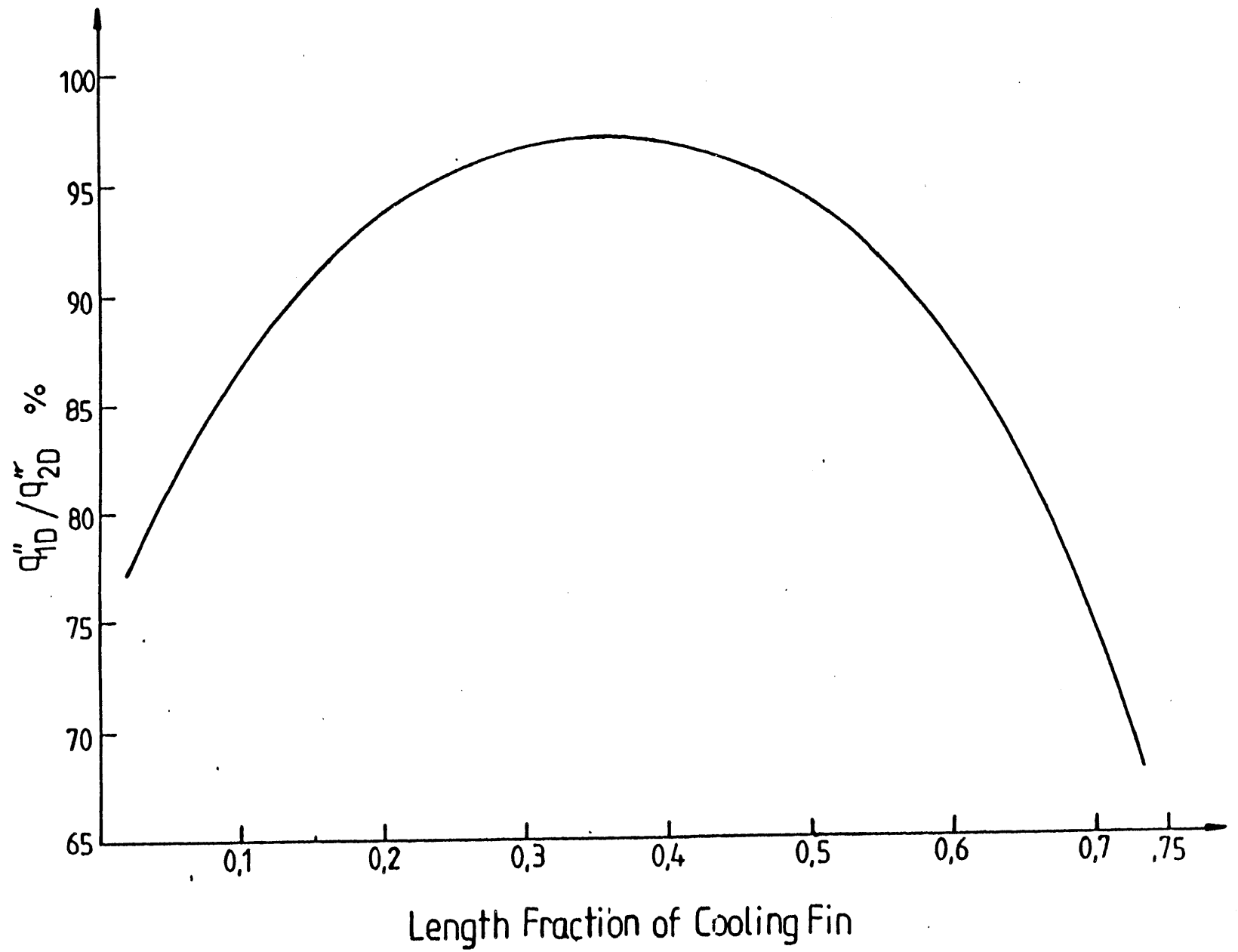
Figure 5.7   Calibration Curve of Cooling Fin

the thermal conductivity of the porous plate have been changed within reasonable ranges to check their effects on the calibration curve shown in Fig.5.7. It turned out that the calibration curve is relatively independent of these values. This conclusion is important in analyzing the temperature data from the thermocouples embeded in the cooling fins. As we can calculate the actual heat flux by a simple one-dimensional heat conduction equation and then use the calibration curve to make corrections.

5.3.3 Selection of the Pool Material

In Corium/Concrete Interaction, neither the metallic nor the oxidic phase is a pure substance. Their solidification points are not uniquely defined. For the metallic phase, iron plus some impurities, the liquidus and solidus temperatures differ by 10 $^\circ K$. For oxidic phase, a mixture of UO_2, ZrO_2, Al_2O_3, CaO etc., the difference between the liquidus and solidus temperatures is around 300 $^\circ K$ initally. This difference is even greater. around 700 $^\circ K$, as more decomposed concrete is added to the oxidic phase. Since it is difficult to find comparable materials. this characteristic of Corium/Concrete Interaction was not simulated in the present stage of experiment.

The pool material has to meet the following requirements:

1. The solidification point and evaporation point should be within a reasonable range to avoid a more complicated experimental set up.

2. The material should not react with bronze and oxygen at the operating temperature of the experiments.

3. The material should be transparent so that the phenomena occurring in the pool can be observed.

4. The material should have a high surface tension and large liquid-solid contact angle so that it can be confined by the porous boundaries.

5. The materials should be common, inexpensive. nontoxic, noncorrosive and have known properties.

In practice, the hardest requirement to satisfy was #3. After some searching, it was decided that water will be used in this experiment for it is easy to handle and has well known properties.

A calculation based on Epstein's model showed that with a reasonable crust thickness, 1 mm, the most critical wave length for water/air system is around 100 mm. This value is smaller than the size of the test cell in this experiment.

5.4 Experimental Results

5.4.1 General Description

Experiments have been conducted with different amounts of water, different volumetric gas flow rates and different opertaing temperatures of the condensing unit. The conditions of the different experiments are summarized in Table 5.1.

During the experiments, the temperature of the pool, the air flow and the temperature distributions of the cooling fins were continuously measured with Type E thermocouples. Data were recorded by a KAYE ramp processor and scanner system at a prespecified time interval.

In the experiment, the air passes around the cooling coil before it moves to the open area between the cooling and porous plates. The temperature of the air was significantly reduced by the cooling coil. The measurements showed that the temperature of the air between the porous and copper cooling plates was inversely proportional to the volumetric air flow rate. These values are also shown in Table 5.1.

The superficial gas velocity of the experiment ranges between 6.46 and 132 mm/sec. The flooding limit based on Kutateladze's criterion is 950 mm/sec for water/air system. The minimum stable gas film limit based on Benerson's criterion is 14.8 mm/sec. No continuous film was observed across the horizontal liquid/solid interface.

Table 5.1

Conditions for Crust Stability Experiment

Run No.	Amount of of Water (kg)	% Volumetric Air Flow	Superficial Gas Velocity (mm/sec)	Inlet Gas Temp. (°C)	Pressure (psig)	Freon Sat. Temp. (°C)	Water Supercooling(°C)
1	2	10%	6.46	-12.2	~1	-20.6	0
2	2	20%	13.5	-11.8	~3.5	-20.6	0
3	2	20%	13.5	-11.8	~3.5	-20.6	3.39
4	2	20%	13.5	-11.8	~3.5	-20.6	0
5	2	20%	13.5	-11.8	~3.5	-20.6	2.94
6	2	30%	21.3	-11.1	~5.5	-20.6	2.89
7	2	40%	29.8	-10.4	~7.5	-20.6	2.72
8	2	40%	29.8	-10.4	~7.5	-20.6	2.94
9	2	50%	39.2	-9.8	~10.	-20.6	0
10	2	50%	39.2	-9.8	~10.	-20.6	1.67
11	2	60%	52.4	-8.8	~16.	-20.6	2.17
12	2	70%	67.7	-8.5	~23	-20.6	1.72
13	2	90%	106.5	-7.0	~42	-20.6	1.83
14	2	100%	132.0	-5.9	~56	-20.6	1.44
15	4	30%	21.3	-11.1	~5.5	-20.6	2.61
16	4	50%	39.2	-9.8	~10.	-20.6	1.56
17	2	50%	39.0	-6.4	~10.	-17.8	1.67
18	2	50%	38.7	-2.5	~10.	-20.6	2.44

The pressure needed to force the air through the porous plate increases significantly with volumetric air the flow rate, especially as the flow rate exceeds 50% of the rotameter rating. When the volumetric air flow rate is 100% of the rating, the pressure head was 56 *psig*. The high pressure will cause some leakage at the seals of the penetrations of thermocouple wires on the main structure. This prevented further increase of the volumetric air flow rate. The equivalent superficial gas velocity in the pool at 100% rating is 132 *mm/sec* which is 0.1 to 0.5 times the gas velocity in the BETA experiment.

The measurements of the temperature distribution within the pool showed that a nearly isothermal condition was achieved within the pool due to bubble agitation. The temperature of the upper surface of the porous plate was measured with a thermocouple put in contact with the surface. Results from similar experiments showed that the temperature difference between the pool and the surface was around 0.3 °C for all the runs [K6]. This measurement probably involves some uncertainty because it is difficult to quantify the contact resistance between the thermocouple and the surface.

5.4.2 Observed Phenomena

At the moment of first freezing of the pool. two different phenemona were observed. In both cases, a stable crust was observed on the horizontal bubble agitated liquid/solid interface.

In 14 out of 18 runs. the pool could be cooled below the freezing point of water without any major change in the behavior of the water pool. Then freezing occurred suddenly. the liquid/solid interface was covered by a thin layer of ice crust and the bulk temperature of the pool jumped up to the freezing point of water. The thickness of the crust was on the order of a fraction of *mm*. It was also observed that on top of the crust there were some slices of ice crystal attached vertically to the crust. These ice crystals were fixed in the pool, not floating around with water. A post-test

examination of the crust showed that the crust was not directly in contact with the porous plate. The crust could be removed from the porous surface very easily.

Upon freezing of the pool, the flow pattern of the pool changed drastically. The uniformly distributed bubble sites pattern was destroyed and bubbles were only generated from some preferred locations. Meanwhile the pressure in the main structure built up. Sometimes. this pressure increase was large enough to break the seals of the thermocouple wires' penetrations.

In the other 4 out of 18 runs. freezing occurred gradually. There was no supercooling in the pool. As the pool bulk temperature reached the freezing point. a very thin slice of ice layer was observed on the porous surface at a preferred position. The thickness and the surface area of the ice layer increased gradually. The bubble generating sites under the crust layer were completely blocked by the ice. Some air bubbles were trapped by the ice layer. The post-test examination of the ice layer showed that the ice layer was in close contact with the porous plate.

The reasons causing the differences in these two cases are still unclear. No meaningful conclusion can be withdrawn from the limited runs of the experiments. For these runs that have supercoolings. it seems that the amount of supercooling achieved decreases as the superficial gas velocity increases, as shown in Fig.5.8.

5.4.3 Heat Transfer Analysis

The pool temperature histories of Runs 3, 11 and 14 are shown in Fig.5.9. The superficial gas velocities of these runs are 13.5, 52.4 and 132 mm/sec respectively. As shown in Fig.5.9, the pool cooling down rate is proportional to the superficial gas velocity. The drastic temperature rise upon freezing can be easily seen in this figure. This rise could be releated to heat release due to phase transition or due to the slowing down of the heat removal rate from the pool.

The downward heat flux of Runs 3. 11 and 14 are estimated based on the method
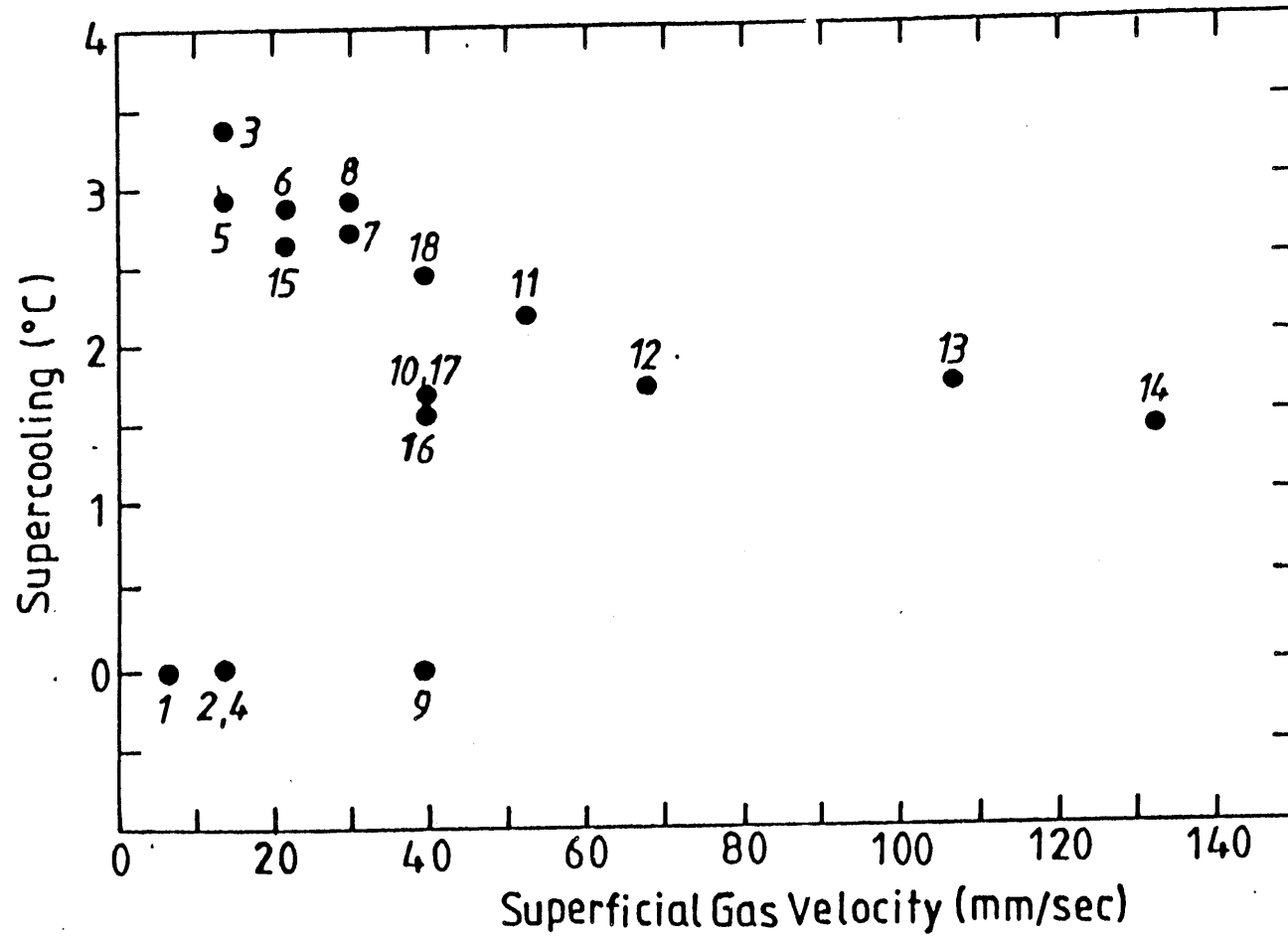
Figure 5.8   Supercooling Achieved
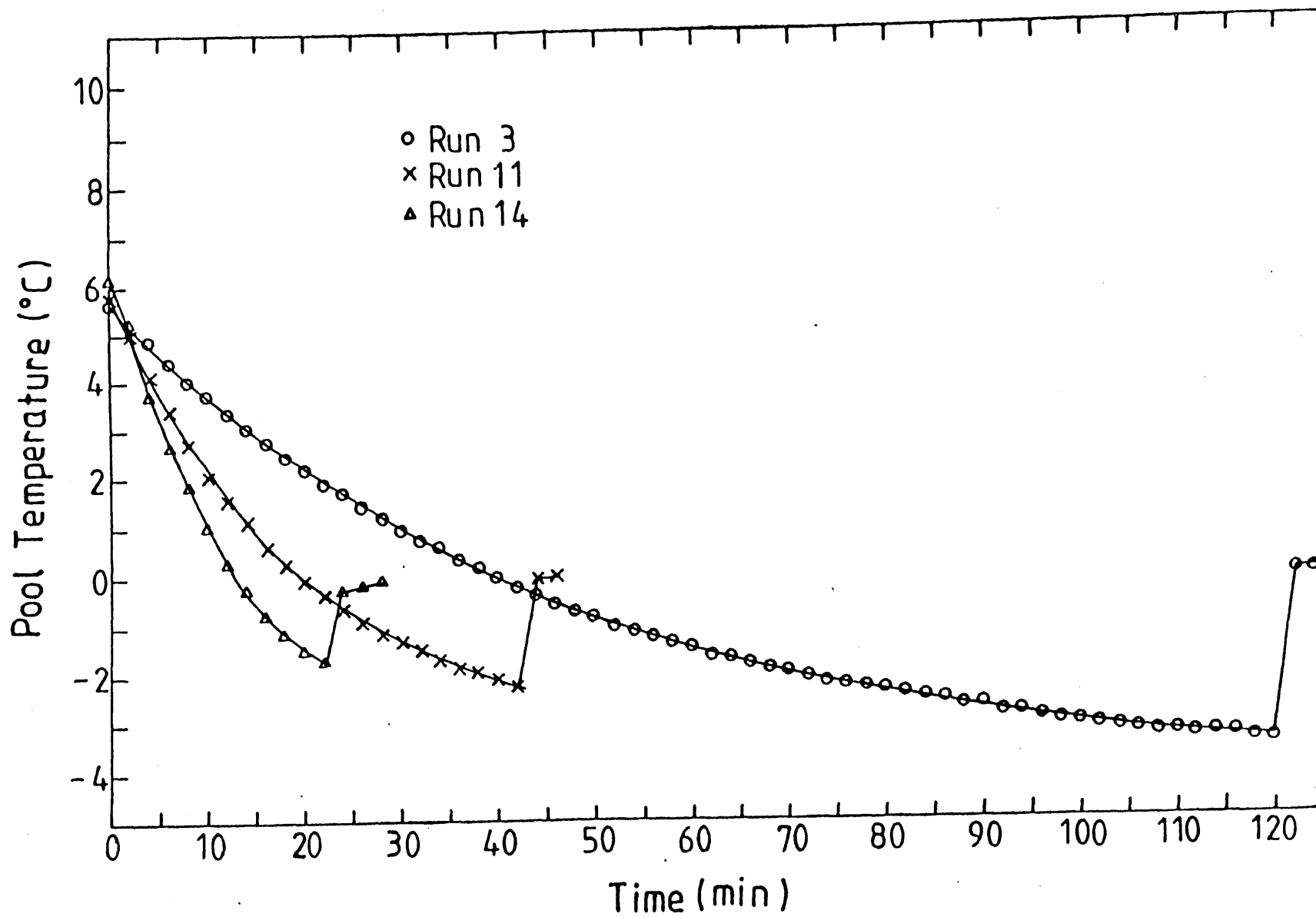
Figure 5.9   Temperature Histories of Runs 3, 11 and 14

proposed in Section 5.3.2.4 and the results are shown in Fig.5.10. The values shown in Fig.5.10 are the average values of all the cooling fins (totally 7 fins) with embedded thermocouples. As shown in Fig.5.10, the calculated heat flux fluctuated during the experiments. An average over these transient values shows that the downward heat flux increases with the gas superficial velocity. The average downward heat flux of Runs 3, 11 and 14 are 380, 396 and 510 W/m^2 respectively. Based on the assumed temperature difference, 0.3 $^\circ C$, between the pool and porous surface, the downward heat transfer coefficients of these runs are comparable with the values predicted by the correlation of U. of Wisconsin (Eq.3.8). The differences are within 20%. A comparison with the proposed periodic contact model, shows that the downward heat transfer coefficients in this experiment are 3.5 to 10 times higher than the calculated values of Eq.3.32. The difference is larger as the gas superficial velocity is higher.

In the derivation of the periodic contact model, several constants were determined by curve fitting of the UCLA dry ice experimental data. The fundamental phenomena involved in dry ice experiment and this experiment are different. In the dry ice experiment, the gas was generated by melting a solid substrate. The decomposition process was not involved in this experiment.

In all the runs, the experiments did not last long enough to study the impact of crust formation on the downward heat transfer rate. It is difficult to ascertain these effects with this experimental apparatus. The experimental results showed that the temperature drop from the pool to cooling coil was around 17 to 18 $^\circ C$ and that from the pool to porous surface was only around 1 $^\circ C$. The structure of the cooling assembly, Fig.5.3, constitutes the major heat transfer resistance. If the effects of crust formation on the downward heat transfer rate are not large enough, they can not be detected.

The overall energy balance of Run 11 is analyzed and the results are shown in Fig.5.11. Figure 5.11 shows the internal energy change of the pool, Q_{pool}, the downward heat transfer rate, Q_{down}, and the heat addition from the atmosphere by

143
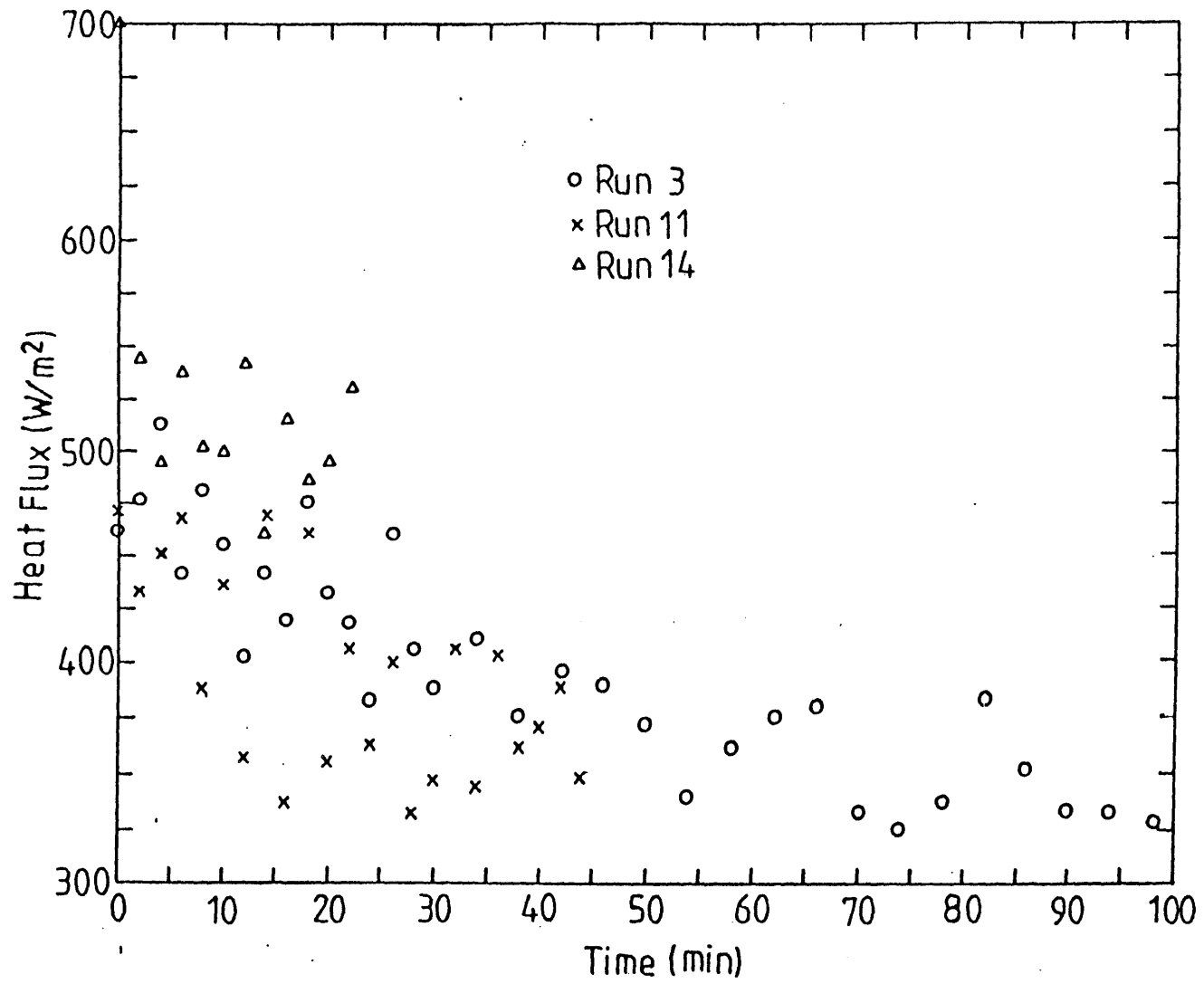
Figure 5.10   Downward Heat Flux of Runs 3, 11 and 14

natural convection, Q_{add}. The heat addition from the atmosphere is estimated by assuming that the heat transfer coefficient at the pool upper surface is 10 W/m^2 $^\circ K$ and the driving force is the temperature difference between the envieorment and the pool. Since the air inlet temperature is lower than that of the pool bulk, about 5 $\sim$ 20 $^\circ C$. some heat will be carried away by the air flow. This part of heat loss is very difficult to estimate because the air temperature at the pool upper surface was not measured. An assumption of thermal equilibrium between the gas and the pool will not be correct. It is quite doubtful that a thermal equilibrium can be reached within a pool of 37.3 mm depth.

From Fig.5.11. it can be seen that the difference between Q_{pool} $+$ Q_{add} and Q_{down} decreases as time proceeds. This is because the pool cools down gradually and the temperature difference between the pool and gas decreases. It is also possible that some heat was transferred into the pool through the side walls of the pool. This term is also very difficult to estimate because of the complicated structure of the side walls.

Figure 5.12 provides the pool temperature histories of Runs 9. 10 and 16. Run 9 is one of the four runs that showed gradual pool freezing. As shown in Fig.11, for Run 9 the temperature of the pool did not change much upon freezing, only around 0.1 $^\circ C$, upon freezing.

Figure 5.13 shows the pool temperature histories of Runs 10, 17 and 18 which correspond to different operating temperatures of the condensing unit, as summarized in Table 5.1. The operating temperature of the condensing unit controls the driving force of downward heat transfer. A decrease in this temperature can increase the driving force and cool down the pool faster. For Run 18. the condensing unit was initially operated at -14.4 $^\circ C$. after 145 $minutes$ the pool temperature reached a steady value and freezing could not be achieved. Freezing was then achieved by adjusting the dial on the back pressure regulator, Fig.5.1, to decrease the operating temperature of the condensing unit to -18.9 $^\circ C$.
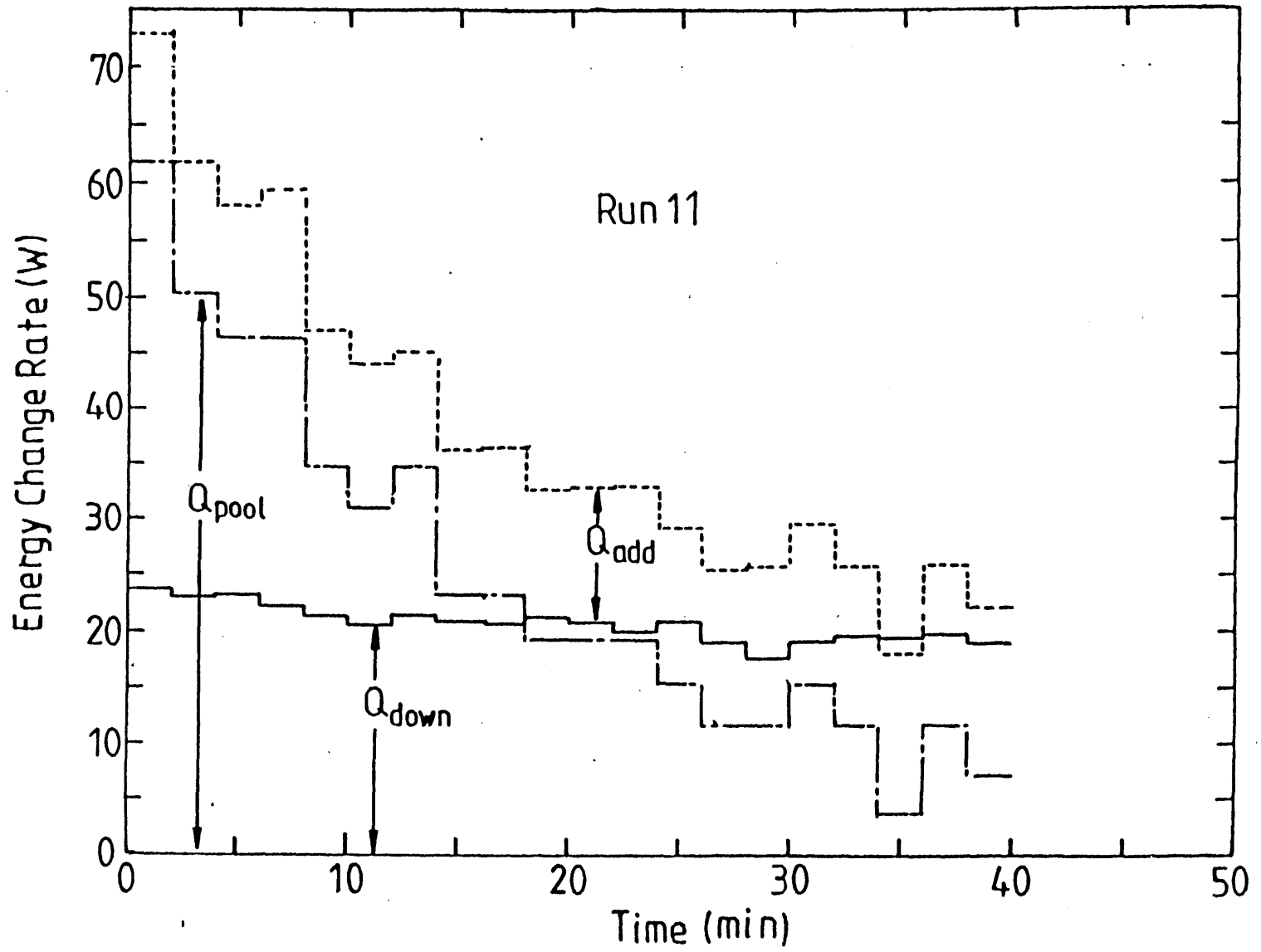
Figure 5.11   Energy Balance of Run 11
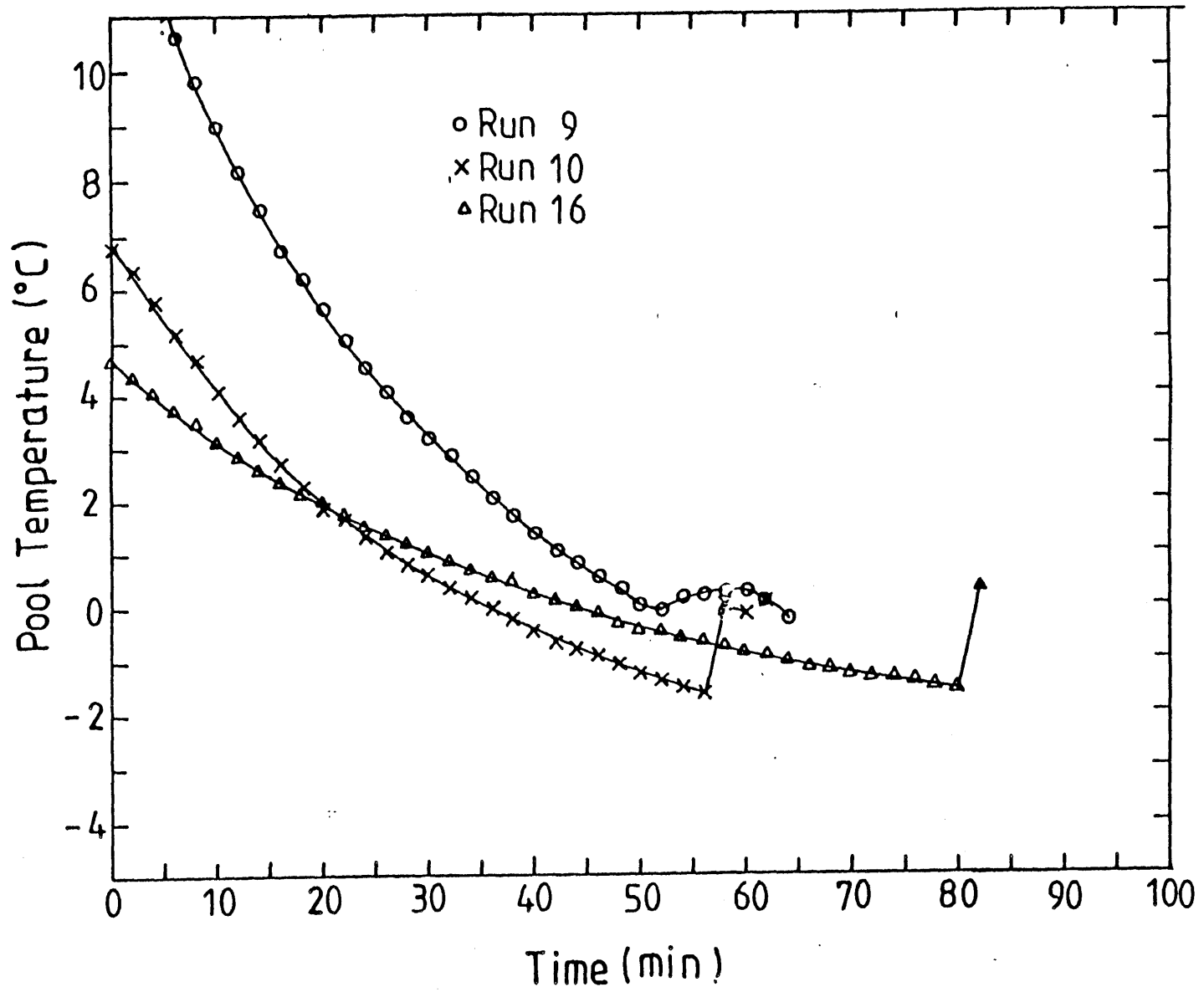
Figure 5.12   Temperature Histories of Runs 9, 11 and 16

147
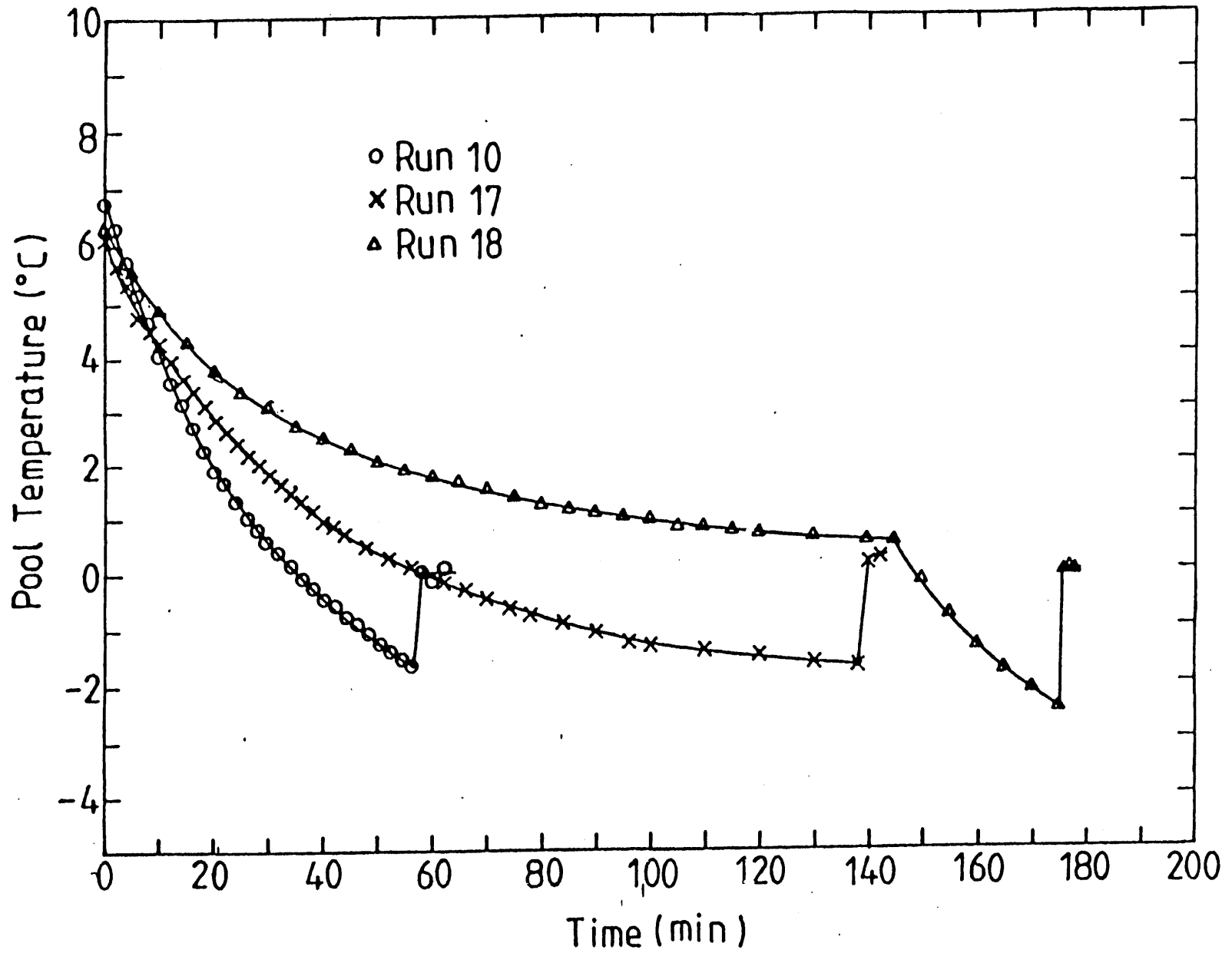
Figure 5.13 Temperature Histories of Runs 11, 17 and 18

5.4.4 Possible Improvements of Apparatus for Future Experiments

Based on the experience gained from previous runs. the following suggestions are made:

1. Insulation materials can be placed around the test cell to cut down both the sideward and upward heat addition to the pool.

2. A more elaborate set up is needed for measuring the surface temperature of the porous plate.

3. The heat transfer resistance within the cooling assembly should be reduced to increase the capability of the apparatus in quantifying the impact of crust fromation on downward heat transfer rate. This can be done by improving the thermal contact between the cooling fins and copper plate. also the contact between the cooling fins and the porous plate.

4. A more elaborate technique is needed for sealing the penetrations of thermo-couple wires on the main structure to prevent the leakage at higher superficial gas velocity. By doing this. the experiments can be conducted at higher gas velocity to respresent a more realistc case.

5.5 Conclusion

In the cases studied. a stable solidified layer is formed across the bubble agitated horizontal liquid/soild interface.

Two different phenomena were observed. In some of the cases. the pool was cooled below its freezing point. Then freezing occured suddenly. the liquid/solid interface was covered by a thin layer of ice and the bulk temperature of the pool jumped up to the freezing point of water. In other cases. the freezing occurred gradually. There is no supercooling in the pool. The causes of these differences remain unclear.

The experiments conducted here are of scoping nature. Several features of MCCI

were not included in the experiment. namely. the internal heat generating and the difference in liquidus and solidus temperature of corium. The direct application of the results of this experiment to MCCI analysis needs further justification. However. in this experiment it was observed that a crust layer could be formed even in the presence of bubble agitation. This validates the concepts used in the current MCCI integral analysis code. such as CORCON/Mod2. WECHSL and DECOMP.

CHAPTER 6

INTEGRAL ANALYSIS OF
MELT/CONCRETE INTERACTION

6.1 Melt/Concrete Interaction with Sustained Heating
- BETA Experiment

6.1.1 Description of BETA Facility

The BETA project, a key experimental program of Melt/Concrete Interaction is currently undertaken at KfK. The BETA facility is unique with regard to size and experimental capability. A schematic diagram of the BETA facility is shown in Fig.6.1.

The hot melt is contained in a concrete crucible. The initial inner diameter of the crucible is 380 mm. This diameter guarantees that gas release and heat transfer at the bottom of crucible is not affected by the vertical walls. The effects of the crucible inner diameter will be observed in a future test with a crucible of 600 mm inner diameter. The dimensions of the concrete crucible are shown in Fig.6.2. The dots in the figure are the locations of thermocouples. Failure of a thermocouple indicates the position of the melt front.

The concrete crucible is enclosed by an induction coil. A maximum electric power of 8400 kW can be fed to the induction coil. However, the large outer diameter of the crucible, needed to allow for radial melt penetration, limits the efficiency of the induction heating. Therefore, a maximum power of 1700 kW may be induced in the melt.

Up to 300 kg metallic and 300 kg oxidic melt can be generated outside the

PERIPHERY SYSTEMS

THERMITE MASS GAUGES
THERMITE JET PYROMETER

MOLTEN POOL

MATERIAL SAMPLING AND
THERMOCOUPLES
MOVIE AND TV CAMERAS
INFRARED PYROMETER
RATIO PYROMETER

EXHAUST GAS

THERMOCOUPLES
PRESSURES TRANSDUCERS
MASS SPETROSCOPE
AEROSOL DETECTOR

INPUT POWER
HEAT LOSSES
WATER CONDENSATE
BALANCE

CONCRETE CRUCIBLE

THERMOCOUPLES
MOISTURE DETECTORS
LIGHT SENSORS
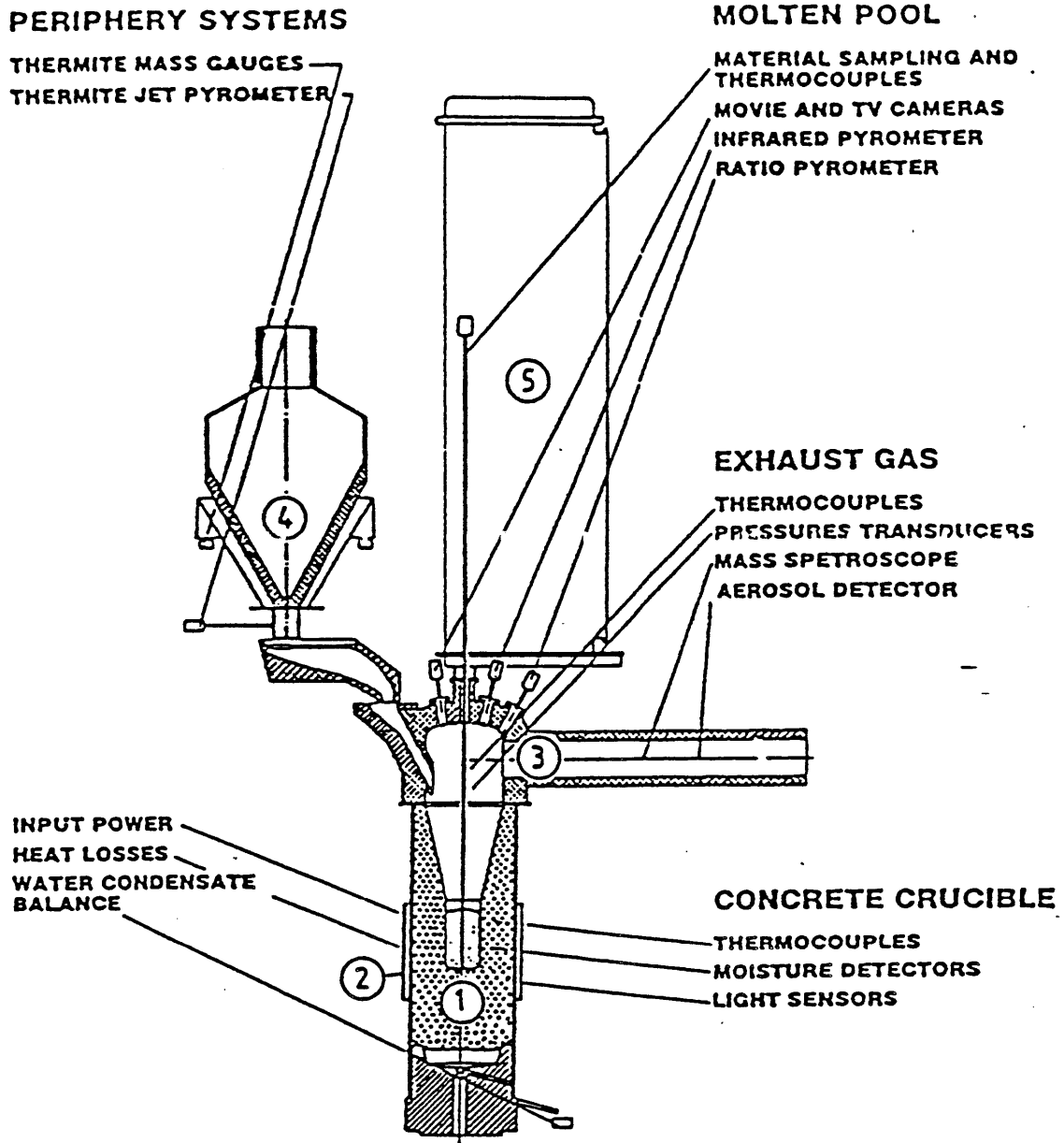
1 CONCRETE CRUCIBLE
2. INDUCTION COIL
3 OFFGAS SYSTEM

4 THERMITE REACTION TANK
5 CONTAINER FOR MEASUREMENT
PROBES

Figure 6.1   Schematic Diagram of BETA Facility
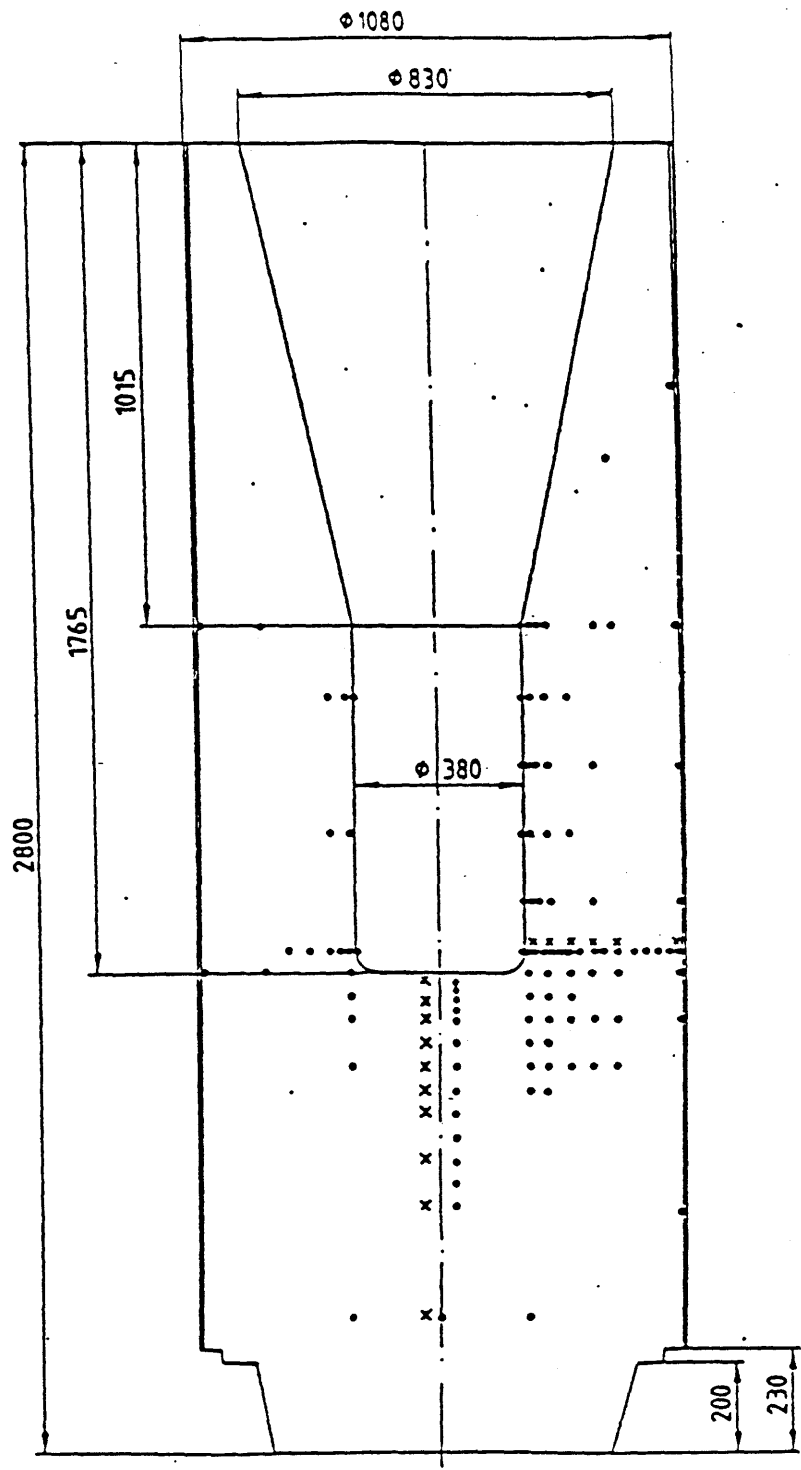
Figure 6.2   Concrete Crucibles of BETA Experiments

crucible by a thermite reaction and then poured into the crucible. The amount of melt poured into the concrete crucible can be controlled. The initial temperature of the melt depends on the composition of thermite. There is no direct measurement of the initial melt temperature. A ratio pyrometer is installed in the pouring channel to measure the surface temperature of the melt.

On top of the crucible, there is a container with a dip-in material sampling and temperature measurement system for melt analysis. The temperature of the melt is measured at predefined time intervals by W - Re thermocouples which are dipped simultaneously into the metallic and oxidic phases. Also, the lances of dip-in thermocouple may collect samples from the melt for chemical analysis. The surface temperature of the melt is measured continuously by a ratio pyrometer installed on top of the crucible.

The hood and offgas pipe collect all gaseous products generated during melt concrete interaction for physical and chemical analysis. The composition and the release rate of the gases are analyzed by on-line and off-line mass spectrometry, where an Argon cover gas flow acts as tracer gas. Aerosol concentration in the offgas is analyzed by an on-line scattering device and by probe analysis.

Throughout the experiments, the behavior of the melt surface is observed by a TV camera. This provides valuable information on gas flow through the melt, surface crust formation and aerosol production.

6.1.2 BETA Test Matrix and Results

The test matrix of the BETA experiments contains two major parts; the high power or high temperature tests and the low power or low temperature tests. The principal idea is to investigate the different regimes which occur in the process of Corium/Concrete Interaction with a sequence of experiments at different temperature levels at approximately quasi-steady-state conditions. This approach has the

154

advantage that the complex physical and chemical reactions can be observed in more detail.

Operation of the BETA facility began in February 1984. By February, 1985 six high power tests and one low power test had been performed successfully. All experiments used a basaltic concrete crucible. Some experiments with calcareous concrete will be made at a later stage. The experimental conditions for these high power tests are summarized in Table 6.1. The initial temperatures of the melt shown in Table 6.1 are estimated based on the energy balance of the thermite reaction and the heat loss before the melt was poured into the crucible. In general, the melt was poured into the crucible 2 minutes after igniting the thermite to have a complete separation of the oxidic and metallic melts.

For tests V0.1 through V1.2, the thermite mixture is identical, pure thermite plus metallic iron. For the V1.3 to V1.6, Cr and Ni were added to produce stainless steel melt and, quartz sand was added to reduce the oxide melting point. The amount of quartz sand was greater in V1.3 than in the other experiments. The uncertainty involved in the temperature is probably around 100 to 200 $^c K$. The initial temperature shown in Table 6.1 are the standard values selected by a working group at KfK for the purpose of code comparison.

In each test before the melt was poured into the crucible the inductor was operated at a predetermined power level for at least 45 minutes. The actual power coupled to the melt was calculated as the difference of the inductor power with and without the melt in the crucible. The recorded power histories have some samll scale fluctuations. The records of tests V1.3 and V1.5 are extremely noisy. For the purposes of input to computer codes, those records have been reduced to numerical form. In Appendix C. the smoothed power history and numerical values of all the high power tests are summarized. Again. those values are the standard values decided by the working group.

155

Table 6.1

Test Matrix of BETA Experiment

Test	Mass		Initial Temperature	Planned Power	Average Power	Erosion Rate
	Metallic	Oxidic				
	(kg)		($^\circ K$)	(kW)	(kW)	(mm/sec)
V0.1	Fe (300)	–	2473	no		
V0.2	Fe (300)	–	2473	200~400	370.3	0.18
V0.3	Fe (300)	Al_2O_3 (150)	2473	1700	827.1	1.00
V1.1	Fe (20)	–	2473	Pulse	Failed	
V1.2	Fe (190)	Al_2O_3 (190)	2473	Pulse	374.4	0.25
V1.3	Fe (246)	Al_2O_3 (105)				
	Cr (30)	SiO_2 (45)	2173	1000	788.8*	0.76
	Ni (24)	–				
V1.4	Fe (328)	–				
	Cr (40)	–	2273		Failed	
	Ni (32)	–				
V1.5	Fe (246)	–				
	Cr (30)	–	2273	450	195.8	0.23
	Ni (24)	–				
V1.6	Fe (246)	Al_2O_3 (45)				
	Cr (30)	SiO_2 (5)	2273	1000	523.0	0.67

* over first five hundred seconds

In all the high power tests it was found that the downward penetration of the metallic melt dominates, which is quite different from the results of the previous experiments without internal heating. The downward erosion rate varies from 0.18 to 1.00 mm/sec and is roughly proportional to the power input. The influence of magnetic Lorentz-forces, resulting from induction heating, on the melt front proporgation was investigated both experimentally and theoretically when the BETA facility was planned. Compared with that of gas agitation of the melt, the influence was found to be negligible R3 . However, because of the unexpected melt front shape, the test V1.2 was carried out to validate the influence of magnetic Lorentz-froces. With pulsed heating, at maximum input power, the melt was repeatedly heated in the crucible to high temperatures and then allowed to interact with the crucible with zero induction field. After a series of ten power cycles, comparison of the post-test crucible shape with that of V0.2 shows no significant difference, and it was concluded that the radial and axial penetrations are not affected by the heating method. The cross sections of post-test crucibles of all power tests are shown in Appendix C.

Another important phenomenon observed in the BETA experiments, especially at high power level, is the dispersal of the metallic phase into the oxidic phase. Test V0.3, with a rather high sustained heating power of 1700 kW, began with oxidic and metallic melts in the crucible, with the metallic phase initally at the bottom. With the high gas release from the concrete the steel melt was entrained into the oxidic phase in fine droplets. After 5 to 6 $minutes$ of interaction, an almost complete dispersion of the metallic phase into oxidic phase was noted, and consequently no continuous steel phase existed to be heated by the induction field. Therefore, the heating power dropped to a low value, ending the experiment. From the post-test examinations of concrete crucibles, it was found that, for all the high power tests except V0.2 and V1.2, a complete dispersal of the metallic phase occured. For V1.2, an estimated 106 kg of metallic phase remained at the end of the experiment. This phenonemon was not observed in other melt/concrete interaction test, primarily because BETA experiments have been the first large scale steady-state experiments ever attempted.

This phenomenon is presently not modeled in any code. The dispersion was not observed in the first low power test. test V2.1.

From the post-test examinations of the concrete crucibles it was found that, in all the high power tests with dispersion. the shape of the crucibles became very irregular at the later stage of the experiment. In Tests V1.2 and V1.5, the shape was not symmetric with respect to the center line of crucible. In tests V0.3 and V1.6, the metallic melt penetrated into the concrete from the corners, with a chunk of concrete remaining in the center of the bottom surface. Test V1.3 also had the tendancy to form this configuration. It seems that the unentrained metallic melt separated into two parts and eroded the concrete independently. Due to the limited number of thermocouples being located in specific positions the time dependent cavity shapes is difficult to generate.

One of the important findings of the BETA experiment with respect to the source term evaluation is that the aerosol concentration in the off-gas is relatively low, on the order of one mg/m^3. These results differ from those of Sandia's small scale experiments. The difference is probably due to the different concretes used in the experiments.

The detailed analysis of typical samples of actual BETA concrete has not been reported. Until such results become available. it was decided that the composition of KWU type [H6] concrete will be used for all code calculations. The composition. together with some other properties of KWU type concrete are summarized in Table 6.2.

6.2 Analysis of BETA Experiments

6.2.1 Computer Code

A modified version of the CORCON/Mod1 is used in the following analysis. The major assumptions and limitations of CORCON/Mod1 are:

Table 6.2

Specification of KWU Type Concrete

Compositions	Weight Fraction(%)
SiO_2	76.7
Al_2O_3	5.4
$CaCO_3$	6.6
$Ca(OH)_2$	7.3
$(H_2O)_{evap}$	4.0
Total Gas Content	8.7
T_{abl} $(°K)$	1570
T_{sol} $(°K)$	1350
T_{liq} $(°K)$	1650
Decomposition Enthalpy (MJ/kg)	2.00

- Isothermal pool layers are well stirred by concrete decomposition gases and steady ablation of concrete. As a consequence of this. CORCON/Mod1 is applicable only to the early, high temperature phase of melt/concrete interaction when the melt is hot enough. Once the melt temperature decreases to the point below the metallic- or oxidic-phase liquidus temperature. or the concrete erosion is low so that transient and two dimensional conduction effects become important. the code is no longer valid.

- The atmosphere and surroundings are included only as thermal reservoirs to facilitate heat transfer from the pool surface. The convective heat transfer coefficient in the atmosphere at the pool surface was assumed to be constant. A simplified form factor is used in calculating the radiative heat transfer between the pool surface and surroundings. Neither the atmosphere temperature nor pressure is coupled to the system.

- The metallic and oxidic melt stratify into separated layers. No dispersion is considered. Heterogenous mixtures of the melt are not permitted.

- The gas properties for heat transfer calculations are assumed to be constant.

- The oxidation reactions between the metallic elements and concrete decomposition gases only occur when the gases bubble through the melt pool. Oxidation of metallic elements by gases at the interface with a gas film is not included.

Due to the limitations of the code, only the high power tests of BETA have been analyzed.

6.2.2 Modeling of Melt/Concrete Interaction

In CORCON, it is assumed that both the downward and sideward heat transfer to concrete are governed by the gas film model. It gives the results that the downward and sideward erosion are about equal. This is contradictory to the BETA experimental results. It could be argued that the film at the horizontal interface

160

collapses (quench) when the superficial gas velocity at melt/concrete interface is not high enough to support the film. After the film collapses, the downward heat transfer is governed by either a pseudo transition boiling or pseudo nucleate boiling which has a higher heat transfer coefficient. Therefore, the downward erosion is enhanced. However, to reproduce the results of different BETA tests by the WECHSL code, the quench limit had to be varied from test to test R3.

Based on hydrodynamic considerations, the formation of a very stable gas film requires that the superficial gas velocity exceeds a certain critical value i.e. the flooding limit. As the superficial gas velocity decreases, the film may collapse due to Taylor hydrodynamic instability, which provides a limit of minimum gas velocity for supporting an existing film. For the case of melt/concrete interaction, those limits differ by two orders of magnitude. Figure 6.3 shows the heat fluxes corresponding to these decomposition gas limits for basaltic concrete in contact with the metallic corium. Those limits are calculated based on Kutateladze's flooding limit (Eq.3.5) and Berenson's minimum stable gas film criterion (Eq.3.6) respectively.

Figure 6.3 also shows the heat flux predicted by the pseudo nucleate boiling downward heat transfer correlation derived in Chapter 3 (Eq.3.32), with a slip ratio equal to the cubic root of the density ratio of slag and concrete gases, and the heat flux predicted by the original CORCON film model (Fig.3.11). The intersections of solid and dotted curves are the corresponding limits. As shown in Fig.6.3, the temperature difference needed to form a stable film (Taylor limit) is smaller than that of the flooding limit. This is different from the traditional boiling curve i.e. there is no transition boiling regime. Therefore, the heat transfer mechanism will either be pseudo nucleate boiling or pseudo film boiling. The actual heat transfer mode depends on the initial temperature of the melt. If the temperature is initially very high, the heat flux will be high enough to generate a film, and the interaction starts with a film at the interface and follows the gas film model to the minimum stable gas film limit. After the film collapses, the heat transfer mode switchs to pseudo

161
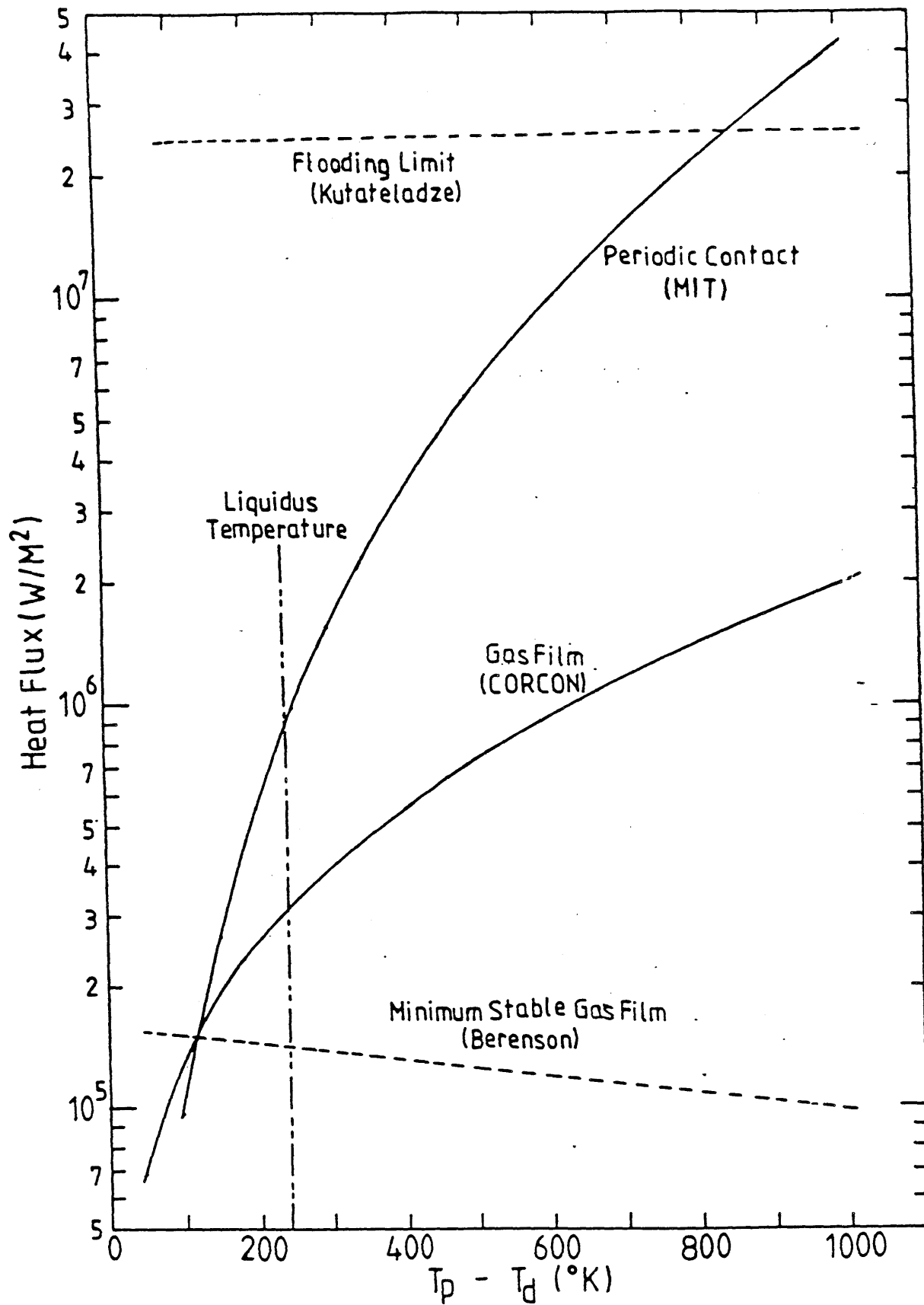
Figure 6.3   Modeling of Melt/Concrete Interaction

nucleate boiling. If the temperature is not high enough to generate the film the heat transfer mechanism will be pseudo nucleate boiling all the time until freezing takes place. Obviously, the gas film may also be disturbed prior to reaching the minimum flux, and the periodic contact mode may be initiated at higher heat flux than the Taylor limit.

6.2.3 Modifications of CORCON/Mod1

The CORCON/Mod1 has been modified based on preceeding argument. The MIT periodic contact model was incorporated to calculate the downward heat transfer coefficient in the pseudo nucleate boiling regime. The interfacial heat transfer correlation derived in Chapter 4 was also incorporated into CORCON/Mod1.

Another major change of CORCON/Mod1 concerning the heat transfer calculation is to make the properties of gas mixture dependent on the temperature and composition of the decomposed concrete gases. The specific heat of the gas mixture is calculated based on the weight fraction of each species. The viscosity and thermal conductivity of the gas mixture (carbon dioxide and water vapor) are determined by Wilke's formula [B7]:

$$X_{mix} = \sum_{i=1}^{n} \frac{x_i X_i}{\sum_{j=1}^{n} x_j \varphi_{ij}} \tag{6.1}$$

where

$$\varphi_{ij} = \frac{1}{\sqrt{8}}(1 + \frac{M_i}{M_j})^{-1/2}(1 + (\frac{\mu_i}{\mu_j})^{1/2}(\frac{M_j}{M_i})^{1/4})^2$$

X = either thermal conductivity or viscosity

x = mole fraction

M = molecular weight

μ = viscosity

n = number of species in the mixture

i, j = the index of species

Based on the above equation, for basaltic concrete. the calculated thermal conductivity of gases mixture varies from 0.32 $W/m\,^\circ K$ at 2000 $^\circ K$ to 0.21 $W/m\,^\circ K$ at 1700 $^\circ K$. For limestone/common sand concrete. it varies from 0.21 $W/m\,^\circ K$ at 2000 $^\circ K$ to 0.15 $W/m\,^\circ K$ at 1700 $^\circ K$. In the original CORCON. the thermal conductivity of the gas mixture is assumed to be 0.1973 $W/m\,^\circ K$.

The simplified containment response model in Chapter 2 has also been incorporated into CORCON/Mod1 [K1] to calculate the containment pressure and its effects on Corium/Concrete Interaction. The details of this modification will be described in section 6.1. The BETA facility is an open system. the system pressure is nearly constant. Therefore. this modification was not used in the following analysis of BETA experiments.

The details of all the above modifications on CORCON/Mod1 and the changes of input data are summarized in Appendix D.

6.3 Comparison of the Analytical Predictions and Experimental Results of BETA

6.3.1 Post-test Calculation of Tests V0.2 - V1.3

After some preliminary calculations. it was decided that the best fit to the results of the BETA tests V0.2 - V1.3 can be obtained if a set of correction factors (multipliers) is applied to the correlations mentioned above. The correction factors used in the following analysis are summarized in Table 6.3. A sensitivity study of these correction factors will be described in Section 6.3.2.

Among these correction factors, the interfacial heat transfer correlation has the highest uncertainty. For the situations of the BETA experiments. the superficial gas velocity at the layers' interafce could be as high as 0.5 m/sec. Based on the MIT model. the interfacial heat transfer coefficient would be around 10^6 $W/m^2\,^\circ K$. This value is unreasonably high for the oxidic phase with a viscosity as high as 7

Table 6.3

Modification Factors of Correlation

Correlation	Multiplier
MIT Downward Heat Transfer Coefficient	0.6
Interfacial Heat Transfer Coefficient	0.1
Flooding Limit (Heat Flux)	0.85
Minimum Stable Gas Film (Heat Flux)	6.0

$kg/m\,sec$. The MIT model was derived based on the experimental data at relatively low superficial gas velocity, around 0.01 m/sec. Besides that, the real oxidic materials are of high viscosity. The effect of the viscosity was not included in the proposed model.

(a) Test V0.2

The calculated radial and axial erosions of test V0.2 are compared with the experimental results in Fig.6.4. In Fig.6.4. for certain elevations there is more than one data point. These correspond to the failure time of thermocouples located at different radial positions. From Fig.6.4 it can be seen that, for test V0.2 the gas film collapsed at 620 sec. from then on the axial erosion rate increased from 0.13 mm/sec to 0.26 mm/sec while the radial erosion rate is still the same as before. around 0.08 mm/sec.

Figure 6.5 shows the predicted temperature history of the metallic melt of test V0.2. As shown in Fig.6.5, after the film quench limit was reached. around 1900 $^\circ K$, the downward heat transfer mechanism switched from the stable film model to periodic contact model and the temperature of the melt dropped quickly. The calculation of V0.2 stopped when the temperature of the metallic phase reached $(T_{liq} - 0.25(T_{liq} - T_{sol}))$. The temperatures of metallic phase measured by the dip-in thermocouples were around 1780 $^\circ K$ which are below the theoretical solidus temperature calculated by the code. It is believed that there are some systematic errors in the temperature measurements of both V0.2 and V0.3 tests. Besides that, a small amount of impurity e.g. Al, Si, or C in the pure iron can decrease its solidius temperature. It is possible that the analysis did not account for the impurity correctly.

Figure 6.5 also shows the predicted temperature history of the oxidic phase. After the first 100 sec. a temperature difference of 40 ~ 60 $^\circ K$ are established between the oxidic and metallic phases. The temperature difference becomes smaller when

166

Figure 6.4   Comparison between the Predicted and Experimental Erosion Histories of BETA Test V0.2
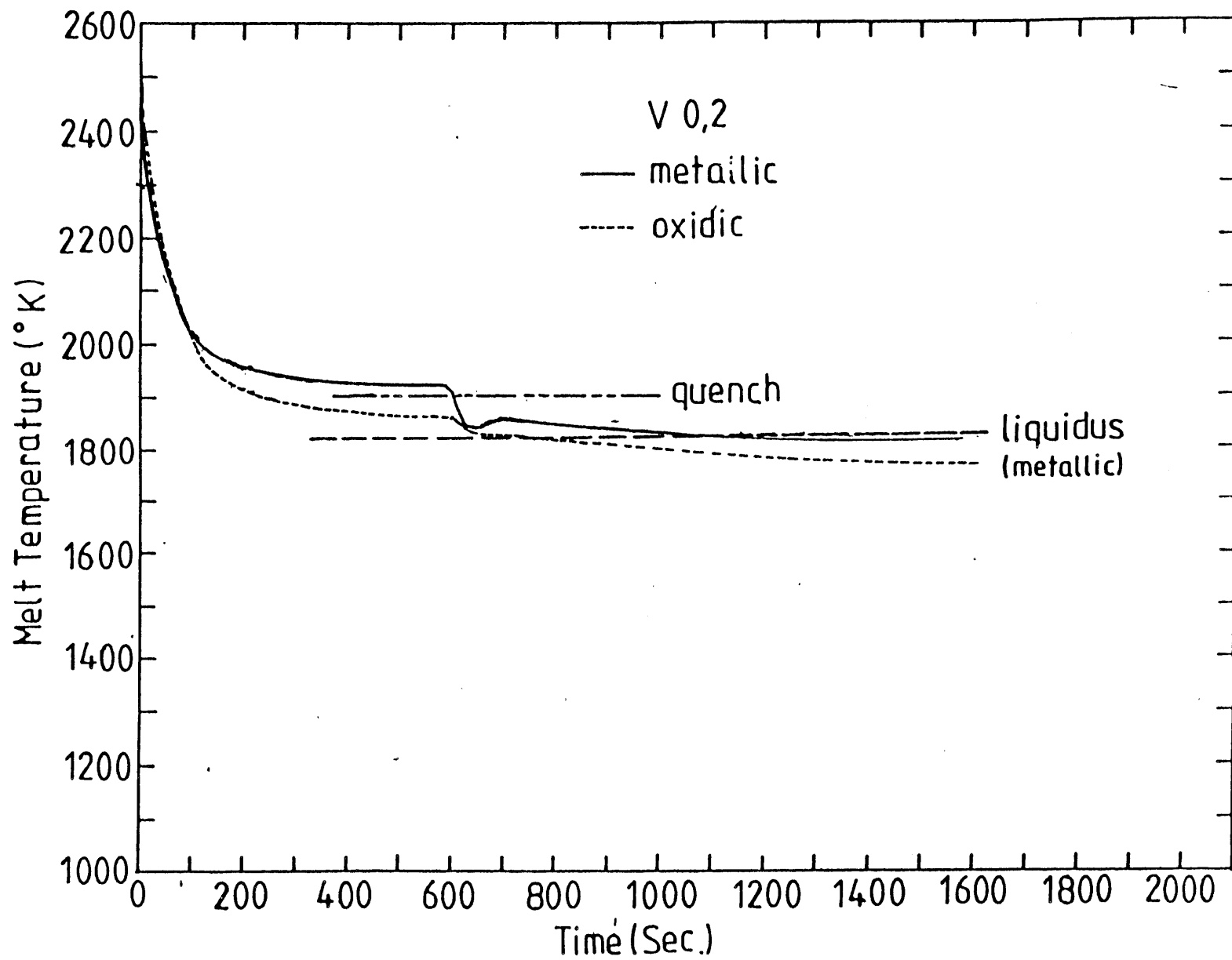
Figure 6.5   Temperature Histories of the Melt, BETA Test V0.2

the film quench limit is reached. This resulted from rapid cooling of the metallic phase. After that. another almost steady temperature difference is established with smaller magnitude compared with previous one.

The predicted cavity shape of test V0.2 is shown in Fig.6.6. The enhancement of downward erosion after the film collapse can also be seen in this figure.

(b) Test V0.3

For test V0.3. with F factor (multiplier for quench heat flux limit) equals to 6.0. the film does not collapse; therefore the axial erosion rate is underpredicted (Fig.6.7a). However, if we assume that the initial temperature of V0.3 is 100 $^{\circ}K$ lower than the standard input value. The interaction starts with nucleate boiling and stays in this regime until freezing takes place which gives a better fit with the experimental results (Fig.6.7b). The calculated axial ablation rate is as high as 2.0 mm/sec initially then decreases gradually to 0.16 mm/sec at 600 sec.

The calculated temperature histories of the metallic and oxidic phases are shown in Fig.6.8. Again the calculation stopped when the temperature of the metallic melt dropped below its liquids temperature. The temperature difference between the oxidic and metallic phases is around 30 ~ 40 $^{\circ}K$. This temperature difference is smaller than that of V0.2. This is because in test V0.3 the superficial gas velocity is higher and therefore results in higher interfacial heat transfer coefficient.

The predicted cavity shape of V0.3 is shown in Fig.6.9. The cavity shape is different from that of test V0.2. This is because the amount of melt poured into the concrete crucible in test V0.3 is greater. It contains 300 kg of iron and 150 kg of Al_2O_3.

(c) Test V1.2

For test V1.2 (pulsed power test) some freezing occurred between power pulses.

169

V 0,2

TIME STEP = 50.0 S

SCALE.CM
0.00   10.00   20.00
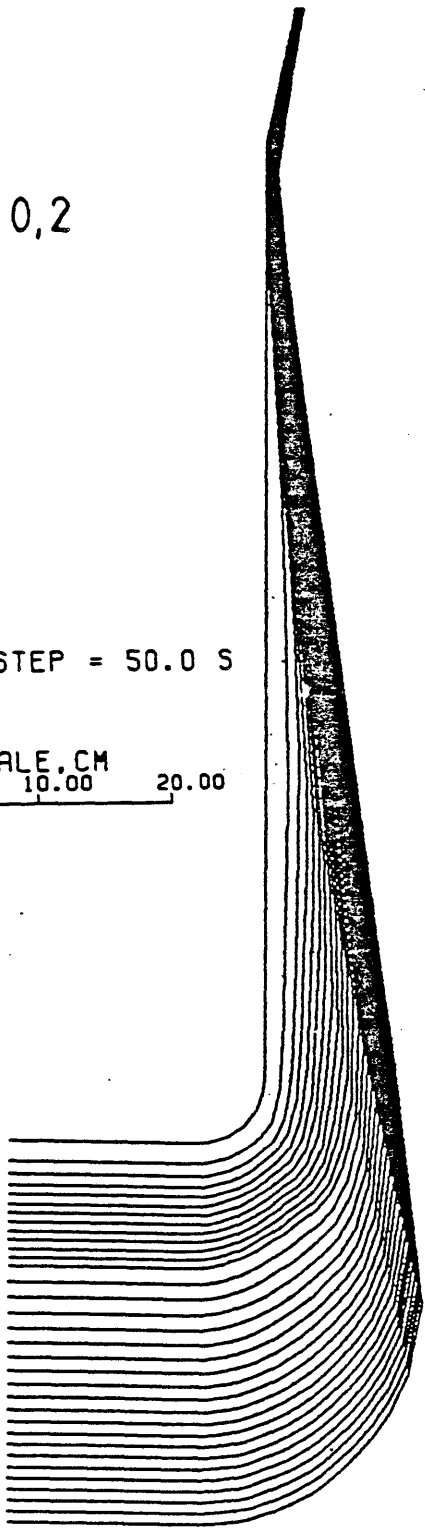
Figure 6.6   Predicted Cavity Shape Of BETA Test V0.2
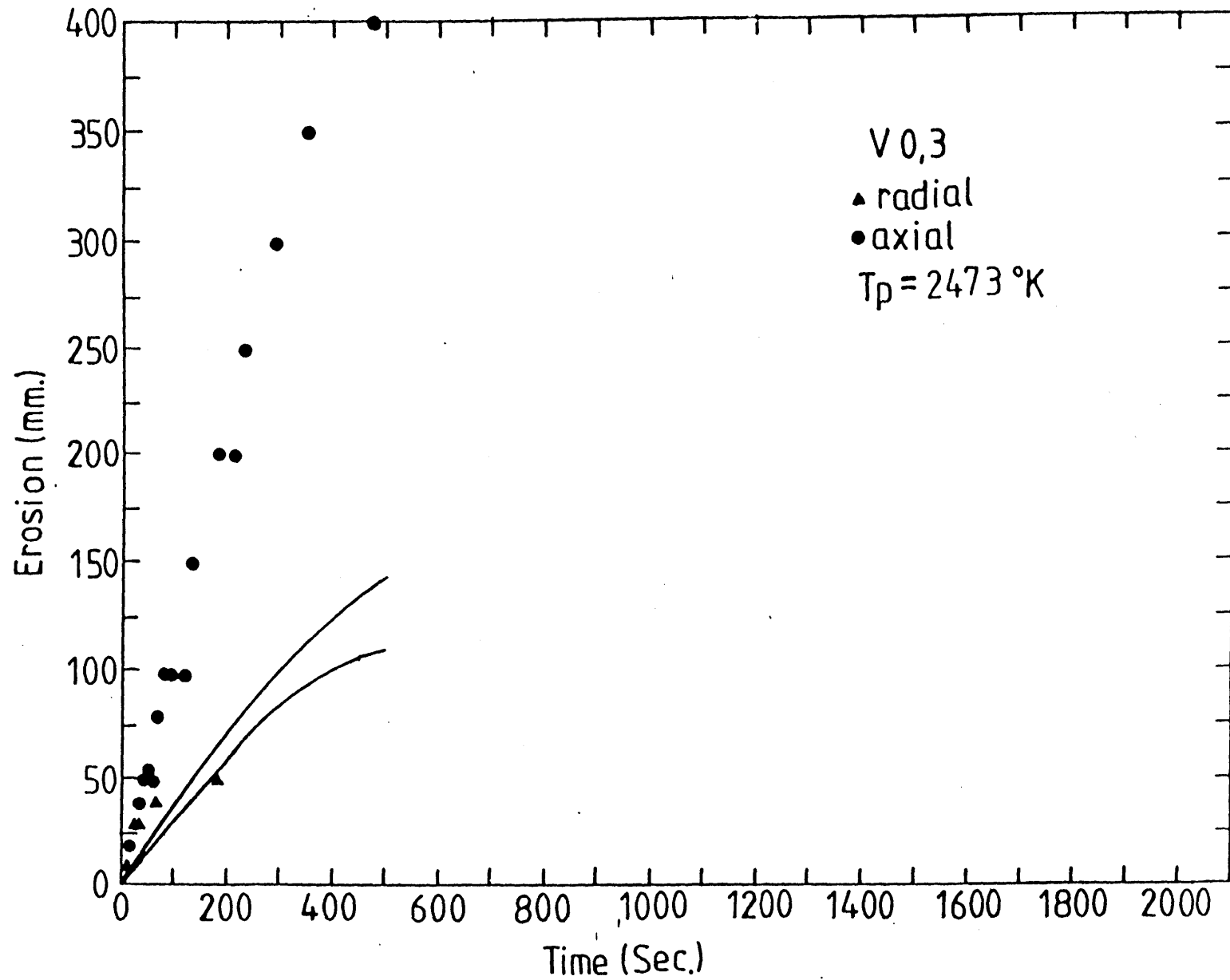
Figure 6.7a   Comparison between the Predicted and Experimental Erosion Histories of BETA Test V0.3 ($T_p = 2473$ °K)
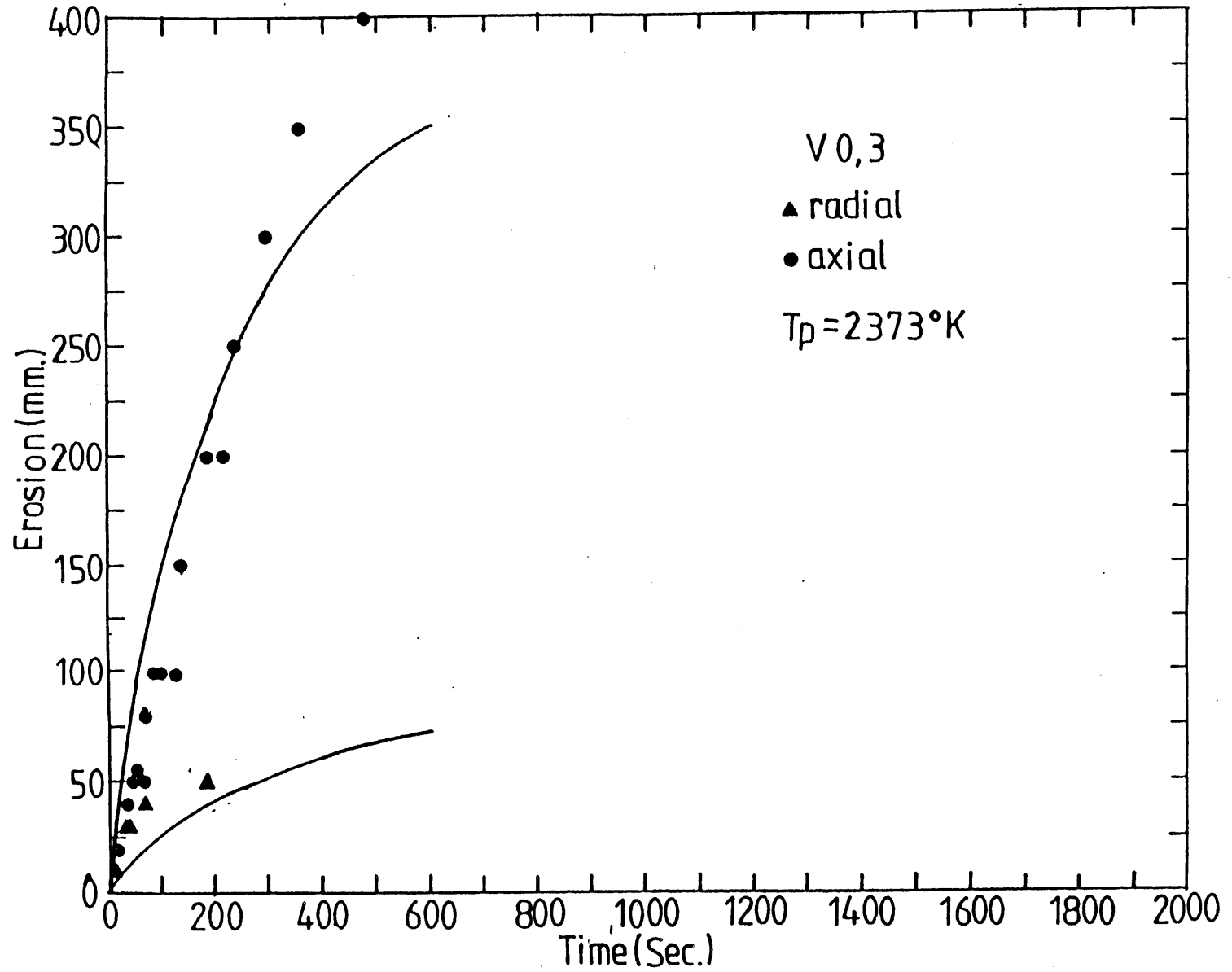
Figure 6.7b   Comparison between the Predicted and Experimental Erosion Histories of BETA Test V0.3 ($T_p = 2373\ °K$)
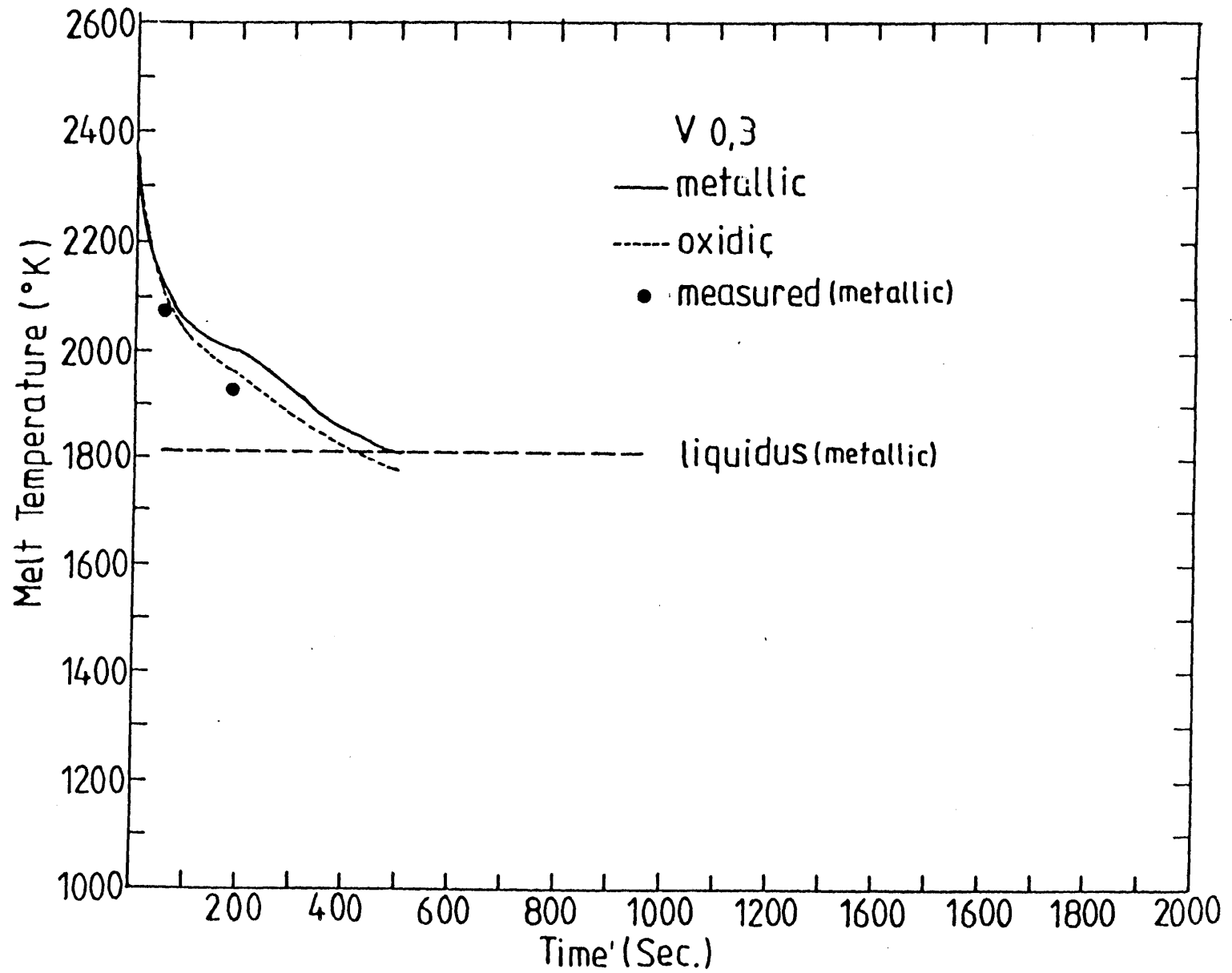
Figure 6.8   Temperature Histories of the Melt, BETA Test V0.3

V0,3

TIME STEP = 25.0 S

SCALE,CM
0.00   10.00   20.00
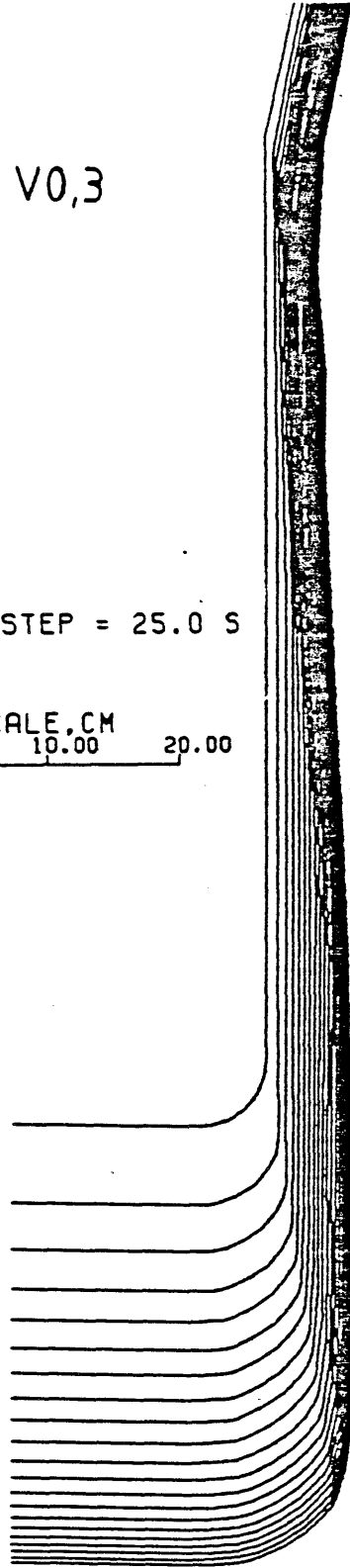
Figure 6.9   Predicted Cavity Shape Of BETA Test V0.3

174

which is beyond the capability of CORCON/Mod1. Therefore, as shown in Fig.6.10 the prediction is not in good agreement with the experimental results.

From Fig.6.11. it can be seen that the predicted temperature history of the metallic phase follows closely the power input. The predicted temperature history of the oxidic phase is also shown in Fig.6.11. The temperature difference between the metallic and oxidic phases is larger when there is internal heating in the metallic phase. The temperature measurements of dual dip-in thermocouples at 140 sec and 300 sec showed that the temperature differences between the metallic and oxidic phase are around 80 ~ 100 $°K$. These are consistent with the calculated results.

From the cavity shape plot of V1.2 (Fig.6.12), the effect of internal heating on downward erosion can be easily seen i.e. the downward erosion rate is higher when the induction power is switch on and is lower when the induction power is off.

(d) Test V1.3

Figure 6.13 shows that the predicted radial and axial erosions of test V1.3 are in good agreement with experimental results. However, as shown in Fig.6.14 the initial rapid cooling of the melt can not be reproduced in the calculation. In test V1.3. some oxidic phase was splashed out of the melt pool and became attached to the concrete wall at the upper part of the crucible which is an effective way to cool down the melt. This mechanism is not included in CORCON/Mod1.

In test V1.3. 10% (30 kg) of Cr and 8% (24 kg) of Ni were added to the melt to simulate stainless steel. The Cr and Ni can be oxidized by the concrete decomposition gases. These reactions can make some contribution to the total heat input to the melt. As shown in Fig.6.15, the calculated chemical heat accumulated to 18 MJ at 600 sec which is about 4% of the total heat input. It is important to point out here, that the amount of chemical energy generated in the melt pool can not be measured in the experiments. It can only be calculated by the chemical

175
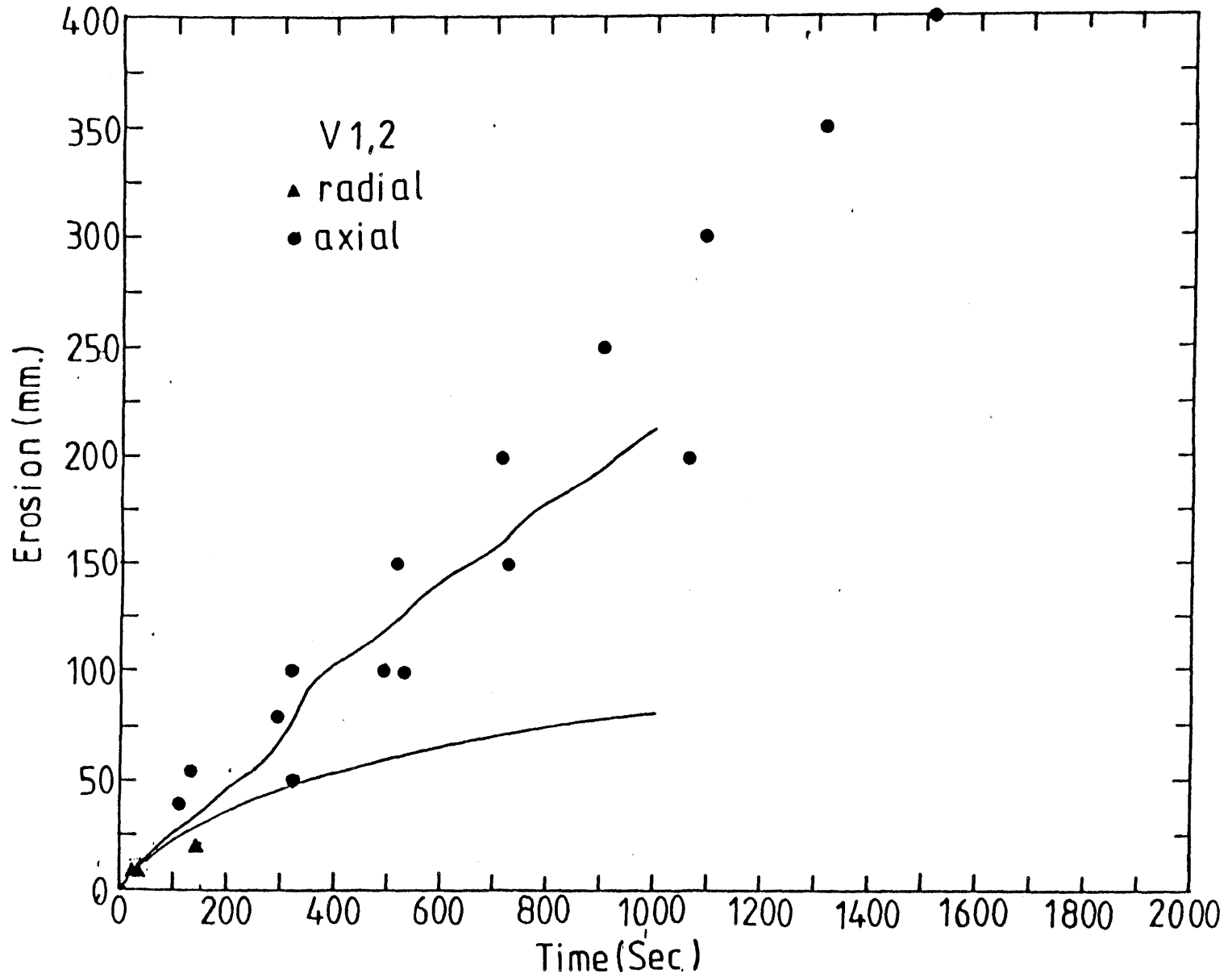
Figure 6.10   Comparison between the Predicted and Experimental Erosion Histories of BETA Test V1.2
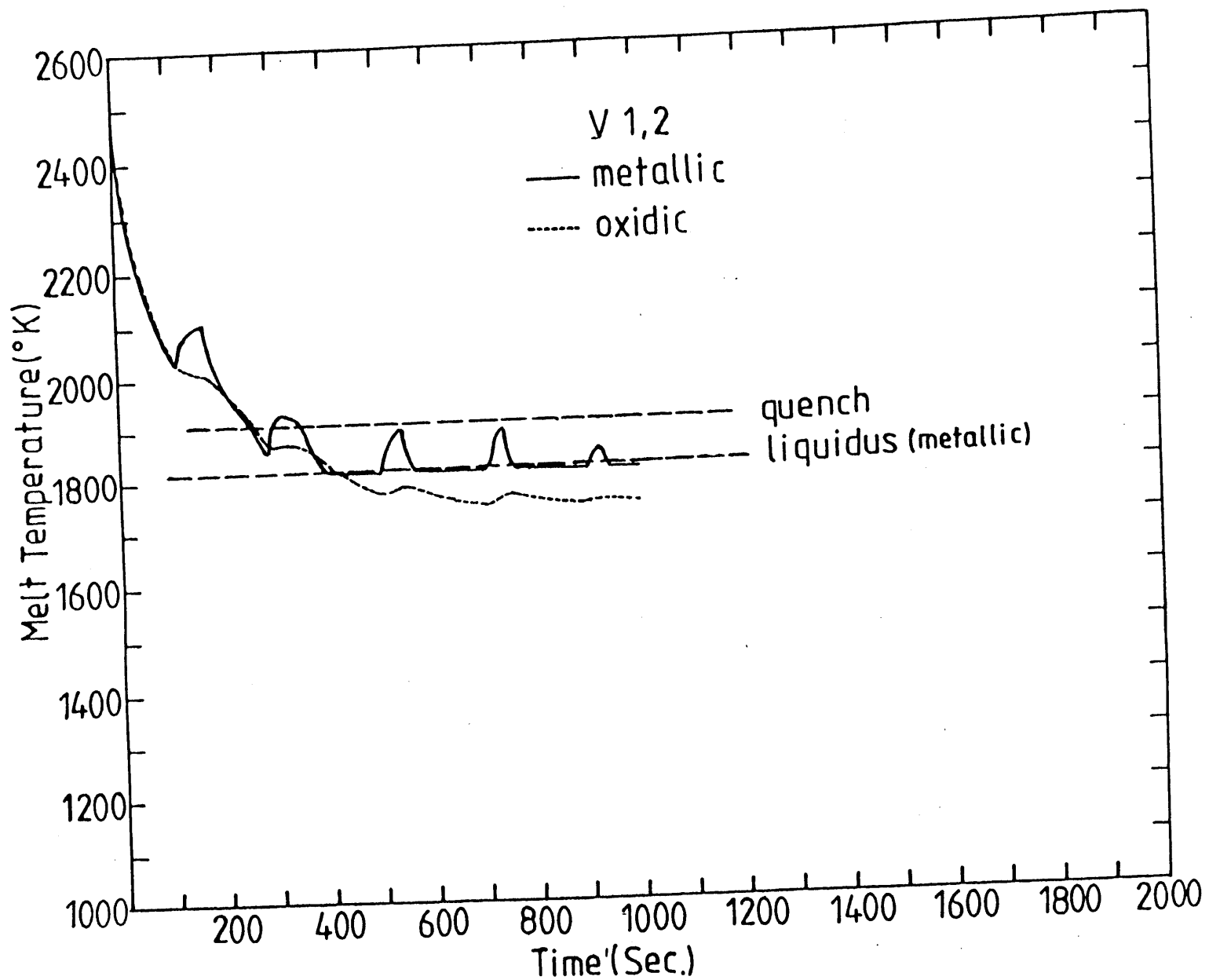
Figure 6.11   Temperature Histories of the Melt, BETA Test V1.2

V 1,2

TIME STEP = 50.0 S

SCALE.CM
0.00   10.00   20.00
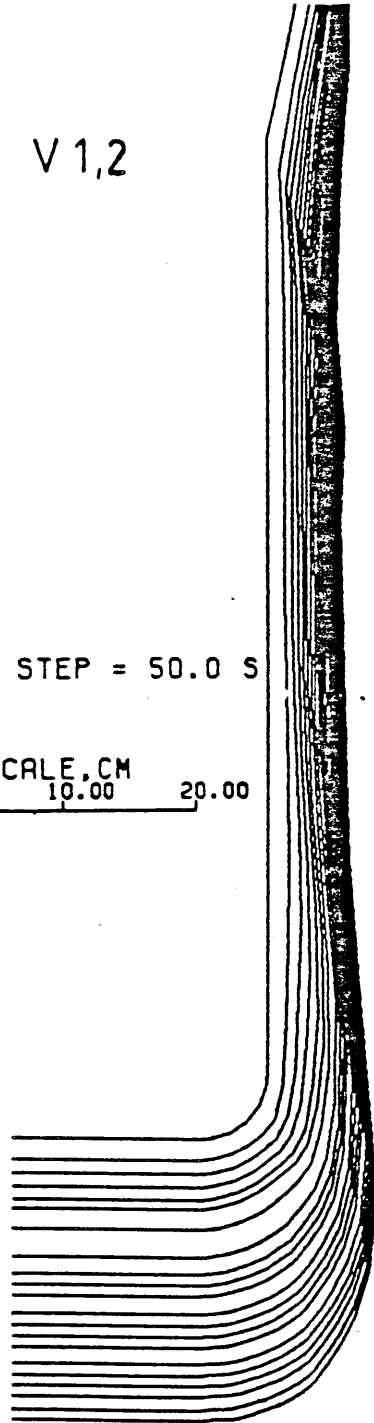
Figure 6.12   Predicted Cavity Shape Of BETA Test V1.2
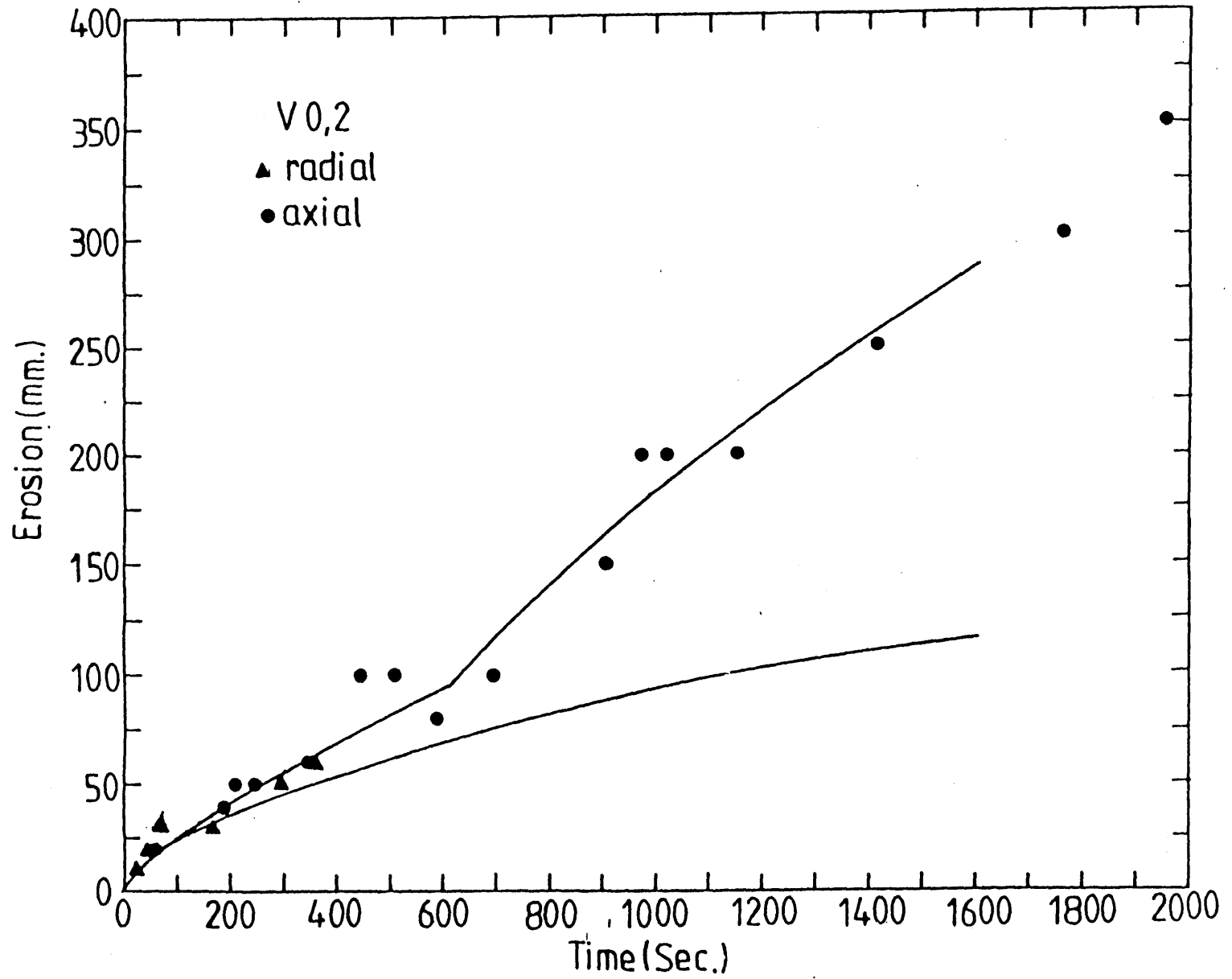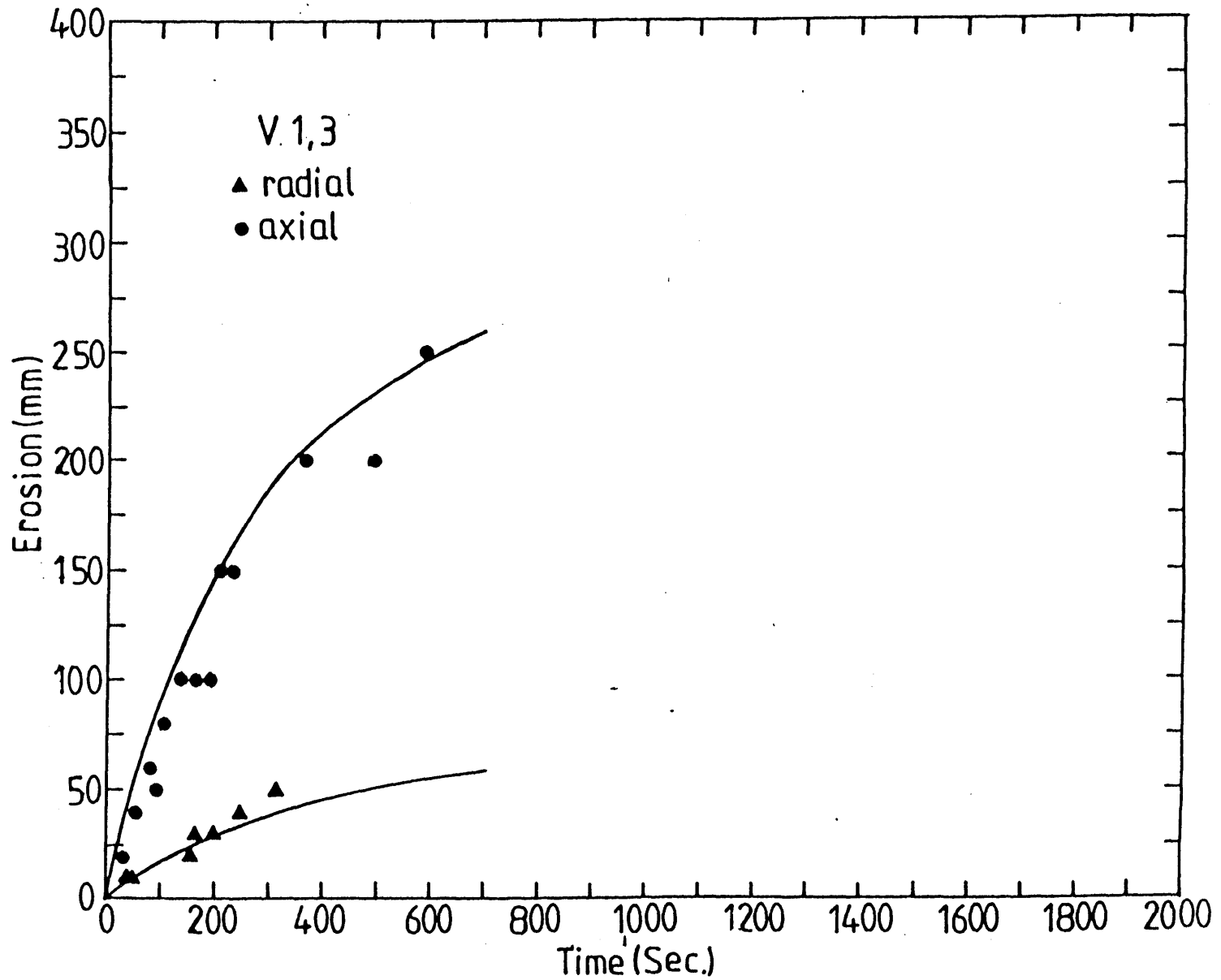
Figure 6.13   Comparison between the Predicted and Experimental Erosion Histories of BETA Test V1.3
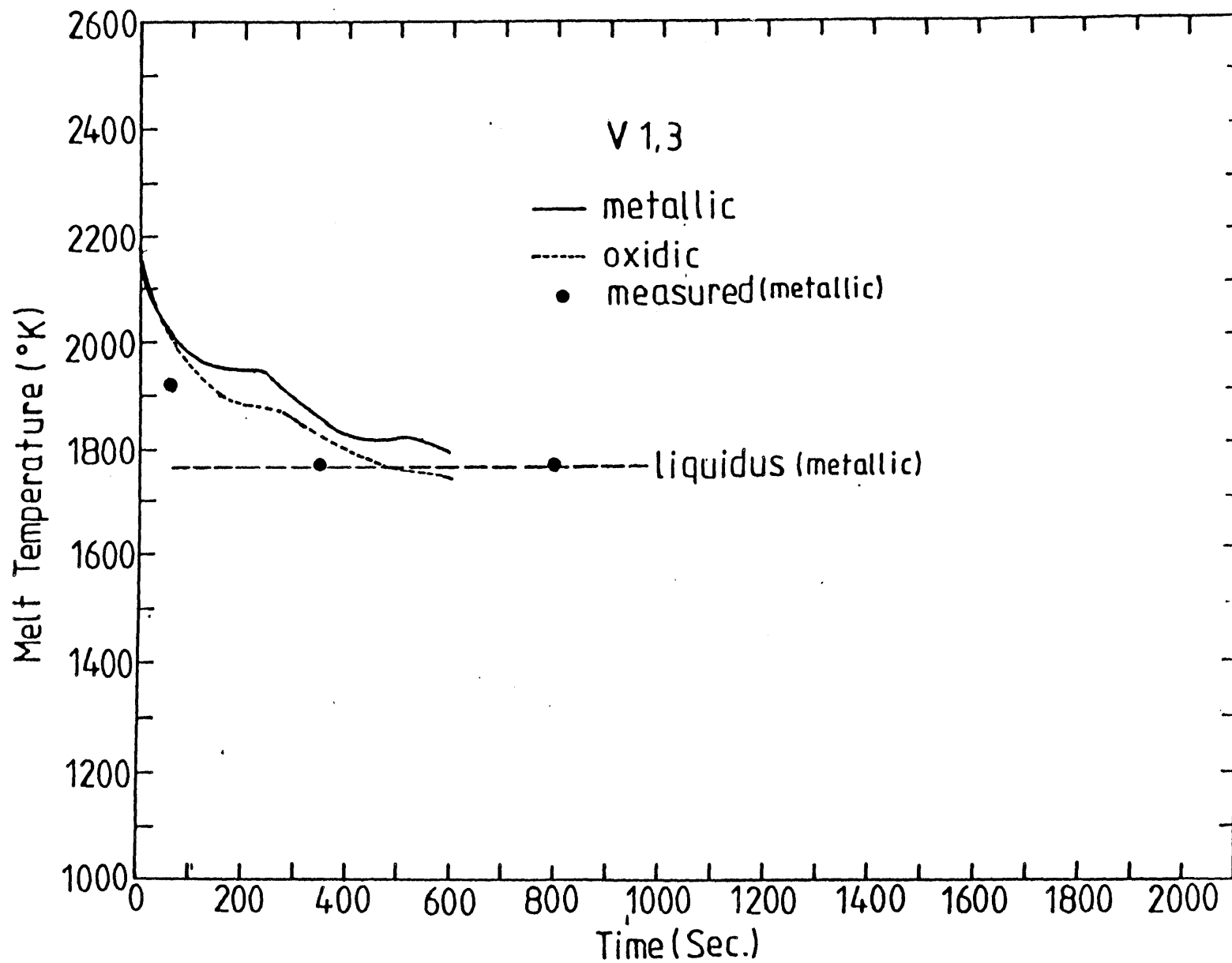
Figure 6.14   Temperature Histories of the Melt, BETA Test V1.3
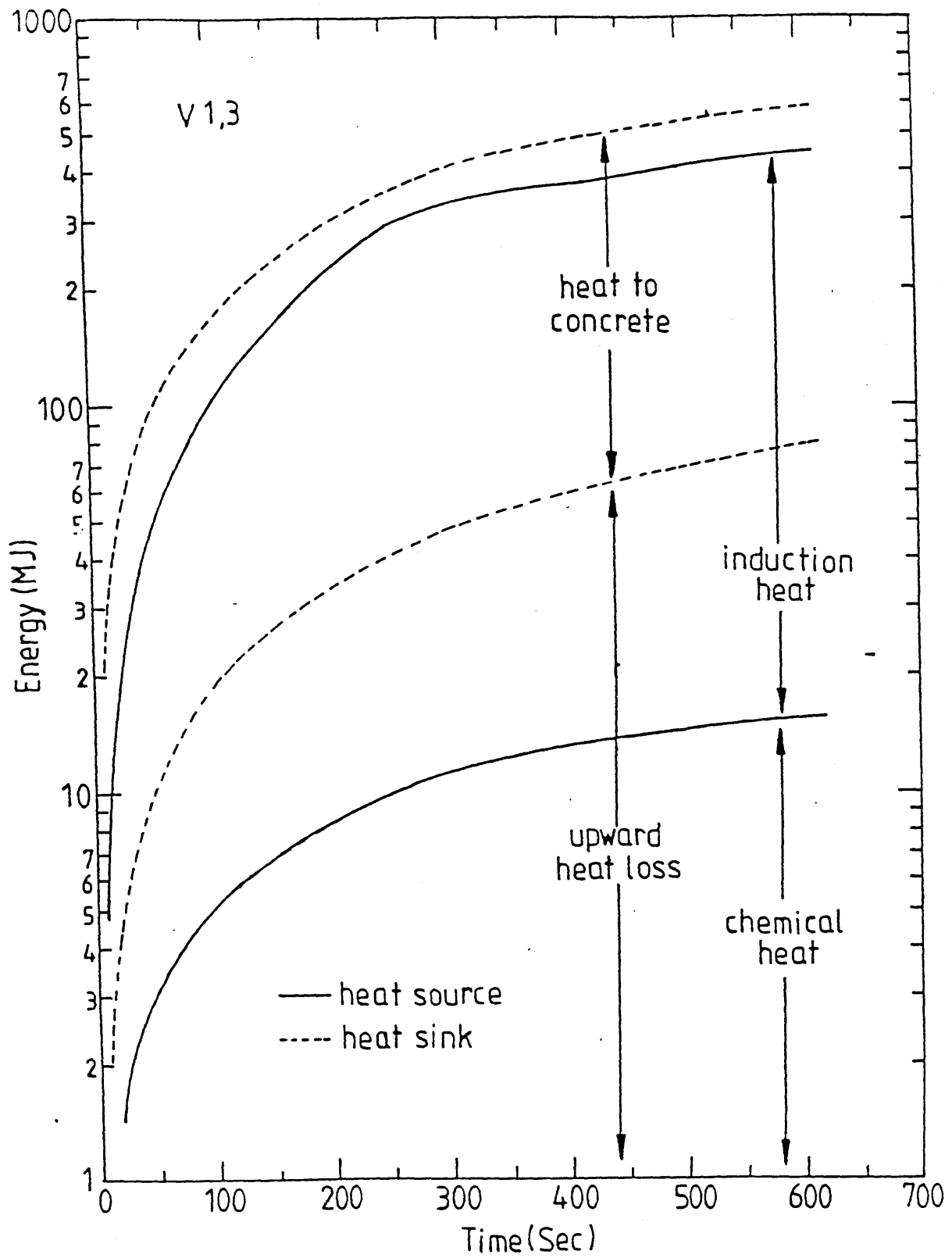
Figure 6.15 Energy Distribution of BETA Test V1.3

reaction package in the integral analysis code which is different for different computer codes.

Figure 6.15 also shows the magnitudes of various heat sources and heat sinks of test V1.3. The sensible heat of the melt and the heat carried out by the decomposed concrete gases are not shown in this figure. From Fig.6.15 it can be seen that most of the heat was consumed in ablating the concrete. A more detailed calculation shows that, in test V1.3, 77.2% of the heat went into the concrete and 12.2% was transferred to the atmosphere. The rest of the heat was carried to the atmosphere by concrete decomposed gases. For test V0.2, the one with smaller axial erosion rate, 75.3% of the heat was transferred to concrete.

The oxidation of Cr and Ni is accompanied by generation of CO and H_2 gases. Fig.6.16 shows the relative concentration of gases exiting from the melt pool. During the BETA experiments, the relative gas concentration in the off-gas line were measured by a mass spectrometer. A comparison between the experimental and calculated results can serve as a validation of the chemical reaction package used in the integral analysis code. The reduction of these experimental data is still unreported by KfK.

6.3.2 Sensitivity Analysis

Among the correction factors shown in Table 6.3, the one for the minimum stable gas film (F factor) has the highest impact on predicted results. As shown in Fig.6.17, an increase or decrease in the F factor by 25% can result in quite different erosion rates for test V0.2. With $F = 7.5$ the film collapses earlier than the Base Case at 140 sec with melt temperature around 1975 $^{\circ}K$, thus leading to overpredicted the erosion in axial direction. With $F = 4.5$, the quench limit is never reached within the time duration of the experiment, leading to underpredicted axial erosion. The value of F also has some effect on the radial erosion. From Fig.6.18, it can be seen that as F increases the radial erosion decreases.

182
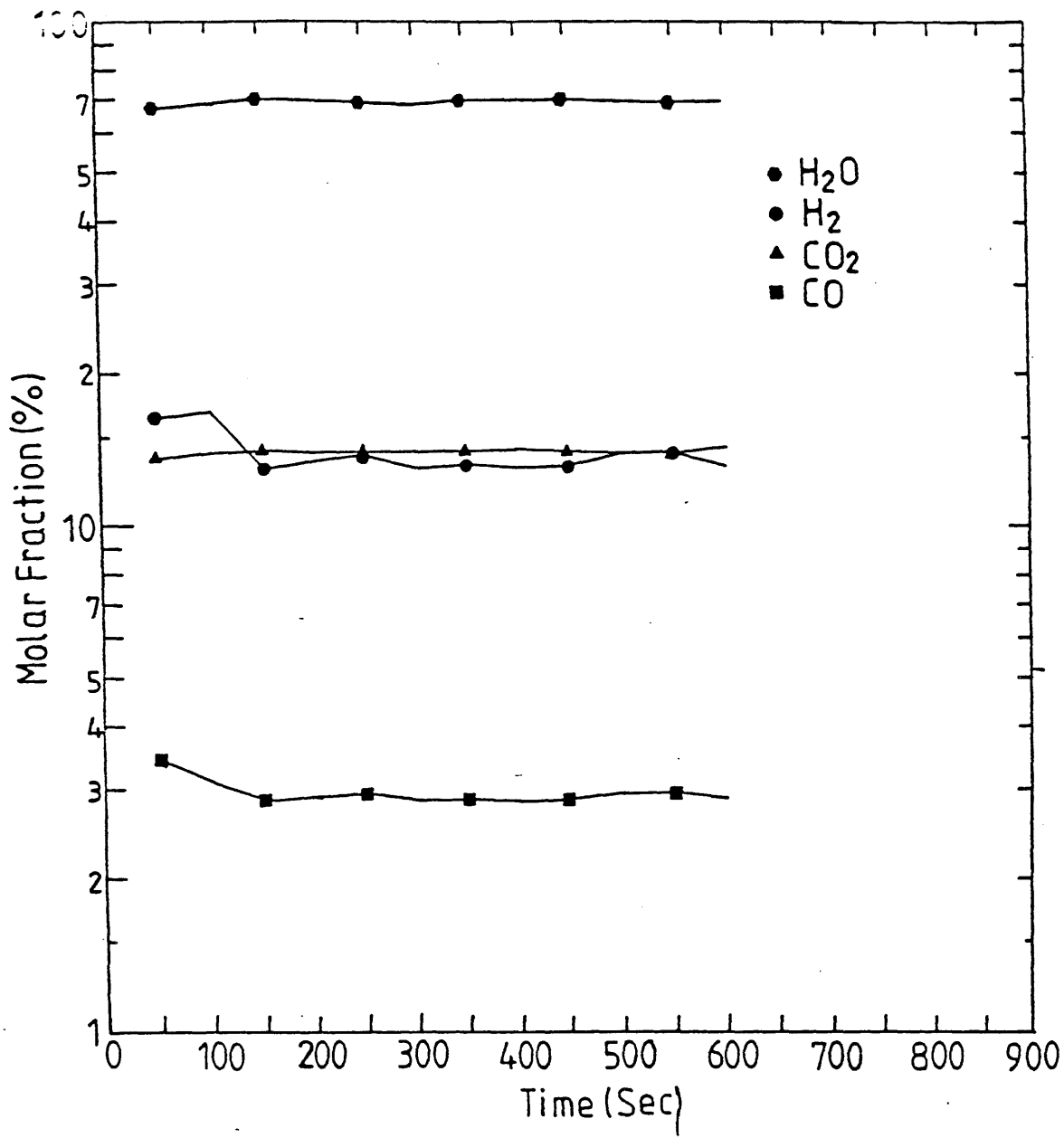
Figure 6.16   Relative Gas Concentration Exits from the Pool, BETA Test V1.3
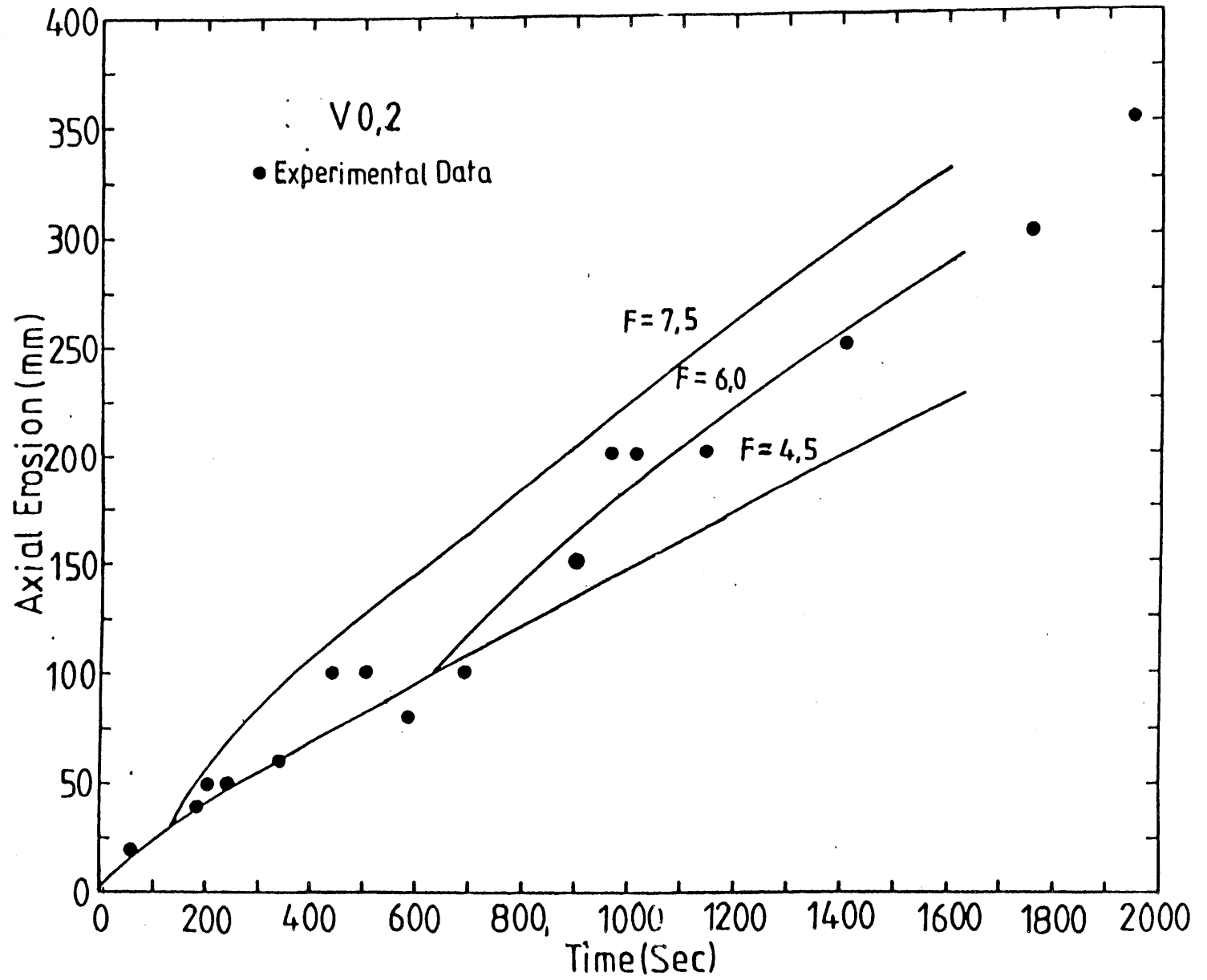
Figure 6.17   Sensitivity Studies of F Factor, BETA Test V0.2, Axial Erosion
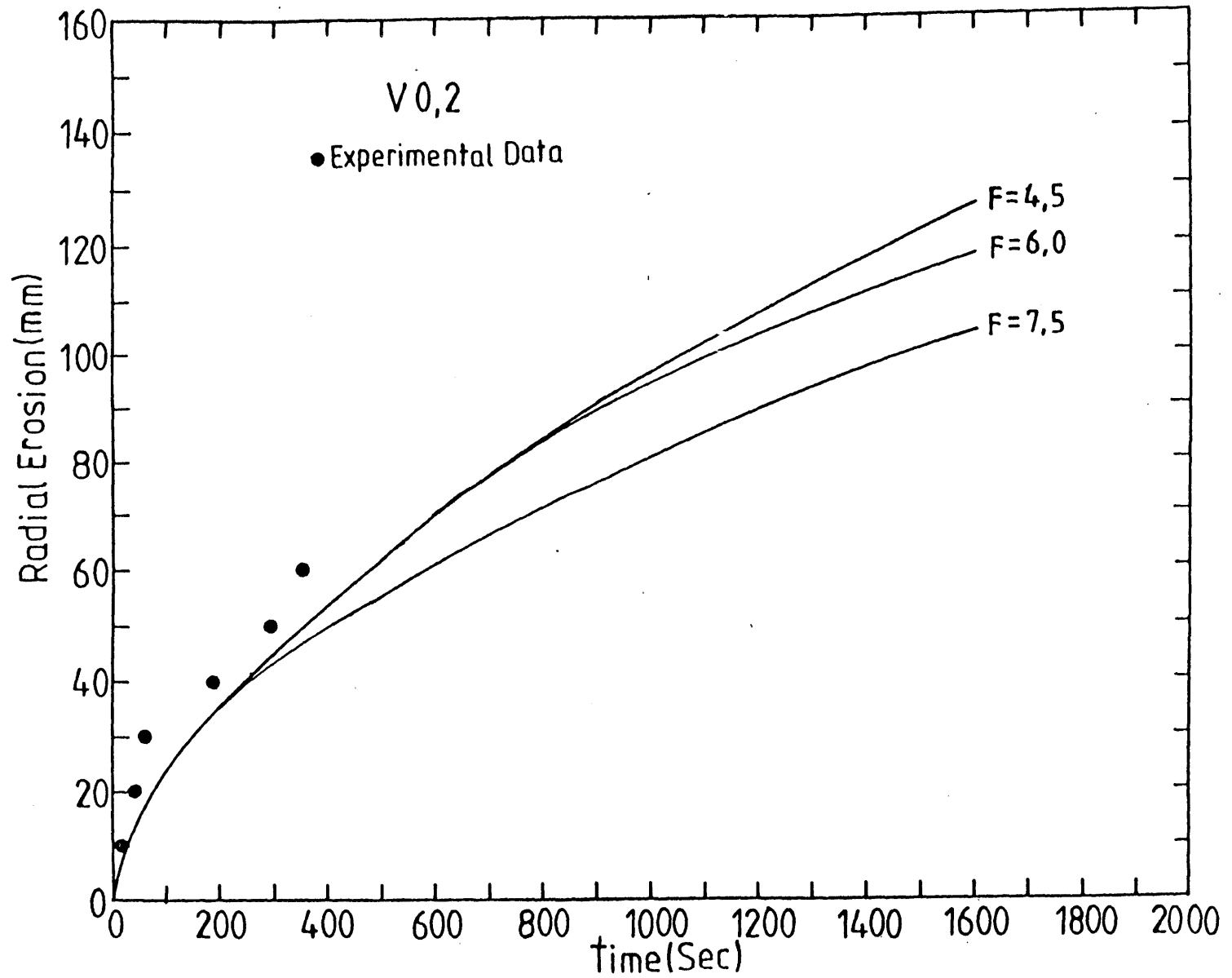
Figure 6.18   Sensitivity Studies of F Factor, BETA Test V0.2, Radial Erosion

A sensitivity study was performed on test V1.3 to determine the importance of the multipliers on the downward and interfacial heat transfer correlations. The cases analyzed are summarized in Table 6.4. and the results are shown in Fig.6.19.

From Fig.6.19 (Base Case and Case 1). it can be seen that the multiplier for the downward heat transfer correlation is important in fitting the experimental results of BETA. The sensivity study also shows that (Fig.6.19, Case 2 and Case 3) the predicted axial erosions become indifferent as the interfacial heat transfer coefficient becomes high enough. Under the condition of high interfacial heat transfer coefficients. the temperatures of the metallic and oxidic phases are almost equal and therefore have no further effects on the integral results.

The choice of 0.1 as the multiplier of the interfacial heat transfer correlation is based on the calculation of V1.2. The predicted temperature difference between the metallic and oxidic phases is comparable with the measured value by the dual dip-in thermocouples.

Figure 6.20 shows the predicted axial erosion of test V1.3 under different initial melt temperatures. A 100 $^\circ K$ difference in the initial temperature of the melt can result in approximately 10% difference in overall axial erosion. As shown in Fig.6.20. with the initial temperature 100 $^\circ K$ lower than the standard input value. the predicted results at the first 300 sec are in better agreement with experimental data.

6.4 Blind Post-test calculations of Test V1.5 and V1.6

Tests V1.5 and V1.6 were used for a blind post-test calculation in order to validate the integral anslysis code. For BETA experiments the pre-test calculation is almost impossible to make, especially for the high power test. The primary reason is that the power coupled to the melt is difficult to quantify before the experiments. The dispersal of the metallic phase into the oxidic phase can change the coupling

Table 6.4

Cases Analyzed of Test V1.3

Case No.	Multiplier for MIT Downward	Multiplier for MIT Interfacial	Initial Temperature of Melt ($^\circ K$)
Base Case	0.6	0.1	2173
Case 1	0.6	0.5	2173
Case 2	0.6	1.0	2173
Case 3	1.0	0.1	2173
Case 4	0.6	0.1	2073
Case 5	0.6	0.1	2273
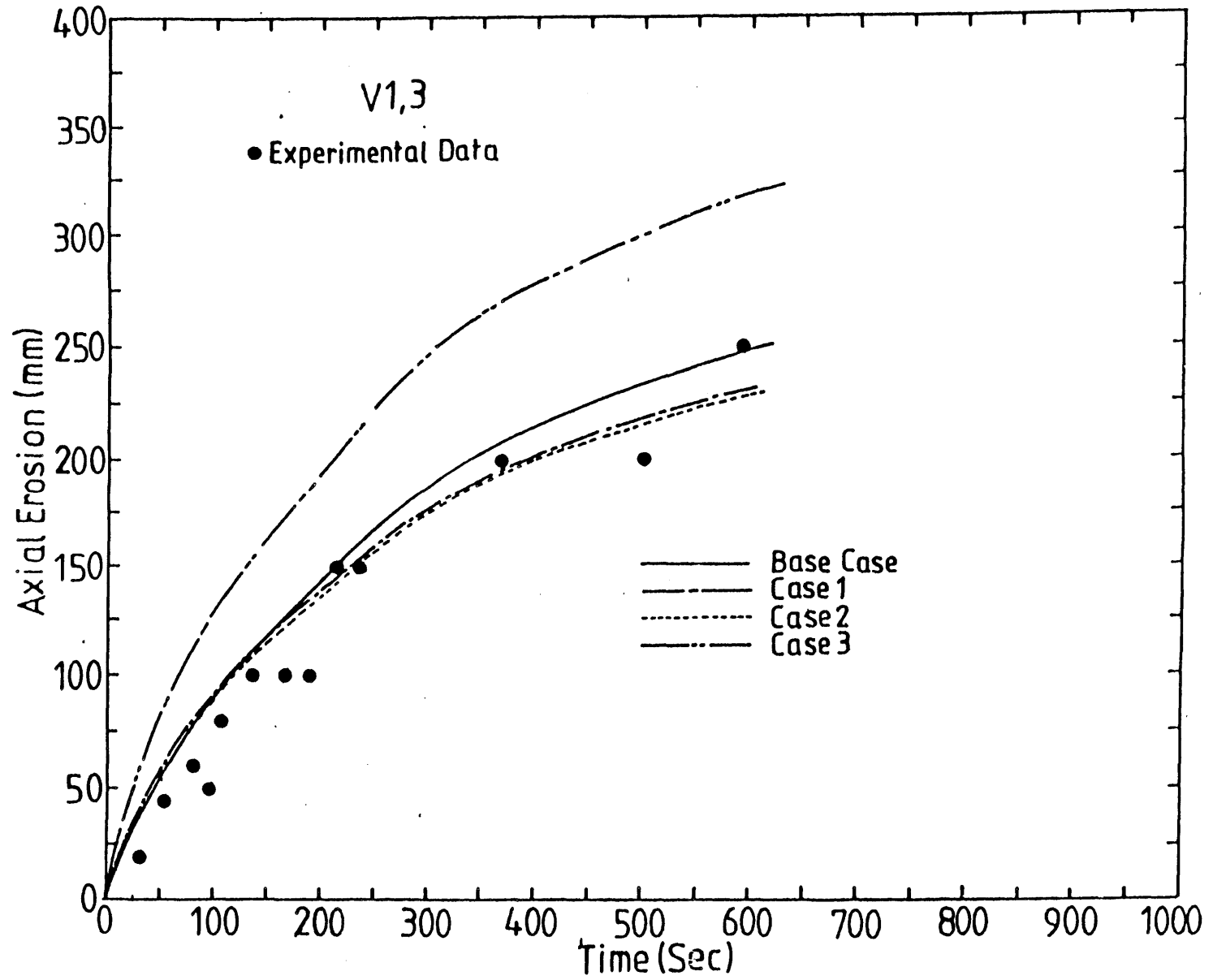
Figure 6.19   Sensitivity Studies of BETA Test V1.3 on Heat Transfer Models
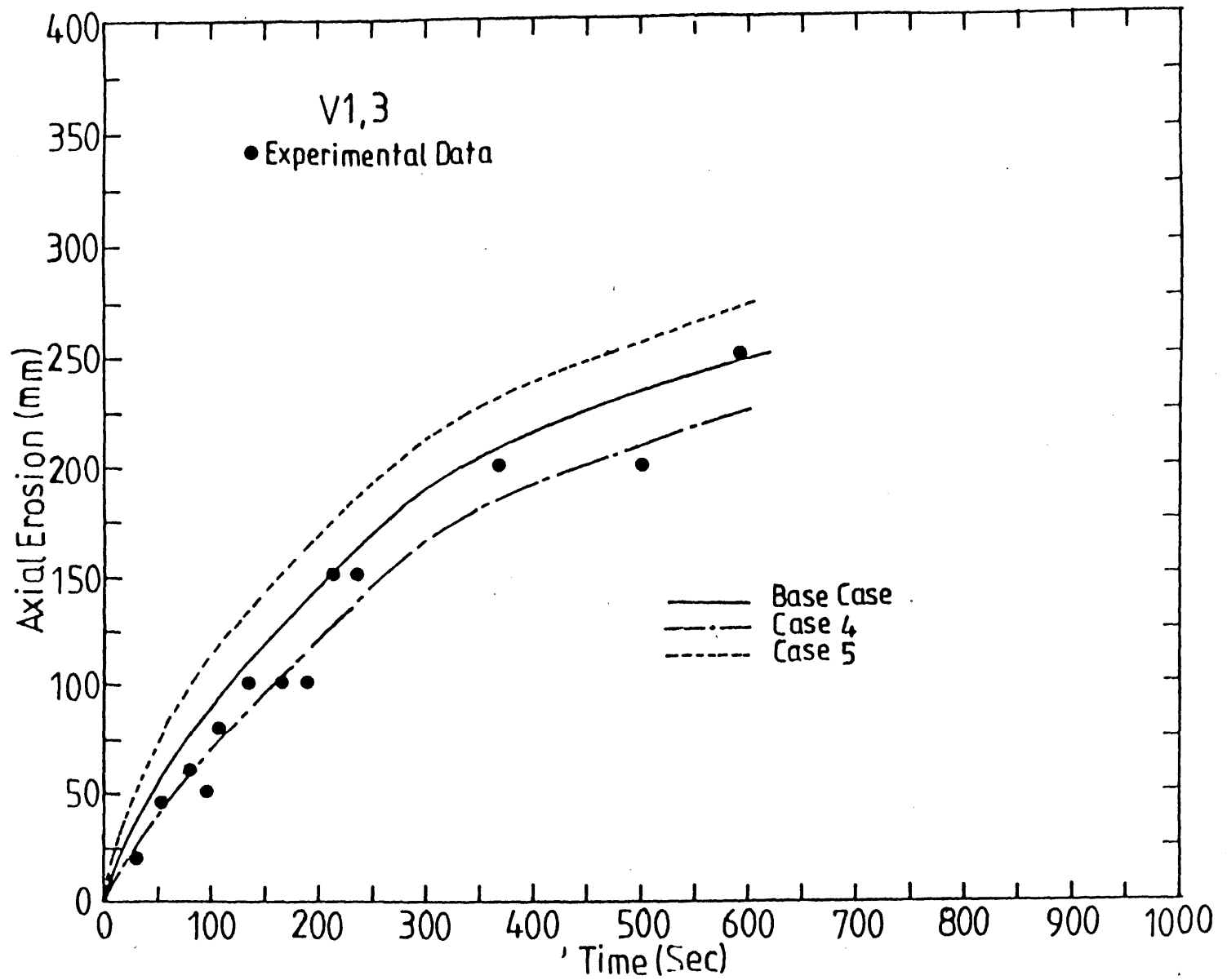
Figure 6.20 Sensitivity Studies of BETA Test V1.3 on the Initial Temperature of the Melt.

coefficient between the inductor and metallic phase, therefore, also changing the power induced to the melt. This kind of calculation may be possible if the dispersion phenomenon is correctly modeled.

As shown in Fig.6.21, the blind post-test calculation of modified CORCON/ Mod1 overpredicts the axial erosion of test V1.5 at early times and then converges to experimental results. The radial erosion is slightly underpredicted. From the trends of the experimental results of V1.5, it looks like that the interaction started with a film and then the film collapsed. A new calculation was made based on this new information. It is assumed that the initial temperature of the melt was 200 $°K$ higher than the standard input value to allow for forming a film at the horizontal melt/concrete interface. The results of this calculation are shown in Fig.6.22.

The results of the new calculation shows that the gas film collapsed at 615 sec with the melt temperature around 1900 $°K$. As shown in Fig.6.22, the new calculation gives a better prediction of radial erosion. For the first 350 sec, the predicted axial erosion fits well with the experimental data. It seems that the film collapsed earlier (around 400 sec) than that calculated by the code. This means that the melt cooled faster than that predicted by the code. This could be due to the splashing of the melt out of melt pool.

For test V1.6, as shown in Fig.6.23 the overall erosion in the axial direction is overpredicted. However, the predicted results follow the trends of the experimental data. Lowering the initial temperature of melt by 100 $°K$ gives a slightly better fit with the experimental results (Fig.6.24).

The post-test examination of the V1.6 crucible showed that (see Fig.6.25) the cavity shape was quite irregular. The maximum erosion was not in the center of the crucible where the thermocouples were located. As shown in Fig.6.25, the maximum erosion was around 500 mm. However, all the embedded thermocouples beyond 250 mm did not fail during the experiment.

190
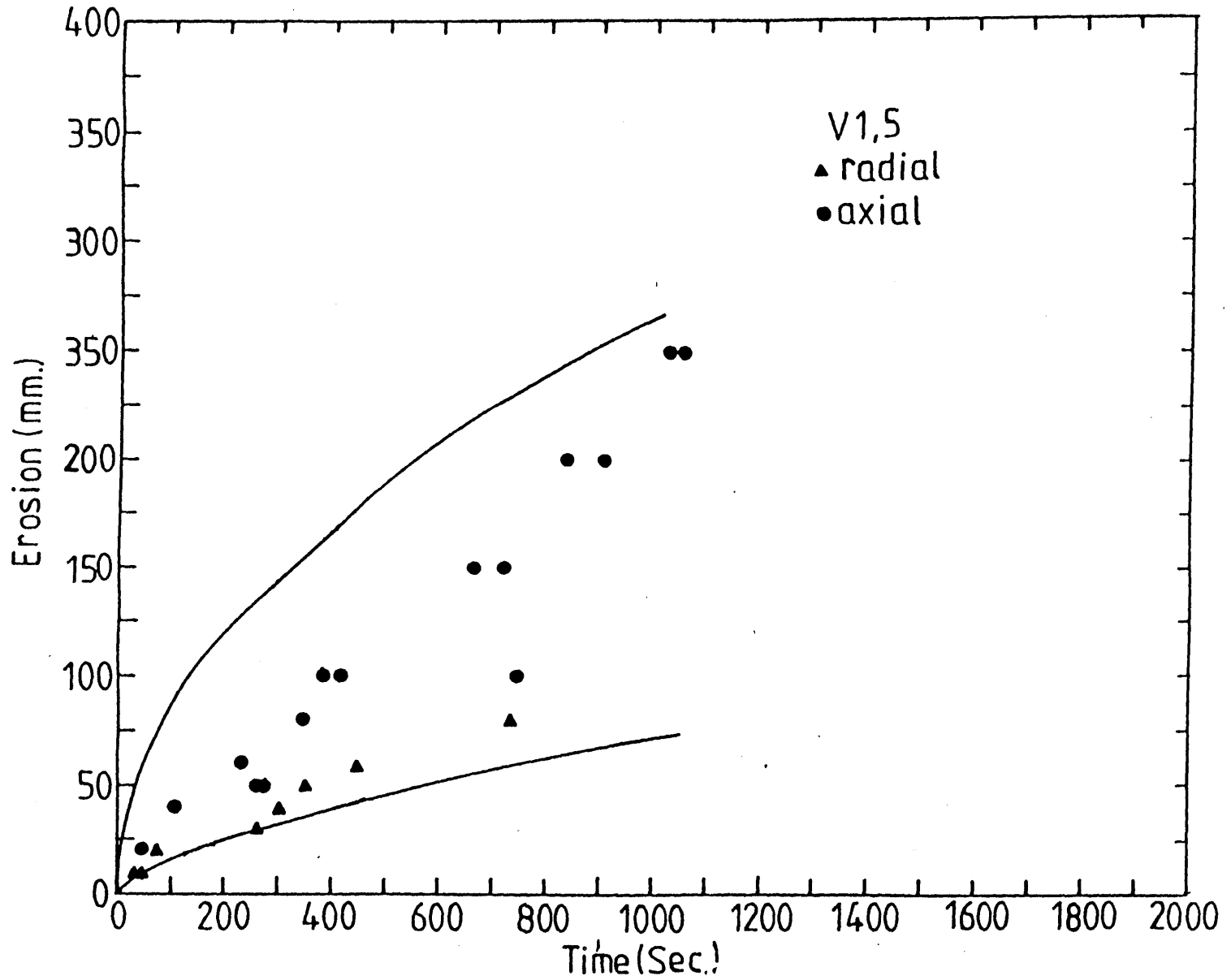
Figure 6.21   Blind Post-test Calculation of BETA Test V1.5
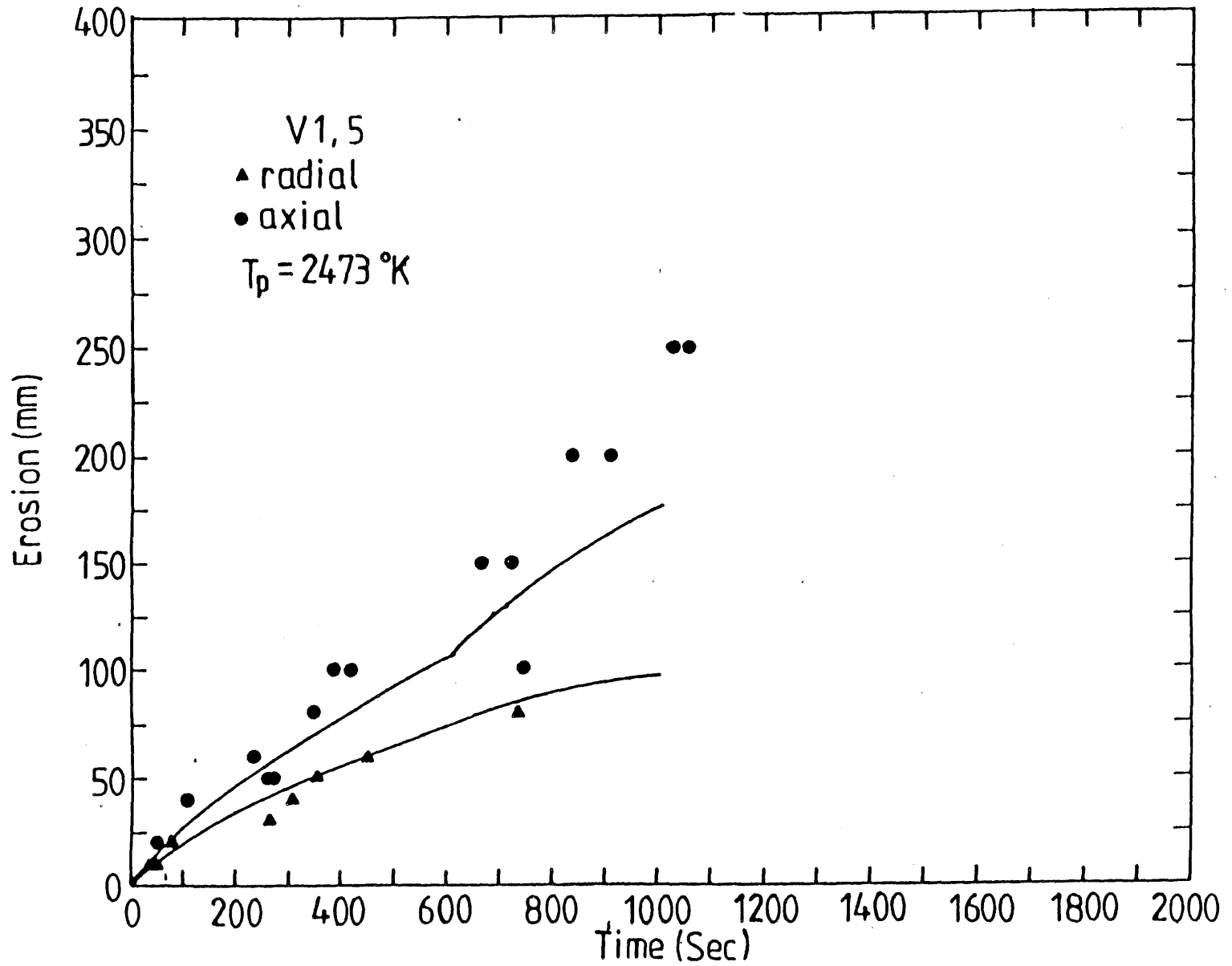
Figure 6.22   Post-test Calculation of BETA Test V1.5 (with T_p = 2473 °K)
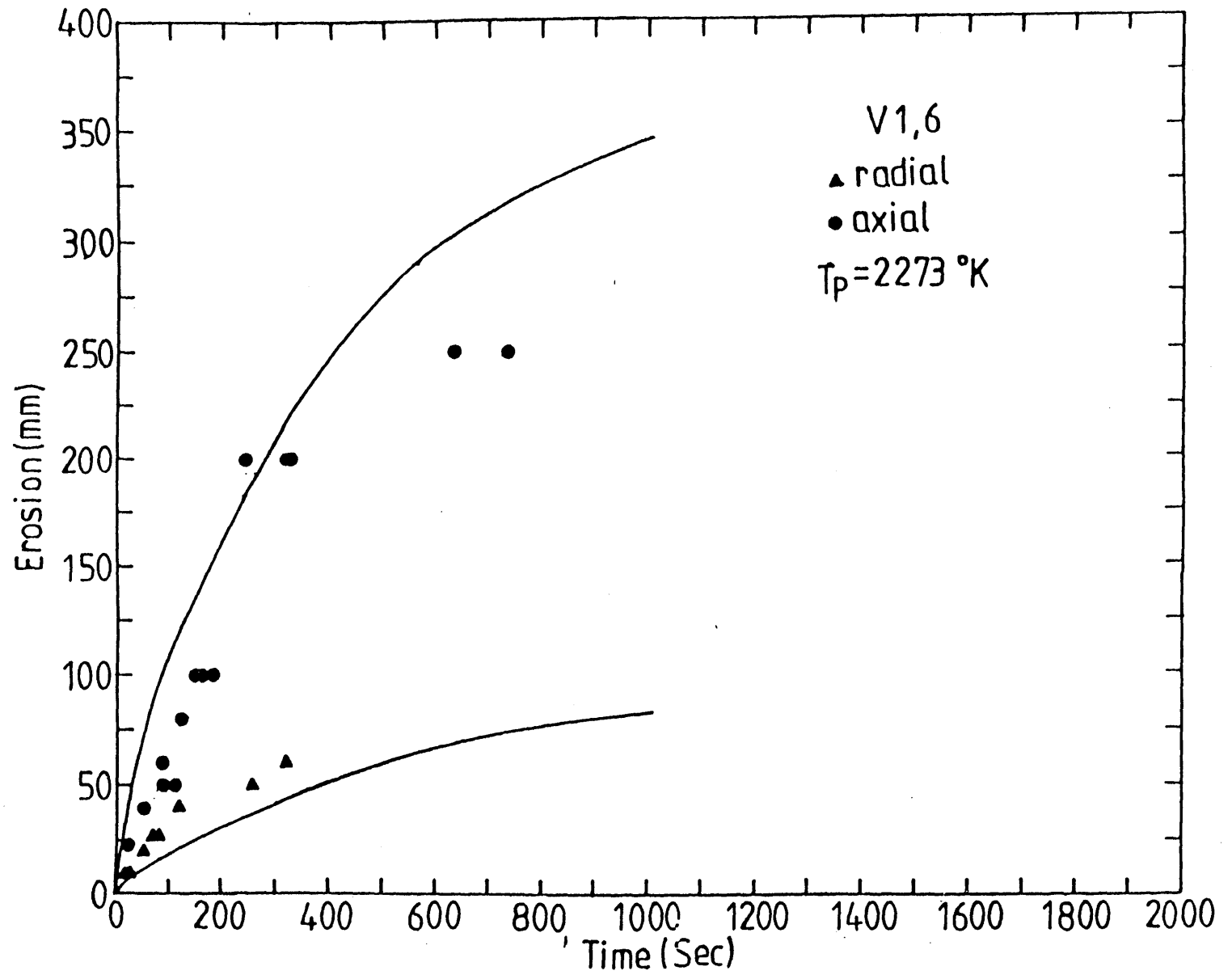
Figure 6.23   Blind Post-test Calculation of BETA test V1.6
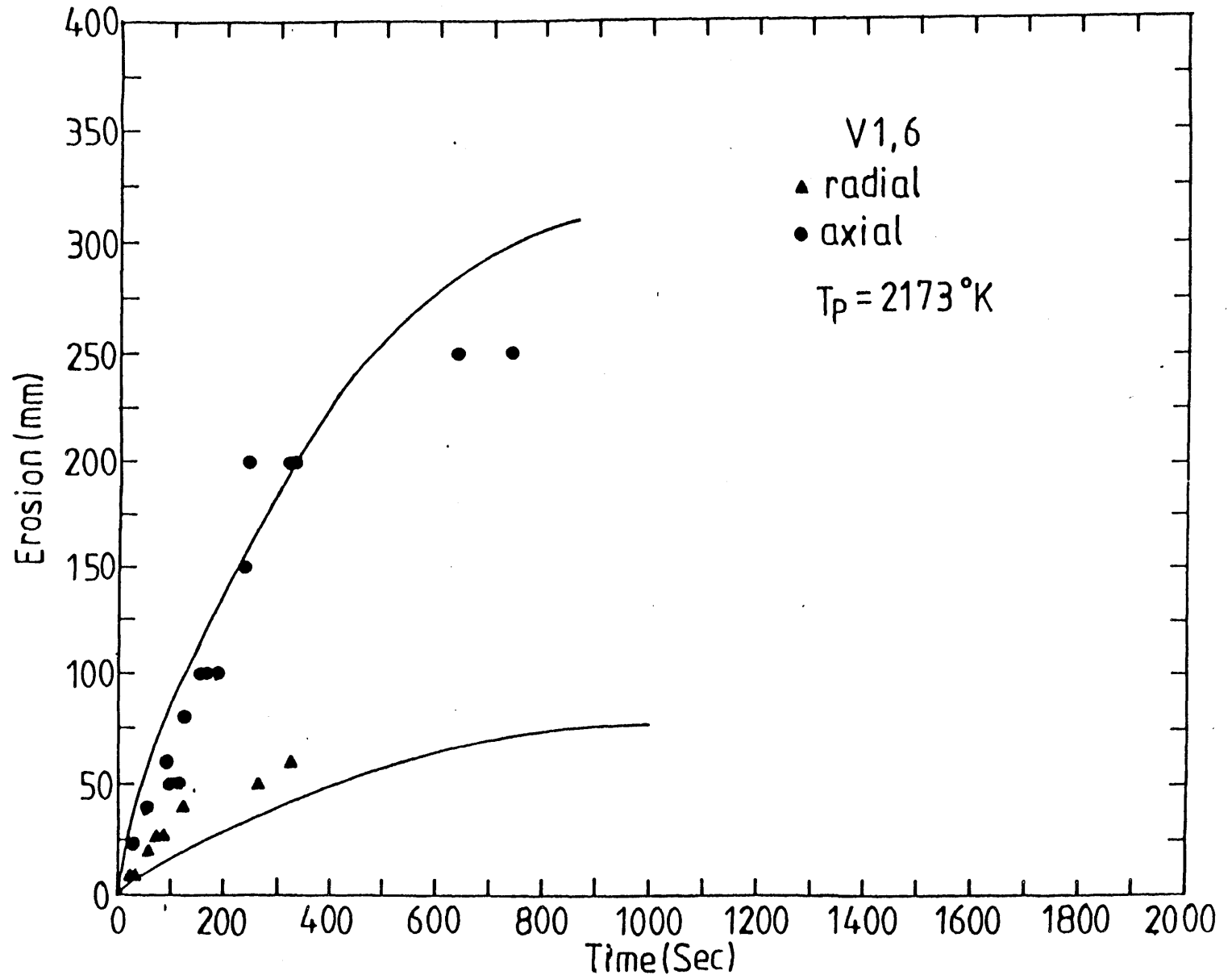
Figure 6.24   Post-test Calculation of BETA Test V1.6 (with $T_p = 2173\ °K$)
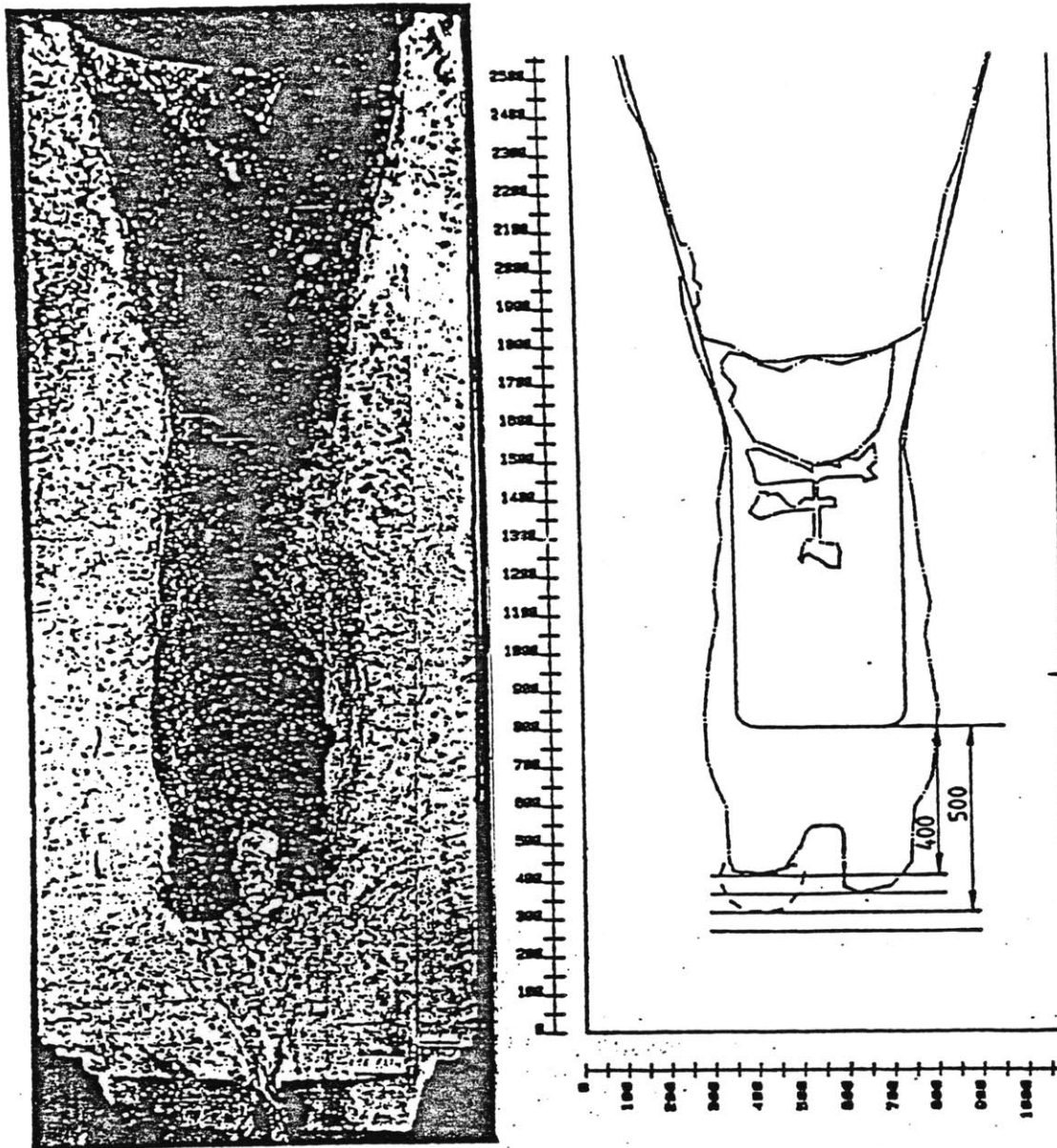
Figure 6.25   Post-test Concrete Crucible of BETA Test V1.6

6.5 Conclusions

With the modified CORCON/Mod1. the trends of the high power tests of the BETA experiments can be predicted. Accurate prediction of the collapse of the stable gas film is very important in calculating the experimental results. There is a need for predicting the entrainment phenomena at high gas velocity.

CHAPTER 7

LWR CONTAINMENT RESPONSE: THE CORCELL MODEL

7.1 Containment Model

7.1.1 Pressure Calculation

The simplified one cell containment model derived in Chapter 2 was incorporated into CORCON/Mod1 (K1). The combined model, from here on called CORCELL, considers the containment atmosphere as a single control volume. It assumes thermal equilibrium and homogenous mixture of containment water, air and gases evolved from the decomposed concrete. The ideal gas law is assumed to apply to all gases, except water vapor. The containment atmosphere is coupled to the corium pool by the heat transfer processes and the mass transfer of concrete gases. The calculations of CORCON/Mod1 provide the time dependent heat transfer and gas generation rates to the containment response model. The results of containment response model provide the temperature and pressure of containment atmosphere which are then coupled to the MCCI analysis. In CORCELL the heat can be removed from the containment atmosphere by fan coolers and by conduction into the concrete wall of the containment building. CORCELL also considers the heat capacity of the structure materials in the containment.

The status of the containment at the begining of Corium/Concrete Interaction is determined by conserving the energy between the time of scram and the start of core-concrete attack. All the Zr is assumed to have reacted prior to the start of MCCI. The heat of radioactive decay and *water-Zr* reaction are either stored in the corium pool or distributed among the constituents of the containment atmosphere. Knowing the containment status before shutdown, the amount of heat stored in

the primary cooling water and the amount of heat removed by fan coolers, along with the assumptions about the starting time of core-concrete attack and the initial corium temperature, the containment pressure and temperature at the begining of Corium/Concrete Interaction can be determined.

In this calculation, the integal decay power before the core-concrete attack is estimated by the correlations in RETRAN02 (R7).

7.1.2 Heat Conducted into the Containment Concrete Wall

The inner surface area of the containment wall is large (about 6800 m^2 for a PWR large dry containment). Therefore, over time, a significant amount of heat can be transferred through this area into the massive concrete structure, which would reduce the threat of overpressurization.

A transient heat conduction model is employed to characterize the heat flow into the concrete wall of the containment building. The analytical solution of the transient heat conduction for a semi-infinite plate, whose surface temperature is suddenly raised, can be given as:

$$\frac{T(x,t) - T_c}{T_\infty - T_c} = 1 - erf \, x^* \tag{7.1}$$

where

$x^* = x/\sqrt{\alpha t}$, normalized distance into the wall

T_c = initial temperature of containment concrete wall

T_∞ = containment atmosphere temperature, assumed equal to surface temperature of wall

α = thermal diffusivity of concrete

The total heat absorbed in the containment wall can be witten as:

198

$$Q = \rho C A \int_{0}^{L} [T(x,t) - T_c] \, dx \tag{7.2}$$

where

ρ = density of concrete

C = heat capacity of concrete

A = heat transfer area of containment inner wall

L = thickness of containment concrete wall

Substituting Eq.7.1 into Eq.7.2 gives:

$$Q = \rho C A (T_\infty - T_c)(2\sqrt{\alpha t}) I(t) \tag{7.3}$$

where the integral factor I(t) is given by:

$$I(t) = \int_{0}^{L/2\sqrt{\alpha t}} (1 - erf \, Y) dY \tag{7.4}$$

and can be approximately evaluated from tabular values of the error function. The value of error function approachs unity very quickly. As $Y = 3.5$, the $erf \, Y$ is 0.9995. Therefore, for $L/2\sqrt{\alpha t}$ greater than 3.5, the limits in the above integration can be replaced by 0 to ∞. For $L = 1.2 \, m$, it takes 15 hr for $L/2\sqrt{\alpha t}$ to be reduced to 3.5. In the following calculations, $I(t)$ is assumed to be constant and equals to 0.5632 which corresponds to integration between $Y = 0$ and $Y = \infty$.

In a discretized manner, the transient behavior of the containment atmosphere temperature may be used to obtain the total heat absorbed after n time steps as:

$$Q^{(n)} = \rho C A I \sum_{m=1}^{n} \left(T_\infty^{(m)} - T_\infty^{(m-1)} \right) \left(2\sqrt{\alpha(n-m)\Delta t} \right) \tag{7.5}$$

199

where

$$T_\infty^{(m)} = \text{containment atmosphere temperature at time step m}$$

$$T_\infty^{(0)} = \text{initial temperature of containment}$$

$$\triangle t = \text{time interval of each calculational time step}$$

7.2 Cases Analyzed

The heat transfer model described in section 5.2 was used to analyze the MCCI process in a typical plant and to characterize the impact of MCCI on containment pressure. The cases analyzed covered different types of containments, different types of concrete, the uncertainties in the modeling of MCCI and the effects of various heat sources and sinks.

A 3411 MWt PWR with large dry containment was chosen as the Base Case for this study. The assumptions and parameters used in the Base Case are summarized in Table 7.1. The shape of the reactor cavity was assumed to be cylindrical with 3.125 m radius. The initial temperature of corium and the time of first contact of corium with concrete after scram are accident sequence dependent. These parameters involve a lot of uncertainties, which can be important, therefore sensitivity studies will be performed on these parameters. The cases of sensitivity studies with different parameters from the Base Case are listed in Table 7.2.

Three different types of containments are analyzed. These are PWR large dry containment, PWR ice condenser containment and BWR supression pool containment. The principal features together with the major parameters of these containment types used in the analysis are summarized in Table 7.3. In these calculations, it is assumed that the fan coolers are partially available at a reduced efficiency so that the net effective rate of cooling is roughly 10% of the rated capacity. For the composition of different types of concrete, the default values of the physical properties in CORCON/Mod1 are used. These compositions have been summarized in Table 1.1.

200

Table 7.1

Parameters Used in the Base Case
of Containment Pressure Calculation

Containment Type	PWR large dry
Concrete	limestone/common sand
Initial Temperature of Corium	$3100\ ^\circ K$
Initiation Time of MCCI	$2\ hr$
Heat Transfer Correlations:	
Downward Heat Transfer	
Gas Film	CORCON/Mod1
Periodic Contact	MIT model with a multiplier of 0.6
Film Quench Limit	Eq.3.6 with a multiplier of 6.0
Flooding Limit	Eq.3.5 with a multiplier of 0.85
Interfacial Heat Transfer	MIT model with a multiplier of 0.1
Convective H.T.C. at Upper Pool Surface	$10\ W/m^2\,^\circ K$
Chemical Reaction Heat in Corium Pool	Yes
Chemical Reaction Heat in Atmosphere	No
Heat Conducted into the Concrete	
Wall of Containment Building	Yes

Table 7.2

Cases Analyzed in the Containment
Pressure Calculation

Case No.	Difference from Base Case
1	Base case
2	Film quench limit with F = 1.0
3	Flooding limit is infinite
4	Interfacial heat transfer uses MIT model without multiplier
5	Convective H.T.C. at upper pool surface is 100 $W/m^2 {}^\circ K$
6	Initial temperature of corium is 2800 ${}^\circ K$
7	Initation time of MCCI is 4 hr after Scram
8	Without heat conducted into concrete wall of containment building
9a	Base Case with combustion reactions heat
9b	Case 2 with combustion reactions heat
9c	Case 3 with combustion reactions heat
10	Basaltic concrete
11	PWR ice condensor containment
12	BWR supression pool containment

Table 7.3

Characteristics of Containments

Containment Types	PWR Large Dry	PWR Ice Condenser	BWR Supression Pool
Power (MWt)	3411	3411	3411
Core Size (Metric *tons* of Uranium)	86.3	86.3	120.0
Free Volume (m^3)	5.25×10^4	3.52×10^4	1.17×10^4
Primary Water (kg)	2.3386×10^5	2.3386×10^5	2.6058×10^5
Accumulator Water (kg)	1.0925×10^5	1.0925×10^5	–
Spray Water (kg)	7.0157×10^5	7.0157×10^5	7.5173×10^5
Ice (kg)	–	1.0×10^6	–
Water in Supression Pool (kg)	–	–	3.8220×10^6
Amount of Structure Acts as Passive Heat Sink (*tons*)	1800	1800	1800
Composition of Corium (*tons*)			
UO_2	97.89	97.89	137.00
ZrO_2	25.73	25.73	44.10
FeO	5.0	5.0	5.0
Fe	119.0	119.0	119.0
Ni	9.74	9.74	9.74
Cr	17.45	17.45	17.45
Fan Cooler	10% of 70 MW	–	10% of 80 MW
Containment Wall Heat Transfer Area (m^2)	6.8×10^3	5.58×10^3	2.49×10^4

7.3 Results and Discussion

7.3.1 Base Case

For a PWR large dry containment with limestone/common sand concrete the calculation shows (Fig.7.1) that the containment pressure increases monotonically from 0.302 MPa (43.9 psi) to 0.381 MPa (55.3 psi) before the corium pool has significant solidification at 1.4 hr after the initation of MCCI. Within this 1.4 hr, the temperature of the containment atmosphere increases from 389 $^\circ K$ to 395 $^\circ K$.

The calculation shows that the three layers structure assumed in the CORCON Mod1 does not last for a long time. The layer flips, i.e. the heavy oxidic layer floats up and is combined with the light oxidic layer and the metallic phase becomes the bottom layer, at 220 sec after starting the MCCI. Note that, the time of layer flipping depends on the initial density of the oxidic phase. If a large amount of ZrO_2 were in the oxidic phase initially, the density of the oxide phase would be smaller and layer flipping would occur earlier.

The temperature histories of the corium are shown in Fig.7.2. In the case of corium, the temperature of the oxidic phase is higher because the decay heat is generated within the oxidic phase. The calculation stopped when the temperature of the metallic phase reached $T_{liq} - 0.25(T_{liq} - T_{sol})$. Figure 7.3 shows the calculated temperature difference between the metallic and oxidic phases. In the first 3 $minutes$, the temperature of the oxidic phase is lower. This is because the oxidic phase is on the bottom at first ($3\sim4$ min) and cools down faster than the metallic phase. The sharp peak in Fig.7.3 results from the collapse of the gas film. This enhances the downward heat transfer, cools down the metallic phase faster and enlarges the temperature difference between the metallic and oxidic phases. After that, a temperature difference around 40 to 50 $^\circ K$ is established between these two phases. The temperature difference between these two phases becomes smaller as the temperature of the metallic phase reaches its liquidus point. From this point on, the metallic phase

204
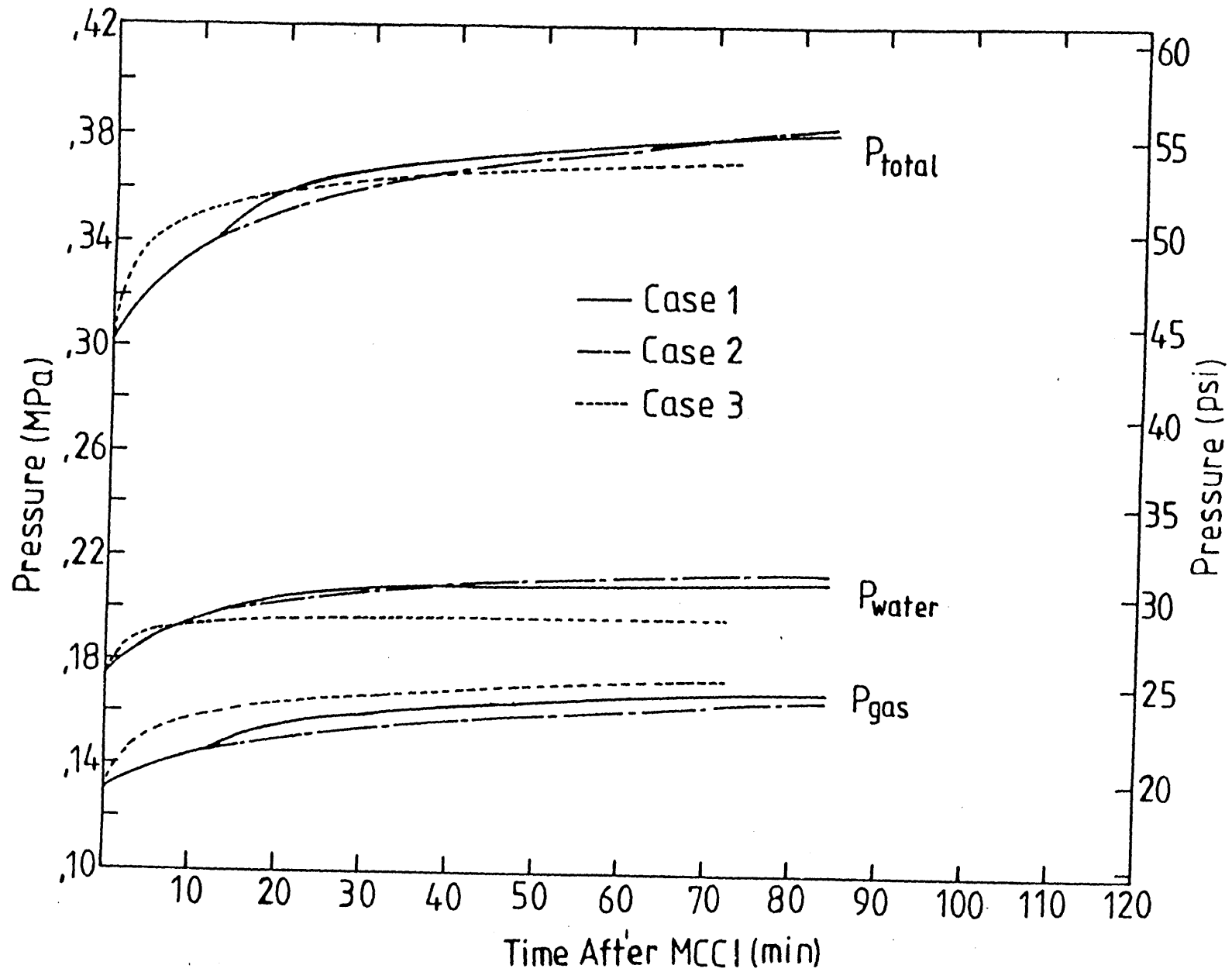
Figure 7.1   Containment Pressure Responses of Case 1, Case 2 and Case 3
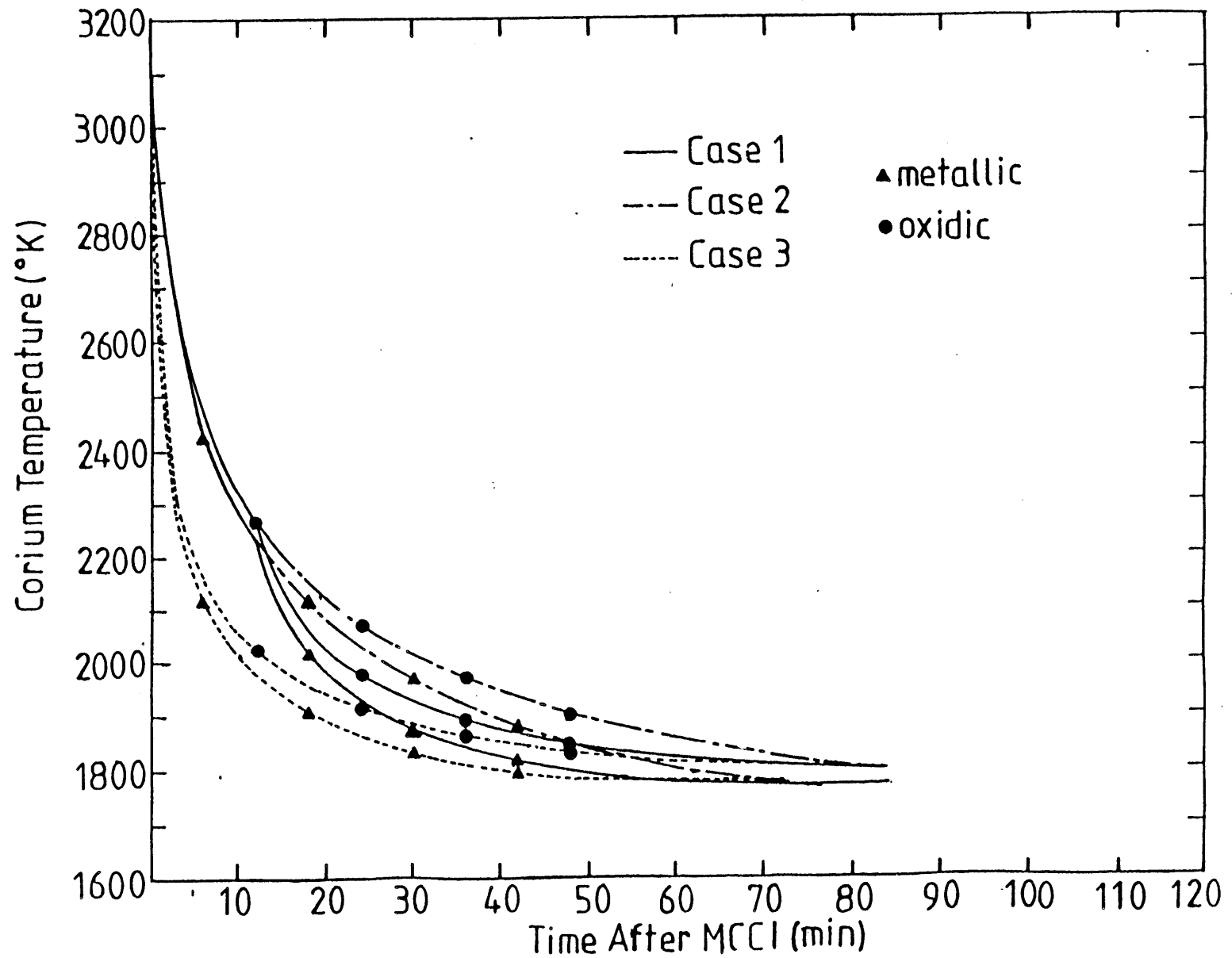
Figure 7.2 Corium Temperature Histories of Case 1, Case 2 and Case 3
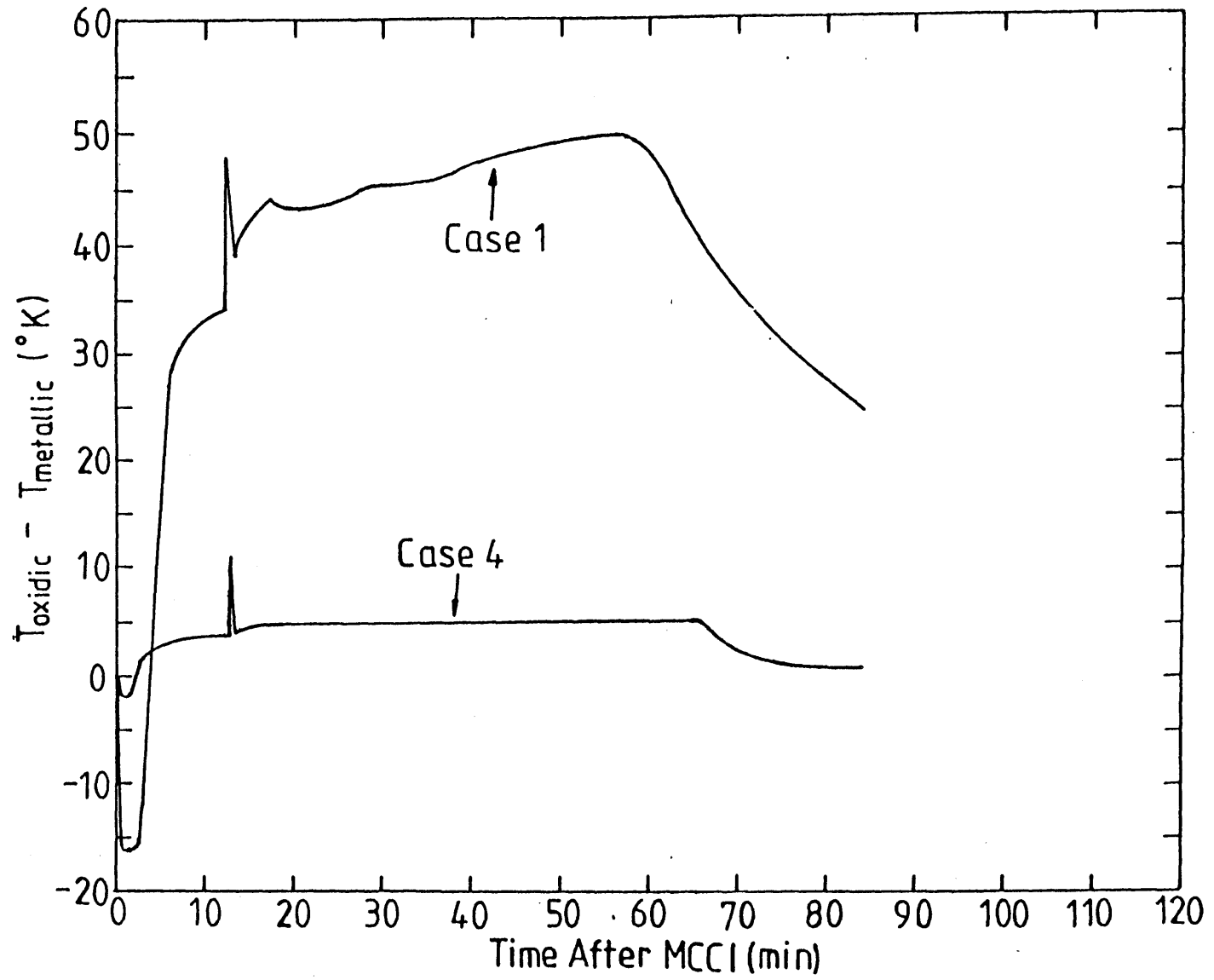
Figure 7.3 Temperature Difference between Oxidic and Metallic Phases of Case 1 and Case 4

begins to liberate its latent heat of fusion. This occurs at about 1 *hr* after MCCI begins.

The calculation predicts that until solidification starts the overall concrete erosion in the axial direction is about 0.5 times higher than that in the radial direction. As shown in Fig.7.4, the initial ablation is higher in the radial direction. After gas film collapses. the axial erosion exceeds the radial erosion. The calculated cavity shape is shown in Fig.7.5.

In this calculation. the film collapses at 730 *sec* after the start of MCCI with the temperature of the metallic phase around 2230 $^\circ K$. This is higher than that of BETA experiments. This is because the system pressure in this calculation is 1~2 times higher than that in BETA experiments. In the present modeling. the stability of the film depends on the superficial velocity of the concrete decomposed gas. With a specified type of concrete and fixed erosion rate. the superficial velocity of concrete gas is inversely proportional to the gas density.

Figure 7.6 shows the various accumulated energies involved in the containment pressure calculation of the Base Case. It can be seen that: (1) Most (62.8%) of the heat generated in the corium pool is consumed by the concrete ablation, (2) The heat transferred directly into the containment from the corium pool has the same order of magnitude as that conducted into the containment concrete wall (24.5%). (3) A significant amount of heat (12.6%) is brought up by the concrete decomposed gas into the containment atmosphere, (4) At the beginning of the MCCI. the generation rate of chemical reaction heat (between H_2O, CO_2 and metal) has the same magnitude as that of decay heat. However, the chemical reaction heat decreases as time proceeds. This is because of the decreasing concrete erosion rate and therefore the gas generation rate.

In the base case. it is assumed that the fan coolers are operated at 10% efficiency. Over the 1.4 *hr* of MCCI. 10.8% of the heat transferred into the containment
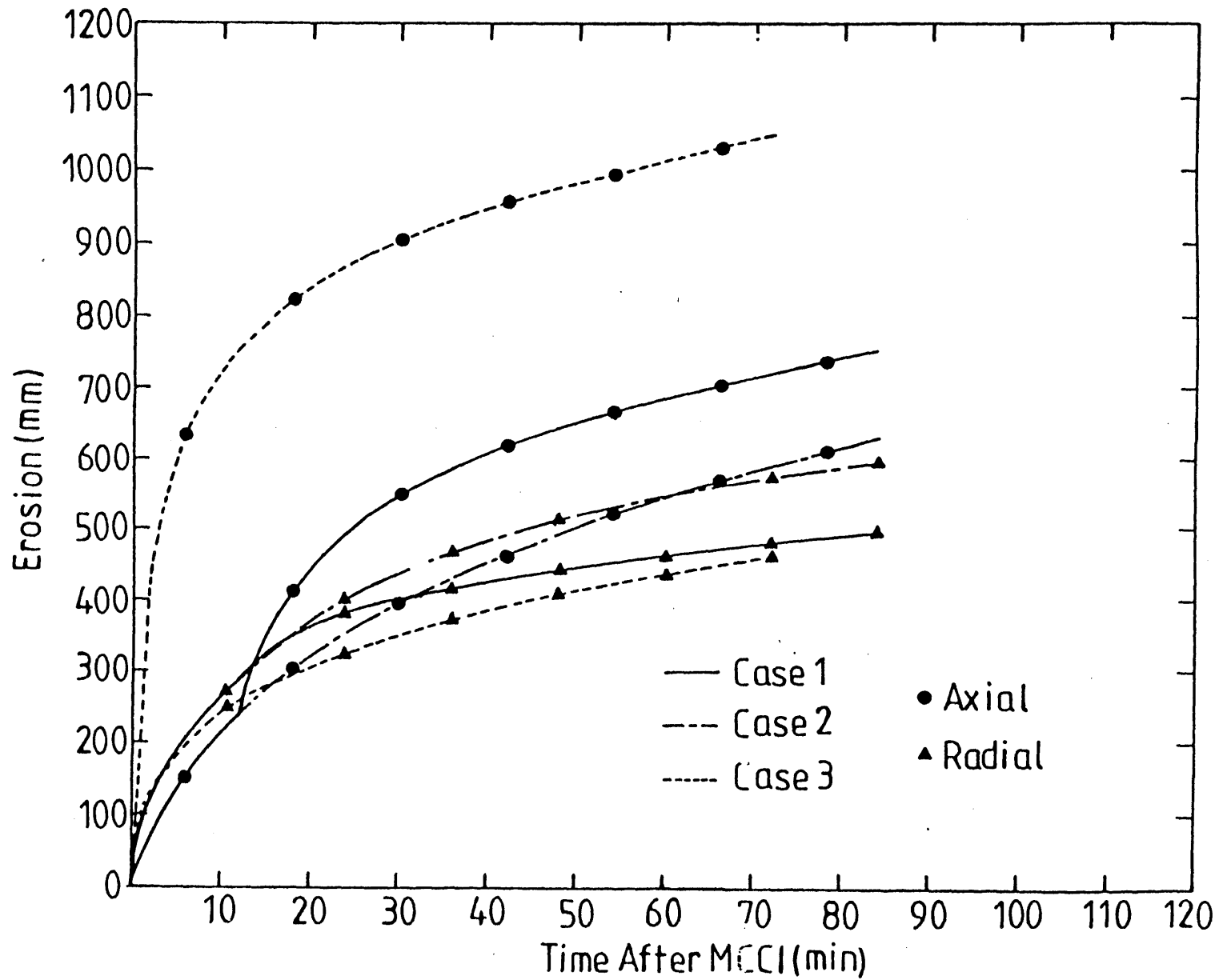
Figure 7.4   Concrete Erosion Histories of Case 1, Case 2 and Case 3

TIME STEP = 200.0 S

SCALE, CM $\times 10^{1}$
0.00   10.00   20.00
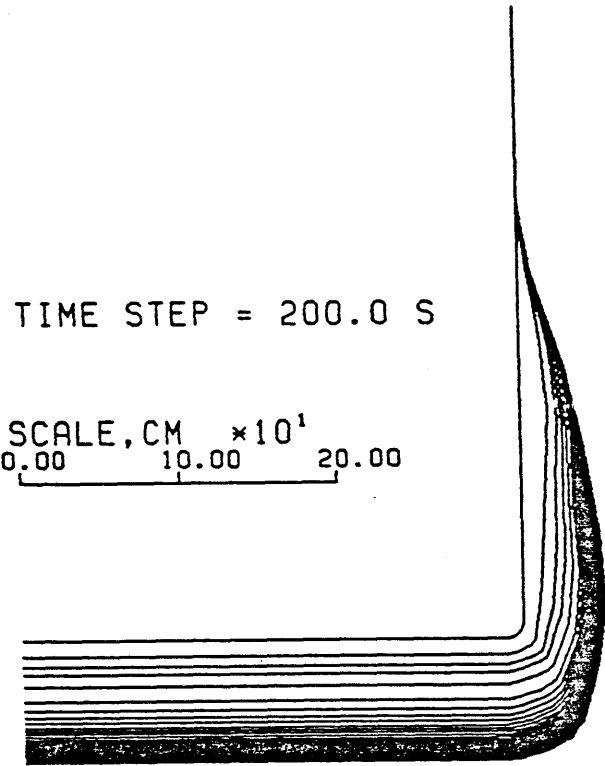
Figure 7.5 Predicted Reactor Cavity Shape of Base Case (Case 1)
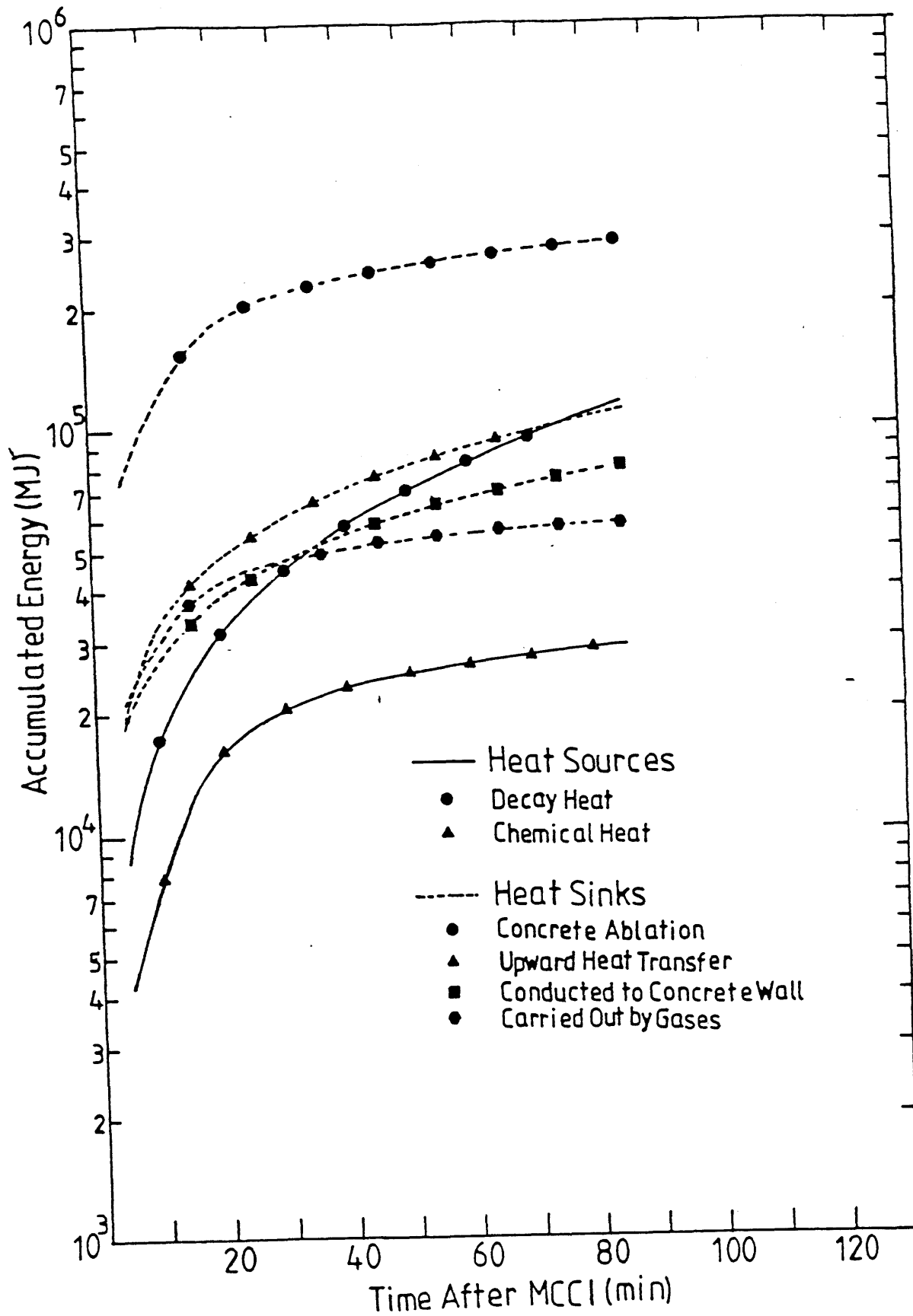
Figure 7.6   Energy Distribution of Base Case (Case 1)

211

atmosphere is removed by the fan coolers and 47.6% of these heat is conducted into the concrete wall of the containment building.

7.3.2 Sensitivity Studies

The following summarizes the results of the sensitivity studies.

7.3.2.1 The Downward Heat Transfer Model

One of the major findings of BETA experiments is that the heat generated in a high temperature melt is transferred out of pool dominantly in the axial downward direction. In the present modeling. the same effect is achieved by allowing the gas film at the horizontal interface to collapse at relatively high superficial gas velocity of concrete decomposed gas. As stated in Section 5.3.3 the film quench limit is important in reproducing the BETA experimental results. The impact of the film quench limit on containment pressurization will be studied here.

Three cases are analyzed. In the Base Case the film is assumed to quench at a superficial velocity 6 times that predicted by Berenson's minimum stable gas film criterion. In Case 2, the film is not allowed to collapse, the downward heat transfer mechanism is pseudo film boiling all the time. In Case 3 the film is not even allowed to form. the downward heat transfer is governed by the periodic contact between the corium and concrete (pseudo nucleate boiling. MIT model) from the beginning of MCCl.

The results of containment pressure response. corium temperature and overall concrete erosions of these results are shown in Figs.7.1. 7.2 and 7.4 respectively. As shown in Fig.7.1. there is no significant difference in containment pressure among these three cases. Among these. Case 2 is the highest one and Case 3 is the lowest one. the difference between these two is less than 2.5%. The total pressure for Case 3 is higher initially due to the large amount of heat carried into the containment atmosphere by the concrete decomposed gas.

212

From Fig.7.2. it can be seen that the corium of Case 3 cools down significantly faster than the other two cases initially. However, they all approach the solidification point approximately about the same time. The liquidus and solidus temperatures of metallic phase for these three cases are slightly different because of the degree of chemical reactions involved in each case.

As shown in Fig.7.4. for Case 3 the erosion is predominantly downward due to the more effective downward heat transfer mechanism. For Case 2, the radial and axial erosions are about equal. Compared with that of Base Case, the amount of heat consumed in ablating the concrete is 12.8% higher in Case 3 and 7.1% lower in Case 2. It is important to point out that the total amount of heat generated in the corium pool of these three cases are different. Among these, Case 3 has the largest amount of gas generation and, therefore, has the highest amount of chemical reaction heat.

The numerical values of some major variables in these calculations at 1 hr after MCCI begins are summarized in Table 7.4 for comparison.

7.3.2.2 Interfacial and Upawrd Heat Transfer

In Case 4, the interfacial heat transfer coefficient of the Base Case is raised by one order of magnitude. However, the predicted pressure is not significantly different from that of the Base Case. (Fig.6.7, Case 1 and Case 4). Compared with that of Base Case. the overall concrete erosions in the axial direction is decreased by 5.2%.

In Case 5, the convective heat transfer coefficient at the pool upper surface is raised by one order of magnitude. This situation is like having a coolant layer on top of the corium pool. Again. the difference in the total pressure from the Base Case is insignificant: less than 3%. Compared with the Base Case, the overall concrete erosions in the axial and radial directions are decreased by 2.7% and 3.7% respectively.

The magnitude of the interfacial and upward heat transfer coefficients may not

Table 7.4

Summarization of Results of

Case 1, Case 2 and Case 3*

	Case 1	Case 2	Case 3
Pressure, MPa (psi)			
Gas	0.166(24.12)	0.162(23.54)	0.172(25.00)
Water Vapor	0.210(30.48)	0.213(30.97)	0.197(28.54)
Total	0.376(54.60)	0.376(54.52)	0.369(53.54)
Energy Distribution, MJ			
Carried out by gases	5.526×10^4	5.225×10^4	5.789×10^4
Transferred out of Pool	9.057×10^4	9.873×10^4	6.669×10^4
Concrete Ablation	2.653×10^5	2.410×10^5	2.987×10^5
Chemical in the Pool	2.626×10^4	2.049×10^4	3.591×10^4
Temperature, $^\circ K$			
Metallic	1777.3	1807.9	1781.7
Oxidic	1826.4	1861.7	1818.8
Liquidus of Metallic	1777.3	1776.2	1783.3
Solidus of Metallic	1767.3	1766.2	1772.3
Accumulated Gases (moles)			
H_2	1.153×10^5	9.116×10^4	1.610×10^5
CO	2.214×10^5	1.765×10^5	3.187×10^5
CO_2	2.380×10^5	2.414×10^5	1.940×10^5
H_2O	1.330×10^5	1.346×10^5	1.132×10^5
total	7.075×10^5	6.437×10^5	7.869×10^5

* 1 hr after initiation of MCCI
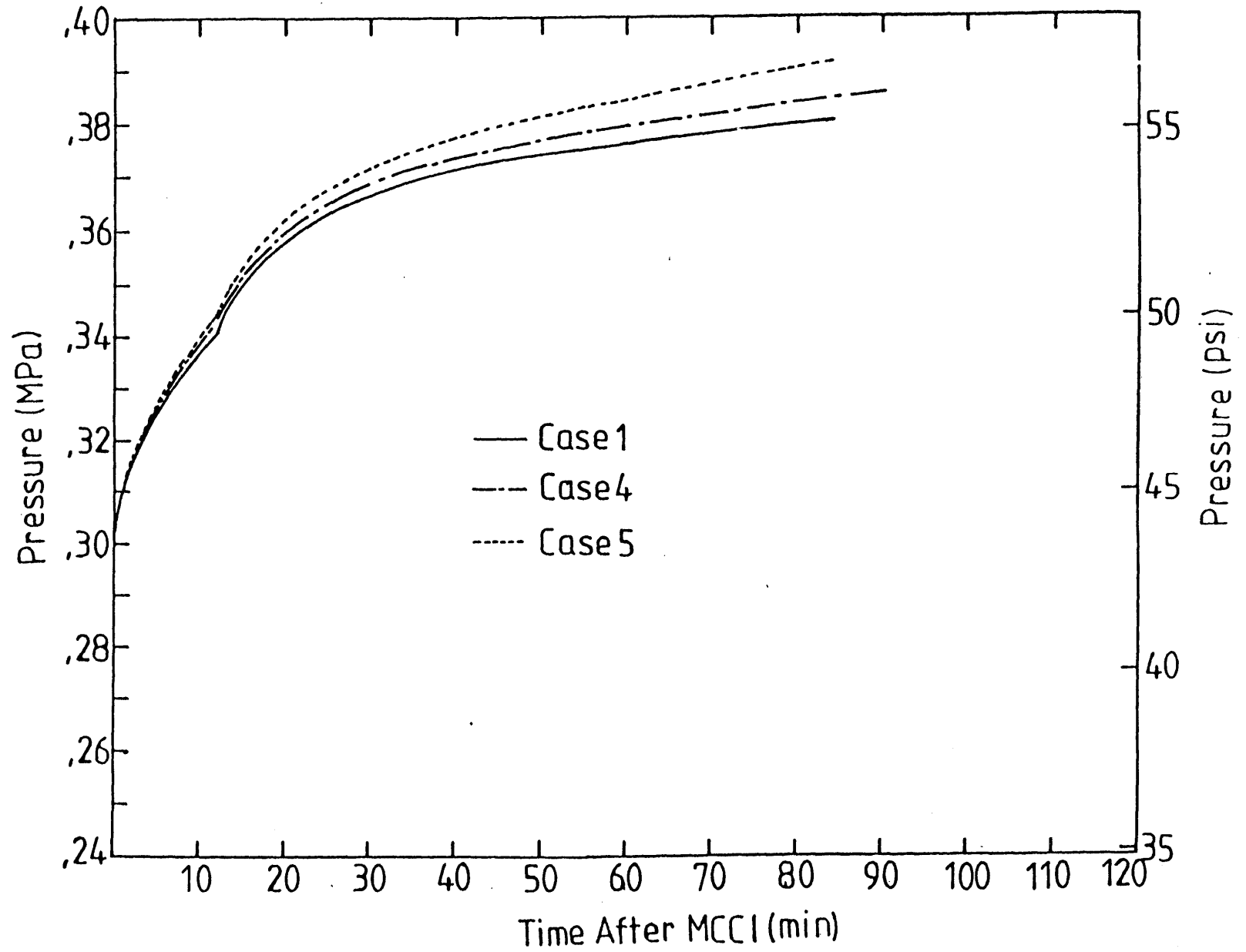
Figure 7.7   Containment Pressure Responses of Case 1, Case 4 and Case 5

have a major effect on the containment pressure response. But different values of the heat transfer coefficients can change the temperature profile of the corium pool (as shown in Fig.7.3) and might have some effect on the freezing characteristics of the debris pool and on the behavior of aerosol release. As shown in Fig.7.3. the calculated temperature difference between the metallic and oxidic phases in Case 4 is only few degrees.

7.3.2.3 Initial Temperature of Corium and the Initiation Time of MCCI

The impact of initial temperature of corium on containment pressure is investigated in Case 6. In this case. the initial temperature of corium is assumed to be 300 $^\circ K$ lower than that of the Base Case.

The calculation of Case 6 shows that the film collapses at 540 sec after MCCI begins. with the metallic temperature around 2252 $^\circ K$ which is not significantly different from the Base Case. It is also found that the temperature of metallic phase reachs the liquidus temperature at about the same time as that of the Base Case. For the results of concrete erosion, the axial erosion in Case 6 is 4.4% lower than that of Base Case. However, the erosion in the radial direction in Case 6 is decreased by 26.8%. The total amount of concrete ablated is decreased by 14.6%.

The predicted pressure response of Case 6 is shown in Fig.7.8. The initial pressure of this case is higher than that of the Base Case. This is because the stored heat of corium is less and. therefore. the internal energy of the constituents of the containment atmosphere is higher in Case 6. As shown in Fig.7.8. the pressure responses of Case 6 and the Base Case approaching each other. The pressure difference at 1.4 hr after the initation of MCCI is around 0.017 MPa (2.5 psi). For the Base Case, the total pressure increase over the first 1.4 hr of MCCI is 0.079 MPa (11.47 psi). For that of Case 6. the total pressure increase is 0.057 MPa (8.33 psi).

In Case 7. the starting time of MCCI is assumed to be 2 hr later than that of

216
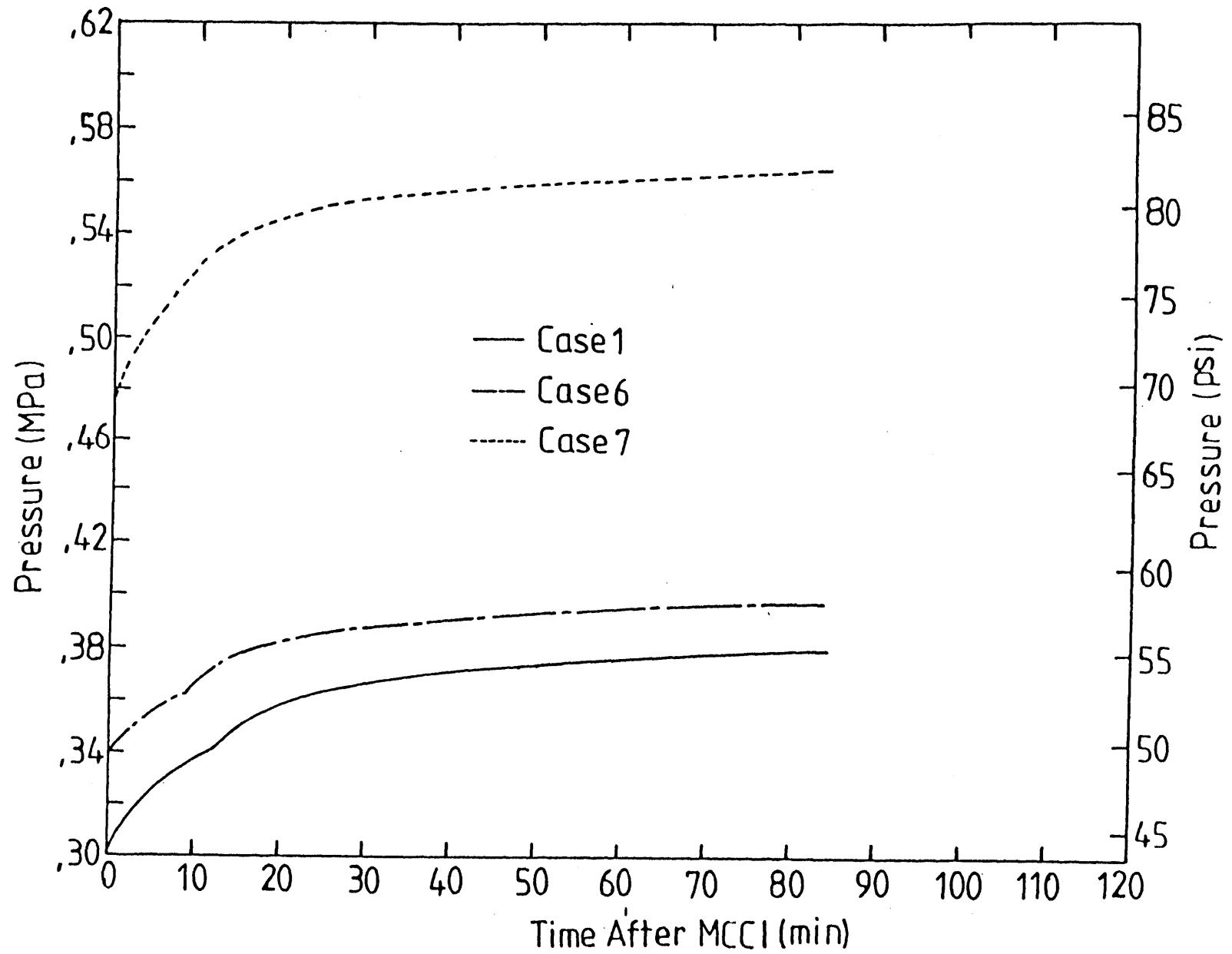
Figure 7.8   Containment Pressure Responses of Case 1, Case 6 and Case 7

the Base Case i.e. 4 hr after the scram. The pressure response of Case 7 is compared with that of the Base Case in Fig.7.9. The pressure in Case 7 is higher due to the larger amount of decay heat accumulated in the containment. The total pressure increase of Case 7 over the first 1.4 hr of MCCI is 0.087 MPa (12.61 psi) which is not significantly different from the Base Case. Because the system pressure of Case 7 is always approximately 0.175 MPa (25 psi) higher than that of the Base Case. The results of Case 7 can be used to study the effect of the system pressure on the MCCI.

In this calculation, the film collapses at 420 sec after the initiation of MCCI with the metallic temperature around 2369 $^\circ K$ which is higher than the Base Case. This resulted from the density of concrete gas being larger as the system pressure is higher. Compared with the Base Case, the downward erosion is increased by 7.4% and sideward erosion is decreased by 13.5%. It seems that the corium has the tendency to move more downward as the system pressure is higher. However, the overall energy distribution is not greatly affected by the system pressure: 64.3% consumed by concrete ablation, 12.7% carried out by concrete decomposed gas and 23.0% transferred to the containment atmosphere.

7.3.2.4 Effect of Conducted Heat into the Containment Concrete Wall

As Fig.7.9 indicates, the heat conducted into the containment concrete wall is an important passive heat sink. By considering this, the containment pressure can be reduced by a significant amount (compared the Case 1 and Case 8 in Fig.7.9)

After 1.4 hr of MCCI, the amount of heat transferred into the concrete wall of the containment building is around 8.08×10^4 MJ in Base Case. With $x^* = 3.5$ in Eq.7.1, the penetration distance at 1.4 hr is 0.185 m which is about 15% of the concrete wall thickness. The average temperature rise of concrete within this penetration distance is around 30.5 $^\circ K$.
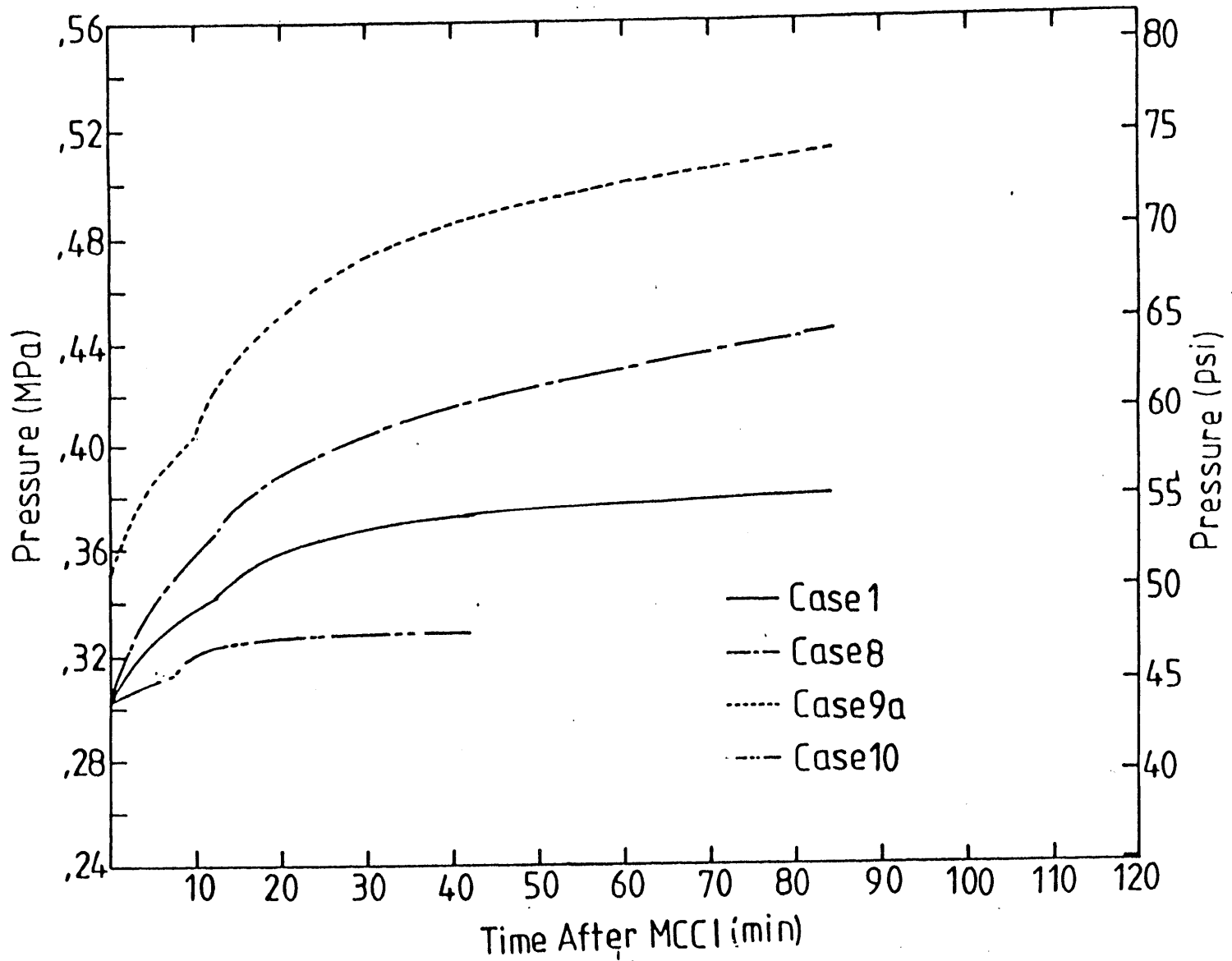
Figure 7.9   Containment Pressure Responses of Case 1, Case 8, Case 9a and Case 10

In the present calculation, it is assumed that the heat conduction to the concrete wall starts from the begining of MCCI. A more realistic assumption is to consider this heat conduction effect from the begining of the accident. However, with this simplified containment model, it is difficult to obtain the transient behavior of the containment atmosphere before MCCI. The heat conducted into the containment concrete wall before the MCCI will not be considered here. Neglecting this effect will keep more energy within the containment atmosphere and have conservative results.

7.3.2.5 Effect of Heat Generated from Combustion Reaction

In MCCI, large amount of CO_2 and H_2O generated from the decomposed concrete is reduced to CO and H_2 by the metallic elements in the corium. These gases can react with O_2 in the containment atmosphere and generate large amounts of heat. A study was performed to investigate the effect of this potential heat source on containment pressurization. The reaction heats of combustion reactions are based on the values summarized in Table 2.1. It is also assumed that reactions proceed to completion i.e. one of the reactants is exhausted.

As shown in Fig.7.9, by considering this potential heat source, the containment pressure can increase significantly amount (Case 9a), 34% over the Base Case. 1.4 hr after the initation of MCCI, the heat generation due to combustion can accumulate up to 1.03×10^5 MJ which is almost 20% of the decay heat generated within 3.4 hr after shutdown.

By considering the combustion reactions heat of CO and H_2 with O_2, the containment pressure is more sensitive to the downward heat transfer model used in the MCCI anslysis. For the case that the amount of gas generation is higher, the containment pressure is higher. This trend is opposite to that described in Section 7.3.2.1.

As shown in Fig.7.10, the pressure of Case 9b is 0.015 Mpa (2.19 psi) higher than that of Case 9a at 1.4 hr after MCCI. This is because that in Case 9b the
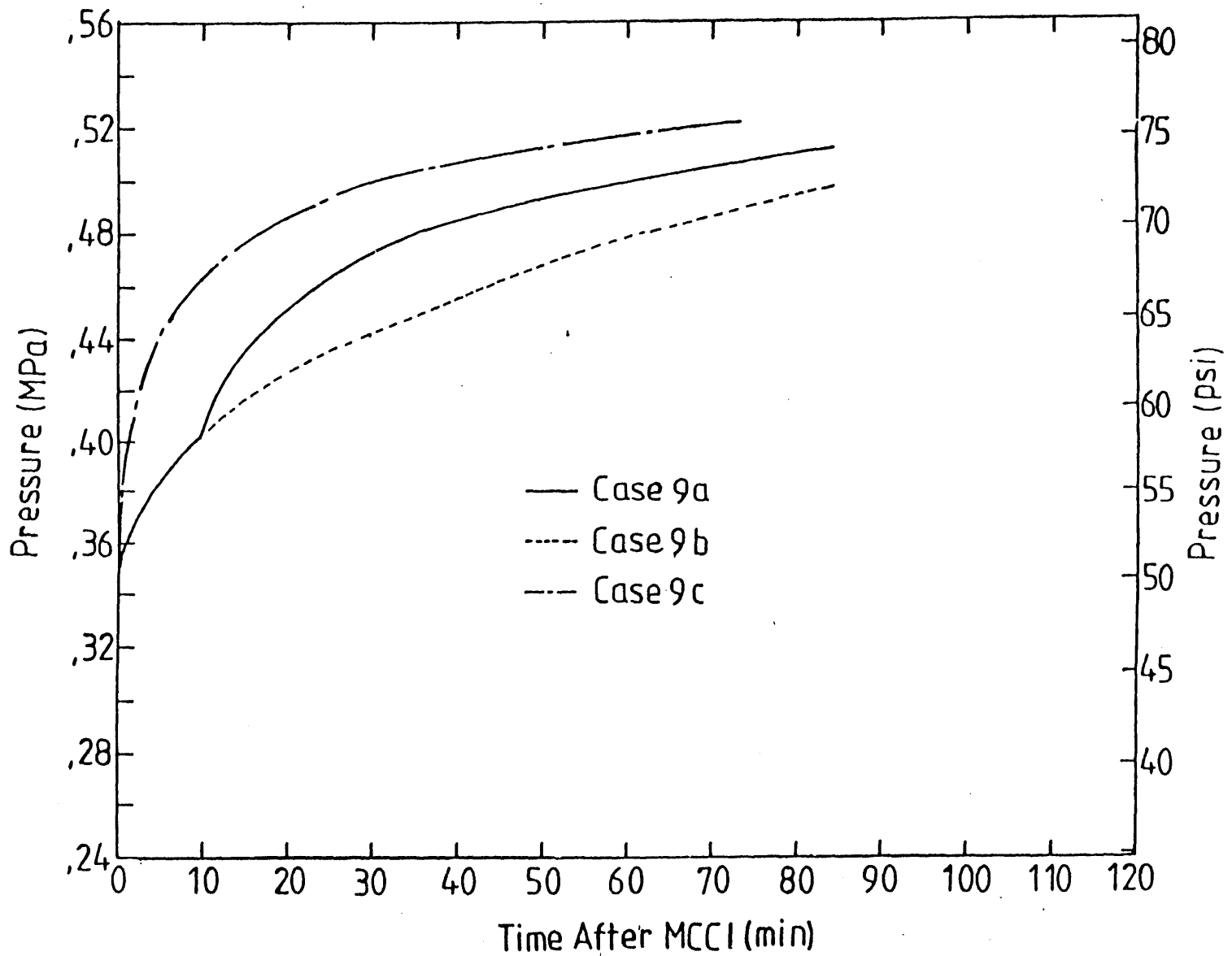
Figure 7.10   Containment Pressure Responses of Case 9a, Case 9b, and Case 9c

downward heat transfer model is pseudo gas film model all the time and this results in less gas generation and therefore. less amount of combustion reactions heat. The amount of combustion reactions heat is Case 9b is 18.9% less than that in Case 9a.

In Case 9c. the downward heat transfer model is periodic contact model of MIT all the time. the O_2 in the containment atmosphere is exhausted at 1.2 hr after MCCI. The amount of combustion reaction heat generated is 1.34×10^5 MJ. The containment pressure of Case 9c is 0.017 Mpa (3.21 psi) higher than that of Case 9a.

7.3.2.6 Effect of Concrete Types

The pressure responses of the PWR large dry containment with limestone/common sand and basaltic concrete are compared in Fig.7.9. At 42 min after the initiation of MCCI. the pressure of the containment with basaltic concrete is about 12% lower than that of a containment with limestone/common sand concrete. The calculation for the basaltic concrete case stops at 42 min due to significant (more than 20%) metallic phase solidification. Compared with the limestone/common sand case. this is much eralier. This is because the decomposition enthalpy of basaltic concrete is 23.7% lower than that of the limestone/common sand concrete.

Based on the MIT downward heat transfer correlation of Chapter 2. the downward heat transfer coefficient is inversely proportional to the effective decomposition enthalpy. Lower decomposition enthalpy results in higher heat transfer coefficient. For the same amount of heat transferred to the concrete. lower decomposition enthalpy can result in higher ablation rate. The decomposed concrete (slag) will be brought into the oxidic phase at the concrete decomposition temperature and then reach an equilibrium temperature with the oxidic melt. This mechanism can also cool down the corium. The calculation show that. at 42 $mins$ after the initation of MCCI. 121 $tons$ of the basaltic concrete is eroded. 39% more than that of the Base Case.

222

For the case of basaltic concrete. the film collapses at 450 sec after the initation of MCCI with metallic temperature around 2329 $^\circ K$.

7.3.2.7 Effect of Containment Types

Two types of containment, besides that of the PWR large dry containment were analyzed. The results are shown in Fig.7.11. For a PWR ice condenser containment (Case 11). the total system pressure is considerably lower than that of large dry containment. This is because of the large amount of heat absorbed by the ice. The pressure increase of the ice condenser containment over the first 1.4 hr of MCCI is 0.064 MPa (9 psi) which is comparable with that of a large dry containment. Compared with that of a PWR large dry containment. the atmosphere temperature of the ice condenser containment is also lower. The temperature of the containment atmosphere changes from 317.7 to 332.7 $^\circ K$ over the first 1.4 hr of MCCI.

For a BWR supression pool containment (Case 12). as shown in Fig.7.11, the pressure lies between the other two containment types. In this case the pressure increase over the first 1.4 hr of MCCI is 0.168 MPa (23.92 psi) which is almost double that of the PWR large dry containment. This is because the BWR supression pool containment has relatively smaller free volume. It can be easily pressurized by the noncondensible gases generated from the MCCI. Compared with that of a PWR large dry containment, the atmosphere temperature of the BWR supression pool containment is also lower. The atmosphere temperature changes from 320.0 to 323.8 $^\circ K$ over the 1.6 kr of MCCI.

7.4 Conclusions

1. The downward heat transfer model is very important in determining the concrete erosion rates. For the cases studied. the containment pressurization rate is less sensitive to the amount of gas generation. Should combustion of H_2 and CO occur. the pressure would be larger for the higher downward heat transfer.
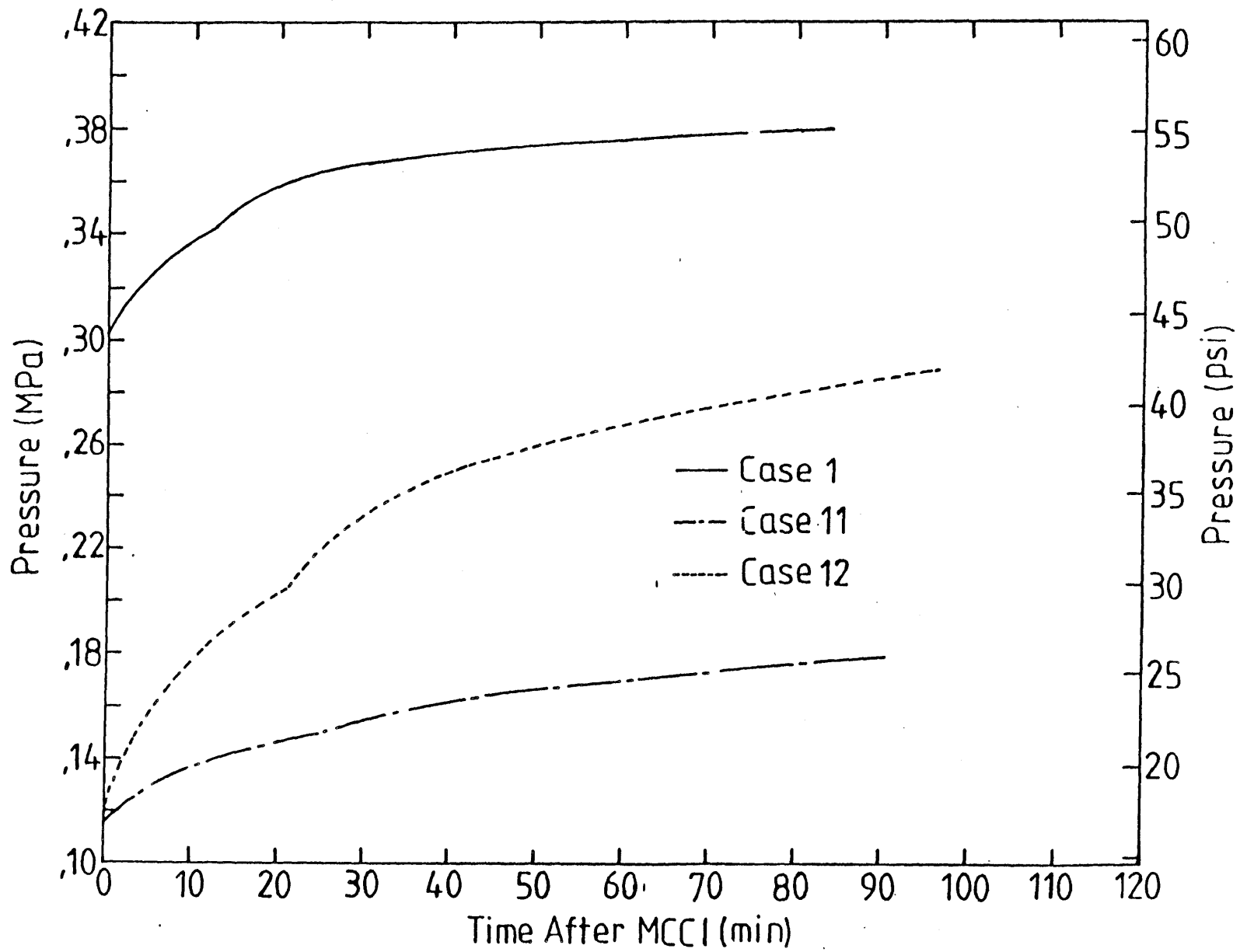
Figure 7.11   Containment Pressure Responses of Case 1, Case 11 and Case 12

2. For consideration of containment pressurization, the interfacial and upward convective heat transfer coefficients are relatively unimportant. However, the temperature profile of the corium pool will be significantly different for different assumptions on these parameters. This might have some effect in characterizing the freezing phenomena of debris pool and the generation of aerosol.

3. The heat conducted into the containment concrete wall is a very important heat sink. The heat generated from the combustion reactions in the containment atmosphere is a large heat source for containment pressurization.

4. The temperature of corium at the beginning of MCCI is important in determining the concrete erosion but has a small effect on containment pressurization.

CHAPTER 8

SUMMARY AND CONCLUSIONS

8.1 Summary of This Work

Concern about the potential for containment failure following core meltdown due to high pressure and temperature casued by Molten Corium/Concrete Interaction (MCCI) has motivated this work. A simplified model was used to quantify the impact of heat transfer from the core melt to concrete on the pressure rise in the containment. Limited heat removal from the the containment, by fan coolers, and thermal equilibrium among all components were assumed. It was found that the fraction of heat transferred to concrete is important in determining the pressurization rate of containment. For a PWR large dry containment as the fraction is larger (above 30%) the pressurization rate is smaller. The extent of chemical reactions between the concrete gases and core melt will be a major factor in determining the containment pressure. especially for a concrete type with high gas content.

One of the major uncertainties in modeling the corium pool heat transfer is the partition of the heat generated from the radioactive decay and chemical reactions between the containment atmosphere and the surrounding concrete. This depends on the heat transfer resistance through each path and also on the freezing phenomena involved in the corium pool. In the first generation of MCCI integral analysis codes, it was assumed that the downward heat transfer of the corium pool is governed by a stable gas film across the corium/concrete interface. However, a stable gas film has not actually been observed in real materials experiments. but only inferred from the simulant tests of water or benzene on dry ice.

A calcualtion based on the Kutateladze's flooding criterion showed that the superficial gas velocity required for forming a stable gas film is far beyond the data

226

ranges of dry ice experiments (approximately 30 times higher). Therefore. it is possible that the gas film observed in the dry ice experiment was not stable. An alternative view was proposed to interpret the water or benzene/dry ice experimental data. It was assumed that the heat transfer between the hot pool and a melting substrate is governed by the periodic contact between the hot pool and the relatively cold substrate. Based on this assumption. a semiempirical heat transfer correlation for calculating the downward heat transfer rate was derived. The correlation predicted that the heat transfer coefficient across the interface between a hot pool and a melting substrate increases with the superficial velocity of melted substrate. This trend is consistent with the dry ice experimental results.

In MCCI, the oxidic melt may separate from the metallic melt due to the density difference. The interfacial heat transfer between the immiscible oxidic and metallic layers is complicated by the agitation of gas flow. The interfacial heat transfer between the bubble agitated immiscible liquid layers is governed by three mechanisms. These are: natural convection. bubble agitation and bubble induced entrainment. Among these three mechanisms. the contribution of the natural convection to the total heat transfer rate is relatively small. The heat transfer rate resulting from bubble agitation can be modeled by the surface renewal concepts. A new method was proposed to modify the surface renewal model originally proposed by Szekely. The new correlation compared favorably with the results of water/mercury and oil/wood's metal experiments.

Based on the observations of the simulant experiments, the bubble induced entrainment only occured in certain liquid pairs. The liquid entrainment can be caused by two mechanisms: splashing and bursting of bubbles at the interface. Splashing is due to interfacial shear and only occurs in systems containing localized areas of high gas velocity. A simple calculation based on the criterion for the onset of entrainment in annular flow showed that the required superficial gas velocity is orders of magnitude higher than the ranges of the existing simulant experiments. A simple

analytical model was proposed to model the liquid jet resulting from the bursting of bubbles at the interface. Based on consideration of hydrodynamic instability of the liquid jet, it can be determined whether for certain liquid pairs the bubble will induce entrainment. The model explained the observed behavior of different liquid pairs. From this analytical model, it was concluded that the bubble induced liquid entrainment resulting from bubble bursting will not occur in MCCI. The model is pertinent to low gas velocity areas. This is consisent with the results of low power test of BETA experiments. At high gas velocity, entrainment is due to interfacial shear.

The proposed downward and interfacial heat transfer models have been incorporated into CORCON/Mod1 – an integral analysis code of MCCI. The qualification of the proposed models was achieved by comparing the code predictions to the results of BETA experiments. The BETA project, a key experimental program of Melt/Concrete Interaction is currently undertaken at KfK. Up to 300 kg metallic and 300 kg oxidic melt can be generated outside the concrete crucible by a thermite reaction and then poured into the crucible. The concrete crucible is enclosed by an induction coil. A maximum power of 1700 kW may be induced to the melt.

Based on hydrodyamic considerations, the formation of a very stable gas film requires that the superficial gas velocity exceeds certain critical value i.e. the flooding limit. As the superficial gas velocity decreases, the film may collapse due to Taylor instability which provides a limit of minimum superficial gas velocity for supporting an existing film. For the case of MCCI, these limits differ by two orders of magnitude.

In MCCI, the actual downward heat transfer mode depends on the initial temperature of the melt. If the temperature of the melt is initially very high, the heat flux will be high enough to generate a film, and the interaction starts with a film at the interface and then follows the gas film model to the minimum stable gas film limit. After the film collapses, the heat transfer mode switchs to pseudo nucleate boiling (i.e. periodic contact between the melt and the concrete). If the initial

temperature is not high enough to generate the film the heat transfer mechanism will be pseudo nucleate boiling all the time until the freezing takes place.

The downward heat transfer in CORCON/Mod1 was modified based on the preceeding arguement. The heat transfer coefficient in pseudo nucleate boiling regime is calculated by the proposed periodic contact model and that in pseudo film boiling regime is calculated by original CORCON gas film model. The criterion for forming a gas film is determined by Kutateladze's flooding limit. The transition between the pseudo film boiling and pseudo nucleate boiling is determined by Berenson's minimum stable gas film criterion. With a set of correction factors (multipliers) applied to the gas velocity determined from the correlations above. the results of BETA tests V0.2 – V1.6 can be reproduced by the modified CORCON/Mod1. However, the calculated results are very sensitive to the multiplier used for Berenson's minimum stable film criterion.

The CORCELL code which combined the simplified containment model with the modified CORCON/Mod1 is used to study the impact of MCCI on containment pressurization. It was found that the downward heat transfer medel is very important in determining the concrete erosion rates. However. for the cases studied, the containment pressurization rate is less sensitive to the amount of gas generation. Should combustion of H_2 and CO occur. the containment pressure would be higher for higher concrete erosion. For containment pressurization. the interfacial and upward convective heat transfer coefficients are relatively unimportant. However. the temperature profile of the corium pool will be significantly different for different assumptions of these parameters, and may affect fission products release.

The stability of a horizontal crust layer under the impact of gas injection was studied by a simulant experiment. A test apparatus was designed. with heat removal from the cell via porous plates at the boundaries. Water and air were used in the experiment. In the cases studied a stable solidified layer was formed across the bubble agitated horizontal liquid/solid interface.

229

Two different phenomena were observed upon freezing of the pool. In some of the cases. the pool can be cooled below its freezing point. Then the freezing occured suddenly. the liquid/solid interface was covered by a thin layer of ice and the bulk temperature of the pool jumped up to the freezing point of water. In other cases, the freezing occured grauually and there was no supercooling in the pool. The causes of these differences remain unclear.

8.2 Future Work

In some of the high power tests of BETA experiments. considerable amount of metallic phase was entrained into the oxidic phase. This phenomenon is presently not modeled in any MCCI integral analysis code. The dispersion of the metallic phase is important in characterizing the MCCI. The importance is not because its effect on the interfacial heat transfer rate, but because of its implication for the possibility of forming a metallic and oxidic mixed layer. If a mixed layer were formed. the freezing characteristic of the corium pool would be different. Therefore, it is recommended that some experiments be performed to study the phenomena and, if necessary. an appropriate model be developed to characterize the phenomena.

Entrainment of metallic phase into the oxidic phase observed in the BETA tests occured mainly at high temperature levels of the melt and seems to be controlled by the gas release rate. A question remains to be answered whether the separation of these two phases is possible when the gas release rate decreases as the interaction proceeds.

The experimental apparatus of crust stability experiments can be improved so that the impact of crust formation on downward heat transfer rate can be quantified. The crust stability experiment should be conducted at higher gas velocity to represent the more realist case.

The heat generated from the oxidation reactions between the metallic elements

in the corium pool and the concrete decomposed gases is an important heat source in MCCI. There are some differences in the chemical reaction packages among different integral MCCI analysis codes. Further justifications of these chemical reaction packages are necessary. This question is further important for source term characterization.

The major impact of MCCI on the reactor safety assessment is the generation of aerosols. In BETA experiments, relatively insignificant amount of aerosol was observed. These results differ from those of Sandia's real materials experiments. Further experiment on MCCI should focus upon this subject more closely. The types of concrete used, the core melt as well as the temperature level of the pool should be varied to ascertain their effects.

REFERENCES

A1.   Abdel-Khalik, S.I., Private Communication. July 18 1983.

A2.   Ahmed, S.Z. and Dhir, V.K., "On the Simulation of Penetration of Solidified Core Material into Concrete," Proc. of the ANS/ENS Int. Mtg. on Light Water Reactor Severe Accident Evaluation, Aug.28 - Sept.1, 1983, Cambridge Ma.

A3.   Aiba, S. and Yamada, T., "Studies on Entrainment," AIChE Journal, No.4, Vol.5, 1959.

A4.   Alsmeyer, H. and Reimann, M., "On the Heat and Mass Transport Process of A Horizontal Melting or Decomposing Layer under Molten Pool," The Winter Annual Meeting of ASME, Nov.27 - Dec.2, 1977, Altanta Ga.

A5.   Alsmeyer, H. and Reimann, M. and Hosemann, J.P. " Preliminary Results of the KfK Molten Core/Concrete Experimental BETA Facility," a paper presented at Water Reactor Safety Information Meeting, Oct. 1984, Washington D.C.

B1.   Baker ,L., et al., "Interaction of LMFBR Core Debris with Concrete," Proc. of Int. Mtg. on Fast Reactor Safety and Related Physics, Oct.5 - 8, 1976, Chicago Ill.

B2.   Baker, L., et al., "Thermal Interaction of Molten Core Debris Pool with Surrounding Structure Materials," Proc. of the Int. Mtg. on Fast Reactor Safety Technology, Aug.19 - 23, 1979, Seattle Wa.

B3.   Beck, J.V. and Knight, R.L., "User's Manual for USINT," NUREG/CR-1375, SAND 79 - 1694, 1980.

B4.   Benjamin, A.S., "Core - Concrete Pool Dynamics and Interfacial Heat Transfer," Proc. of ANS/ASME NRC Topical Meeting on Nuclear Reactor Thermalhydraulics, NUREG/CP-0014, Vol.2, Oct.5 - 8, 1980, Saratoga Spring Ny.

B5.   Berenson, P.J., "Film Boiling Heat Transfer from A Horizontal Surface," Journal of Heat Transfer, pp351 -358, Vol. 38, 1961.

B6.   Blottner, F.G., "Hydrodynamics and Heat Transfer Characteristic of Liquid Pool with Bubble Agitation," SAND79-1132, 1979.

B7.   Bird, R.B., et al., "Transport Phenomena," John Wiley & Sons Inc.

C1.   Carslaw, H.S. and Jaeger, J.G., "Heat Conduction in Solids," 2nd Edition Oxford, 1959.

C2.   Chandrasekhar, S., "Hydrodynamic and Hydromagnetic Stability," Oxford, 1961.

232

C3. Chasanov, M.G. et al., "The Production of Molten UO2 Pools by Internal Heating: Apparatus and Preliminary Experimental Heat Transfer Results," Nucl. Tech. PP120 - 127. Vol.36. Nov. 1977.

C4. Chu, T.Y.. "Radiant Heat Evaluation of Concrete - A Study Of the Erosion of Concrete due to Surface Heating," SAND77-0922, Jan.. 1978.

C5. Cole. R.K. Jr., "A Crust Formation and Refreezing Model for Molten Fuel/ Concrete Interaction Codes," Proc. of the ANS/ENS Int. Mtg. on Light Water Reactor Severe Accident Evaluation, Aug.28 - Sept.1, 1983, Cambridge Ma.

C6. Cole. R.K. Jr., Kelly, D.P and Ellis, M.A.. "CORCON/Mod2, A Computer Program for Analysis ofMolten - Core Concrete Interaction," NUREG/CR-3920, SAND84-1246, Aug. 1984.

C7. Collier. J.G.. "Convective Boiling and Condensation," 2nd. Ed., McGraw Hill Book Co.. 1981.

C8. Corradini. M.L., "A Transient Model for the Ablation and Decomposition of Concrete." Nucl. Tech.. pp263 - 273. Vol.62. Sept. 1983.

C9. Catton. 1., Brinsfield. W.A. and Ghiaasiaan.S.M.,"Heat Transfer from A Heated Pool to A Melting Miscible Substrate." Journal of Heat Transfer, pp447 - 453. Vol.105. Aug. 1983.

D1. Davies. R.F.. "The Physical Aspect of Steam Generation at High Pressure and the Problem for Steam Contamination," Proc. Inst. Mech. Engrs., pp149 -168. 1960.

D2. Dhir, V.K., Castle, J.N. and Catton, I., "Role of Taylor Instability Sublimation of HorizontalSlab of Dry Ice," Journal of Heat Transfer, pp411 - 418. Vol.99, 1977.

E1. Eck, G. and Werle, H., " Experimental Studies of Penetration of Hot Liquid Pool into A Melting Miscible Substrate," Nucl. Tech. pp275 - 289, Vol.64, March 1984.

E2. Epstein, E., "Stability of Submerged Frozen Crust." Journal of Heat Transfer. pp527 - 532. Vol.29, Nov. 1977

F1. Farhadieh. R. and Baker, L.. "Experimental Studies of the Growth of An Internally Heated Liquid Pool in a Solid Bed," Nucl. Sci. & Eng.. pp394 - 400, Vol.65. 1978.

F2. Farhadieh, R. and Gunther, W.H.. "One Dimensional Penetration of Molten UO2 into Substrate Limestone Concrete," Nucl. Tech.. pp298 - 306, Vol.50, Oct. 1980.

F3. Farhadieh. R. and Baker, L., "Heat Transfer Phenomenology of A Hydro- dynamically Unstable Melting System." Journal of Heat Transfer, pp 305 - 310, Vol.100, May 1978.

F4.   Farhadieh, R. and Epstein, M., "Downward Penetration of A Hot Liquid Pool into the Horizontal Surface of A Solid," Journal of Heat Transfer, pp199 - 201, Vol.104, Feb. 1982.

F5.   Felde, D.K., Kim, H.S. and Abdel-Khalik, S.I., " Convective Heat Transfer Correlation for Molten Core Debris Pools Growing in Concrete,"Nucl. Eng. Des., pp65 - 74, Vol.58, 1980.

F6.   Fieg, G. and Werle, H., "Experimental Investigation of Heat Transfer in Pools," Proc. of Int. Mtg. on Fast Reactor Safety Technology, Aug.19 - 23, 1979, Seattle Wa.

G1.   Garner, F.G., "The Size Distribution and Entrainment of Droplets," Trans. Instn. Chem. Engr., pp222 - 235, Vol.32, 1954.

G2.   Ginsberg, T. and Greene, G.A., "BNL Program in Support of LWR Degraded Core Accident Analysis," Proc. of U.S. NRC Tenth Water Reactor Safety Research Information Meeting, NUREG/CP-0041, Vol.2, Oct.12 - 15, 1982, Gaithersburg Md.

G3.   Glasstone, S. and Sesonske, A., "Nuclear Reactor Engineering," 3rd. Ed., Chapter 2, Van Nostrand and Reinhold Company, 1981.

G4.   Grief, R., "Heat Transfer with Gas Injected at the Surface," Int. J. Heat Mass Transfer, pp1253 - 1254, Vol.9, 1965.

G5.   Greene, G.A., et al., "Heat Transfer between Immiscible Liquid Enhanced by Gas Bubbling," Int. Mtg. on Thermal Nuclear Reactor Safety, Aug.29 - Sept.2 1982, Chicago Ill.

G6.   Gerstmann, J. and Griffith, P., "Laminar Film Condensation on the Underside of Horizontal and Inclined Surface," Int. Journal of Heat Mass Transfer, pp567 - 580, Vol.10, 1967.

H1.   Haberstroh, R.D. and Reinders, R., "Conducting - Sheet Model for Natural Convection through a Density Stratified Interface," Int. J. Heat Mass Transfer, pp307 - 311, Vol.17, 1974.

H2.   Han, C.Y. and Griffith, P.G., "The Mechanism of Heat Transfer in Nucleate Boiling," MIT Heat Transfer Lab., Report No. 7673-19.

H3.   "CRC Handbook of Chemistry and Physics", 50th. Edition, The Chemical Rubber Co., 1969.

H4.   Henry, R.E., "A Model for Core-Concrete Interaction," Proc. of the ANS/ENS Int. Mtg. on Light Water Reactor Severe Accident Evaluation, Aug.28 - Sept.1, 1983, Cambridge Ma.

H5.   Hsu, Y.Y. and Graham, R.W., "Transport Process in Boiling and Two Phase System," Hemisphere Publishing Coporation.

H6.   Hassmann, K., et al.."Gas Release and Containment History during Melt-Concrete Interactions." Second International Workshop on the Impact of Hydrogen on Reactor Safty, Albquerque NM, Oct 3 - 7, 1982

I1.   Ivey, H.J., "Relationships between Bubble Frequency, Departure Diameter and Rise Velocity in Nucleate Boiling," Int. J. Heat Mass Transfer, pp1023 - 1040, Vol.10, 1967.

K1.   Kao, L.S. and Kazimi, M.S.. "Containment Pressure Response to A Meltdown Condition of the Light Water Reactor." a paper presented at Sixth Information Exchange Meeting on Debris Coolability, Nov.7 - 9 1984, UCLA.

K2.   Kataoka, I. and Ishii, M., "Mechanistic Modelling and Correlation for Pool Entrainment Phenomena." NUREG/CR-3304, ANL83-37.

K3.   Konsetov, K.K.. "Heat Transfer during Bubbling of Gas through Liquid ," Int. J. Heat Mass Transfer, pp1103 - 1108, Vol.9, 1966.

K4.   Kutateladze, S.S.. "Heat Transfer in Condensation and Boiling (1952) ." Translated as U.S. Atomic Energy Commision Report,AEC-tr-3220.

K5.   Kutateladze, S.S. and Malenkov, I., "Boiling and Bubbling Heat Transfer under the Condition of Free and Forced Convection," 6th. International Heat Transfer Conference, Toronto. Canada, 1978.

K6.   Kao, L.S.. "An experiment on the Pool Freezing with Bubble Agitation." A Report of Special Problem, Nuclear Engineering Department, MIT, to be finished.

L1.   Lock, R.C., "The Velocity Distribution in the Laminar Boundary Layer between Parallel Stream." Quart. Jour. Appl. Math., PP42 - 63, Vol.4, 1951.

M1.   Muir, J.F., Powers, D.A. and Dahlgren,D.A.. " Studies on Molten Fuel - Concrete Interaction," Proc. of the Int. Mtg. on Fast Reactor Safety and Related Physics, Oct.5 - 8, Chicago ill.

M2.   Muir, J.F.,"Response of Concrete Exposed to a High Heat Flux on One Surface." SAND77-1467, Nov. 1977.

M3.   Muir, J.F.. et al.. "CORCON/Mod1: An Improved Model for Molten Core/ Concrete Interaction." NUREG/CR-2142. SAND80-2415. July 1981

M4.   Murfin. W.B.. "A Preliminary Model for Core/Concrete Interactions," SAND77-0370. Aug. 1977.

N1.   Newitt, D.M.. "Liquid Entrainment 1. The Mechanism of Drop Formation from Gas or Vapor Bubbles," Trans. Instn. Chem. Engrs., pp244 - 261 , Vol.32, 1954.

P1.   Paik, I.K.. Abdel-Hhalik,S.I. and Corradini,M.L.. "Assessment of Heat Transfer Model in Molten-Core-Concrete Interaction Codes." Proc. of Int. Mtg. on Thermal Nuclear Reactor Safety, Aug.29 - Sept.2 1982. Chicago Ill.

P2. Peehs. M.. Skokan. A. and Reimann. M.. "The Behavior of Concrete in contact with Molten Corium in the Case of A Hypothetical Core Melt Accident." Nucl. Tech. pp192 - 198. Vol.46. Dec.1979.

P3. Plys, M.. Heising. C. and Henry. R.. "Simulant Fluid Experiments for Core- Concrete Thermal Attack." Proc. of ANS/ENS Int. Mtg. on Light Water Reactor Severe Accident Evaluation, Aug.28 - Sept.1 1983. Cambridge Ma.

P4. Plys. M., "An Experimental Investigation of the Core-Concrete Interaction," Sc.D. Thesis, Nuclear Engineering Department. MIT.. Feb. 1984.

P5. Powers. D.A., "Exploratory Study of Molten Core Material/Concrete Interactions, July 1975 - March 1977," SAND77-2042, Feb. 1978.

P6. Powers, D.A., "Sustained Molten Steel/Concrete Interaction Tests, A Preliminary Report on the Feasibility of Experimental Technique." SAND77-1423, NUREC/CR-0166. June 1978.

P7. Powers. D.A. and Arellano, F.E.. "Large-Scale Transient Tests of the Interaction of Molten Steel with Concrete," NUREG/CR-2282, Jan. 1982.

P8. Powers, D.A. and Arellano, F.E.. "Direct Observation of Melt Behavior during High Temperature Melt/Concrete Interaction." SAND81-1754, Jan. 1982.

R1. Rausmussen. N.C., "Reactor Safety Study - An Accessment of Accidents Risks in U.S. Commerical Nuclear Power Plants." WASH-1400. Oct. 1975

R2. Reimann, M. and Murfin. W.B.. "The WECHSL Code: A Computer Program for the Interaction of Core Melt with Concrete." KfK-2890, Nov. 1981.

R3. Reimann, M. and Alsmeyer. H.. "Core Melt- Concrete Interaction: Status of the WECHSL Code Development and Present Results." a paper presented at Sixth Information Exchange Meeting on Debris Coolibility. Nov.7 - 9 1984, UCLA.

R4. Rininsland, H.. "BETA (Core-Concrete Interaction) and DEMONA (Demonstration of NAUA) - Key Experimental Programs for Validation and Demonstration of Source Term in Hypothetical Accident Situation ." Proc. of the ANS/ ENS Int. Mtg. on Light Water Reactor Severe Accident Evaluation, Aug.28 - Sept.1. 1983. Cambridge Ma.

R5. Rohsenow. W.M. and Hartnett. J.P.. "Handbook of Heat Transfer." McGraw Hill Book Co., 1973.

R6. Reimann. M.. Private Communication. Dec. 1984.

R7. " RETRAN02 —-A program for Transient Thermal-Hydraulic Analysis of Complex Fluid Flow Systems:" EPRI/NP-1850. May. 1981.

S1. "Light Water Reactor Safety Research Program Quarterly Report April - June 1978," Vol. 8, SAND78-1901, NUREG/CR-0422. Jan. 1979.

S2.   "Light Water Reactor Safety Research Program Quarterly Report July - September 1978." Vol. 9, SAND79-0359, NUREG/CR-0661, Apr. 1978.

S3.   "Light Water Reactor Safety Research Program Quarterly Report Oct. - Dec. 1978." Vol. 10, SAND79-0820, NUREG/CR-0768, July 1979.

S4.   "Light Water Reactor Safety Research Program Quarterly Report Jan. - March 1980." SAND80-1304/1 of 4, NUREG/CR-1509/1 of 4, July 1980.

S5.   Sowa.E. and Pavlik.J., "The Interaction of High Temperature Core Debris with Concrete and Refractory Material," Nucl. Tech. PP234 - 238, Vol. 54, 1981.

S6.   Szekely, J.. "Mathematical Model for Heat and Mass Transfer at the Bubble-Stirred Interface of Two Immiscible Liquids," Int. J. Heat Mass Transfer, pp307 - 311, Vol.6, 1963.

T1.   Taghavi-Tafreshi, K., Dhir, V.K. and Catton,I., "Thermal and Hydro- dynamic Phenomena associated with Melting of A Horizontal Substrate Placed beneathA Heavier Immiscible Liquid," Journal of Heat Transfer, pp318 - 325, Vol. , May 1979.

T2.   Turner. W.D. and Crowell, J.S.. "Notes on HEATING – An IBM 360 Heat Conduction Program," CTC-INF-980,1969

V1.   Vandervort, C.L.. "CORCON/Mod1 Modeling Improvements and Sensitivity

Analysis ," M.S. Thesis, Nuclear Engineering Department, U. of Wisconsion, Madison, 1984.

W1.   Wallis, G.B., "One Dimensional Two Phase Flow," McGraw-Hill Book Co. New York, 1969.

W2.   Werle, H.. "Enhancement of eat   Transfer between Two Horizontal Liqu Liquid Layers by Gas Injection at the Bottom." Nucl. Tech. pp160 - 164, Vol. 59, Oct. 1982.

W3.   Wooton. R.O. and Avci, H.I., "MARCH (Meltdown Accident Response CHaracteristic)." Battelle Columbus Laboratories, Jan. 1980.

Z1.   Zuber. N.. "Nucleate Boiling: The Region of Isolates Bubbles and the Similarity with the Natural Convection," Int. J. Heat Mass Transfer, pp53 - 78, Vol. 6, 1963.

Appendix A

The heat necessary to raise the concrete from room temperature and convert it to melt is calculated by following equation:

$$h_{decom} = \int_{T_o}^{T_D} C_p dt + \sum_{i=1}^{3} \phi_i + L \qquad (A.1)$$

where

T_o = initial temperature of concrete

T_D = decomposition temperature of concrete

C_p = specific heat capacity of concrete

ϕ_i = heat of decomposition associated with
   (1) loss of free water
   (2) loss of bound water
   (3) decarboxylation of the concrete
L = latent heat of concrete melting

The heats of decomposition associated with loss of free water, loss of bound water and decarboxylation of concrete together with the latent heat of concrete melt for different types of concrete are summarized in Table A.1. The temperature dependency of heat capacity $(J/kg\,^\circ K)$ of different types of concrete is obtained from following equations:

(a). Basaltic Concrete

$$C_p(T) = 939.75 + 0.55758T - \frac{1.9669 \times 10^7}{T^2} \qquad (A.2a)$$

(b). Limestone/Common Sand Concrete

$$C_p(T) = 710.36 + 0.43158T - \frac{1.3715 \times 10^7}{T^2} \qquad (A.2b)$$

(c). Limestone Concrete

$$C_p(T) = 454.18 + 0.20804T - \frac{5.9995 \times 10^6}{T^2} \qquad (A.2c)$$

where T is absolute temperature $(^\circ K)$.

To correct for the volatile species, the following correction factors should be added:

1. $0 < T < 373\,^\circ K$

$$C_{P1} = W_e(26.045 + 0.019716T) \qquad (A.3a)$$

1. $0 < T < 658\,^\circ K$

$$C_{P2} = W_{ch}(21.951 + 0.016786T) \qquad (A.3b)$$

1. $0 < T < 873\,^\circ K$

$$C_{P3} = W_{CO}(7.3255 + 0.005023T - 7.9115 \times 10^{-7}T^2) \qquad (A.3c)$$

where

W_e = weight fraction of evaporable water
W_{ch} = weight fraction of chemically bound water
W_{co} = weight fraction of carbon dioxide

A formula for the heat capacity of concrete that takes into account the mass loss may be written as:

$$C_p(T) = C_p(res) + C_{p1}\, G(T, 393) + C_{p2} G(T, 693) + C_{p3}\, G(T, 993) \qquad (A.4)$$

where $C_p(res)$ is calculated by Eq.(A.2) and $G(T, T_o)$ is:

$$G(T, T_o) = erfc\,[5(T - T_o/T_o] \qquad (A.5)$$

Table A.1

Thermal Events in the Decomposition of Concrete

	Basaltic	Limestone/Common Sand	Limestone
loss of free water (kJ/kg)	84.3±9.0	66.8±7.0	81.6±9.0
loss of bound water (kJ/kg)	120±20	120±20	109±15
decarboxy-lation (kJ/kg)	69.5±21	965.1±51	1560±100
enthalpy of melting (kJ/kg)	550±80	560±75	760±140

Appendix B

Table B.1 and Table B.2 summarize the thermal-physical properties of materials used in this report.

Table B.1

Properties of Corium and Slag[B6]

	Oxidic	Metallic	Slag
Density (kg/m^3)	7000	5750	2500
Viscosity $(kg/m\,sec)$	4.0×10^{-3}	4.0×10^{-3}	1.0
Specific Heat $(kJ/kg\,^\circ K)$	0.6	0.74	1.04
Thermal Conductivity $(W/m\,sec)$	3.0	40.0	1.3
Volumetric Thermal Expansion Coef. $(1/^\circ K)$	1.0×10^{-4}	6.0×10^{-5}	5.0×10^{-6}
Surface Tension (N/m)	0.45	1.5	0.3

Table B.2

Thermal-Physical Properties of
Silicone Oil, Mercury and Wood's Metal

	Silicone Oil	Mercury	Wood's Metal
Density (kg/m^3)	910	13500	9835
Viscosity $(kg/m\,sec)$	4.186×10^{-3}	1.15×10^{-3}	1.40×10^{-3}
Specific Heat $(kJ/kg\,^\circ K)$	1.42	0.157	0.175
Thermal Conductivity $(W/m\,sec)$	0.117	8.39	10.7
Volumetric Thermal Expansion Coef. $(1/^\circ K)$	1.05×10^{-3}	1.82×10^{-4}	6.0×10^{-5}
Surface Tension (N/m)	0.020	0.484	0.5

Appendix C

Following 13 pages show the power histories and post-test concrete crucible shapes of BETA tests V0.2 to V1.6.

V 0.2

Time(s)	Power(KW)	Energy(MJ)
0.0	0.0	0.0
100.0	0.0	0.0
110.0	370.0	1.9
590.0	430.0	193.9
600.0	0.0	196.0
620.0	0.0	196.0
650.0	510.0	203.7
1400.0	360.0	529.9
1810.0	310.0	667.3
1820.0	1600.0	676.8
1835.0	1600.0	700.8
1845.0	310.0	710.4
1940.0	300.0	739.3
1950.0	2300.0	752.3
1960.0	2300.0	775.3
1970.0	300.0	788.3
2530.0	240.0	939.5
2540.0	0.0	940.7
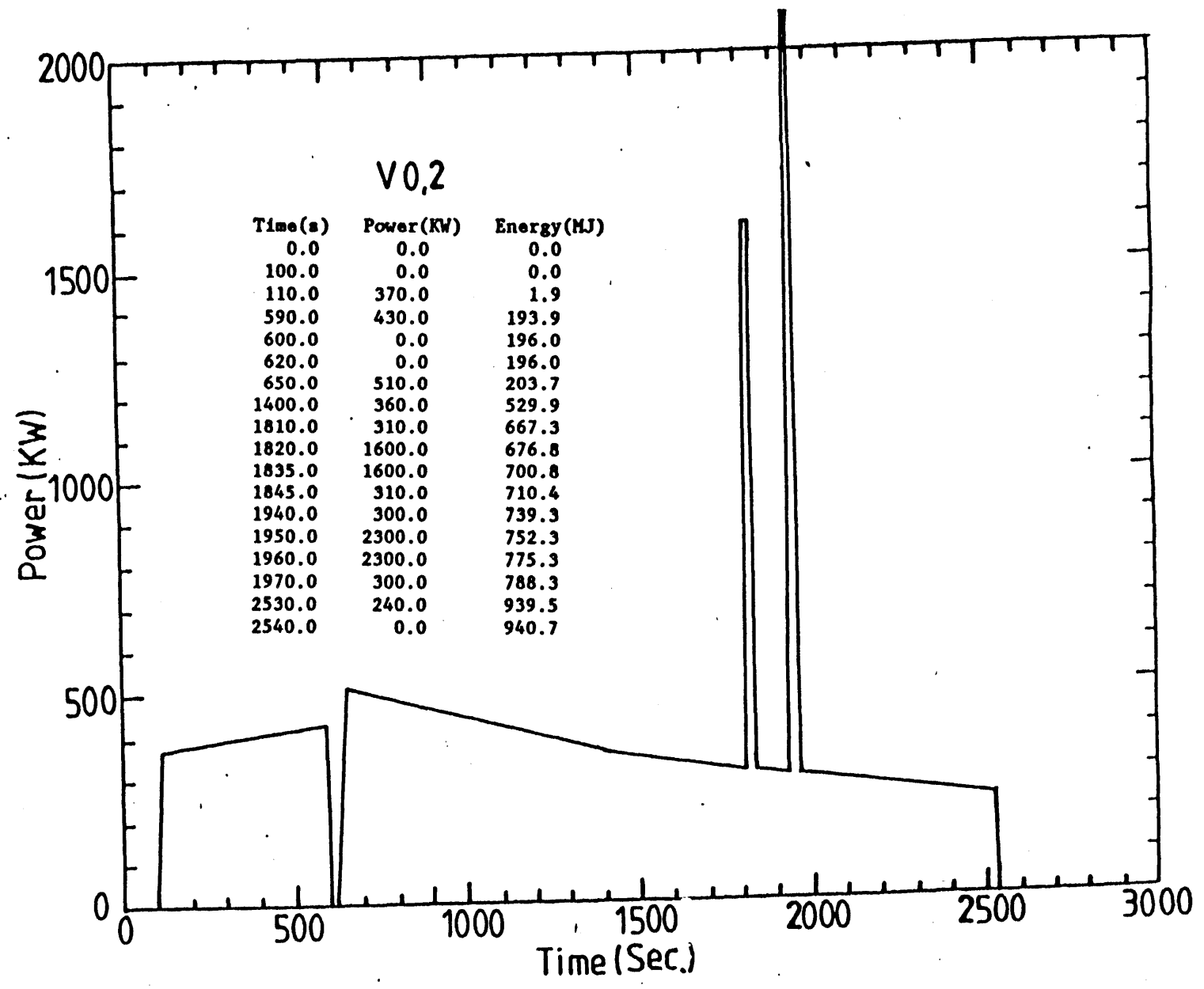
Figure B.1 Power History of BETA Test V0.2
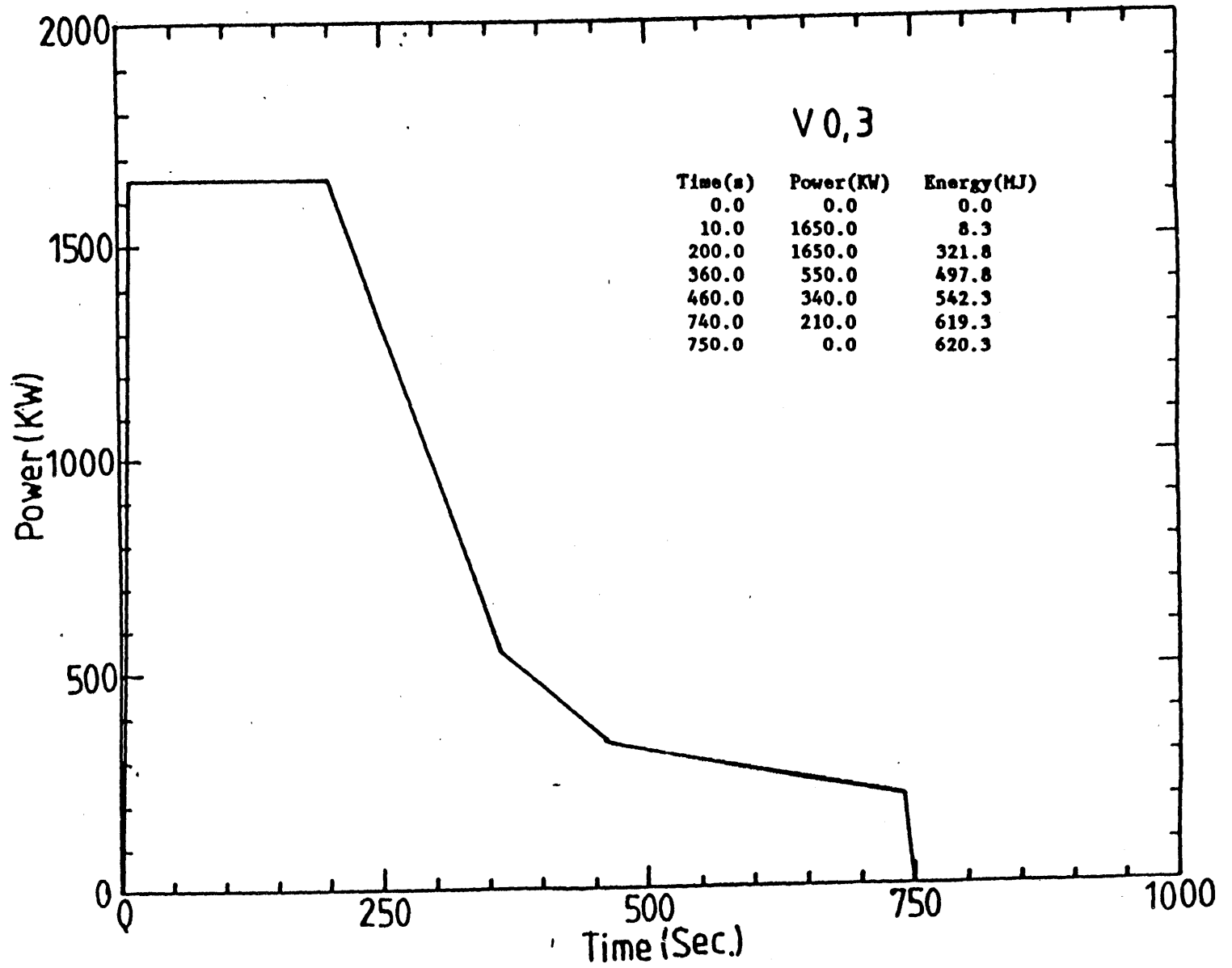
Figure B.2 Power History of BETA Test V0.3
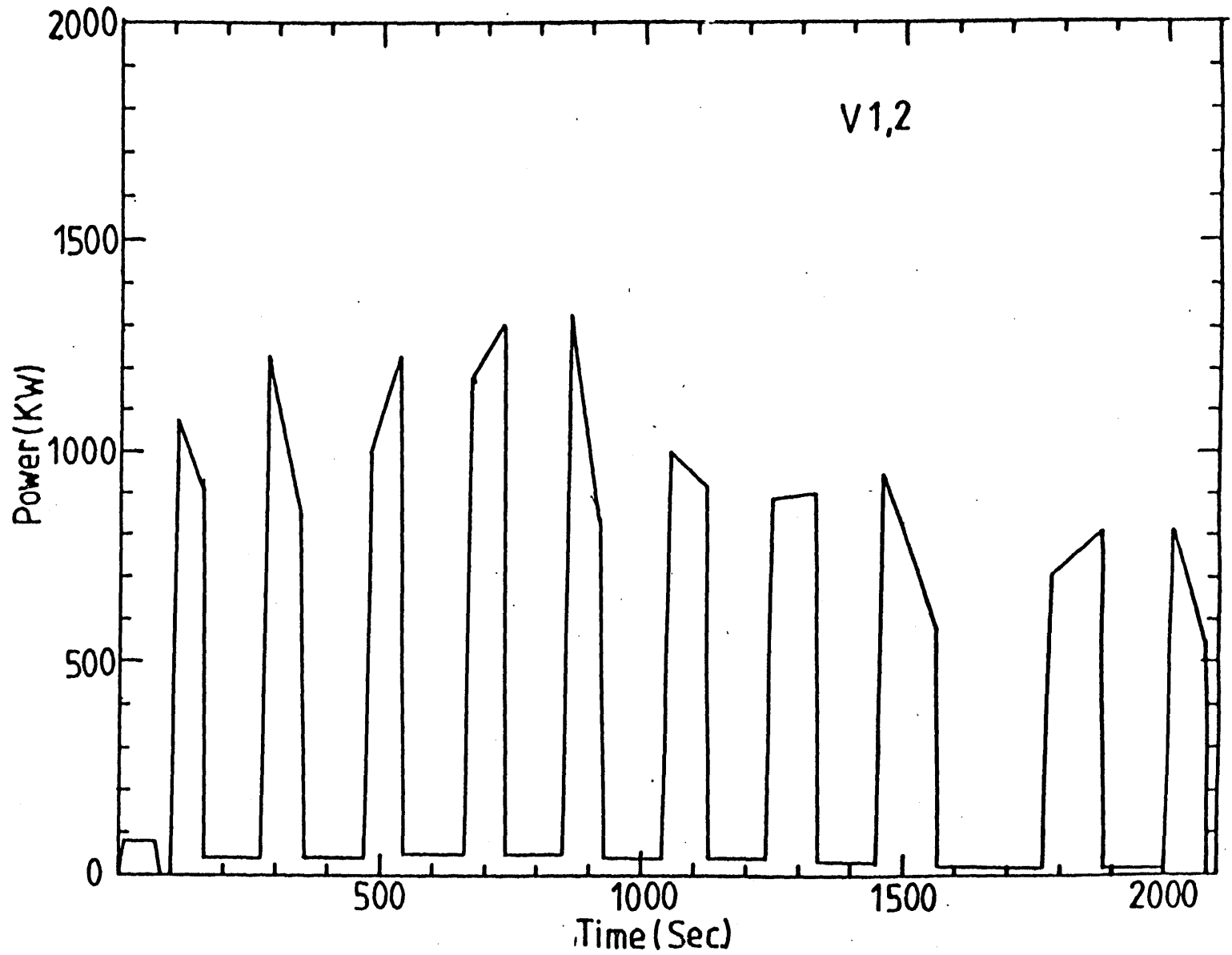
Figure B.3 Power History of BETA Test V1.2

V1.2

Time(s)	Power(KW)	Energy(MJ)
0.0	0.0	0.0
10.0	80.0	0.4
70.0	80.0	5.2
80.0	0.0	5.6
100.0	0.0	5.6
110.0	1070.0	11.0
155.0	910.0	55.5
165.0	40.0	60.3
275.0	40.0	64.7
285.0	1225.0	71.0
345.0	840.0	132.6
355.0	40.0	137.3
470.0	40.0	141.9
480.0	990.0	147.1
535.0	1230.0	208.1
545.0	50.0	214.5
660.0	50.0	220.3
670.0	1180.0	226.4
730.0	1300.0	300.8
740.0	50.0	307.6
850.0	50.0	313.1
860.0	1330.0	320.0
920.0	830.0	384.8
930.0	40.0	389.1
1040.0	40.0	393.5
1050.0	1000.0	398.7
1120.0	920.0	465.9
1130.0	40.0	470.7
1240.0	40.0	475.1
1250.0	890.0	479.8
1330.0	900.0	551.4
1340.0	30.0	556.0
1450.0	30.0	559.3
1460.0	940.0	564.2
1560.0	580.0	640.2
1570.0	20.0	643.2
1770.0	20.0	647.2
1780.0	710.0	650.8
1875.0	810.0	723.0
1885.0	20.0	727.2
2000.0	20.0	729.5
2010.0	810.0	733.6
2075.0	550.0	777.8
2085.0	0.0	780.6

V1,3

Time(s)	Power(KW)	Energy(MJ)
0.0	0.0	0.0
10.0	1020.0	5.1
100.0	1020.0	96.9
220.0	1400.0	242.1
270.0	740.0	295.6
370.0	260.0	345.6
500.0	490.0	394.4
560.0	300.0	418.1
980.0	90.0	500.0
1730.0	70.0	560.0
1740.0	0.0	560.3
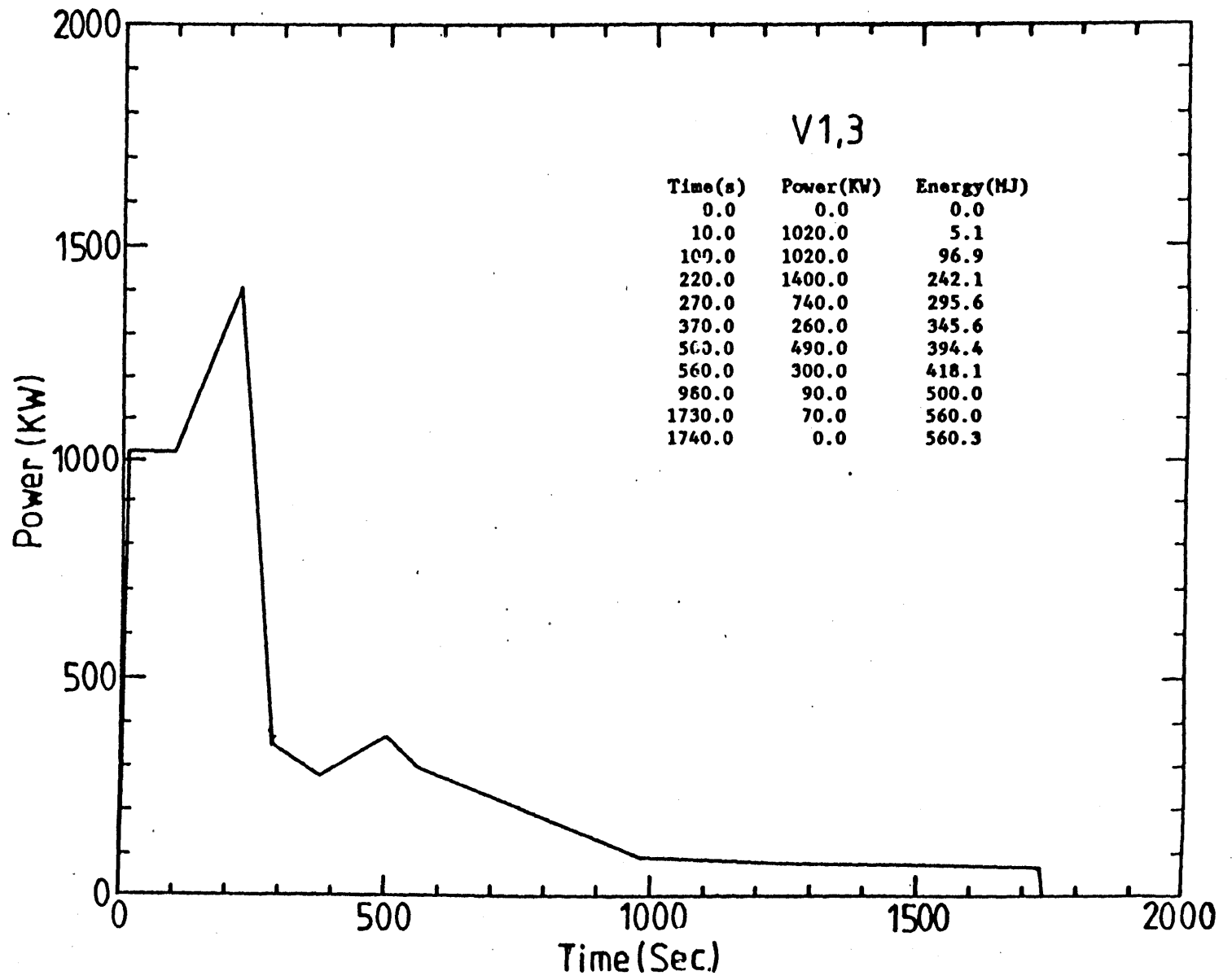
Figure B.4 Power History of BETA Test V1.3
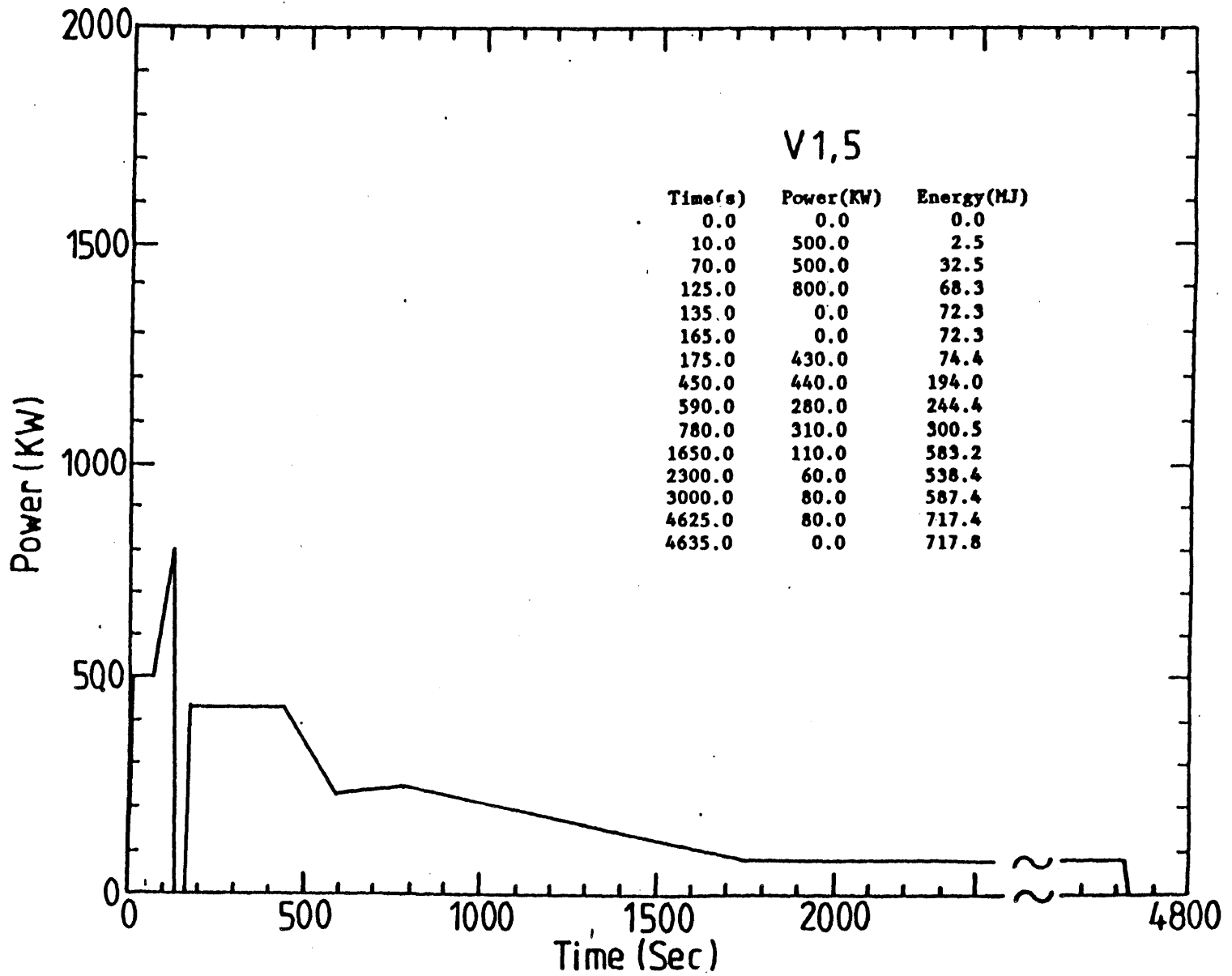
Figure B.5 Power History of BETA Test V1.5

V1,6

Time(s)	Power(KW)	Energy(MJ)
0.0	0.0	0.0
10.0	1080.0	5.4
110.0	940.0	106.4
290.0	1300.0	308.0
350.0	620.0	365.6
750.0	180.0	525.6
1095.9	120.0	577.4
1105.0	0.0	577.9
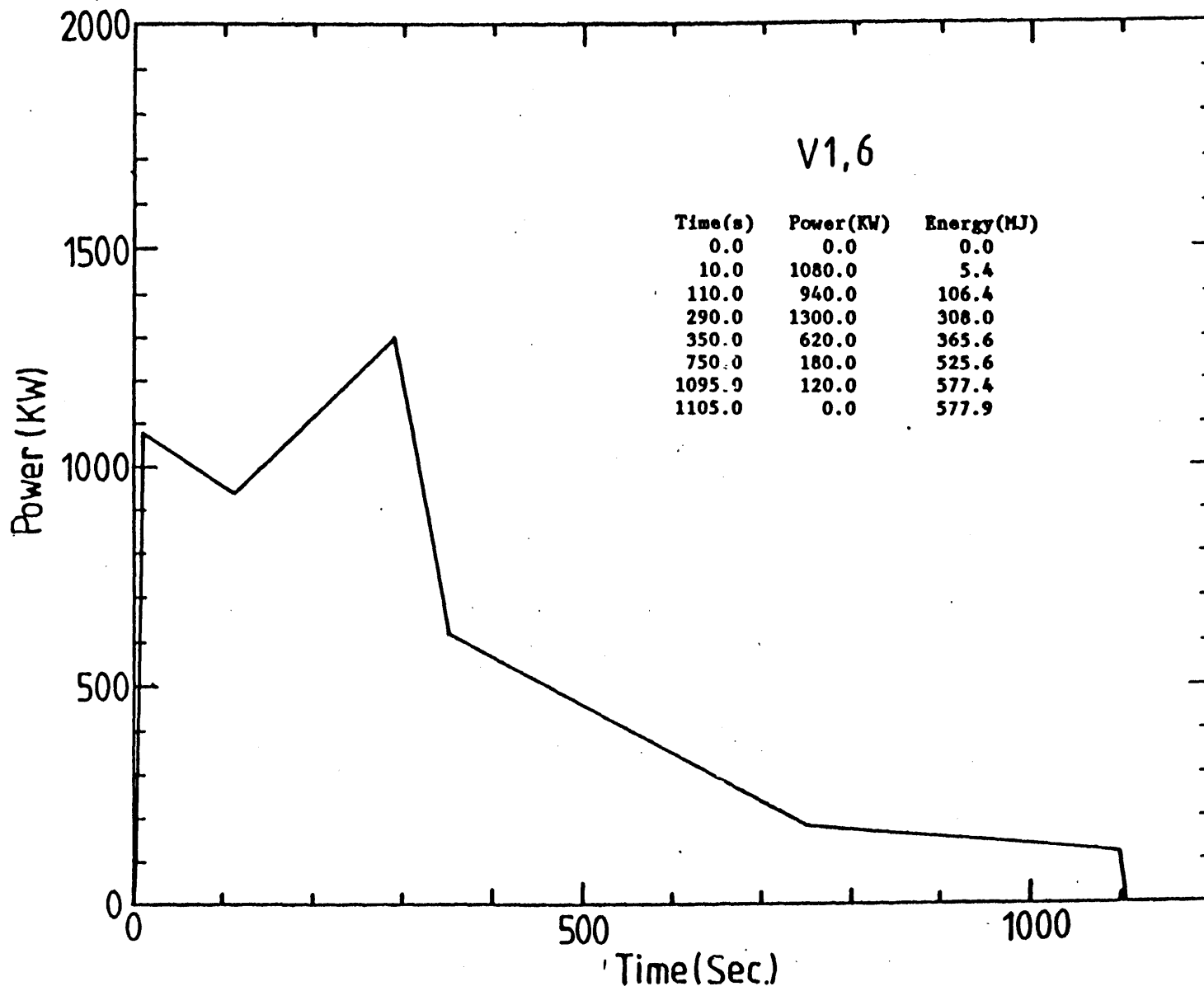
Figure B.6 Power History of BETA Test V1.6
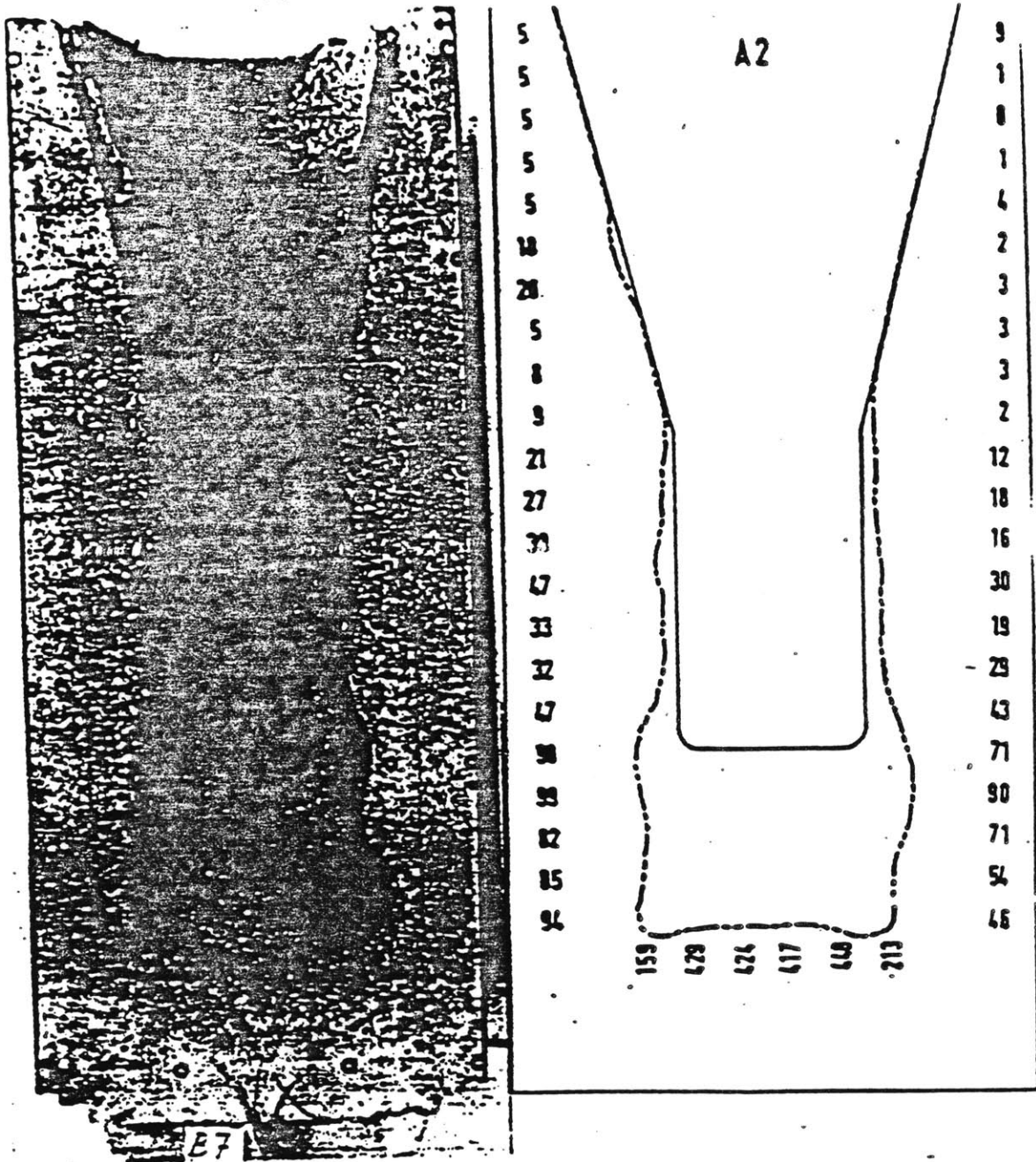
Figure B.7 Post-Test Concrete Crucible of BETA Test V0.2
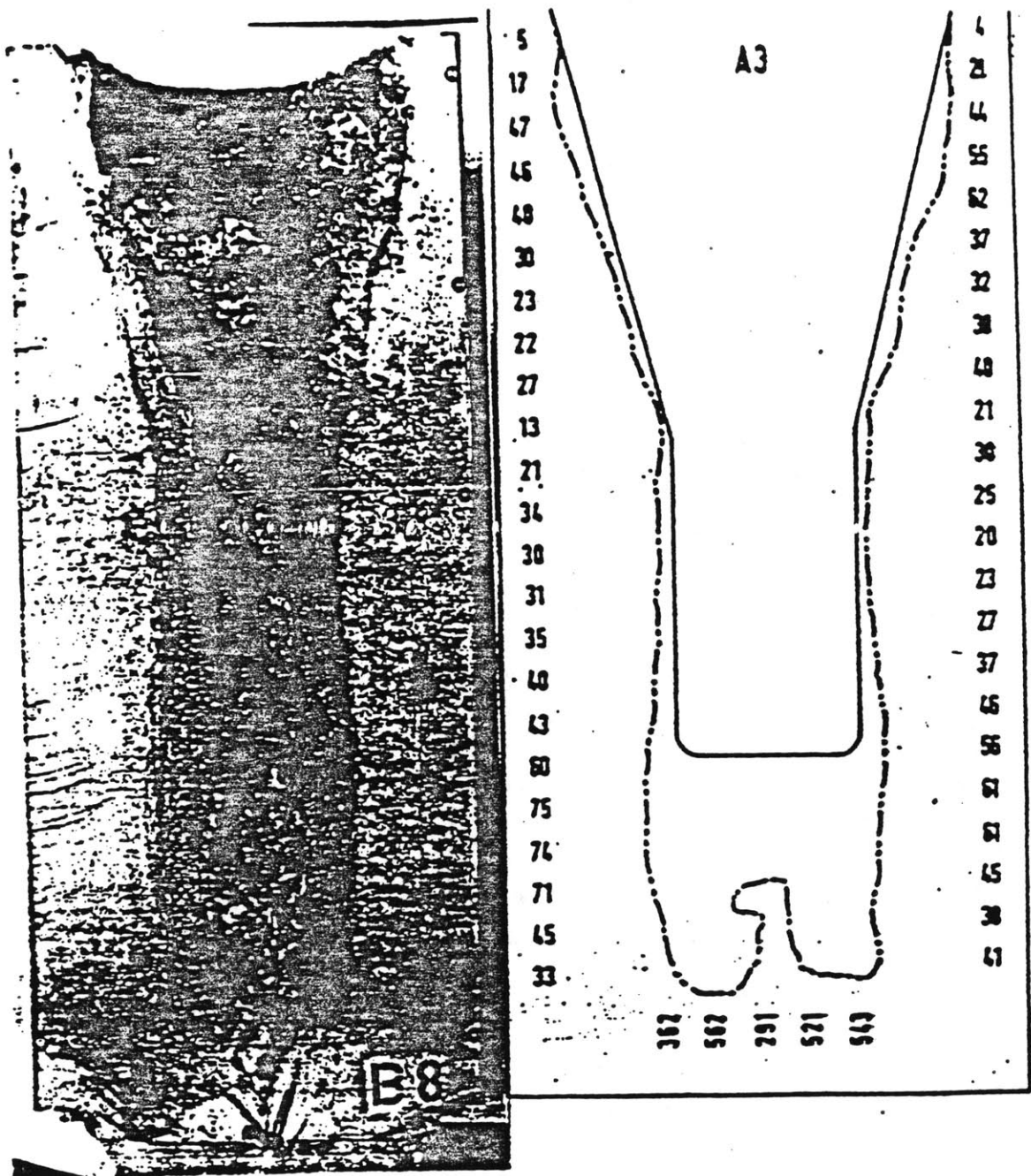
Figure B.8 Post-Test Concrete Crucible of BETA Test V0.3
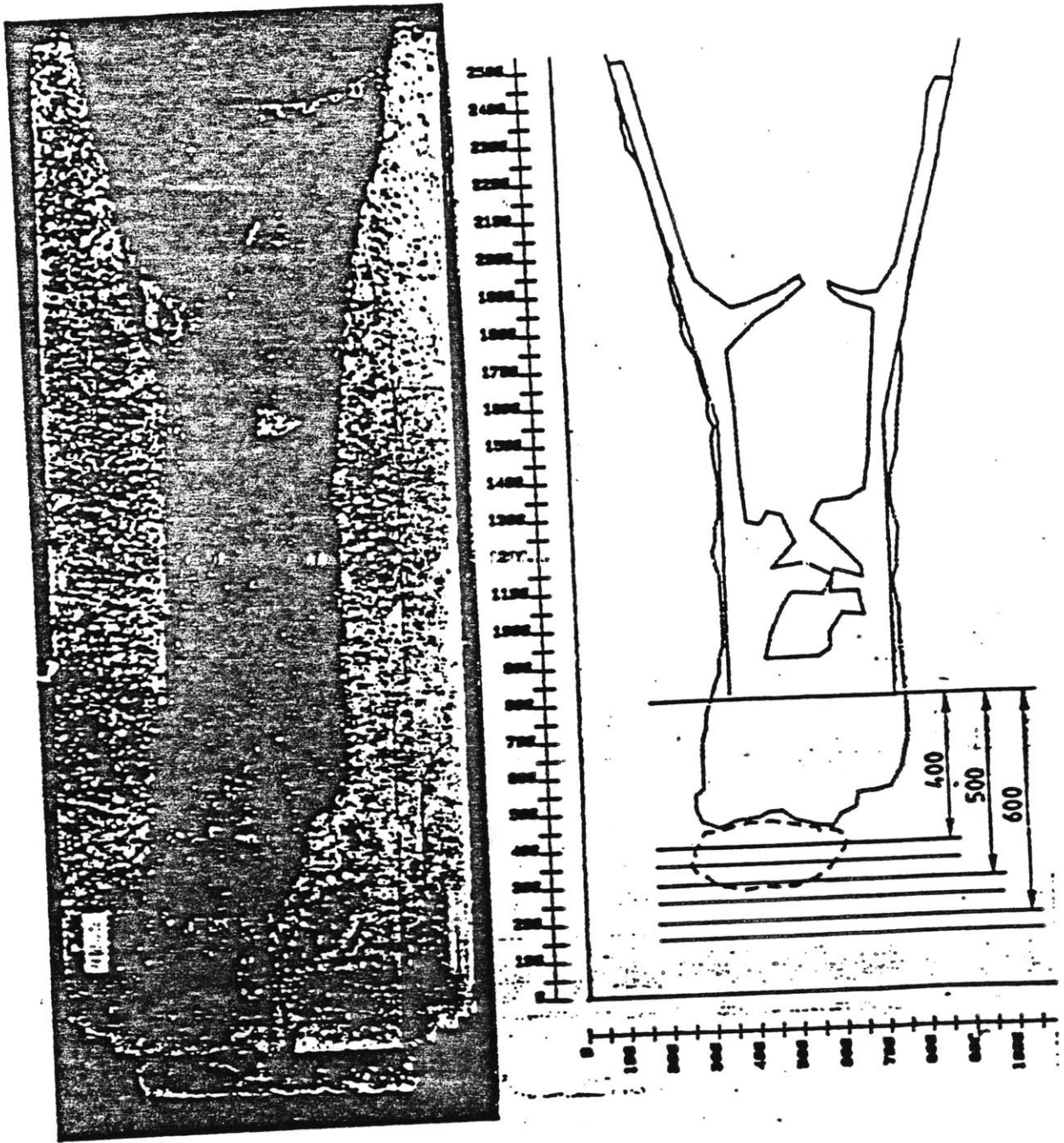
Figure B.9 Post-Test Concrete Crucible of BETA Test V1.2
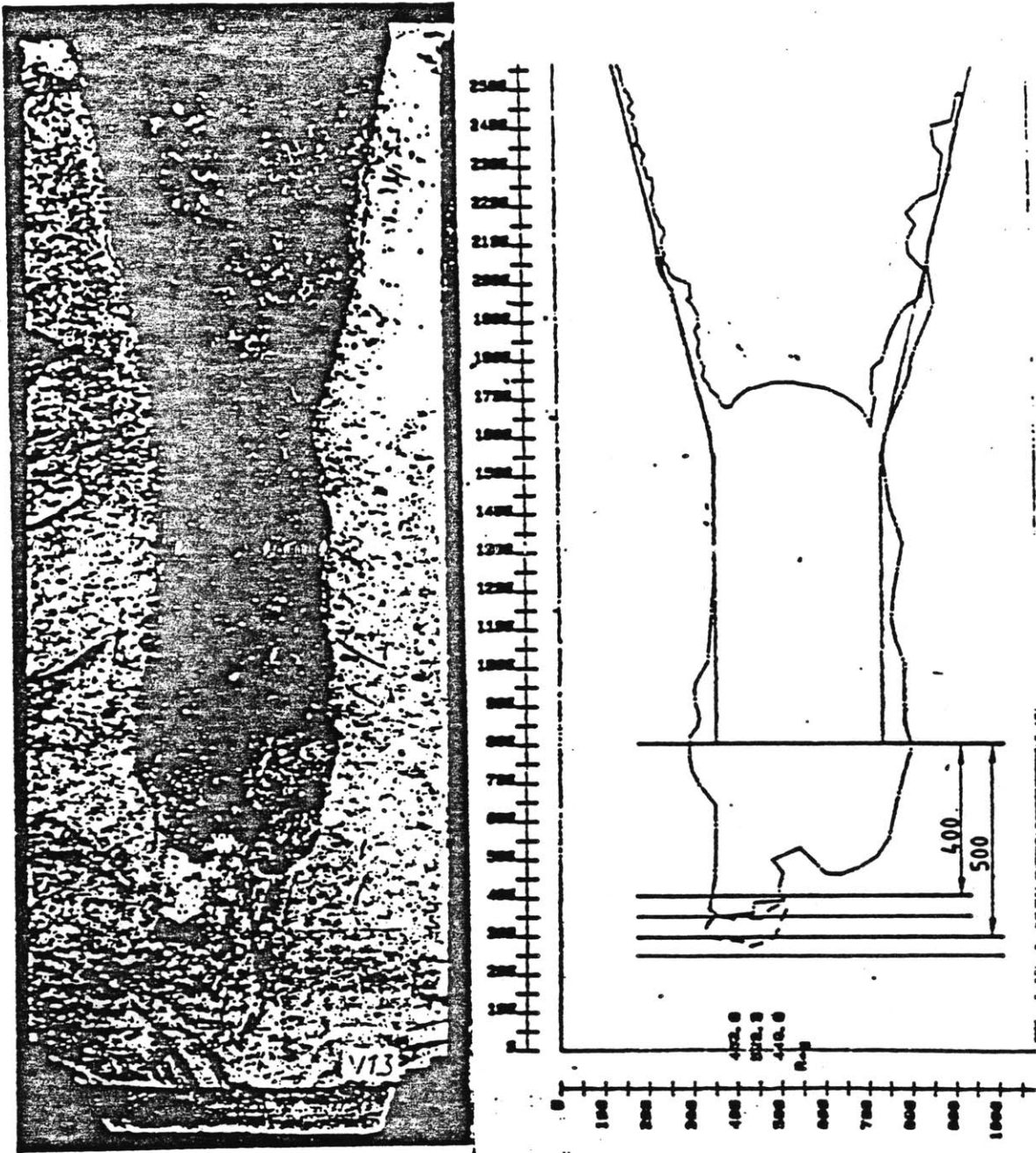
Figure B.10 Post-Test Concrete Crucible of BETA Test V1.3

255
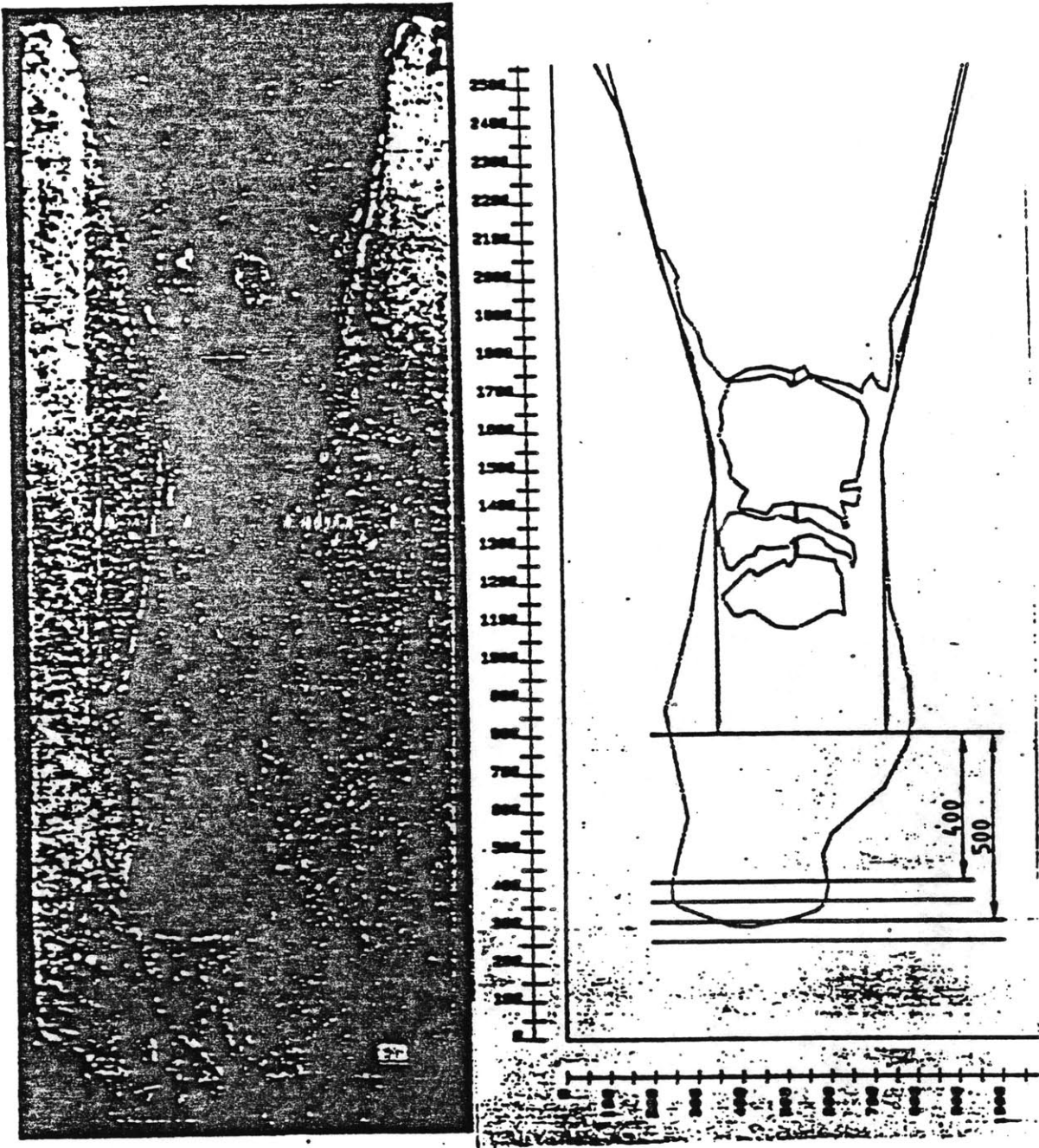
Figure B.11 Post-Test Concrete Crucible of BETA Test V1.5
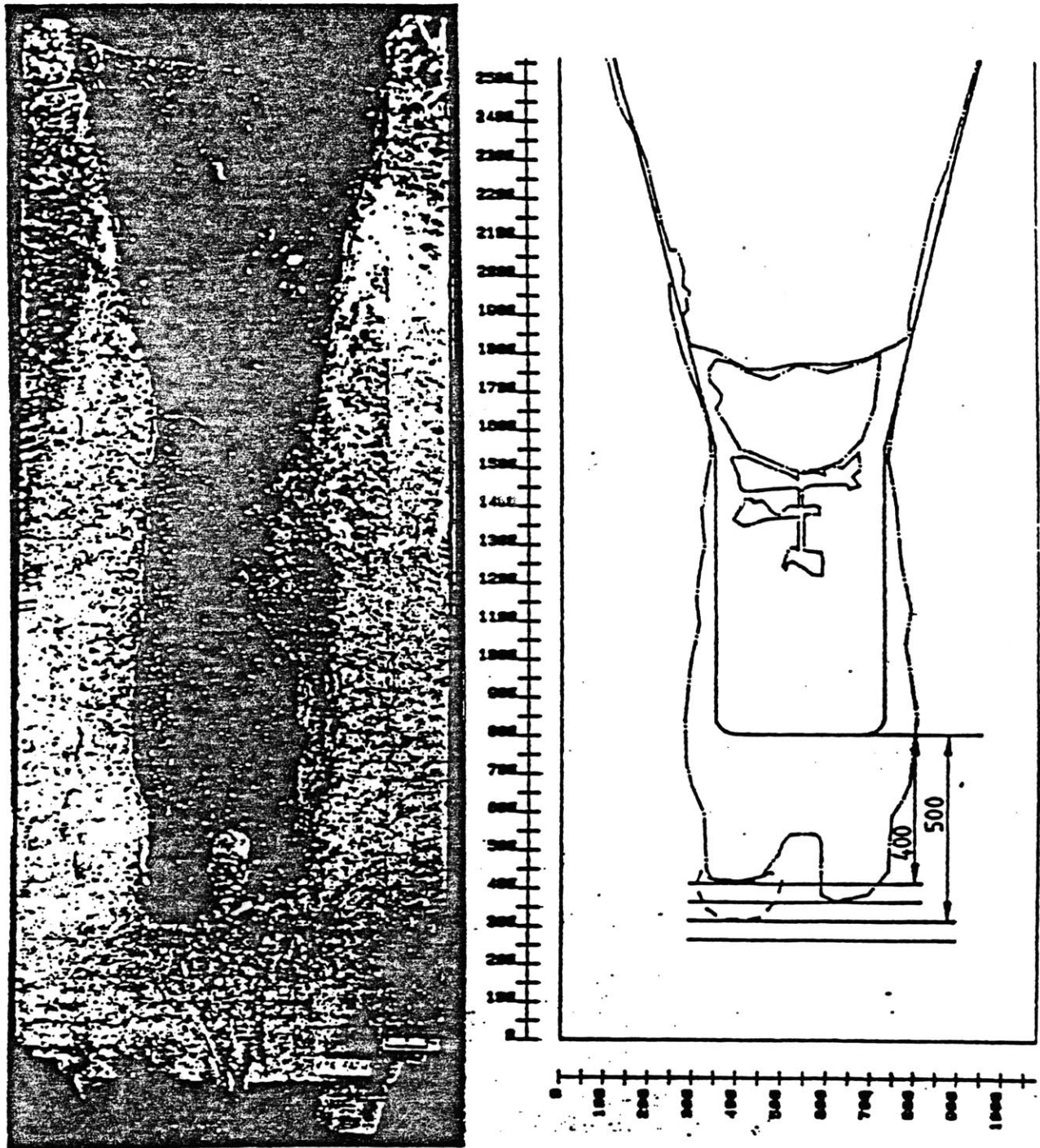
Figure B.12 Post-Test Concrete Crucible of BETA Test V1.6

Appendix D

I Modifications of CORCON/Mod1:

Main Program:

1. Before the calculation proceeds, determine the time step size and print interval according to a user specified table. The corresponding data are read in routine DATAIN and stored in Common Block /MLEE1/

2. Call subroutine INITL0 to process the input data for containment pressure calculation if the option is specified.

3. Call subroutine CPRESS to calculate the containment pressure if the option is specified.

Routine GFLMPR:

1. GFLMPR calculates the gas properties for heat transfer calculation. It calls routines STH2O and STCO2 to determine the physical properties of water vapor and carbon dioxide. The tabulated values in those routines were copied from WECHSL code. The properties of mixture are calculated based on the equation on p.24 of 'Transport Phenomena, Bird et al.'.

Routine MASRAT:

1. The downward heat transfer coefficient for original CORCON film model and MIT model is calculated in routines BOTFIM and BOTMIT respectively.

2. The Flooding and Minimum Stable Film Boiling limits are calculated based on Kutateladze and Berenson criteria respectively. These limits are adjusted by user specified multipliers. The multipliers are read in routine DATAIN and stored in Common Block /MLEE/.

3. The actual heat transfer mode in the calculation of downward heat transfer is

determined by the heat transfer mode of previous time step (variable MOHD) and current calculated superficial gas velocity. The initial value of MOHD is specified by user.

4. A new subroutine BSNFT was written for calculating the transition of heat transfer coefficient from horizontal to vertical interface if the downward heat transfer mode is in pseudo nucleate boiling regime. In BSNFT, it is assumed that heat flux decreases linearly from 15° to 90°.

5. For DO loop 'DO 610 J=1,NRAYS', the erosion rate at body point J is determined by an average of the integrating points between body points J-1 and J−1. The purpose of doing this is to get a better cavity shape.

Routine HPOOL:

1. The MIT interfacial heat transfer correlation has been incorporated as an option. There are also some minor changes in the rest of coding for doing some sensitivity studies.

Routine DATAIN

1. The necessary changes for processing new input data described above.

Routine EDIT

1. The necessary changes for processing new input data described above.

Following subroutines are incorporated to calculate the containment pressure.

Routine INITL0

1. Process the corresponding input data and then calls subroutines QDECAY, MELTDO, ATMGAS and BALANS to calculate the status of the containment at the beginning of Corium/Concrete Interaction.

259

ROUTINE CPRESS

1. Main routine for containment pressure calculation. called by the main program. It updates the energy equation and calls ATMGAS. CONDUT and BALANS to determine the containment pressure.

Routine ATMGAS

1. Update the gas concentration of containment atmosphere. The changes resulting from the generation of concrete decomposition gases and depletion of oxygen by combustion reactions are calculated. The reaction heat of combustion reactions are also calculated in this routine. It is assumed that the reactions will preceed to complete i.e.. one of the reactant depleted.

Routine BALANS

1. Solve the energy equation iteratively to determine the containment pressure.

Routine QUALITY

Calculate the vapor quality of containment atmosphere, called by BALANS. It is part of the iteration loop in BALANS.

Routine CONDUT

1. Calculate the heat conducted into the containement concrete wall.

Routine QDECAY

1. Calcualte the total decay heat generated before the the Crium Concrete Interaction begins. The calculation is based on the correlation used in code RETRAN-02.

Routine STATE

1. Equation of states of water, the correlations are from RETRAN-02.

II. Changes of Input Data

Followings are the modifications to the original CORCON/Mod1 input. The preparation of input data should follow the manual of CORCON/Mod1 and incorporate the following changes.

Card 1

    46 - 50   I5   IPINC   Number of cards for time step control

Card 2

    1 - 10   E10.0   DPRIN   Original CORCON input

    21 - 30   E10.0   TPRIN   Original CORCON input

Card 2a   Totally IPINC cards

    1 - 10   E10.0   DELT   Time step size

    11 - 20   E10.0   TIMEI   Starting time of above time step size

    21 - 30   E10.0   TIMEF   Ending time of above time step size

    31 - 35   I5   IPINE   Print interval

Card 13

    31 - 40   E10.0   CONCK   Thermal conductivity of concrete

Card 35

    1 - 10   E10.0   CCPB   Multiplier for downward heat transfer

    11 - 20   E10.0   CCPT   Multiplier for interficial heat transfer

    21 - 30   E10.0   CCPS   Multiplier for sideward heat transfer

    31 - 40   E10.0   CCAB   Upward convective heat transfer coefficient

    41 - 50   E10.0   CCB1   Some multipliers for the transition between

    51 - 60   E10.0   CCB2   the bottom and sideward heat transfer.

    61 - 70   E10.0   CCB3   (by U. of Wisconsin)

71 - 75	I5	NCCF	Downward Heat Transfer Model
		0:	original CORCON
		1:	Wisconsin
		2:	MIT
		3:	hybrid
		4:	MIT and CORCON combined

Card 36

Card 37   Aerosol gerneration input (by U. of Wisconsin)

Card 38

Card 39

1 - 5	I5	IQULT	
		0:	solidify fraction use temperature ratio
		1:	solidify fraction use enthalpy ratio
6 - 10	I5	ITHKD	
		0:	thermal conductivity based on molar fraction
		1:	thermal conductivity based on weight fraction
11 - 15	I5	ISIGN	
		0:	surface tension based on molar fraction
		1:	surface tension based on weight fraction
16 - 20	I5	IVIS2P	2 - phase multiplier of viscosity
		1:	Kunity model
		2.	Hawkesly model
		3:	Jaki model
21 - 25	I5	KOND	Thermal conductivity of uranium as function of temperature
		1:	C.E. correlation
		2:	Westinghouse correlation
26 - 35	E10.0	SPOWER	Power for slip ratio of MIT correlation

36 - 45   E10.0   WEIGHT   Weight fraction for viscosity calculation

Card 40   only if NCCF equals to 3 or 4

  1 - 5   I5   MODHDO   Downward heat transfer mode

            2:   MIT

            3:   Wisconsin

     other: original CORCON

     (not important if NCCF equals 4)

  6 - 10   I5   MODHSD   Sideward heat transfer mode

            1:   Wisconsin

     other: original CORCON

  11 - 16   I5   MODHIN   Interficial heat transfer model

            2:   MIT

     other: original CORCON

Card 41   only if NCCF equals 4

  1 - 10   E10.0   FLM   Multiplier for flooding limit

  11 - 20   E10.0   SFM   Multiplier for minimun stable film boiling limit

  21 - 25   I5   MOHD   Initial mode for downward heat transfer

            1:   film boiling

            0:   nucleate boiling

Card 42

  1 - 5   I5   IPRESS   Flag for containment pressure calculation

            1:   Yes

            0:   No

  6 - 78   18A4   PTITLE   Problem title of pressure calculation

Following 12 cards are input for containment pressure calculation, only needed if IPRESS equals to 1.

Card 46

    1 - 10   E10.0   WPRM   Amount of primary water (kg)

    11 - 20   E10.0   HPRM   Specific enthalpy of primary water (J/kg)

Card 47

    1 - 10   E10.0   WSPR   Amount of spray water (kg)

    11 - 20   E10.0   HSPR   Specific enthalpy of spray water (J/kg)

Card 48

    1 - 10   E10.0   WACU   Amount of water in accumulatot (kg)

    11 - 20   E10.0   HACU   Specific enthalpy of accumulator water(J/kg)

Card 49

    1 - 10   E10.0   WHUM   Amount of water vapor in atmosphere (kg)

    11 - 20   E10.0   UHUM   Internal energy of water vapor (J/kg)

Card 50

    1 - 10   E10.0   WICE   Amount of ice in the containment (kg)

    11 - 20   E10.0   UICE   Internal energy of ice (J/kg)

Card 51

    1 - 10   E10.0   WSPP   Amount of water in supression pool (kg)

    11 - 20   E10.0   USPP   Internal energy of water in supression pool (J/kg)

Card 52

    1 - 10   E10.0   TOXYNM   Temperature of oxidic phase at normal operation $(^{\circ}K)$

    11 - 20   E10.0   TMETNM   Temperature of metallic phase at normal operation $(^{\circ}K)$

Card 53

    1 - 10   E10.0 HTZRWA   Zr - Water reaction heat before the Corium/ Concrete Interaction (J)

Card 54

    1 - 10   E10.0 QFAN   Heat removal capacity of fan coolers (W)

    11 - 20 E10.0 FNEFF   Operating efficiency of fan coolers

Card 55

    1 - 10   E10.0 STRUCM   Amount of structural can act as passive heat sinks (kg)

    11 - 20 E10.0 STRUCC   Specific heat of structure material $(J/kg\,°K)$

    21 - 30 E10.0 STRUCT   Initial temperature of structure material $(°K)$

Card 56

    1 - 10   E10.0 AIRO2   Amount of O2 in the containment (kg)

    11 - 20 E10.0 AIRN2   Amount of N2 in the containment (kg)

Card 57

    1 - 10   E10.0 CONHTA   Heat transfer area of containment Wall (m^2)

Card 58

    1 - 10   E10.0 PLOW   Lower bound of pressure for iteration (Pa)

    11 - 20 E10.0 PHIGH   Upper bound of pressure for iteration (Pa)

                            (only for first time step)

III. CORCON/Mod1 Input for BETA Test V0.2

```
BETA Test V0.2
    1       0      4      0      0      2      1      0      0      2      0      0      0      0      0
        30.0    10000.0
          5.0         0.0        1000.0    100
         10.0      1000.0        1600.0     50
    61          0.0       0.25
    25          0.14      0.05          2.8
          0.0          1.5
  0.147452   1.499441
  0.161694   1.495048
  0.174009   1.486652
  0.183301   1.474999
  0.188746   1.461125
  0.190000   1.450000
  0.190000   1.390908
  0.190000   1.331818
  0.190000   1.272727
  0.190000   1.213635
  0.190000   1.154545
  0.190000   1.095454
  0.190000   1.036363
  0.190000   0.977273
  0.190000   0.918182
  0.190000   0.859091
  0.190000   0.800000
  0.190000   0.750000
  0.203099   0.690910
  0.216198   0.631820
  0.229296   0.572730
  0.242395   0.513640
  0.255494   0.454550
  0.268593   0.395460
  0.281691   0.336370
  0.294790   0.277280
  0.307889   0.218190
  0.320988   0.159100
  0.334086   0.100010
  0.347185   0.040920
  0.360284  -0.01817
  0.373383  -0.07726
  0.386482  -0.13635
  0.399580  -0.19544
  0.415000  -0.26500
        298.0      1573.0          0.8          0.0
      5
```

```
CACO3              0.066
CA(OH)2            0.073
AL2O3              0.054
SIO2               0.767
H2OEVAP            0.040
    2200.0      1350.0      1650.0         1.59
       0     1  2473.0      2473.0
FE                 300.0
    1000.0      1.05E5      380.0          1
H2                 1.0
    2    18
       0.0         0.0     10000.0         0.0
       0.0         0.0       100.0         0.0      110.0  370000.0      590.0  430000.0
     600.0         0.0       620.0         0.0      650.0  510000.0     1400.0  360000.0
    1810.0    310000.0      1820.0   1600000.0     1835.0 1600000.0     1845.0  310000.0
    1940.0    300000.0      1950.0   2300000.0     1960.0 2300000.0     1970.0  300000.0
    2530.0    240000.0      2540.0         0.0
    2
       0.0       300.0      3000.0      1000.0
TIMETIMETIME
    2     2     2
       0.0         0.8     10000.0         0.8
       0.0         0.8     10000.0         0.8
       0.0         0.8     10000.0         0.8
       1.0       - 1.0         1.0        10.0        1.0       1.0    1.0       4
       0.01        1.0       0.003         0.4      400.0  200000.0 2250000.0
       1000        3.0       0.073      4184.       0.001  0.000036      0.7    -     0.1
       0
       0     0     0     1  10.33333333          1.0
       0     0     2
       0.50        6.00         0
       0
```

```
LARGE DRY PWR: LIMESTONE COMMON SAND            [Base Case]
    0    0    2    2    0    0    1    0    0    3    0    0    0    0    0
        60.0    30000.0
        10.0     7200.0     9000.0    30
        20.0     9000.0    10800.0    30
        30.0    10800.0    14400.0    30
    50           0.0        5.0
         0.0     3.125       10.0       0.1     4.625       1.5     20     2
        298.     1550.        0.8     0.125
     3    3     3100.        3100.
UO2         97890.0
ZRO2        25730.
FEO          5000.0
FE         119000.
NI           9744.
CR          17450.0
        86.3     3411.        0
     5.2528E4  101325.        300.        1
H2O             1.
     2
         0.0      300.     ,300C0.      37P.
TIMETIMETIME
     2    2    2
         0.0       0.8    100000.       0.8
         0.0       0.8    100000.       0.8
         0.0       0.8    100000.       0.8
         1.0       1.0        1.0      10.0       1.0       1.0       1.0    - 4
         0.01      1.0       0.003      0.4      400.   200000.   2250000.
      1000.        3.0       0.073    4184.      0.001   0.000036      0.7       0.1
     0
     0    0    0    1    1    0.33333       0.0
     0    0    2
        .85        1.0        0
     1
     2.3386E5  1.32943E6
     1.0925E5  3.89929E5
     7.0157E5  1.57856E5
     1.0505E3  2.41014E6
         0.0        0.0
         0.0        0.0
      1033.0      620.0
      1.0E11
         7.0E7       0.1
         3.0E6      460.0      450.0
      1.3328E4   4.6672E4
      6.777E3
         1.0E5       6.0E5
```